Initiation of the Wrangell arc: A record of tectonic changes in an arc-transform junction revealed by new geochemistry and geochronology of the ~29–18 ma Sonya Creek volcanic field, Alaska

by

Samuel Ethan Berkelhammer

B.S., University of Puget Sound, 2013

A THESIS

submitted in partial fulfillment of the requirements for the degree

MASTER OF SCIENCE

Department of Geology
College of Arts and Sciences

KANSAS STATE UNIVERSITY
Manhattan, Kansas

2017

Approved by:

Major Professor
Matthew Brueseke

Abstract

The Sonya Creek volcanic field (SCVF) contains the oldest *in situ* magmatic products in the ~29 Ma–modern Wrangell arc (WA) in south-central Alaska. The WA is located within a transition zone between Aleutian subduction to the west and dextral strike-slip tectonics along the Queen Charlotte-Fairweather and Denali-Duke River fault systems to the east. WA magmatism is due to the shallow subduction (11–16°) of the Yakutat microplate. New $^{40}Ar/^{39}Ar$ and U-Pb geochronology of bedrock and modern river sediments shows that SCVF magmatism occurred from ~29–18 Ma. Volcanic units are divided based on field mapping, physical characteristics, geochronology, and new major and trace element geochemistry. A dacite dome yields a ~29 Ma $^{40}Ar/^{39}Ar$ age and was followed by eruptions of basaltic-andesite to dacite lavas and domes (~28–23 Ma Rocker Creek lavas and domes) that record hydrous, subduction-related, calc-alkaline magmatism with an apparent adakite-like component. This was followed by a westward shift to continued subduction-related magmatism without the adakite-like component (e.g., mantle wedge melting), represented by ~23–21 Ma basaltic-andesite to dacite domes and associated diorites ("intermediate domes"). These eruptions were followed by a westward shift in volcanism to anhydrous, transitional, basaltic-andesite to rhyolite lavas of the ~23–18 Ma Sonya Creek shield volcano (Cabin Creek lavas), including a rhyolite ignimbrite unit (~19 Ma Flat Top tuff), recording the influence of local intra-arc extension. The end of SCVF activity was marked by a southward shift in volcanism back to hydrous calc-alkaline lavas at ~22–19 Ma (Young Creek rocks and Border Lavas). SCVF geochemical types are very similar to those from the <5 WA, and no alkaline lavas that characterize the ~18–10 Ma Yukon WA are present. Sr-Nd-Pb-Hf radiogenic isotope data suggest the SCVF data were generated by contamination of a depleted mantle wedge by ~0.2–4% subducted terrigenous sediment, agreeing with geologic evidence

from many places along the southern Alaskan margin. Our combined dataset reveals geochemical and spatial transitions through the lifetime of the SCVF, which record changing tectonic processes during the early evolution of the WA. The earliest SCVF phases suggest the initiation of Yakutat microplate subduction. Early SCVF igneous rocks are also chemically similar to hypabyssal intrusive rocks of similar ages that crop out to the west; together these ~29–20 Ma rocks imply that WA initiation occurred over a <100 km belt, ~50–60 km inboard from the modern WA and current loci of arc magmatism that extends from Mt. Drum to Mt. Churchill.

Table of Contents

List of Figures

List of Tables

Acknowledgements

I could not have accomplished this task without the help, support, guidance, and love of many people. None of this would have been possible without funding from NSF grants awarded to Dr. Matt Brueseke at Kansas State University (EAR-1450689), Drs. Jeff Benowitz and Paul Layer at University of Alaska Fairbanks (EAR-1450730), and Dr. Jeff Trop at Bucknell University (EAR-1450687). Additionally, a UAF-Undergraduate Research and Scholarly Activity grant awarded to Kailyn Davis assisted with field work. Thank you to Lori Page-Willyard for patiently putting up with my recurring financial problems, and helping me through them. Thank you to the friendly folks at Bluestem Bistro for providing an enjoyable atmosphere outside of Thompson Hall to get work done, and the coffee and food to do it. Thank you to Paul and Deana Strunk for their generous scholarship for the 2016-2017 school year.

Thank you to Stan Mertzman at Franklin & Marshall College for speedy major and trace element analyses. Thanks to Jeff Vervoort and Scott Boroughs at the GeoAnalytical lab at Washington State University for handling the bulk of our geochemical analyses, including invaluable rare earth element and radiogenic isotope data. Thank you to pilot Kirk Ellis of Nabesna, AK for spending long days flying us to study areas and keeping an eye on the weather for us. Thanks to Cole Ellis for helping fly when we needed to come home quickly, and the whole Ellis family for allowing us to camp dangerously close to their airstrip. Legendary Alaskan pilot and backcountry hunting guide Urban Rahoi graciously let us occupy his horse shed at Ptarmigan Lake Lodge for over a week, and Jeff Harris lent advice on how to access areas of interest, gave us ATV and boat rides, and cooked us crab cakes and crockpot moose.

Photographer Todd Paris from UAF documented our first few days with amazing photography, and provided good company. Paul Layer from UAF has worked on Alaskan

geology for decades, and took time from his busy schedule to fly into the wilderness for a few days, as well as provided geochronology data. Kailyn Davis was the only other student in the field with a bunch of (old) professors, and was an asset when I needed photographs or geochronology advice after the fact.

Jeff Benowitz provided us with our geochronological data and was in perpetual contact as this project developed. Just as importantly, however, he shared his extensive knowledge on how to conduct field work in the extreme terrain of Alaska, and offered bad jokes, good jokes, extra food, and Scandinavian mystery novels. Mazel Tov!

Jeff Trop is a two-decade veteran on southern Alaskan geology and I learned a lot from his field work experience. As a committee member, he has given me valuable edits and insightful comments on my writing and the many figures in this document, as well as reassurance that the hard work will pay off in the end. He made sure that this project and I were ready to contribute to the state of knowledge. He also carried a shotgun the whole time in the field, and only had to use it twice! (Side note: thank you to Knucklehead, the adolescent black bear, for leaving us alone. Eventually).

Thank you to Pamela Kempton for being an amazing head of the geology department, and for her patience with my many questions about isotopes, and guidance about how to present the accuracy and precision of my data. She helped turn this thesis from a cool project on Alaskan volcanic rocks into a professional piece of science. The department is in good hands.

I couldn't have done this without Beth Morter and her indispensable friendship and solidarity during long weeks and months of crushing rocks. Other friends that were shipmates on a similar boat: Jacob, Grant, Kyle, Katie, Michelle, Brooks, Ian, Colleen, Ben, Anna, Austin, Trenton, Brent, David, Victoria, Ryan, Eric, Maridee, Mikaela, Dr. Matt Kirk, Dr. Joel Spencer,

Roxy T. Dog, John, Samantha, Stephen, Sophie, Ryan, Leah, Kent, Eric, Anne, Priscilla, various frisbee people.

Matt Brueseke took a chance on me when he chose me for this project, after a gap of two years following only two weeks together at field camp in 2013, and I owe him a lot. The prospect of a month of field work in the wilderness of Wrangell–St. Elias National Park was too good to pass up, but it turned out that this project truly captivated my curiosity, and conversations with Matt simulated my interest to really dig into the data. He let me run new ideas by him, and would do the same with me. He had the important task of keeping the project in check and pulling me back when I started to go down a rabbit hole, but he always encouraged me go the extra step and to push through to the end. Thank you.

Thanks to my family (Mom, Dad, Sara, Casey T. Dog, Minerva, Mischief, Fish #1-37) for picking up the phone when I called, for making the trip to Kansas a few times to visit, and for always supporting me. I promise I won't make you read the whole thing. I love you.

Finally, I wouldn't have been able to get through the past two years (at least with any sense of sanity) if an amazing person at Graduate Student Orientation hadn't asked me if I wanted to ride bikes. CC, thank you for your patience, kindness, and your sense of humor. Thank you for showing me to how to float a river, and for introducing me to the microbes that are all around us. Thank you for being there for me, always.

Dedication

This thesis is dedicated to the memory of my grandfather, Ronald K. Ogle, whom we lost in December 2015. He completed a Master's in Geology in 1959, and worked as a seismologist in the petroleum industry for decades, including some time close to the study area of this thesis in the Gulf of Alaska. It was too late that he and I discovered our shared love of the earth, and I wish he could see what I have accomplished.

Chapter 1 - Introduction

Objectives

This study presents new data on the physical, spatial, and temporal characteristics of a largely unstudied volcanic field within the Wrangell Arc in south-central Alaska. The primary objective of this thesis is to evaluate the geochemical, isotopic, geochronologic, and stratigraphic characteristics of the volcanic and shallow intrusive rocks of the Sonya Creek volcanic field (SCVF), with the goal of constraining their petrogenetic processes and tectonic setting in which they originated.

Regional Tectonic Framework

Convergent margins worldwide ubiquitously contain a "transition zone" between a volcanic arc and a transform boundary (e.g., Central America, Tibaldi et al., 2010; Kamchatka, Park et al., 2002; the Philippine Sea region, Fitch, 1972). The position of the actively subducting slab and translation of the upper plate along strike-slip faults occurs as the directions and rates of plate convergence change, and these variations are recorded in the volcanic arc portion of the arc-transform transition zone (Park et al., 2002; Portnyagin et al., 2005).

Along-strike variations in tectonic style of convergence create a wide range of geochemistries, from "typical" calc-alkaline magmas normally associated with subduction zones, to alkaline magmatism associated with upwelling asthenosphere around slab-edges/windows and "leaky" strike-slip faults. In these complex tectonic settings, the geochemistry of an erupted magma will depend on proximity to intrabelt strike-slip faults and slab-edges (Thorkelson and Taylor, 1989: Maury et al., 2004). Additionally, the angle of the subducted slab plays a control on magma geochemistry, position of the volcanic arc, and deformation of the overlying plate. Flat slab subduction is a feature of ~10% of modern convergent plate margins (Gutscher et al.,

2010), which adds an increased role for slab-edge effects as a control on magma geochemistry and eruptive frequency of these volcanic belts (Portnyagin et al., 2005; Gutscher et al., 2010).

The northeastern Pacific plate margin is characterized by northward convergence with the North American plate along the southern Alaskan margin, and shows a west to east transition from typical subduction to shallow-slab subduction to strike-slip tectonics (e.g., Eberhart-Phillips et al., 2006; Hauessler, 2008; Gulick et al., 2013) (Fig 1.1). Previous geochemical studies, as well as the new data presented here, show that subduction-related magmatism in the Wrangell Mountains of south-central Alaska has been active since at least ~30 Ma, based on calc-alkaline to transitional geochemistries of sampled eruptive products (Nye, 1983; Richter et al., 1990; Skulski et al., 1991, 1992; Preece and Hart, 2004; Trop et al., 2012), and the presence of a geophysically imaged northward-dipping subducting slab (Eberhart-Phillips et al., 2006; Bauer et al., 2014) (Fig. 1.1). However, there is little evidence of a subducting slab forming an arcuate chain of volcanoes (i.e., a "typical" volcanic arc) across the entire Wrangell Mountains throughout the entire history of the subduction zone. In Yukon Territory, Miocene volcanic centers are spatially correlated along strike-slip faults and show alkaline, transitional, and calc-alkaline geochemical affinities, suggesting that volcanism along "leaky" strike-slip faults was important, due in part to low-degree melting of upwelling asthenosphere in an extensional regime, as well as subduction-related processes (Skulski et al., 1991, 1992). Further inboard is a broad province of alkaline volcanism that formed in response to changes in Pacific plate convergence angles and rates (Edwards and Russel, 1999; 2000). Richter et al., (1990) demonstrated that calc-alkaline volcanism in the Wrangell Mountains has shown a northwestward migration from ~26–0.2 Ma, and Preece and Hart (2004) showed that subduction, slab-edge effects, and intra-arc extension controlled magma geochemistries of <5 Ma volcanic

rocks. Changes in the relative locations of volcanism in the upper plate, as controlled by the position of the subducting slab and strike-slip faults, as well as variations in magma geochemistry, are common features of volcanic fields in arc-transform transition zones (Park et al., 2002).

In the western region of the arc-transform transition zone, subduction of Pacific oceanic lithosphere produces a Wadati-Benioff zone that reaches 100-150 km depth within ~400 km of the trench, and is responsible for the well-defined Aleutian volcanic arc (Fig. 1.1). In the central region, from approximately 145°-152° west longitude, the Yakutat microplate is subducting below southern Alaska (Fig. 1.1). Based on seismic and drilling data, the Yakutat microplate is interpreted to represent anomalously thick and buoyant oceanic crust that originated at lower latitudes and has been translated northward to its current position along right-lateral transform faults (Plafker and Berg, 1994; Pavlis et al., 2004; Gulick et al., 2007; Worthington et al., 2012). The Yakutat microplate increases in thickness from 15 km in the west to 30 km in the east, and subduction and underthrusting has resulted in increased topography and exhumation in the Chugach and St. Elias Ranges on the overriding Alaskan continental crust (Enkelmann et al., 2010; Finzel et al., 2011; Worthington et al., 2012; Pavlis et al., 2014; Falkowski et al., 2014; Enkelmann et al., 2017). The Yakutat microplate is bounded to the northwest by the Aleutian megathrust, to the north by the Chugach-St. Elias thrust fault, the east by the Fairweather right-lateral transform fault, and to the southwest by the Transition fault (Fig. 1.1). The modern rate of Yakutat subduction is ~45-46 mm/yr to the northwest (Fletcher and Freymueller, 2003; Elliot et al., 2010), and the subducted portion of the Yakutat microplate extends for ~250 km to the northwest at a ~6° angle, and ultimately reaches a depth of 150 km below the Alaska Range, more than 600 km from the trench (Eberhart-Phillips et al., 2006). Recent geophysical studies

beneath south-central Alaska reveal an eastward increase in the angle of the subducted Yakutat slab, from ~6° below the Talkeetna Mountains, and ~11° to 16° below the volcanoes of the Wrangell Mountains, with a projected depth of 80 km to the top of the slab (Bauer et al., 2014). Previously termed the Wrangell volcanic field (Richter et al, 1990) and the Wrangell volcanic belt (Skulski et al., 1991; Preece and Hart, 2004), we propose that the linear chain of young volcanoes located above this seismically-imgaed subduction zone should be called the Wrangell Arc (WA).

The eastern region of the tectonic transition zone displays active volcanism in the Wrangell arc, shallow seismicity (<50 km), and displacement along the Denali-Duke River, Totschunda, and Fairweather right-lateral strike-slip fault systems (Page et al., 1991; Eberhart-Phillips et al., 2003; Preece and Hart, 2004; Qi et al., 2007; Benowitz et al., 2011) (Fig. 1.1). The paucity of earthquakes along the section of the Denali fault adjacent to the Wrangell Mountains suggests that the eastern section of the fault is relatively inactive (Page et al., 1991; Matmon et al., 2006). The Totschunda and Fairweather faults instead accommodate a large component of right-lateral motion. A possible connecting fault that links the Totschunda and Fairweather may strike to the southeast between the two faults (Richter and Matson, 1971; Kalbas et al., 2008), or alternatively take a westward bend and merge with thrust faults that accommodate compressive forces (Fig 1.1) (Doser and Lomas, 2000; Doser, 2014). The entire Denali-Duke River-Totschunda fault system comprises a northward extension of right-lateral transform motion between the Pacific plate and Yakutat microplate past the North American continent along the Queen Charlotte-Fairweather fault systems (Kalbas et al., 2008). Aberrations from pure strike-slip motion along this complex system result in localized areas that show components of extension or compression. It is in this complex setting that the WA is located. Recent studies

have provided major advancements in the understanding of recent (e.g., Neogene) deformation in the zone between Yakutat convergence and the former continental margin in south-central Alaska (e.g., Gulick et al., 2007; Enkelmann et al., 2010; Worthington et al., 2012; Pavlis et al., 2014; Falkowski et al., 2014; Finzel et al, 2015; Finzel et al, 2016; Enkelmann et al, 2017), but the connection between subduction of the northeastern corner of the Yakutat microplate and volcanism in the WA remains largely understudied, including the earliest phases of volcanism.

Wrangell Arc Geology- Underlying Rocks and Wrangell Arc Volcanic Rocks

The Wrangell Mountains and record deformation and uplift of the Wrangellia composite terrane basement rocks, intra-arc extension and deposition, and ~30 million years of subduction-related arc volcanism (Richter et al., 1990; Skulski et al, 1991, 1992; Miller and Richter, 1994; Enkelmann et al., 2010). The WA covers >25,000 km^2 of eastern Alaska, southwestern Yukon Territory, and northwestern British Columbia, and is comprised of ice-covered peaks that exceed 4,900 meters in elevation. The volcanic products of the WA are Oligocene-Holocene (~30 Ma-1500 ka) in age, and are comprised of lava flows, domes, and pyroclastic deposits that erupted from shield volcanoes, stratovolcanoes, caldera complexes, volcanic domes, and cinder cones, as well as relatively minor volcaniclastic deposits that accumulated in intra-arc basins (Skulski et al., 1992, 1992; Richter et al., 2006; Trop et al., 2012). Shallow intrusive rocks crop out in the central and eastern WA, and are interpreted to be sub-volcanic roots of eroded overlying volcanoes (Richter et al., 2000; Trop et al., 2012). WA volcanic and volcaniclastic rocks primarily overlie deformed rocks of the Wrangellia composite terrane (which includes Paleozoic to Mesozoic sedimentary rocks, and a swarm of Cretaceous plutons), and have a preserved thickness of greater than 2 km in places, especially in the central and western WA (i.e., west of ~142.5° W) (Richter, 1976; MacKevett, 1978; Richter et al., 2006).

The age, geochemical characterizations, and structure of WA volcanic rocks vary with position across the arc. WA volcanic rocks in southwestern Yukon Territory and northwestern British Columbia crop out in a discontinuous chain for >300 km along segments of the Duke River and Denali faults (Fig. 1.1). Individual volcanic centers include the Klutlan and Wolverine centers (collectively form the St. Clare Creek volcanic field), Nines Creek, Alsek, and Stanley Creek centers. These volcanic centers are principally comprised of Miocene lavas, with subordinate pyroclastic, intrusive, and sedimentary rocks (Souther and Stanciu, 1975; Dodds and Campbell, 1988; Skulski et al., 1991; 1992; Israel et al., 2005; Israel et al., 2007; Israel and Cobbett, 2008a; Israel and Cobbett, 2008b; Cobbett, 2012; Cobbett, 2013a; Cobbett, 2013b; Israel et al., 2014; Colpron et al., 2016). Underlying these later packages are Eocene-Oligocene sedimentary rocks of the Amphitheater Formation (Cole and Ridgway, 1993; Ridgway and DeCelles, 1993). The Duke River fault cuts the lower sections of these eastern WA lavas, and some sections may be cut by related faults (Souther and Stanciu, 1975; Skulski et al., 1992; Colpron et al., 2016). Eastern WA volcanism is attributed to eruption of lavas along strike-slip faults, based on the presence of primitive alkaline and transitional to calc-alkaline volcanic rocks and their spatially limited extent proximal to large strike-slip faults (Skulski et al., 1991, 1992). Calc-alkaline volcanic rocks are attributed to subduction, and the small-volume of alkaline volcanic rocks is attributed to low-degree melting of asthenosphere and lithospheric mantle following mantle upwelling around the edge of the slab and through a slab-window (Thorkelson et al., 2011). A younger analog to the alkaline magmatism found in the Canadian (eastern) WA is the Neogene-Quaternary Northern Cordilleran volcanic province that ranges ~1200 km from central Yukon Territory to central British Columbia (Edwards and Russell, 1999; 2000).

The central WA stretches from the Alaska-Yukon border to Mt. Blackburn, at roughly 143° west longitude (Fig. 1.1) The central WA is underlain by rock units of the Wrangellia composite terrane, which includes Pennsylvanian-Permian to Cretaceous sedimentary and igneous rocks (Richter, 1976; MacKevett, 1978). Middle Cretaceous intrusive rocks include at least eight distinct plutons. The south flank of the central WA includes the Miocene Fredericka Formation, which records intra-arc transtensional basin subsidence and sedimentation accommodated along north-striking normal faults, followed by progradation of lavas into these basins (MacKevett, 1978; Richter et al., 2000; Eyles and Eyles, 1989; Trop et al., 2012). The uppermost stratigraphy of the central WA is comprised of late Miocene and younger WA lavas and subordinate pyroclastic, intrusive, and sedimentary rocks (Richter, 1976; MacKevett, 1978; Trop et al., 2012). Late Miocene-1500 ka WA volcanism is dominantly characterized by lavas that erupted from shield volcanoes, cinder cones, silicic domes, and small plugs. The adakitic White River Ash is a product of the Holocene Plinian eruption (volcanic explosivity index of 6) from Mount Churchill, a large stratovolcano (Lerbekmo and Campbell, 1969; McGimsey et al., 1992; Richter et al., 1995; Lerbekmo, 2008; Preece et al., 2014). Shallow intrusive and hypabyssal rocks that are coeval with WA volcanic rocks are likely the sub-volcanic roots of eroded volcanic centers (MacKevett, 1978; Trop et al., 2012). Geochemistry of volcanic rocks in the central WA is “typical” of that produced by subduction-related processes, as well as minor intra-arc extension (Preece and Hart, 2004; Trop et al., 2012).

The western WA includes the most recent volcanic activity, expressed as Pliocene-Holocene/modern shield volcanoes, stratovolcanoes, and smaller cinder cones that are covered extensively by ice caps and glaciers at higher elevations (Fig. 1.1; Richter et al., 1990; 1995; 2006). Mount Wrangell (4317 m), and andesitic shield, is the largest volcano in the WA by

volume and has shown occasional historic activity (~1800 A.D.) at the summit caldera, and fumarole activity is common (Nye, 1983; Richter et al., 1990). To the west and north of Mt. Wrangell are Mt. Drum (3661 m), a large stratocone, and Mt. Sanford (4949 m), a large composite shield volcano, respectively, which are less than ~0.7 Ma in age (Richter et al., 1990; 1994). Capital Mountain and Tanada Peak are examples of older (~1 Ma and ~1–2.2 Ma, respectively) erosional remnants of shield volcanoes with summit calderas filled with thick (~900-1200 m) intracaldera lavas. The Skookum Creek volcanic center is a ~3.25–2.25 Ma shield volcano complex, with multiple overlapping phases of volcanism (Preece, 1997; Preece and Hart, 2004). The geochemistry of western WA volcanic rocks is broadly similar to volcanics of the central WA, showing transitional to calc-alkaline affinities, except for adakitic characteristics found at Mt. Drum and Mt. Churchill, which suggests the role of slab-melt (Preece and Hart, 2004; Preece et al., 2014). Western WA magmatism is largely attributed to subduction-related processes, based on the spatial association of shield and stratovolcanoes above a geophysically imaged northward-dipping slab (Fig. 1.1; Page et al., 1989; Miller and Richter, 1994; Preece and Hart, 2004; Fuis et al., 2008).

Previous Geochemical Work

Volcanic and shallow intrusive rocks span a range of geochemical compositions (e.g., mafic to felsic) and include calc-alkaline, transitional, alkaline, and adakite magmas (Nye, 1983; Skulski et al., 1991; 1992; Preece and Hart, 2004; Trop et al., 2012; Preece et al., 2014). These previous studies provide a geochemical framework for interpreting new WA geochemical data.

Western Wrangell Arc Volcanism: Geochemical Trends

Preece and Hart (2004) document three geochemical trends/suites in <5 Ma volcanic rocks in the western WA, and describe the geochemical significance of each trend in three

geographic zones: front-side, interior, and back-side volcanoes (Fig. 1.1). <5 Ma eruptive products are from large composite shield volcanoes (Mts. Wrangell, Sanford, Capital, Tanada, Jarvis, Skookum Creek Volcanic Complex, Blackburn), stratovolcanoes (Mt. Drum and Mt. Churchill), and a series of cinder cones in the interior of the western WA. TiO_2 content, plotted against SiO_2, is used to divide the <5Ma WA samples into trend 1 (TiO_2>1.15 wt. %) and trend 2 (TiO_2<1.15 wt.%) (Fig. 3.17a). Trend 1 samples also show higher Y contents for a given SiO_2 (30-60 ppm at SiO_2>60 wt. %) (Fig. 3.18e). Trend 2 rocks show lower Y values (13-29 ppm at SiO_2>60 wt. %), and in fact show two different arrays for Y content between 61-67 wt. % SiO_2. The higher-Y array samples (trend 2a) are from Mt. Wrangell, Tanada, and the Skookum Creek Volcanic Complex, and the lower array samples (trend 2b) are from Mt. Drum and Mt. Churchill (both are front-side volcanoes, Fig. 1.1). Trend 2b samples also show higher values of Sr, Sr/Y, and La/Yb than trend 1 and 2a, leading to their classification as "adakites" or adakitic (Defant and Drummond, 1990). Generally, trend 1 rocks are transitional to tholeiitic in character, and at a given SiO_2 value have higher TiO_2, Y, and Zr values, and lower Sr values than trend 2a contents. Preece and Hart (2004) suggest that trend 1 rocks (dominantly from the interior of the WA) represent relatively low degrees of melting due to localized intra-arc extension, resulting in fast magma ascent rates and minimal fractional crystallization. Trend 1 lavas erupted from cinder cones that are aligned with the 80-km depth-to-slab contour of Bauer et al. (2014), and Trop et al. (2012) showed that some trend 1 lavas erupted into actively subsiding intra-arc basins.

Trend 2a rocks constitute the largest volume of <5 Ma WA volcanic products, and show "typical" subduction-related calc-alkaline geochemical affinities that suggest somewhat higher degrees of partial melting due to fluid flux into the mantle wedge (Preece and Hart, 2004). The trend 2a parental magmas underwent magma-mixing and magma-mantle/crust interactions,

creating the wide range of erupted geochemical affinities. Nye (1983) documents the high edifice production rates (~30 km^3/km/my) of the youngest (<5 Ma) WA volcanism at Mt. Wrangell, which are many times greater than rates calculated for other volcanic arc segments: 3.11 km^3/km/my in Central America and 9.7 km^3/km/my in the Marianas arc (Stolber and Carr, 1974; Sample and Karig, 1982).

Trend 2b rocks occur only on the front-side and on the two extreme ends of the <5 Ma WA, at Mount Churchill in the southeast and at Mount Drum in the northwest (Fig. 1.1). Adakitic character is attributed to partial melting of the Yakutat slab (Preece and Hart, 2004; Preece et al., 2014). These magmas underwent similar open-system processes as trend 2a magmas (Preece and Hart, 2004). Studies of older seismic data (USGS Trans-Alaska Crustal Transect survey) show what may be a tear in the subducting slab below the westernmost modern WA (Fuis et al., 2008), which may have allowed sub-slab asthenosphere to upwell around the slab-edge and thermally erode the Yakutat slab, leading to adakitic affinities at Mount Drum (e.g., Kamchatka; Yogodzinski et al., 2001). A more recent geophysical study did not find evidence for a tear in the slab, but demonstrated that the slab is continuous from the eastern Aleutian arc to beneath the WA (Fig. 1.1; Bauer et al., 2014). Slab-melting could occur in that scenario if the rate of subduction changes as the angle of the slab changes. Previous study has linked these three geochemical trends to tectonic factors that were important in the <5 Ma WA. We therefore use them here as a means of understanding the roles of intra-arc extension, subduction, and slab-edge effects in the petrogenesis of older phases of WA magmatism.

Eastern Wrangell Arc Volcanism: "Leaky" Strike-Slip

A series of northwest-southeast trending volcanic fields southwestern in Yukon Territory and northwestern British Columbia, Canada, record WA volcanism along the strike-slip Duke

River and Denali faults (fig. 1.1). The Stanley Creek volcanic field, the smallest of these fields and the furthest to the southeast, is comprised of undated transitional and minor alkaline lavas (Skulski et al., 1991). The Alsek field is comprised of ~10.8–13.5 Ma calc-alkaline and volumetrically minor transitional and alkaline lavas, and the Nines Creek field consists of ~13–15.5 Ma transitional lavas (Fig. 1.1; Dodds and Campbell, 1988). The St. Clare Creek field is adjacent to the border with Alaska, and is comprised of ~10–18 Ma transitional and minor alkaline and calc-alkaline lavas that overlie earlier sedimentary rocks and the underlying basement rocks of the Wrangellia and Alexander terranes (Skulski et al., 1992).

The St. Clare Creek volcanic field contains two distinct and overlapping composite volcanoes, termed the Wolverine and Klutlan eruptive centers. The ~16–18 Ma Wolverine center shows a chemo-stratigraphic trend from >17.8 Ma alkaline basalts at the base to transitional lavas in the middle of the section to ~16.2 Ma calc-alkaline lavas at the top of the succession. The ~16–10 Ma Klutlan center shows the opposite trend, with ~11–16 Ma calc-alkaline lavas comprising the lower half of the succession and ~10.4–11 Ma transitional lavas making up the most recent eruptive products in the St. Clare Creek volcanic field (Skulski et al., 1992). The presence of calc-alkaline chemistries, as well as similar isotopic compositions to western WA rocks, suggest that a period of the volcanic history of the St. Clare Creek volcanic field during the mid-Miocene was influenced by subduction. However, the alkaline nature of the lowermost Wolverine lavas (intermediate between Cordilleran intra-plate and arc magmas, e.g., Eiché et al., 1987, Skulski et al., 1991) suggest that subduction input was not constant through the lifetime of the Wolverine volcanic center, and melting of a subduction-affected mantle wedge did not always occur in this location.

To explain the geochemical trend of the Wolverine center, Skulski et al. (1992) suggested that extension across the right-lateral Duke River and Denali faults (i.e., transtension), and associated low-degree melting of asthenosphere, was responsible for the alkaline lavas. Abundant north-trending dikes reinforce the idea of transtension between two strike-slip faults (Skulski et al., 1992). A gradual change to more subduction-related input created the transitional to calc-alkaline chemistries.

The opposite trend seen in the Klutlan center reflects a decreased subduction input. This has been interpreted by Skulski et al., (1992) as evidence that the Yakutat slab rotated and the focus of subduction-related volcanism shifted to the northwest, followed by the upwelling of depleted asthenosphere around the edge of the slab, creating transitional to alkaline chemistries. A similar model is employed by Edwards and Russell (1999; 2000) to explain the bimodal alkaline nature of the Northern Cordilleran volcanic province, where incipient rifting was driven by changes in relative motion between the Pacific and North American plates, and low-degree melting of asthenosphere created alkaline geochemical affinities. Thorkelson et al. (2011) enhances this model by including the influence a slab window, wherein the subsequent upwelling of mantle asthenosphere would induce melting. The changes in geochemistry seen in the St. Clare Creek volcanic field over eight million years demonstrates the sensitivity of volcanic geochemistry to tectonic changes in an arc-transform transition zone.

Central Wrangell Arc Volcanism: Frederika Formation

Large portions of the central WA remain un-sampled, due in part to the rugged and remote nature of the ice-covered high Wrangell Mountains. However, Trop et al., (2012) document a thick package of intra-arc sedimentary and minor volcanic strata capped by a succession of WA lavas, altogether termed the Frederika Formation. Geochemical compositions

of Frederika lavas generally overlap with calc-alkaline lavas from the St. Clare Creek volcanic field in the Yukon (Skulski et al., 1992), the Sonya Creek volcanic field (Richter et al., 1990; 2000), and trends 1 and 2a lavas from the <5 Ma western WA (Preece and Hart, 2004). These combined associations suggest that the ~12.5–5.3 Ma central WA Frederika lavas reflect the effects of subduction and minor intra-arc extensional processes on magma genesis. Lavas in the eastern section have ages of ~12.5–9.3 Ma (coeval with the latest St. Clare Creek volcanism, e.g., Skulski et al. 1992), and lavas in the western section have ages of ~9.6–5.3 Ma, reflecting the northwestward migration of WA magmatism suggested by Richter et al. (1990). The late Miocene subduction of thickened oceanic crust (Yakutat microplate), and the resulting intra-arc extension of the upper plate, are similar processes that operated to produce the trend 2a calc-alkaline and trend 1 transitional-tholeiitic series of Preece and Hart (2004) in the <5 Ma western WA.

Age Progression of Wrangell Arc Volcanism

Richter et al. (1990) proposed a model of northwesterly progression of WA volcanism through time, from 26.3 Ma near the Alaska-Yukon border to ~0.2 Ma at the northwest edge of the WA. The oldest age documenting the inception of the WA was based on K-Ar dating of one lava sample from the Sonya Creek volcanic field. Mt. Churchill is an exception to the overall northwestward migration as it is in the central WA, and produced the White River Ash at 1147 and 1886 years BP (Clague et al., 1995; Preece et al., 2014). Richter et al. (1990) attributes the earliest WA volcanism (~25-15 Ma) to the onset of Yakutat microplate subduction. The subsequent northwestward migration accelerated through time, with about half occurring overthe last 5 million years, concurrently with a change in the rate and direction of Pacific plate movement (Engebretson et al., 1985; Richter et al., 1990). Richter et al. (1990) suggests that the

faster subduction rate and more direct angle of convergence allowed increased magma production, resulting in the large andesitic shield volcanoes seen in the modern western WA.

>20 Ma Magmatism From the Central Wrangell Arc

Samples of ~24-20 Ma hypabyssal rocks (Tp unit of Richter, 1976; Th unit of MacKevett, 1978) that intrude Cretaceous plutons on the northern flank of the central WA show subduction-related geochemical compositions (green dots on Fig. 1.1; Brueseke et al., 2015). These samples are calc-alkaline and medium-K, show Ba/Nb values (75-234 ppm) and primitive mantle-normalized Sr/P values (2.8-4.8), similar to the moderately-spiked suggestive of a subduction-fluid affected source; high Sr/Y values reflect adakitic characteristics as defined by Castillo (2012). These features suggest that these plutons are like trend 2b rocks of Preece and Hart (2004) from the <5 Ma WA (Weber et al., 2017). The ages of these rocks are similar to the earliest published ages of WA volcanic rocks (~26 Ma, Rocker Creek; Richter et al., 1990; 2000), and their location along the northern flank of the WA suggests that the northwest-younging trend of WA volcanism proposed by Richter et al., (1990) is an oversimplification (Fig. 1.1). These rocks, together with new detrital geochronologic ages from modern rivers encircling the WA, provide evidence of a previously unrecognized southward shift of volcanism during the initiation and early stages of the WA (Trop et al., 2017). The only known area with ~20–30 Ma *in situ* bedrock ages is the well-exposed Sonya Creek volcanic field, for which limited data has been reported previously. Located in the north-central WA, this 28.8–18.5 Ma volcanic field contains volcanic and shallow intrusive rocks that have been carefully mapped to provide spatial and temporal position to help evaluate this issue (Fig. 1.1).

Sonya Creek Volcanic Field Study Area

The 28.8–18.5 Ma (Richter et al., 1990; 2000) Sonya Creek volcanic field (SCVF) is in an area of relatively low elevation (~970-2300 m above sea level), easily accessible by aircraft and on foot, and is well-exposed and ice-free. This is in stark contrast to the rugged, remote, and ice-covered terrain of the high mountains that make up much of the central WA. Thus, the SCVF is an ideal location for a stratigraphic-based study of the early stages of WA magmatism.

The SCVF (Fig. 1.2) is dominated by the Sonya Creek shield volcano, which was interpreted to contain an inferred 10 x 14 km caldera that is similar to (but larger than) the summit calderas of the younger Wrangell, Tanada, and Capital volcanoes (Richter et al., 1990). Richter et al. (2000) interpreted the inferred caldera to be filled with more than 1 km of 18.5–23.3 Ma flat-lying basaltic-andesite to dacite lavas, with minor pyroclastic and volcaniclastic rocks. One of the lavas is obsidian-bearing and was apparently an important obsidian source among native peoples as far away as >460 km to the northwest (Layer, 1994, 1995; Cook, 1995; Patterson, 2008; Rasic et al., 2009). These thick lavas are adjacent to the rocks that make up the distal flanks of the Sonya Creek shield volcano, which include ~400 m of shallowly-dipping lavas (Flat Top, 24.5 Ma and 19.7–19.3 Ma), lahars, and a welded ash-flow tuff unit. Basalt to rhyolite plugs, domes, dikes, and lavas associated with a marginal fracture system of the volcano stratigraphically overlie rocks of the shield volcano along the northeast margin. Another package of 19–21.3 Ma northwest-dipping andesite lavas and interbedded mudflows, named the Young Creek lavas after a nearby river, underlie the rocks of the shield volcano and may be more than 300-m-thick, but the base of the section is not exposed. The Young Creek lavas are adjacent to a 22.9 ± 2.2 Ma subvolcanic/hypabyssal diorite that is roughly 5 km^3 in volume. A broad field of 20.34–25.9 Ma coalesced andesitic subvolcanic/hypabyssal diorites and dacite domes/lavas form

an arcuate band from southwest to northeast around the perimeter of the shield volcano, and are locally overlain by the shield volcano rocks (Richter et al., 2000). In the extreme southern and eastern areas of the SCVF are thick packages of lavas of unknown origin (referred to as the Border Lavas) that may be contemporaneous with the Sonya Creek shield (Richter et al., 2000). To the east of the Sonya Creek shield volcano are the 27.2–22.9 Ma Rocker Creek lavas and domes, a package of >1200-meter-thick basaltic to dacitic lavas that dip to the southwest, and are intruded by silicic domes (Richter et al., 2000). Richter et al., (1990) documented a single Rocker Creek basalt that yielded a K-Ar age of 26.3 Ma, which has been repeatedly cited to represent the onset of WA magmatism and the inception of the arc.

Bedrock lithologies south of the Denali fault that are pre-WA in age include late Paleozoic through Tertiary sedimentary and igneous rocks, as described by MacKevett (1978) and Richter et al. (2000). The Pennsylvanian-Permian Station Creek Formation consists of amygdaloidal andesitic lavas and associated volcaniclastic rocks. The Permian Hasen Creek Formation is a marine argillite with minor sandstone and chert, with minor volcaniclastic rocks. Gabbroic sills of Triassic age are found within this unit, and are likely associated with the Triassic Nikolai Formation. The Nikolai Greenstone is composed of amygdaloidal tholeiitic basalt lavas and minor associated volcaniclastic rocks. These pre-WA bedrock lithologies underlie the volcanic rocks of the SCVF and crop out in a limited part of the map area, inside the Sonya Creek shield volcano margin and along marginal fractures. Cretaceous-Jurassic marine sedimentary rocks that crop out in the northern part of the map area are part of the Nutzotin Mountains sequence of Berg et al., (1972), and consist of thin- to medium-bedded argillite and rhythmically bedded and graded graywacke. Cretaceous volcanic and intrusive rocks of the

Chisana Formation intrude and overlie the marine sediments, including the Klein Creek pluton, which is found in the northeast part of the study area (Fig. 1.2), is composed of hornblende-biotite granodiorite and quartz monzonite, and locally metamorphoses the Nutzotin Mountains sedimentary sequence. An unnamed unit of continental sedimentary rocks about 130-m-thick consists of clast-supported conglomerate, conglomeratic sandstone, and coarse sandstone. Clasts in the conglomerates as large as 20 cm in diameter are composed of crystalline gneiss, chert, greenstone, and quartz of Cretaceous age and older. Course sandstones are cross-bedded, and lignitized wood is locally abundant. Hornblende dacite sills intrude the unit in lower Rocker Creek (Richter et al, 2000). Quaternary surficial deposits consist of Pleistocene fluvio-glacial and glacial deposits of Wisconsin-age glaciation, to Holocene Alaskan-age glaciation glacial deposits, rock glacier, solifluction, landslide, colluvium, and alluvium deposits (Richter et al. 2000). The Yukon-Tanana terrane is juxtaposed against the Wrangellia Composite Terrane along the Denali fault to the north of the SCVF, and consists of Precambrian-Paleozoic metamorphic rocks intruded by Paleozoic-Mesozoic plutons (Aleinikoff and Nokleberg, 1985; Nokleberg and Aleinikoff, 1985).

Structural Evidence for Local Extensional Faulting

Field relations and map patterns in the SCVF reveal what appears to be a northeast-southwest striking fault (Fig. 1.2 and 1.3). The topographic expression of the inferred fault is indicated by a chain of small lakes that stretches from western Rock Lake to the long southwestern arm of Ptarmigan Lake, and follows the course of Ptarmigan Creek to where it meets Beaver Creek just west of the Yukon border. Maps from across the border in Yukon Territory show a fault (Beaver Creek fault) approximately matching up with this proposed fault, that cuts Pennsylvanian-Cretaceous strata and meets the right-lateral Denali fault (Israel et al,

2007; Israel and Cobbett, 2008b). Because the fault has been mapped in the Yukon, we will refer to it as the Beaver Creek fault. A rough trace of the Beaver Creek fault across the White River to the southwest meets the right-lateral Totschunda fault, and lines up with outcrops of Cretaceous rocks that are uplifted to the southeast of the fault, and at lower elevations or absent on the northwest side of the fault (MacKevett, 1978). This suggests a southeast-side-up sense of motion on the Beaver Creek fault.

There are multiple pieces of evidence for the Beaver Creek fault within the SCVF. Sub-aerial lavas from Cabin Creek are at similar elevations as sub-volcanic/hypabyssal plutonic rocks across the fault, 5 km to the southeast (Fig.1.2, 3.2E). The rocks from the dome field are at elevations of ~1680–1920 m on the southeast side, and are less than 1620 m in elevation on the northeast side of the fault. The contact between the Sonya Creek lavas and the Rock Lake diorite is offset across the fault, with the southeast side higher and the northwest side lower (Figs. 1.2, 3.5). The small fault that cuts through the exposed pre-SCVF Wrangellia basement rocks to the north of Ptarmigan Lake (Fig. 1.2) is sub-parallel to the main fault. Additionally, there is a series of dikes that intrude the dome field and the Young Creek area that are sub-parallel to the fault (Fig. 1.2). These structural features on the Alaskan side of the border suggest that the Beaver Creek fault has a larger extent than what was originally mapped in the Yukon (Israel et al, 2007; Israel and Cobbett, 2008b). It possibly originates at the Totschunda fault, underlies the White River valley, cuts through the middle of the SCVF, extends into Yukon Territory, and possibly meets the Denali fault.

The SCVF is located between two large right-lateral strike-slip faults, the Denali and Totschunda faults. The stress ellipse within a dextral strike-slip stress field shows extensional forces at approximately 30° to the fault, which would result in normal faulting (Christie-Blick

and Biddle, 1985). The kinematic history of the Beaver Creek fault is complicated, as the Yukon portion of the fault is mapped as a normal fault with an opposite sense of motion (i.e., southeast side down), possibly making the Beaver Creek fault a wrench or scissor fault.

Figure 1.1: Map of southern Alaska and western Canada showing major volcanic and tectonic features. Major fault systems are in yellow and black. The Yukon-Tanana composite terrane is north of the Denali fault, the Wrangellia composite terrane is between the Denali fault and the Border Ranges fault, and the Yakutat microplate is south of the suture with the North American plate at the Chugach-St. Elias fault. The Wrangell arc is shown by red fields and triangles (volcanoes active <5 Ma). The easternmost Aleutian arc is shown by orange triangles. Vector arrows in lower right corner show net displacement for Pacific plate relative to North American plate in Miocene-recent time. The location of the Sonya Creek volcanic field is indicated by the yellow box and is expanded in Figure 1.2. Adapted from Pavlis et al. (2004), Kalbas et al. (2008), Fuis et al. (2008), and Trop et al. (2012). Structural features: **BRF**-Border Ranges fault, **CF**-inferred Totschunda-Fairweather connector fault, **CSEF**-Chugach-St. Elias fault, **TF**-Totschunda fault.

<5 Ma Wrangell arc volcanoes: **B**-Mount Blackburn, **C**-Capital Mountain, **cc**-interior cinder cones, **Ch**-Mount Churchill, **D**-Mount Drum, **J**-Mount Jarvis, **S**-Mount Sanford, **Sk**-Skookum Creek Volcanic Center, **T**-Tanada Peak, **W**-Mount Wrangell.

Yukon WA volcanic fields: **A**-Alsek volcanic field, **NC**-Nines Creek volcanic field, **SC**- St. Clare Creek volcanic field, **St**- Stanley Creek volcanic field.

Aleutian arc volcanoes: **AV**-Augustine volcano, **BC**-Buzzard Creek maar, **DG**-Double Glacier volcano, **Do**-Mount Douglas, **FP**-Fourpeaked volcano, **H**-Mount Hayes, **I**-Mount Iliamna, **R**-Mount Redoubt, **Sp**-Mount Spurr.

Towns: **A**-Anchorage, **M**-McCarthy, **V**-Valdez, **Y**-Yakutat.

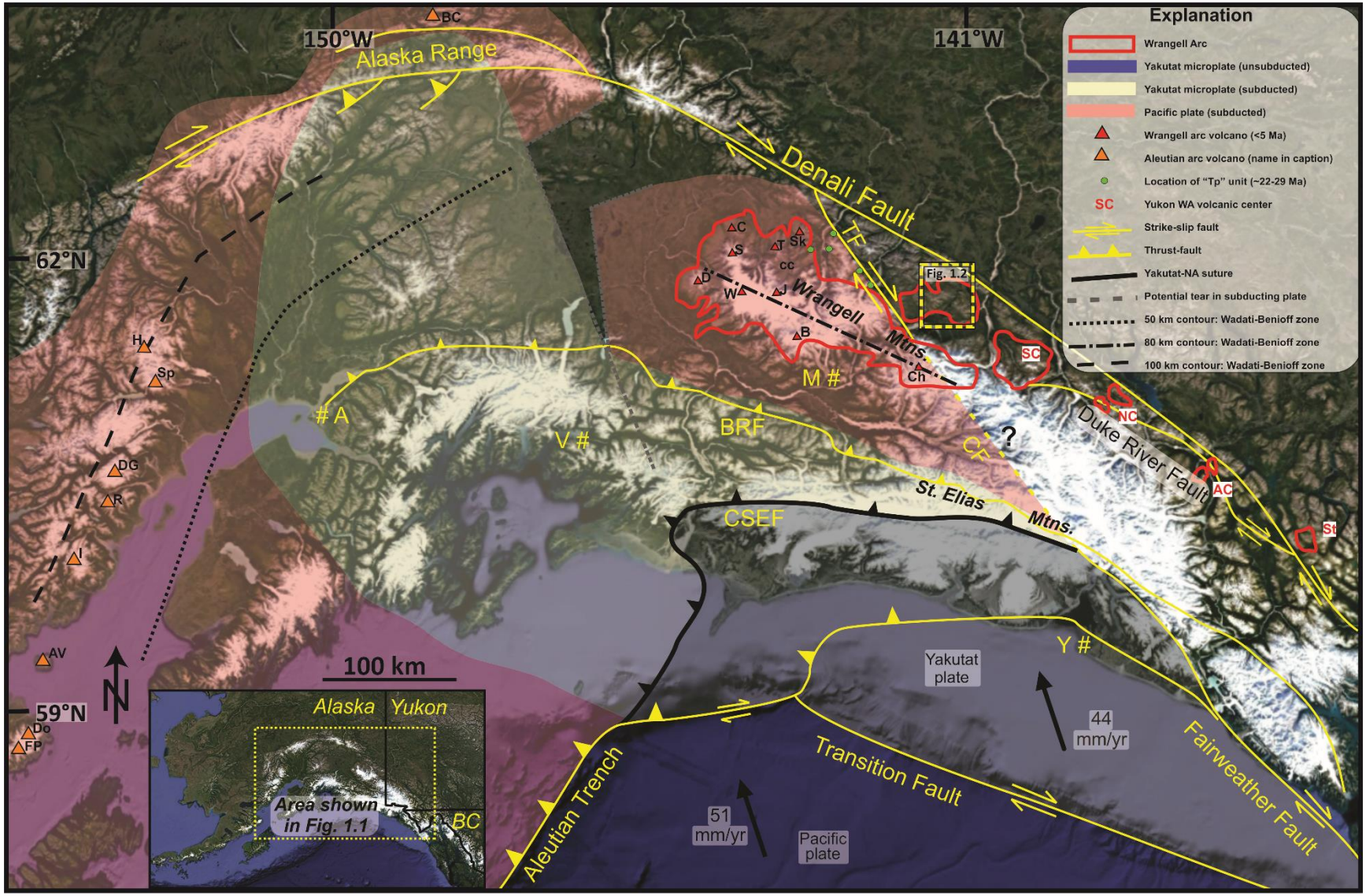
Explanation
Wrangell Arc
Yakutat microplate (unsubducted)
Yakutat microplate (subducted)
Pacific plate (subducted)
Wrangell arc volcano (<5 Ma)
Aleutian arc volcano (name in caption)
Location of "Tp" unit (~22-29 Ma)
SC Yukon WA volcanic center
Strike-slip fault
Thrust-fault
Yakutat-NA suture
Potential tear in subducting plate
50 km contour: Wadati-Benioff zone
80 km contour: Wadati-Benioff zone
100 km contour: Wadati-Benioff zone
150°W
141°W
62°N
59°N
Alaska Range
Denali Fault
TF
Wrangell
Mtns.
Fig. 1.2
SC
NC
AC
St
Duke River Fault
M #
A
V #
BRF
CF
?
CSEF
St. Elias
Mtns.
Y #
Yakutat plate
44 mm/yr
Transition Fault
Fairweather Fault
Aleutian Trench
51 mm/yr
Pacific plate
100 km
Alaska
Yukon
Area shown in Fig. 1.1
BC
N
BC
C
S
T
Sk
cc
D'
W
J
B
Ch
H
Sp
DG
R
I
AV
Do
FP

Figure 1.2: Simplified geologic map of the Sonya Creek volcanic field (SCVF), adapted from Richter et al. (2000). Below is a legend for Figure 1.2. Location of bedrock samples indicated by black dots and lines. Samples beginning with "SB" follow the SB15-xx numbering scheme, and samples ending with "LA" follow the 15JBxxLA scheme. Bedrock units are lumped into the geographic units described in the text (e.g., Flat Top rocks). Lines of cross-sections shown in Figure 3.5 are shown by lines X-X' and Y-Y'. Inferred fault shown by dashed line from southwest to northeast. Location is shown in Figure 1.1.

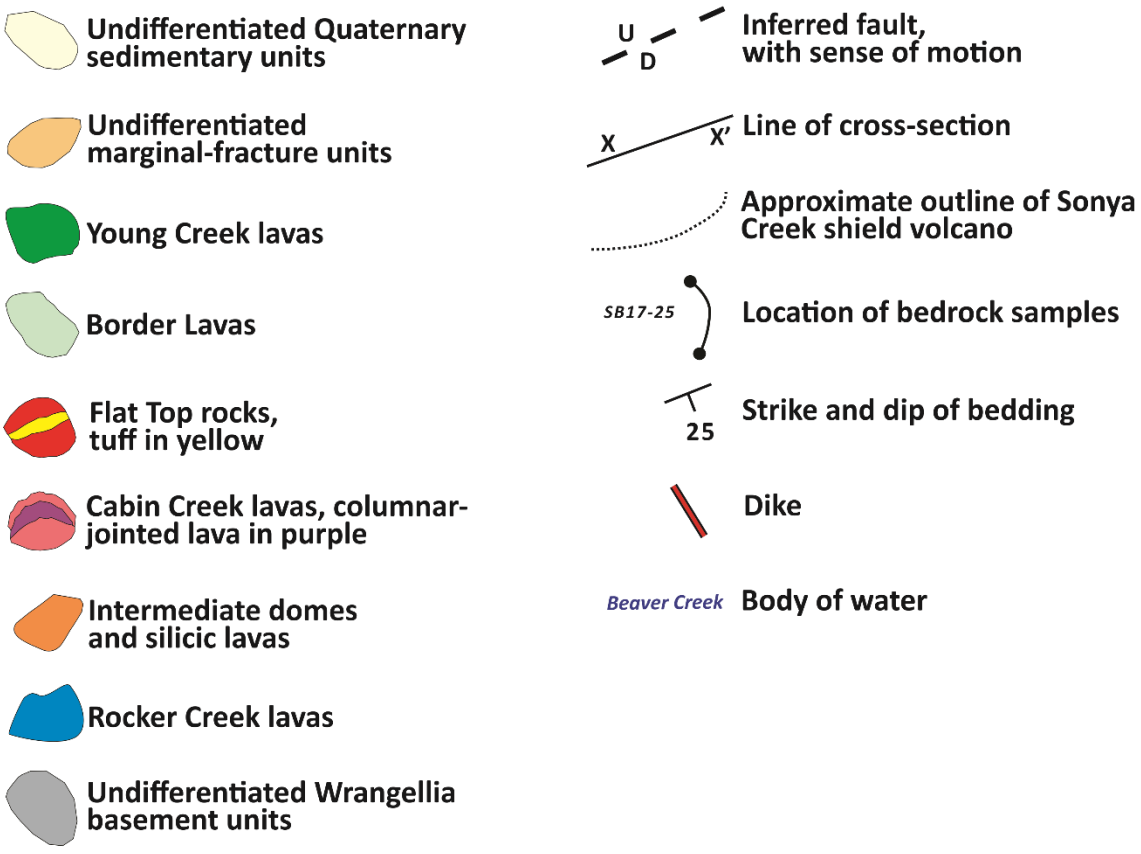

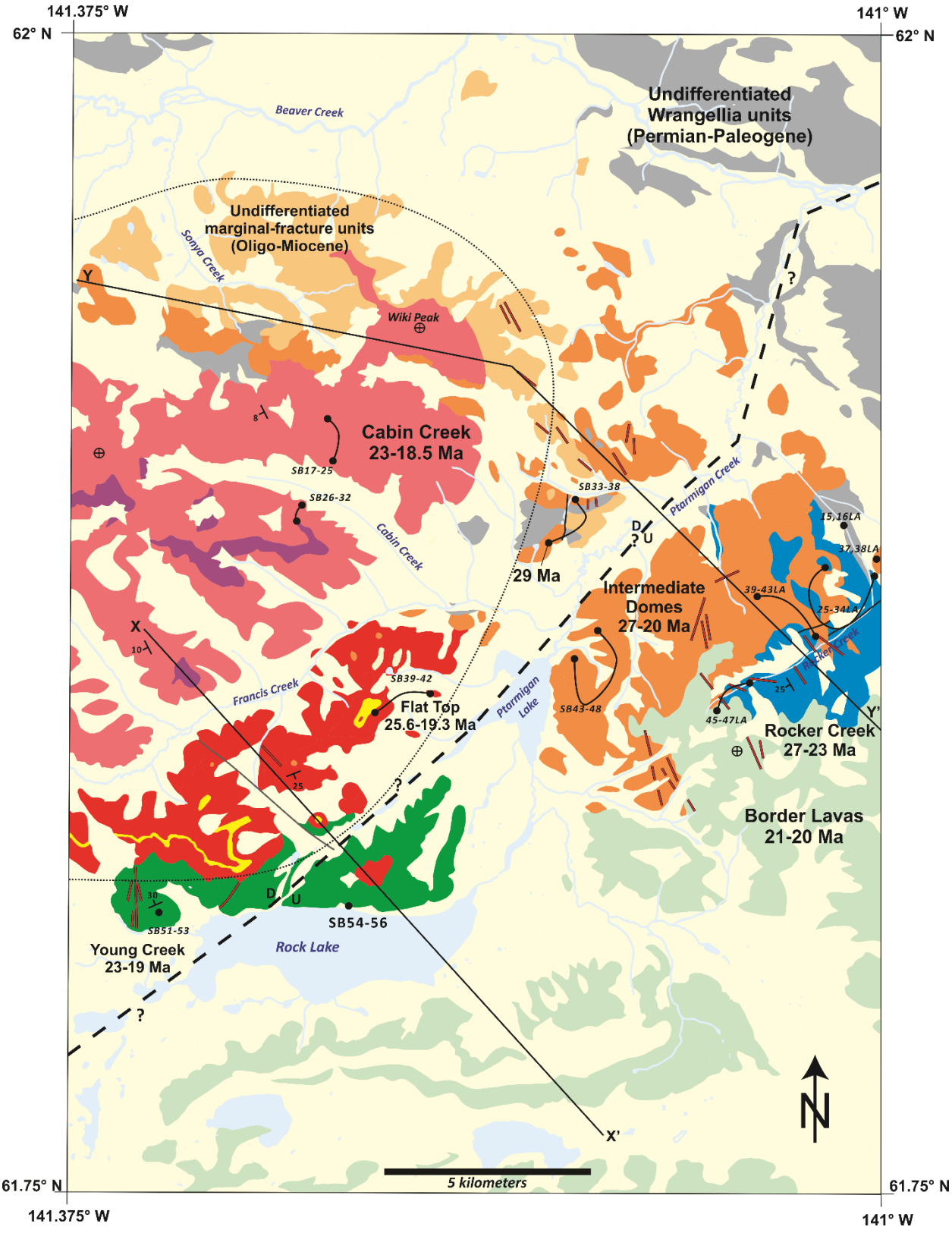
141.375° W
141° W
62° N
62° N
Undifferentiated
Wrangellia units
(Permian-Paleogene)
Beaver Creek
Undifferentiated
marginal-fracture units
(Oligo-Miocene)
Sonya Creek
Y
Wiki Peak
Cabin Creek
23-18.5 Ma
SB17-25
SB26-32
Cabin Creek
SB33-38
29 Ma
Ptarmigan Creek
D
? U
15,16LA
37,38LA
39-43LA
25-34LA
Intermediate
Domes
27-20 Ma
X
Francis Creek
SB39-42
Flat Top
25.6-19.3 Ma
Ptarmigan
Lake
SB43-48
45-47LA
Y'
Rocker Creek
27-23 Ma
Border Lavas
21-20 Ma
D
U
SB54-56
SB51-53
Young Creek
23-19 Ma
Rock Lake
X'
N
5 kilometers
61.75° N
61.75° N
141.375° W
141° W

Figure 1.3: Compiled geologic maps showing the inferred location and sense of motion of the Beaver Creek fault in Alaska and Yukon Territory. Strain ellipses for simple shear across a dextral strike-slip fault are shown. Maps adapted from MacKevett (1978), Richter et al. (2000), and Israel et al. (2007a; 2007b).

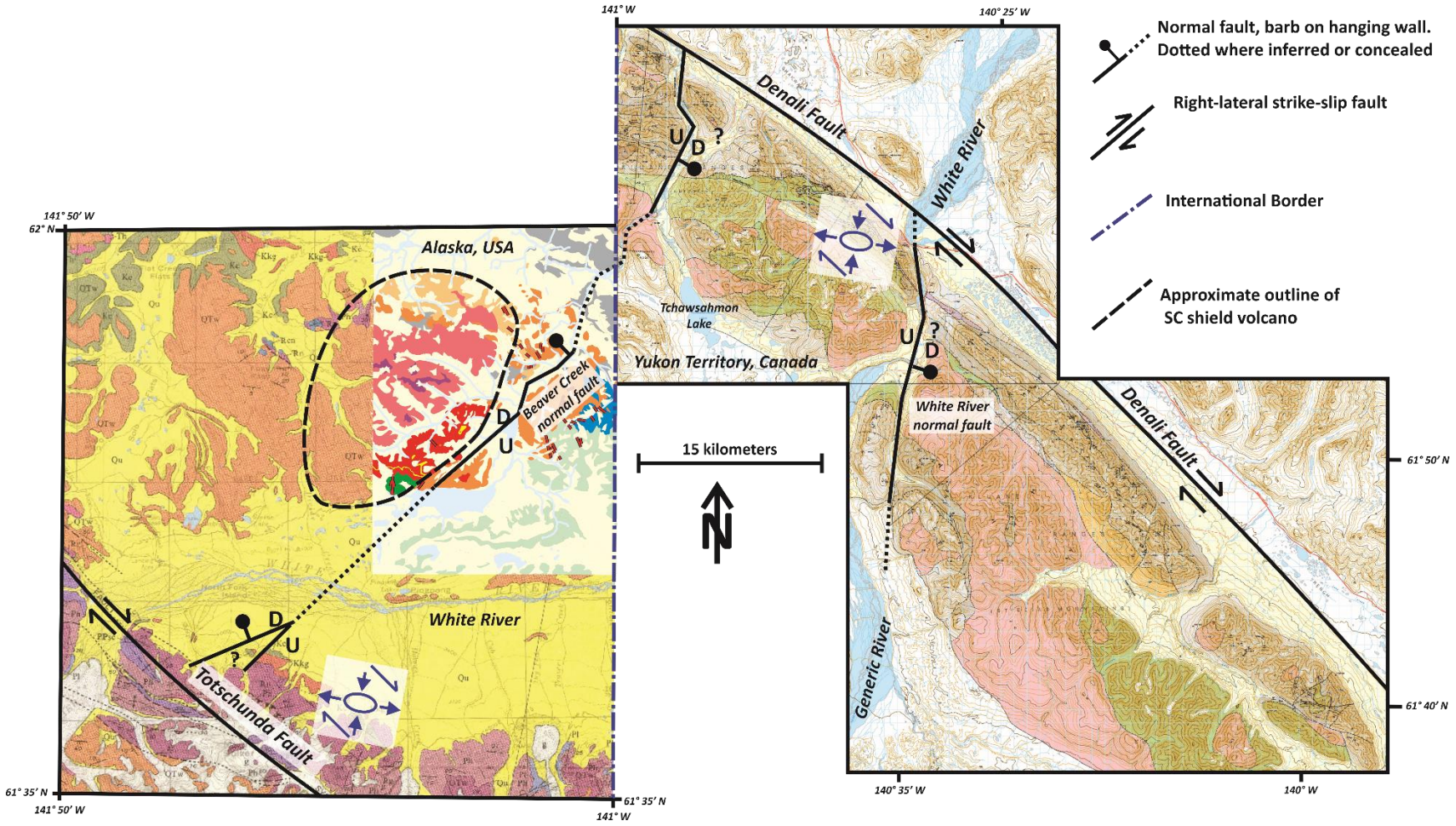
141° W
140° 25′ W
Normal fault, barb on hanging wall.
Dotted where inferred or concealed
Right-lateral strike-slip fault
International Border
Approximate outline of
SC shield volcano
Denali Fault
White River
Tchawsahmon
Lake
Yukon Territory, Canada
Alaska, USA
Beaver Creek
normal fault
White River
normal fault
Denali Fault
15 kilometers
141° 50′ W
62° N
61° 50′ N
61° 40′ N
61° 35′ N
141° 50′ W
141° W
140° 35′ W
140° W
White River
Totschunda Fault
Generic River

Chapter 2 - Methods

Field Methods

Samples were collected during July 2016. Target areas were determined by studying the maps of Richter et al. (1976), MacKevett (1978), and the highly detailed map of Richter et al., (2000), as well as Google Earth imagery. At the Sonya Creek volcano, samples of igneous units were obtained in stratigraphic context and a stratigraphic column was drafted (Figs. 3.11 and 3.12). The Intermediate domes, Flat Top, Young Creek, Rock Lake, Rocker Creek, and Border Lava areas were targeted to get a representative set of the mapped rock units of Richter et al. (2000). Time was spent at each outcrop to obtain the freshest rock sample possible, which involved chipping away weathering rinds to the interior of a large block. Detailed hand sample descriptions were made in the field, as well as relevant stratigraphic or structural information. Coordinates were taken with a GPS device using the 1927 North American Datum (NAD27 CONUS) datum. Coordinates and field descriptions can be found in Appendix A.

Analytical Methods

Samples were split into smaller pieces using a RockLabs Hydraulic Press with tungsten splitting jaws. Weathered surfaces were removed from all samples by cutting with a rock saw with a diamond-tipped blade and grinding on a 60-grit sandpaper grinding wheel. All samples were cleaned in deionized water with an ordinary toothbrush and allowed to dry completely. When dry, all samples were crushed to pea-size and smaller fragments using the tungsten crushing plates of the RockLabs Hydraulic Press, then randomized using a cone-and-quarter method on a glass plate. A small amount (~25 mL) of crushed sample was powdered using a Spec Industries Shatterbox machine and an alumina shatterbox assembly for eight minutes. Powdered samples were shipped in glass vials for analysis.

Major, Trace, and Rare Earth Element Analysis

Fifty-five rock sample powders were sent to Washington State University for XRF analysis of major elements, minor elements and select trace elements (Si, Ti, Al, Fe, Mn, Mg, Ca, Na, K, P, V, Ni, Cr, Ga, Cu, Zn) and ICP-MS analysis of select trace and rare earth elements (Ba, Th, Nb, Y, Hf, Ta, U, Pb, Rb, Cs, Sr, Sc, Zr, La, Ce, Pr, Nd, Sm, Eu, Gd, Tb, Dy, Ho, Er, Tm, Yb, Lu). Loss on ignition (LOI) was also measured. For XRF analysis, 3.5 g aliquots of powder were mixed with 7 g of a lithium tetraborate ($Li_2B_4O_7$) flux and fused in graphite crucibles at ~1000°C. The resulting beads were reground in tungsten-carbide shatterboxes and fused again under the same conditions. Samples were run on a ThermoARL Advant'XP+ sequential X-ray fluorescence spectrometer, following the procedures of Johnson et al. (1999). Nine USGS standards were run with the powders, and pure quartz was used as a blank. The standards BCR-P and GSP-1 were analyzed between every 28 samples to ensure precision within a single run and between runs.

For ICP-MS analysis, 2 g aliquots of powder were mixed with 2 g of lithium tetraborate flux and fused under the same conditions as for XRF aliquots. These samples were then reground in Fe shatterboxes and dissolved using a HF-HNO_3-$HClO_4$ acid mixture. Samples were run on an Argilent 7700 ICP-MS following the procedures of Knaack et al (1994).

Five samples (SB15-30, 15JB16LA, 15JB28LA, 15JB31LA, 15JB41LA; see Appendix B) were sent to Franklin and Marshall College for XRF analysis of major and trace element compositions and LOI, following the method outlined by Mertzmann (2000; 2015). A 1 g aliquot of powder from each sample was placed in clean ceramic crucibles and heated at 900°C in a muffle furnace for 60-75 minutes. After cooling to room temperature, samples were reweighed and the change in percent was reported as LOI. Following LOI measurements, 0.4 g of

anhydrous powder was mixed with 3.6 g of lithium tetraborate flux and melted in 95% Pt - 5% Au crucibles. Once quenched into homogeneous glass disks, the disks were used for XRF analysis of major elements using a Panalytical, Inc. 2404 XRF vacuum spectrometer equipped with a 4 kW Rh X-ray tube. Major elements were reported as weight percent oxide (SiO_2, TiO_2, Al_2O_3, Fe_2O_3, MnO, MgO, CaO, Na_2O, K_2O, P_2O_5). Nineteen trace elements (Rb, Sr, Y, Zr, V, Ni, Cr, Nb, Ga, Cu, Zn, Co, Ba, La, Ce, U, Th, Sc, Pb) were analyzed on pressed powder briquettes made from a mixture of 7.0 g of whole-rock powder ad 1.4 g of high purity Copolywax powder. Trace element concentrations are presented as parts per million (ppm). All major, trace, and rare earth element data are presented in Appendix B.

During analysis, all available Fe was recorded as FeO*. The raw Fe data were corrected for oxidation state, and FeO and Fe_2O_3 were determined based on the method outlined by LeMaitre (1976).

Although care was taken in the field to collect the freshest possible samples of volcanic rocks, loss on ignition (LOI) values and petrographic evidence suggest that some samples have been affected by secondary hydrothermal and/or meteoric fluid alteration/weathering. Based on a sample containing one or more of: (1) petrographic observations of abundant secondary phyllosilicate and/or carbonate phases, (2) LOI> 3.5 wt.%, and/or (3) anomalous (i.e., non-igneous) relationships between Mg, Fe, Ni, Cr, V, and Sc, eight samples are interpreted to be altered and possess non-primary geochemical traits, and were excluded from further consideration. Data from these eliminated samples are presented in Appendix B.

Sr-Nd-Pb-Hf Isotope Analysis

Eight samples that represent important rock units within the SCVF were sent to Washington State University for radiogenic isotope analysis via a Thermo-Finnigan Neptune

multicollector (MC)-ICP-MS. Methods for Sr, Nd, and Hf analysis follow those found in Vervoort & Blichert-Toft, (1999), Vervoort (2004), and Münker et al., (2001), with important steps highlighted here for information. For Sr, Nd, and Hf whole-rock isotopic analysis, ~0.25 g aliquots of whole-rock powders were dissolved at high pressure in sealed, steel-jacketed Teflon bombs with a 10:1 mixture of concentrated HF and HNO_3 acids at 150°C for 5-7 days. After conversion from fluorides to chlorides, samples were spiked with mixed ^{149}Sm-^{150}Nd and ^{176}Lu-^{180}Hf tracers. Hf, Sr, Lu-Yb, and the light REE (LREE) were initially separated on cation exchange columns using ΔG 50W-X8 (200-400 mesh) resin. Hf aliquots were further purified using columns with Ln spec resin following the methods of Münker et al. (2001). Sr aliquots were purified using micro-columns (0.18 ml resin volume) with Sr-spec resin and HNO_3. Lu was separated from Yb on columns with Ln spec resin and HCl (Vervoort et al., 2004). Nd and Sm were separated from the LREE aliquot on columns with HDEHP-coated Teflon powder and HCl (Vervoort & Blichert-Toft, 1999).

Sr analyses were corrected for mass fractionation using $^{86}Sr/^{88}Sr=0.1194$ and normalized to a value of 0.71024 for the $^{87}Sr/^{86}Sr$ ratio of the NBS-987 standard. Nd analyses were corrected for mass fractionation using $^{146}Nd/^{144}Nd=0.7219$ and normalized to a value of 0.512138 for the $^{143}Nd/^{144}Nd$ ratio of the Ames Nd standard and 0.511858 for the LaJolla standard. Sm analyses were corrected for fractionation using $^{147}Sm/^{152}Sm=0.56081$. Whole-rock Hf analyses were corrected for mass fractionation using $^{179}Hf/^{177}Hf=0.7325$ and normalized to a value of 0.28216 for the $^{176}Hf/^{177}Hf$ ratio for the JMC-475 standard (Vervoort and Blichert-Toft, 1999). Lu measurements were made using the methods of Vervoort et al. (2004). All mass fractionation corrections were made using the exponential law.

Pb isotopic concentrations were determined on powder aliquots dissolved separately, and follow the methods of White el al. (2000). These were washed and sonicated in 6M cold HCl at least once to remove any secondary Pb, rinsed with purified H_2O, and dissolved in sealed 15 ml Savillex ^{TM} beakers with a 10:1 HF-HNO_3 mixture on a hot plate at ~120° for 24 hours. After conversion from flourides to bromides, Pb was separated using BioRad AG 1-X8 anion resin. Pb isotopic compositions were measured on the same MC-ICP-MS instrument as Sr, Nd, and Hf, using the thallium doping procedure described by White et al. (2000). Unknowns were doped with 30 ppb Tl and run alternately with the NBS-981 standard with a concentration of 150 ppb and 30 ppb Tl. After correcting for the mass bias using thallium, samples were normalized to the triple-spike values for NBS-981 from Galer & Abouchami (1998): $^{206}Pb/^{204}Pb = 16.9405$; $^{207}Pb/^{204}Pb = 15.4963$; $^{208}Pb/^{204}Pb = 36.7219$. Pb isotopic ratios are presented in Table 3-1 and are presented here as measured present-day values.

$^{40}Ar/^{39}Ar$ Geochronology Analysis

56 SCVF samples were analyzed for $^{40}Ar/^{39}Ar$ ages at the University of Alaska Fairbanks Geochronology lab. Rock samples were crushed using a stainless-steel mortar and pestle, then sieved using 500-1000 micron sieves. Samples were then washed and sonically bathed in de-ionized water to remove and decant clay particles. Samples were then dried in an oven overnight at ~60° C and then homogeneous grains were hand-picked under an optical microscope to select phenocryst-free groundmass chips, hornblende, and biotite mineral separates. The monitor mineral TCR-2 with an age of 28.619 Ma (Renne et al., 2010) was used to monitor neutron flux and calculate the irradiation parameter (J) for all samples. The samples and standards were wrapped in aluminum foil and loaded into aluminum cans of 2.5 cm diameter and 6 cm height. Mineral separates were sent to the uranium enriched research reactor of McMaster University in

Hamilton, Ontario, Canada, and irradiated for 20 megawatt-hours. After irradiation, samples were loaded into 2mm diameter holes in a copper tray and loaded in an ultra-high vacuum extraction line. The monitors were fused, and samples heated, using a 6-watt argon-ion laser following the technique described in York et al. (1981), Layer et al. (1987), and Benowitz et al. (2014). Argon purification was achieved using a liquid nitrogen cold trap and a SAES Zr-Al getter at 400° C.

The samples were analyzed in a VG-3600 mass spectrometer. The argon isotopes measured were corrected for system blank and mass discrimination, as well as calcium, potassium, and chlorine interference reactions following procedures outlined in McDougall and Harrison (1999). Typical full-system 8 min laser blank values (in moles) were generally 2×10^{-18} mol ^{40}Ar, 3×10^{-18} mol ^{39}Ar, 9×10^{-18} mol ^{38}Ar, and 2×10^{-18} mol ^{36}Ar, which are 10 – 50 times smaller than the sample/standard volume fractions. Correction factors for nucleogenic interferences during irradiation were determined from irradiated CaF_2 and K_2SO_4 as follows: $(^{39}Ar/^{37}Ar)Ca = 7.06 \times 10^{-4}$, $(^{36}Ar/^{37}Ar)Ca = 2.79 \times 10^{-4}$ and $(^{40}Ar/^{39}Ar)K = 0.0297$. Mass discrimination was monitored by running calibrated air shots. The mass discrimination during these experiments was 0.8% per mass unit.

The majority of samples were analyzed as single-grain or multi-grain fusion analysis approach. We developed a procedure to limit the effects of alteration by degassing each sample at 0.5 watts for 60 seconds, and the released gas was pumped off for time efficiency and hence increased throughput. The results have a single-grain and/or multi-grain precision of 1%. Samples selected for higher-precision ages were step-heated from relatively low temperatures until reaching fusion temperatures using the 6-watt argon-ion laser (Sliwinski et al., 2012). For

each step, isotopic ratios of Ar were determined, with a range of MSWD values of 0.01 – 6.25 (Table 3-4).

A summary of 14 $^{40}Ar/^{39}Ar$ step-heat ages is given in Table 3-4 with all ages quoted to the ±1 sigma level and calculated using the constants of Renne et al. (2010). The integrated age is the age given by the total gas measured and is equivalent to a potassium – argon (K-Ar) age. The age spectrum provides a plateau age if three or more consecutive gas fractions represent at least 50% of the total gas release and are within two standard deviations of each other (MSWD <2.5). For select samples, inverse isochron ages were calculated from an inverse isochron diagram of $^{36}Ar/^{40}Ar$ vs. $^{39}Ar/^{40}Ar$ ratios measured during each heating step (Roddick, 1978; Roddick et al., 1980; Benowitz et al, 2011).

Petrography

Thin section billets were created at KSU using a diamond-tipped blade saw, and then shipped to National Petrographic Service, Inc. for thin section preparation. Thin sections were used to evaluate "freshness" of samples, which assisted in evaluating LOI data and choosing samples for radiogenic isotope analysis. Thin sections were examined using a Nikon Eclipse E600 POL microscope and photomicrographs were taken with a camera attached to the microscope. Point counts were done on the eight samples used for isotope analysis, using a 1mm step and averaging 695.25 points per slide. Detailed petrographic descriptions can be found in Appendix A.

Chapter 3 - Results

Field Relations, Physical Characteristics, and Geochronology

Sample locations are summarized in Appendix A and on Figure 1.2. A summary of phenocryst occurrence is shown in Table 3.1, and a summary of point count data for the samples chosen for isotope analysis is presented in Table 3.2. Detailed petrographic descriptions of all SCVF samples can be found in Appendix A. A summary of step-heat geochronology is found in Table 3.4, the complete spectra are in Appendix C, and laser-fusion $^{40}Ar/^{39}Ar$ data are summarized in Appendix A. Two schematic cross-sections of the SCVF are shown in Figure 3.5, with the names and ages of the units discussed in the text. Photographs of outcrops and field relations are shown in Figures 3.1 to 3.4.

Lavas from Rocker Creek are poorly exposed due to heavy vegetation, and most crop out as blocky lavas in small gullies of the Rocker Creek drainage (Fig. 3.1a, b). Rocker Creek lavas generally dip to the southwest and are intruded by the domes and sub-volcanic rocks associated with the dome field of Richter et al. (2000). Petrographically, the Rocker Creek lavas are clinopyroxene-plagioclase-phyric (Fig. 3.6a, b). Most have a glassy or microcrystalline groundmass consisting of plagioclase laths, opaque oxide minerals, and/or clinopyroxene. Only the basaltic sample contains olivine (the basaltic-andesite 15JB26LA has pseudomorphs after olivine). Two dacite lavas have hornblende phenocrysts, and one has biotite phenocrysts. Glomerocrysts are rare, and plagioclase crystals show a range of disequilibrium textures. Apatite needles are found as inclusions in plagioclase crystals in nearly every SCVF sample. Rocker Creek lavas yield $^{40}Ar/^{39}Ar$ ages from 27.2 – 23.4 Ma (Fig. 3.10, Appendix B).

The Rocker Creek dome rocks occur as platy and blocky outcrops of hornblende-plagioclase-phyric lavas (Figs. 3.1c, d; Fig. 3.6c, d). They have a glassy and microcrystalline groundmass, consisting of aligned/flow-banded plagioclase laths and opaque minerals. Rocker Creek domes yield $^{40}Ar/^{39}Ar$ ages from 25.96 – 23.17 Ma (Fig. 3.10, Appendix B).

The silicic lavas crop out throughout the SCVF as large extrusive domes (~300 m tall), lavas in valleys, and as small plugs (Fig. 3.1e, f; Fig. 3.2a, c). They are porphyritic with plagioclase and sanidine phenocrysts in a microcrystalline to cryptocrystalline groundmass. Three of the samples (SB15-34, SB15-45, 15JB38LA) have biotite phenocrysts and one (SB15-45) has hornblende and biotite phenocrysts (Fig. 3.6e, f). Rare zircons are also present (Fig. 3.7a, b). The adakite-like silicic rocks are sanidine-phyric lavas in a microcrystalline and glassy groundmass. The silicic domes yield $^{40}Ar/^{39}Ar$ ages from 24.81 – 23.26 Ma, and SB15-45 is 20.34 ± 0.12 Ma (Fig. 3.10, Appendix B).

Intermediate dome rocks crop out as extrusive lava flows, small plugs, medium-grained diorites, and a sinter/breccia deposit that may represent a paleo-hot spring (Fig. 3.2b, d). The intermediate domes show some petrographic diversity. Two samples (dacite SB15-47 and andesite SB15-48) have cumulate textures of anhedral plagioclase crystals with intergranular biotite, clinopyroxene, amphibole, and quartz (in the dacite) (Fig. 3.7c, d). The basaltic-andesite (SB15-46) and andesite (SB15-43) samples have extrusive textures, with plagioclase phenocrysts and altered mafic phases in a glassy groundmass. The two dacites (15JB27LA and 15JB28LA) from the Rocker Creek area have hornblende phenocrysts, and are otherwise plagioclase-phyric lavas (Fig. 3.7e, f). Intermediate domes yield $^{40}Ar/^{39}Ar$ ages from 23.18 – 21.67 Ma (Fig. 3.10, Appendix B).

Lavas from Cabin Creek are flat-lying to gently dipping and range in thickness from 10 – 50 m thick (Fig. 3.2f; Fig. 3.3a; Figs. 3.11, 3.12). Some lava flows occur as platy, ramped and jointed outcrops, others weather into tall, jagged spires, and one lava has ~2-m-wide lava tubes (Fig. 3.3b, c, d). Most lavas have vesicular and oxidized basal and upper breccia zones that form slopes, while the massive lava interiors are cliff-forming. Thin (50 cm) interbedded tuffaceous breccia occurs on the north side of Cabin Creek. The south side of Cabin Creek has dacite flows with well-developed ~30-m-tall columnar joints, as well as a package of four mafic lavas with interbedded volcanic breccias (Fig. 3.3e). The south side has sedimentary units interbedded with lavas; a poorly-sorted boulder conglomerate with rounded volcanic clasts is interpreted as a debris/hyperconcentrated-flow deposit, and a poorly-sorted breccia with volcanic boulders up to one meter in size is interpreted as a lahar deposit (Fig. 3.3f; Fig. 3.12). These sedimentary units represent inter-eruptional deposits on the flanks of the volcano.

Lavas from the north side of Cabin Creek are two-pyroxene, plagioclase-phyric glomeroporphyritic lavas (Fig. 3.8c, d). Clinopyroxene phenocrysts are pink in plane-polarized light and are likely titanaugite. Plagioclase phenocrysts show varying degrees of disequilibrium textures, but sieve texture and embayments are common. The trachydacites and the trachyandesite from the top of the section on the south side of Cabin Creek are plagioclase-phyric and contain clinopyroxene phenocrysts. SB15-27 has a groundmass that consists almost entirely of glass, and is a vitrophyre. The lowermost rocks from the south side ("mafic package" of basaltic-andesites to andesites) are two-pyroxene, plagioclase-olivine-phyric glomeroporphyritic lavas (Fig. 3.8a, b). Clinopyroxene crystals may be titanaugite, and plagioclase phenocrysts show sieve texture and pyroxene inclusions. Cabin Creek lavas yield $^{40}Ar/^{39}Ar$ ages from 23.29 – 18.48 Ma (Fig. 3.10, Appendix B).

The Flat Top basalt outcrops among hillslope colluvium deposits, and is interbedded with volcanic mudflow deposits (Fig. 3.4a). Silicic lavas are blocky outcrops of ~10 m thick lavas with sparse interbedded airfall tuff deposits (Fig. 3.4b). The massively bedded ash-flow tuff is ~30-m-thick and has flattened pumice fragments and volcanic lithic fragments greater than 15 cm long (Fig. 3.4c). Rocks from Flat Top show some petrographic diversity. The basalt from the bottom of the section (SB15-39) is a clinopyroxene-plagioclase-olivine-phyric lava in coarse-grained groundmass (Fig. 3.8e, f). The rhyolite ash-flow tuff/ignimbrite (Flat Top tuff, SB15-40) has embayed plagioclase, anorthoclase, and sanidine phenocrysts, and rare clinopyroxene. The groundmass is cryptocrystalline with a vitrophyric to eutaxitic texture, showing welded pumice fragments (Fig. 3.9a, b). The two trachydacite samples (SB15-41 and -42) are crystal-poor lavas. SB15-41 is vesicular and has a glassy groundmass. The Flat Top basalt yields a $^{40}Ar/^{39}Ar$ age of 24.58 Ma, and two of the upper rocks yield ages of 19.71 and 19.3 Ma (Fig. 3.10, Appendix B).

Young Creek lavas outcrop as massive flows that dip to the northwest, and are intruded by a north-striking dike (Fig. 1.2; Fig. 3.4e). Young Creek rocks are clinopyroxene-plagioclase-phyric lavas. The two basaltic-andesites contain olivine, and one of the andesites has hornblende phenocrysts. The groundmass of these lavas contains glass (Fig. 3.e, f). The Rock Lake diorite (sample SB15-56) has a cumulate texture of large plagioclase crystals with intergranular clinopyroxene and biotite, and is lumped with Young Creek lavas on plots of geochemistry, which will be discussed below. Young Creek rocks yield $^{40}Ar/^{39}Ar$ ages from 21.3 – 19.07 Ma, and the Rock Lake diorite is 22.9 Ma with a large error (±2.2 Ma) (Fig. 3.10, Appendix B). The two Border Lava samples are plagioclase-phyric with a glassy and microcrystalline groundmass, but 15JB37LA has highly embayed plagioclase crystals that show sieve texture, and 15JB46LA

has opaque pseudomorphs after hornblende (Fig. 3.9c, d). The Border Lavas yield $^{40}Ar/^{39}Ar$ ages of 21.27 and 19.62 Ma (Fig. 3.10, Appendix B).

Geochemistry Results

Rock units from the SCVF are named based on geographic location, except for the silicic lavas (SiO_2 >72 wt. %) that are named by composition. See Fig. 1.2 of the SCVF study area for sample locations. Lavas and domes from Rocker Creek are named after the drainage from which they were sampled. The intermediate domes are located physically between the Rocker Creek lavas and the Sonya Creek shield volcano, and they have chemical affinities that are intermediate between those two eruptive centers. The "Silicic Lavas" have SiO_2 >72 wt. %, and two samples (15JB15LA, 15JB16LA) meet geochemical criteria to be considered "adakitic." The Flat Top rocks were collected in stratigraphic context from the southeast margin of the inferred Sonya Creek shield volcano. Cabin Creek (North and South) rocks are from two stratigraphic sections on either side of the Cabin Creek drainage. Young Creek rocks are from a location along the northwest and north side of Rock Lake. The Border lavas (collected in the Rocker Creek area) overlap in time with Young Creek rocks, and are plotted with those on many plots.

Geochemical Classification

Major element data for SCVF rocks show that rock types range from basalt to rhyolite. A total alkali vs. silica (TAS) diagram after LeBas et al. (1986) shows the SCVF rocks spanning a compositional range from sub-alkaline basalt through rhyolite, with some samples plotting within the transitional fields of trachyandesite and trachydacite (Fig. 3.13a). All samples plot below the sub-alkaline discrimination line of Irvine and Barager (1971). Most SCVF rocks plot as medium-K on the classification diagram of Gill (1981), but approximately 10 samples from Cabin Creek, Flat Top, and the silicic lavas show a high-K trend (Fig. 3.14b). An AFM diagram

after Irvine and Baragar (1971) shows that all SCVF intermediate samples are calc-alkaline, with some of the Cabin Creek and Flat Top rocks plotting along the divide between the calc-alkaline and tholeiitic fields (Fig. 3.13b). A FeO*/MgO vs. wt. % SiO_2 diagram after Miyashiro (1974) shows most of the Flat Top and Cabin Creek rocks (as well as one Border Lava and one adakitic silicic lava) plotting within the tholeiitic field, while the remainder of the SCVF rocks plot as calc-alkaline (Fig. 3.14a). Because the Flat Top and Cabin Creek rocks are sub-alkaline to transitional on a TAS diagram, and they plot as either calc-alkaline or tholeiitic depending on what classification diagram is used, they will be referred to as "transitional tholeiitic" in discussions of geochemistry. This term was used by Preece and Hart (2004) to describe their "trend 1" magma series, and because Flat Top and Cabin Creek rocks are geochemically like the trend 1 rocks, we adopt a similar approach. No SCVF rocks show similar chemistry to the fields for primitive alkaline and transitional volcanic rocks from the Yukon WA volcanic field (Figs. 3.13, 3.14; Skulski et al., 1991; 1992), and these fields are not included on additional plots of geochemistry.

All SCVF samples with SiO_2 > 65 wt. % are plotted on discrimination diagrams for granites (Fig. 3.15). SCVF rocks plot as peraluminous to metaluminous based on Shand's alumina saturation index [ASI= Al / (Ca – 1.67*P + Na + K)]. Two Rocker Creek lavas, three Flat Top rocks, three intermediate domes, and one Border Lava plot as metaluminous (ASI < 1).

The five silicic lavas (including the two that are adakitic), two Rocker Creek domes, and one Border lava plot as peraluminous (ASI > 1; Fig. 3.15c). This last group includes the five high-silica rhyolites that are the most silicic in the SCVF. The Y vs. Nb discrimination diagram after Pearce et al. (1984) shows the three Flat Top rocks plot in the within plate granite (WPG) field, while the remainder of the SCVF silicic rocks plot in the volcanic arc granite (VAG) field

(Fig. 3.15b). Similarly, the Flat Top rocks plot in the "A-type granite" field and the remainder plot in the "I & S-types granite" field on the Zr vs. 10^4 Ga/Al discrimination diagram of Whalen et al. (1987) (Fig. 3.15c). This is not to say that the three silicic Flat Top rocks (which are two lavas and an ash-flow tuff) have A-type or within-plate characteristics *sensu stricto*, but the geochemistry of these rocks likely reflects a process that would give rise to a hot and dry felsic magma, which is consistent with their mineralogy.

Major Element Geochemistry

Major element concentrations for SCVF rocks are plotted on Harker diagrams to show geochemical trends with differentiation (Fig. 3.16). All SCVF rocks show decreasing wt.% TiO_2, Al_2O_3, FeO*, MnO, MgO, P_2O_5, and CaO values with increasing SiO_2, but Flat Top and Cabin Creek rocks tend to have higher amounts of TiO_2 and P_2O_5 and lower amounts of MgO and CaO for a given SiO_2 content (Fig. 3.16). Conversely, Rocker Creek and Young Creek rocks tend to have lower TiO_2 and P_2O_5 and higher MgO and CaO at a given SiO_2 value. All SCVF rocks show increasing K_2O and Na_2O values with increasing SiO_2 (Fig. 3.16). Flat Top and Cabin Creek rocks tend to have higher values of both, while Rocker Creek and Young Creek tend to have lower values, at a given SiO_2 content. The intermediate domes have major element compositions that are intermediate between the Flat Top/Cabin Creek rocks and Rocker Creek rocks (i.e., TiO_2, MgO, K_2O), hence their name. The silicic lavas (72.9-76.5 wt. % SiO_2; Figs. 3.16) show trends that are different from the intermediate domes. The silicic lavas show a sharp decrease in Al_2O_3 content at high SiO_2 values, and much lower Na_2O values (3.7-4.6 wt. %) than Flat Top silicic rocks (4.9-5.3 wt. %). Three of the silicic domes belong to the high-K trend, and the two silicic adakitic domes belong to the medium-K trend (Fig. 3.16). Flat Top and Cabin

Creek rocks plot within the field for "trend 1" data of Preece and Hart (2004), and the "calc-alkaline" field of Yukon WA rocks (Skulski et al., 1991; 1992), and will be discussed later.

Trace Element Geochemistry

Trace element values for SCVF rocks are plotted on Harker diagrams to show geochemical trends (Fig. 3.17). All SCVF rocks show decreasing values of the compatible trace elements (Sr, Ni, Sc, Cr, Cu, Zn, and V) with increasing wt.% SiO_2 content, but Flat Top/Cabin Creek rocks tend to have lower amounts of Sr, Ni, and Cr, and higher Zn for a given SiO_2 content (Fig. 3.17, Appendix B). Most Rocker Creek lavas and domes plot within the field for "trend 2b" data of Preece and Hart (2004), the significance of which will be discussed later. All SCVF rocks show increasing values of the large ion lithophile elements (LILE; Rb, Ba, U, Th, Pb, and Cs) with increasing SiO_2, but Flat Top/Cabin Creek rocks tend to have higher amounts of Rb, U, Th, Pb, and Cs at a given SiO_2 content (Fig. 3.17, Appendix B). The silicic domes show a wide range of these incompatible trace elements over a relatively restricted SiO_2 range. The high field strength elements (HFSE; Y, Zr, Nb, Hf, and Ta) show mixed trends for SCVF rocks. Flat Top/Cabin Creek rocks show a strong increase in HFSE values with SiO_2, especially for Y, Zr, and Hf (Fig. 3.17, Appendix B), and plot within the field for "trend 1" data of Preece and Hart (2004) and "calc-alkaline" field from Yukon WA rocks (Skulsi et al., 1991 1992). The intermediate domes have slightly higher Y contents at a given SiO_2 value than te Rocker Creek rocks, and plot within the field for "trend 2a" of Preece and Hart (2004).

Rare Earth Element Geochemistry

Selected rare earth element (REE) values for SCVF rocks are plotted against SiO_2 in Figures 3.17g and h. REE concentrations versus SiO_2 show a geochemical relationship that is

much the same as that for HFSE, with Flat Top/Cabin Creek rocks showing an increase in REE concentrations with increasing SiO_2, and plotting within the "calc-alkaline" field for Yukon WA rocks (Skulski et al., 1991 1992). Rocker Creek, Young Creek, and the intermediate domes show no correlation or a broadly negative correlation of REE with increasing SiO_2 (Fig. 3.17g, h). In fact, the negative correlation for Rocker Creek, Young Creek, and the intermediate domes becomes more evident with increasing atomic number; the light rare earth elements (LREE), especially La and Ce, show no obvious relationship, but the middle and heavy rare earth elements (MREE and HREE) show a more defined negative variation with SiO_2 (Fig. 3.17g, h; Appendix B).

When SCVF REE values are normalized to chondrite values of Sun and McDonough (1989) and plotted on multi-element diagrams, similarities and differences between rock groups are seen (Fig. 3.18). Rocker Creek lavas have similar REE profiles to the domes from Rocker Creek, with absent or small positive Eu-anomalies (3.18a). The one basalt (15JB25LA) is highlighted to show its lower trace element abundances. The intermediate domes show similar chondrite-normalized REE patterns, with subdued negative or positive Eu-anomalies (Fig. 3.18d). The silicic lavas have lower normalized values and more significant negative Eu-anomalies (Fig. 3.18b). An exception is the adakitic silicic lava (15JB15LA), which has a steeper REE profile (i.e., higher LREE/HREE ratio) and a slight positive Eu-anomaly. The rocks from Flat Top show variety in their REE profiles. The three silicic rocks have more elevated chondrite-normalized REE values, and show negative Eu/Eu* anomalies (Fig. 3.18c). The basalt from lower in the stratigraphic section (SB15-39) shows a very different REE profile, with lower REE values and a slight positive Eu/Eu* anomaly (Fig. 3.18c). Rocks from Cabin Creek are very similar to the Flat Top REE profiles, but with slightly lower values and with more subdued

negative Eu/Eu* anomalies (Fig. 3.18e). Young Creek rocks and the two Border Lavas show REE profiles that are similar to the lavas and domes of Rocker Creek, but the Border lavas have slightly steeper REE profiles. Sample SB15-56 (Young Creek) has a less steep profile and shows a slight positive Eu/Eu* anomaly (Fig. 3.18f).

Primitive Mantle Normalized Multi-Element Diagrams

Multi-element diagrams of SCVF rocks, normalized to the primitive mantle values of Sun and McDonough (1989), show important geochemical differences and similarities among the rocks groups (Fig. 3.19). Notably, all SCVF rocks show the enrichment in LILE and depletion in HFSE that is characteristic of subduction-related magmatism. The Rocker Creek lavas and domes show similar profiles to the intermediate domes but with slightly lower normalized trace element values, particularly for REE (Fig. 3.19a, d). The silicic domes have higher values of the most incompatible trace elements, but have similar values of REE (Fig. 3.19b). The three silicic rocks from Flat Top have very similar normalized trace element values, and the subduction signature of HFSE depletion and LILE enrichment is clear (Fig. 3.19c). The basalt from lower in the stratigraphic section (SB15-39) shows a very different trace element profile, with much lower normalized trace element values and a subdued subduction signature, as well as a lack of large Sr, P, or Ti anomalies (Fig. 3.19c). The lavas of Cabin Creek are very similar to each other, except for the basaltic-andesite that is the most primitive rock from the Cabin Creek section (SB15-32; Figs. 3.12 and 3.19e). The rocks from Young Creek show a similar profile to those of Rocker Creek and Cabin Creek, but with intermediate REE values between those two other groups (Fig. 3.19f). The Rock Lake diorite (SB15-56) has a distinctly different profile, with larger depletions in HFSE and REE, but higher Sr values. The two Border Lavas are plotted with the Young Creek rocks, based in part on geochronologic data (Fig. 3.10; Fig. 3.19f).

Trace Element Ratios and Other Parameters: Sr/Y, $(Sr/P)_n$, Ba/Nb, Eu/Eu*

Various trace element ratios are plotted against SiO_2 in Figure 3.20 to show geochemical characteristics that were helpful in classifying some of the rock types. Sr/Y ratio versus SiO_2 shows most of the Rocker Creek lavas and domes have higher Sr/Y values at a given SiO_2 content than the other rock groups, particularly Flat Top and Cabin Creek rocks (Fig. 3.20). At lower SiO_2 values the Young Creek rocks are also elevated in Sr/Y relative to the Cabin Creek rocks. This high Sr/Y trend serves to further distinguish the Rocker Creek dome rocks from the intermediate domes.

The ratios of $(Sr/P)_n$ (normalized to primitive mantle values) and Ba/Nb can be used to infer relative inputs from subduction-mobilized fluids (Borg et al., 1997), because Sr and Ba are fluid-mobile, and P and Nb are fluid-immobile (Stern, 2002). Four SCVF samples (three Rocker Creek lavas and the Flat Top basalt) meet the MgO cutoff of 6 wt.% of Borg et al. (1997) for using the $(Sr/P)_n$ values (Fig. 3.20b). Despite this strict definition, Figure 3.20b shows that among SCVF with SiO_2 < 63 wt. % Rocker Creek, Young Creek, and intermediate dome rocks have higher $(Sr/P)_n$ values than the Cabin Creek rocks (3.20b), and are similar to the "moderately-spiked" basalts of Borg et al. (1997) ($1.3 < (Sr/P)_n < 5.5$), interpreted to have melted via a moderate degree of subduction-fluid fluid addition along the arc axis. The most primitive Cabin Creek lavas have $(Sr/P)_n$ values similar to "weakly-spiked" basalts, which were interpreted by Borg et al. (1997) to represent melting via a lower degree of subduction-fluid addition than the moderately-spiked basalts in a back-arc setting. Ba/Nb ratios of SCVF rocks show a similar distinction between the Rocker Creek/Young Creek rocks from the Flat Top, Cabin Creek, intermediate domes, and silicic lavas (Fig. 3.20c).

Eu/Eu* quantifies the Eu anomalies shown on chondrite-normalized REE plots (Fig. 3.20d). When plotted against SiO_2, the silicic lavas, the Flat Top silicic rocks, and the Cabin Creek lavas show Eu/Eu* <1 (0.9-0.37), values that are generally lower than Rocker Creek and Young Creek rocks at a given SiO_2 content. The three most mafic samples from SCVF show the highest Eu/Eu* values (1.08-1.25; Fig. 3.20d). The Cabin Creek and Flat Top rocks generally plot within the fields for "trend 1" data of Preece and Hart (2004), and the "calc-alkaline" field for Yukon WA rocks (Skulski et al., 1991; 1992).

Cabin Creek Chemostratigraphy

Samples from Cabin Creek were collected in stratigraphic context, so plots of various chemical constituents versus stratigraphic position assess temporal-geochemical trends (Fig. 3.21). Stratigraphic columns from the north and south sides of Cabin Creek are shown in Figure 3.11 and 3.12, with the north column beginning at ~1500 m asl (above sea level), and the south side beginning at ~1750 m asl, with both sections topping out at ~1950 m asl. A plot of SiO_2 on the X-axis (Fig. 3.21a) shows two chemo-stratigraphic trends; samples from the south side show an increase in SiO_2 with increasing elevation, whereas samples from the north side show the opposite trend over the same elevation range (~1750-1950 m asl), but an apparent reversal in trend below that. Similar variations with elevation are observed for Zr and Ba, with a deviation of the uppermost rocks from the north side. The opposite trends are seen for Mg#, Ni, and Sc, where the south side samples decrease in those values with elevation, and the north side samples increase or remain relatively constant (Fig. 3.21). The stratigraphic section on the south side appears to represent a coherent package of mafic rocks consisting of basaltic andesite, andesite, and trachyandesite lavas that may define a differentiation trend. The two trachydacite samples

from the top of the section are from a thick, columnar-jointed lava (SB15-26, -27; Figs. 3.11, 3.12, and 3.21); their relation to the mafic package is unclear.

Samples from the north side show more variance in chemistry with elevation, but a package of four lavas from ~1640-1780 m asl show a consistent trend with increasing elevation (Fig. 3.21a). Otherwise, samples from the north side show very little geochemical variation with elevation. The difference between the north and south side samples is most evident from ~1640-1850 m asl.

Sr-Nd-Pb-Hf Radiogenic Isotope Results

Figures 3.22 to 3.26 illustrate the $^{87}Sr/^{86}Sr_i$, εNd_i, $^{206}Pb/^{204}Pb$, $^{207}Pb/^{204}Pb$, and $^{208}Pb/^{204}Pb$ variations for eight SCVF samples, and the εHf_i values for five SCVF samples. SCVF isotope ratios are summarized in Table 3-1. Sr, Nd, and Hf ratios are age-corrected to the $^{40}Ar/^{39}Ar$ ages that are shown in Table 3-1, and are considered the initial ratios. Regional and local bedrock units are plotted for reference, and are age-corrected to 23 Ma.

$^{87}Sr/^{86}Sr_i$ values for SCVF rocks range from 0.703464 – 0.704347 and εNd_i values range from +4.64 to +7.67 (Table 3-1). The samples define an array that extends to more radiogenic $^{87}Sr/^{86}Sr_i$ values as εNd_i decreases, with sample SB15-34 at a slightly higher εNd_i value than samples with comparable $^{87}Sr/^{86}Sr_i$ values (Fig. 3.22 inset). SCVF samples generally plot within the field for <5 Ma WA volcanism (Preece and Hart, 2004) and the Cretaceous White Mountain Granitoid (Snyder and Hart, 2007), but with slightly lower εNd_i values than those data. SCVF samples plot entirely within the broad fields for the Triassic Nikolai Formation and the Jurassic Talkeetna arc, and at slightly more radiogenic $^{87}Sr/^{86}Sr_i$ and lower εNd_i values than the Aleutian arc (Fig. 3.22).

SCVF $^{206}Pb/^{204}Pb$ values range from 18.814 – 19.031, $^{207}Pb/^{204}Pb$ from 15.549 – 15.579, and $^{208}Pb/^{204}Pb$ from 38.251 – 38.456 (Table 3-1, Figs. 3.23 and 3.24). SCVF rocks define an array that plots almost entirely within the field for <5 Ma WA volcanism and within the array of Wrangellia basement rocks found in the north-central WA (Preece, 1997; Preece and Hart, 2004; Snyder and Hart; 2007). SCVF samples have more radiogenic $^{206}Pb/^{204}Pb$ than the Aleutian arc, but overlap in $^{207}Pb/^{204}Pb$ and $^{208}Pb/^{204}Pb$ values (Fig. 3.23 and 3.24). SCVF samples plot within the least-radiogenic portion of the fields for the Nikolai Formation, and at lower values than crystalline rocks from the Yukon-Tanana terrane (fig. 3.23 and 3.24). The plot of $^{87}Sr/^{86}Sr_i$ vs. $^{206}Pb/^{204}Pb$ shows the SCVF samples in a similar space as the Pb isotope plots; they generally plot between the MORB and Nikolai fields, have a slight overlap with Aleutian arc field, and plot mostly within the field for <5 Ma WA volcanism (Fig. 3.26).

εHf_i values of five SCVF samples range from +7.9 to +13.1 and show a positive trend with εNd_i (Fig. 3.25). SCVF rocks plot below the Terrestrial Array of Vervoort et al. (1999). Samples generally lie between the fields for modern Pacific sediment and Pacific MORB, and three SCVF samples plot within the field for Aleutian arc rocks. SCVF samples plot within the field for the Nikolai Formation.

The insets for Figs. 3.22 to 3.26 show a clear difference in isotope systematics among the SCVF rock groups; samples from the Sonya Creek shield volcano (Cabin Creek and Flat Top) are at lower $^{87}Sr/^{86}Sr_i$, $^{206}Pb/^{204}Pb$, $^{207}Pb/^{204}Pb$, and $^{208}Pb/^{204}Pb$ values, and higher εNd_i values, than the Rocker Creek and silicic lava rocks. The five SCVF samples analyzed for εHf_i do not show as clear a difference between the rock groups, but the three SC shield rocks have higher εHf_i values than the Rocker Creek basalt, and two Flat Top rocks have higher εHf_i values than the Rocker Creek basaltic-andesite (Fig. 3.25 inset).

Figure 3.1: Photographs from the Rocker Creek area. A) and B) many Rocker Creek lavas blocky and exposed in gullies, and most dip to the southwest. C) a typical exposure of a Rocker Creek dome. D) Structural relationship between the Rocker Creek lavas and the younger intermediate domes. E) One of the adakite-like silicic lavas exposed in lower Rocker Creek, showing the highly vegetated nature of the outcrops. F) The large silicic dome is ~300 m thick and erupted through the older Rocker Creek lavas. Sample 15JB38LA was collected from this outcrop. View to the east.

Figure 3.2: A) The silicic lava (sample SB15-34) is shown underlying rocks of the Sonya Creek shield volcano, and on both sides of the small valley. View to the west. B) A view of the area where the intermediate domes were collected, which includes at least two diorites. The inferred Beaver Creek fault is shown with the west-down sense of motion. The location of the silicic plug in (C) is shown by the arrow. View to the east. C) The small silicic plug (SB15-45) shown intruding through the intermediate domes. D) Typical exposures of the intermediate domes. E) The sub-volcanic diorites of the interemediate domes are shown at a similar elevation as the Cabin Creek lavas acros the inferred Beaver Creek fault. View to the east. F) View to the west up the Cabin Creek valley, showing the flat-lying lavas of the Sonya Creek shield volcano.

Figure 3.3: Photographs of Cabin Creek lavas. A) The line of section for the north side of Cabin Creek is indicated by the green line (see Fig. 3.11). The dashed yellow line marks the approximate level below which the lavas dip more steeply to the west, and above which havemore shallow dips. B) Typical exposure of blocky lava flow interiors and oxidized basal breccia from north side lavas. C) Small lava tube found within the upper sample of north side section (SB15-17). D) Typical exposure of platy and ramped lava flow interiors. E) Photograph showing the south side of Cabin Creek section (see Fig. 3.12), with the lower mafic package, interbedded sedimentary units, and thick upper trachydacite flow marked. F) Thick interbedded debris-fow deposits on the south side of Cabin Creek.

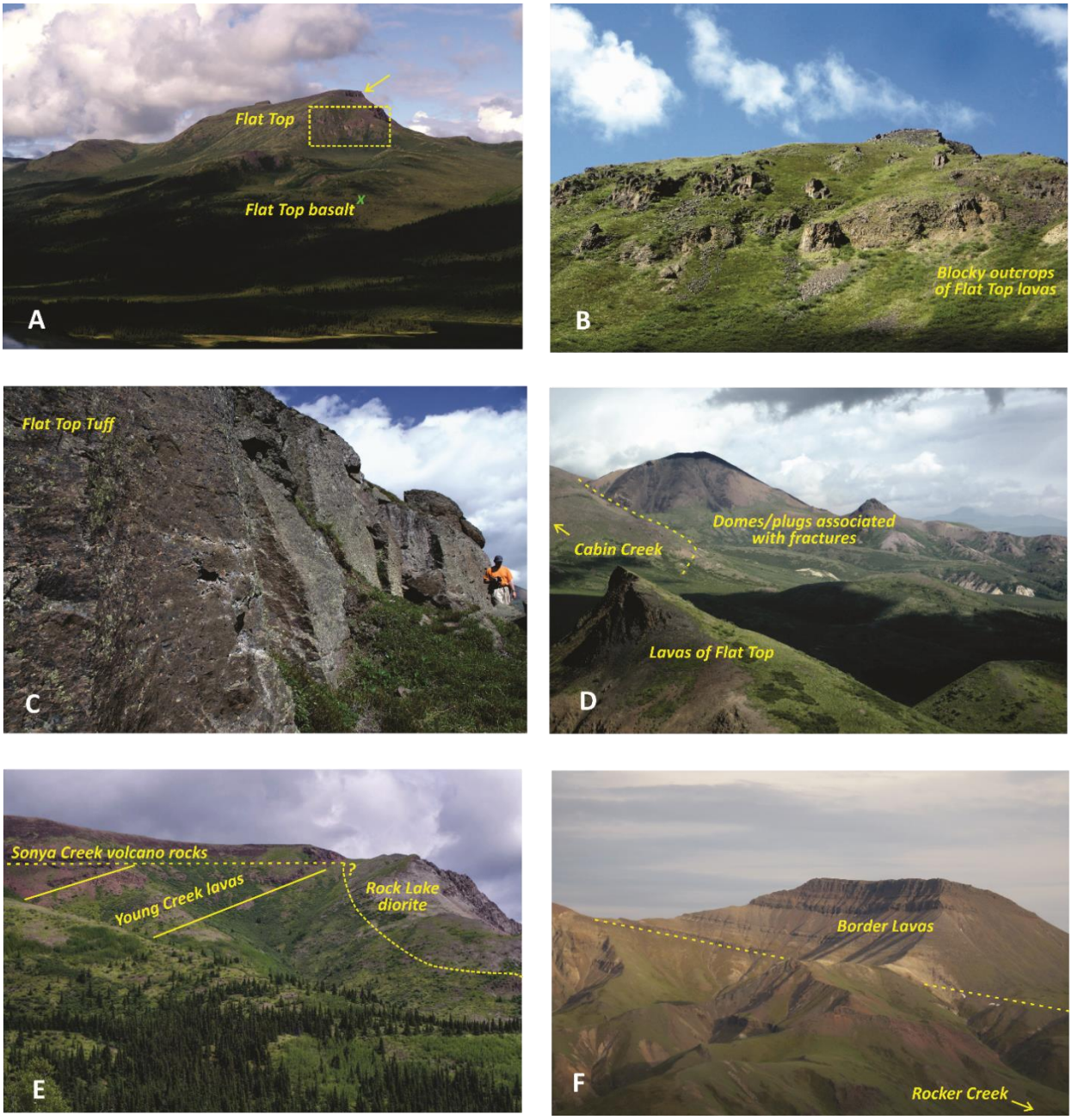

Figure 3.4: A) View to the west of the inferred distal Sonya Creek shield volcano lavas of Flat Top. The location of the Flat Top basalt (SB15-39) is shown by the green X, the Flat Top tuff (SB15-40) is marked by the yellow arrow, and the location of (B) is shown by the yellow box. B) Typical exposure of blocky Flat Top trachydacite lavas. C) A portion of the welded Flat Top tuff. D) View to the north from Flat Top, showing the large domes and plugs associated with marginal fractures of the Sonya Creek shield volcano. E) Complex structural relationships of the northwest-dipping Young Creek lavas, Rock Lake diorite (SB15-56), and flat-lying distal rocks of the Sonya Creek shield volcano. View to the northeast. F) View of a thick section of the Border Lavas in the upper Rocker Creek area, showing them overlying the Rocker Creek lavas. These lavas are just across the border in Yukon Territory. View to the southeast.

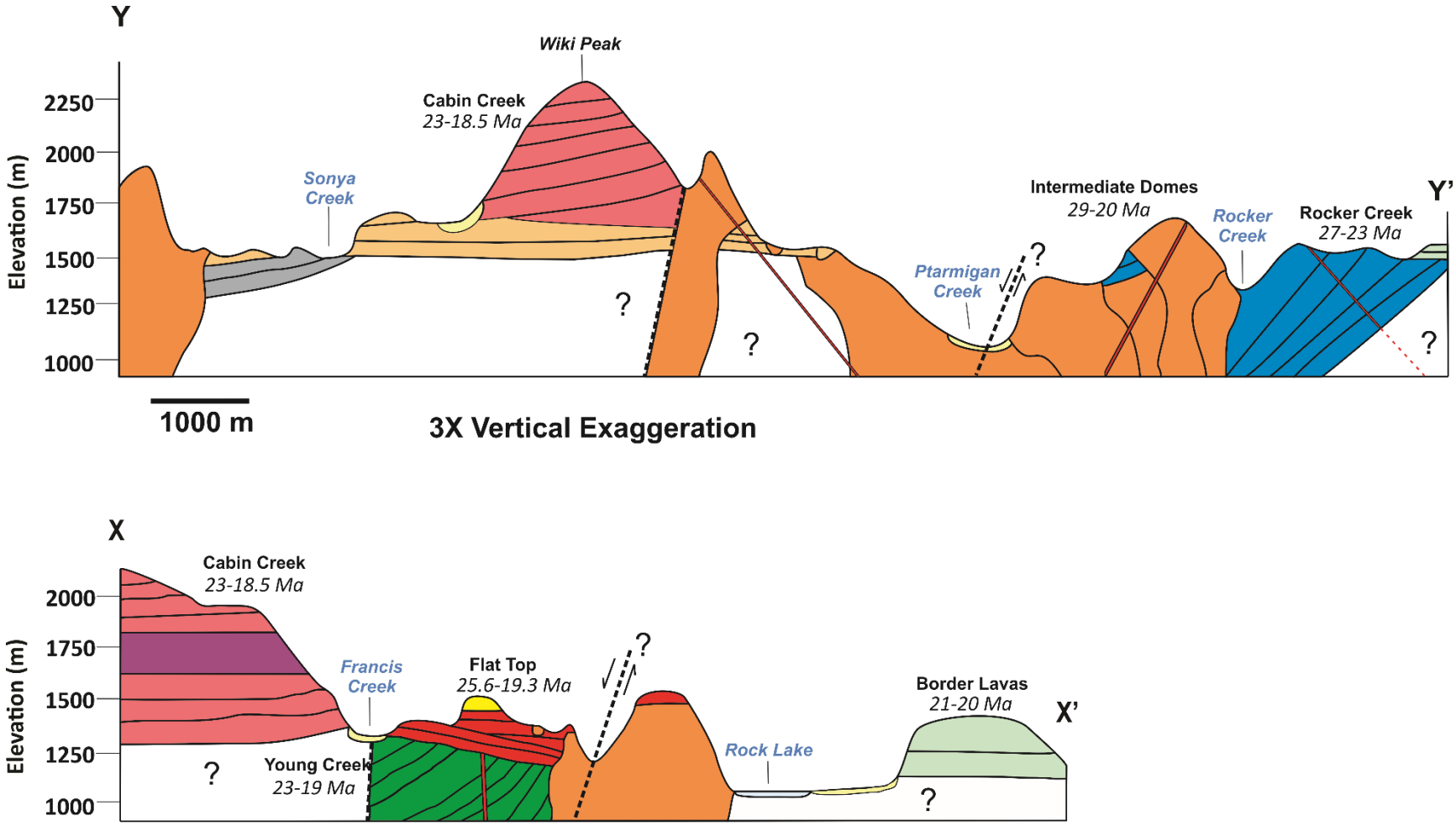

Figure 3.5: Schematic geologic cross-sections of the SCVF. Lines X-X' and Y-Y' are shown in Figure 1.2.

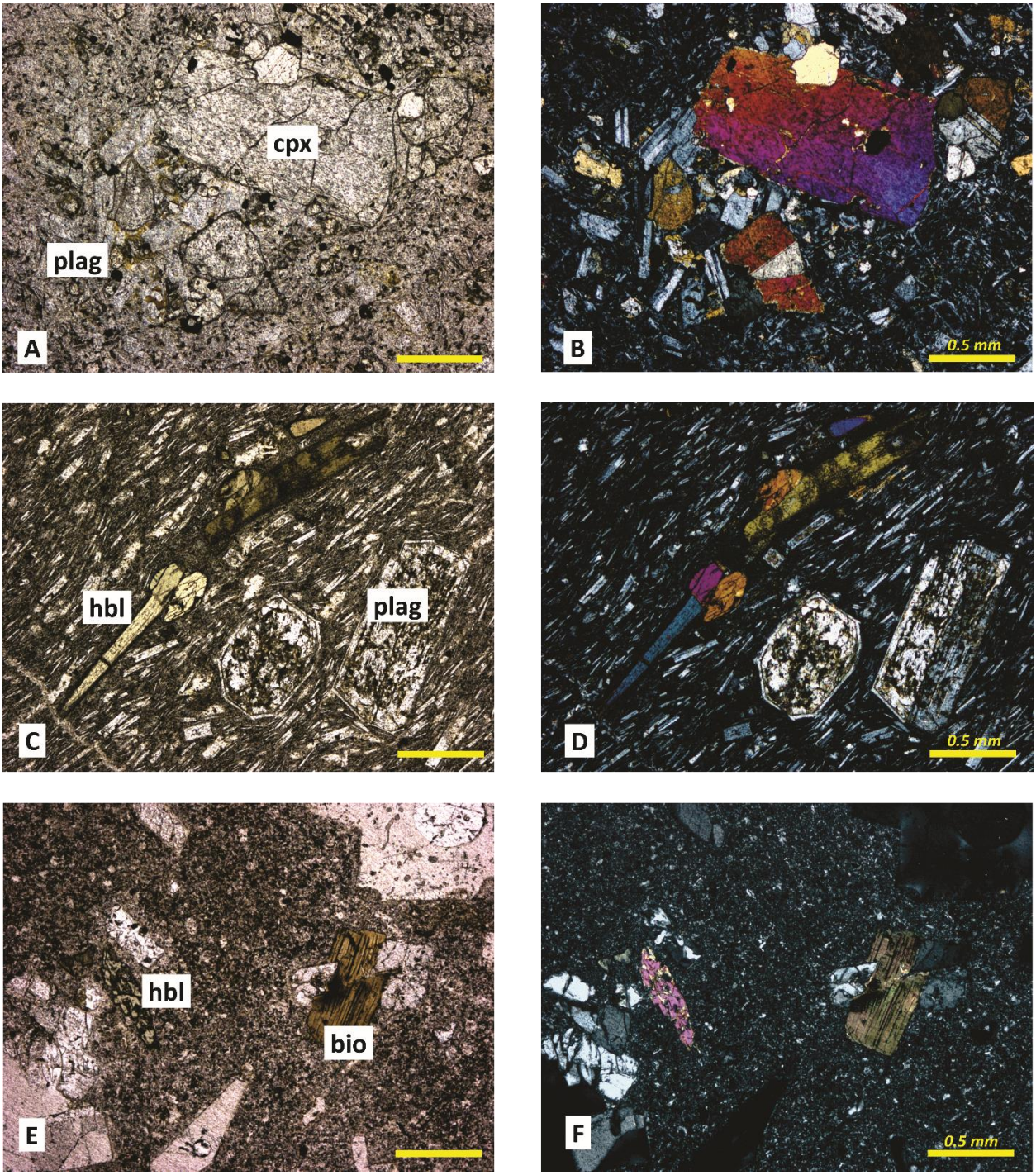

Figure 3.6: Photomicrographs of SCVF thin sections, all at 4x magnification. A) PPL and B) XPL images of Rocker Creek basaltic-andesite 15JB47LA. C) PPL and D) XPL images of Rocker Creek dacite dome 15JB40LA, showing hornblende phenocryst, sieved plagioclase, and trachytic groundmass. E) PPL and F) XPL images of silicic plug SB15-45, showing two hydrous phenocryst phases (hornblende and biotite).

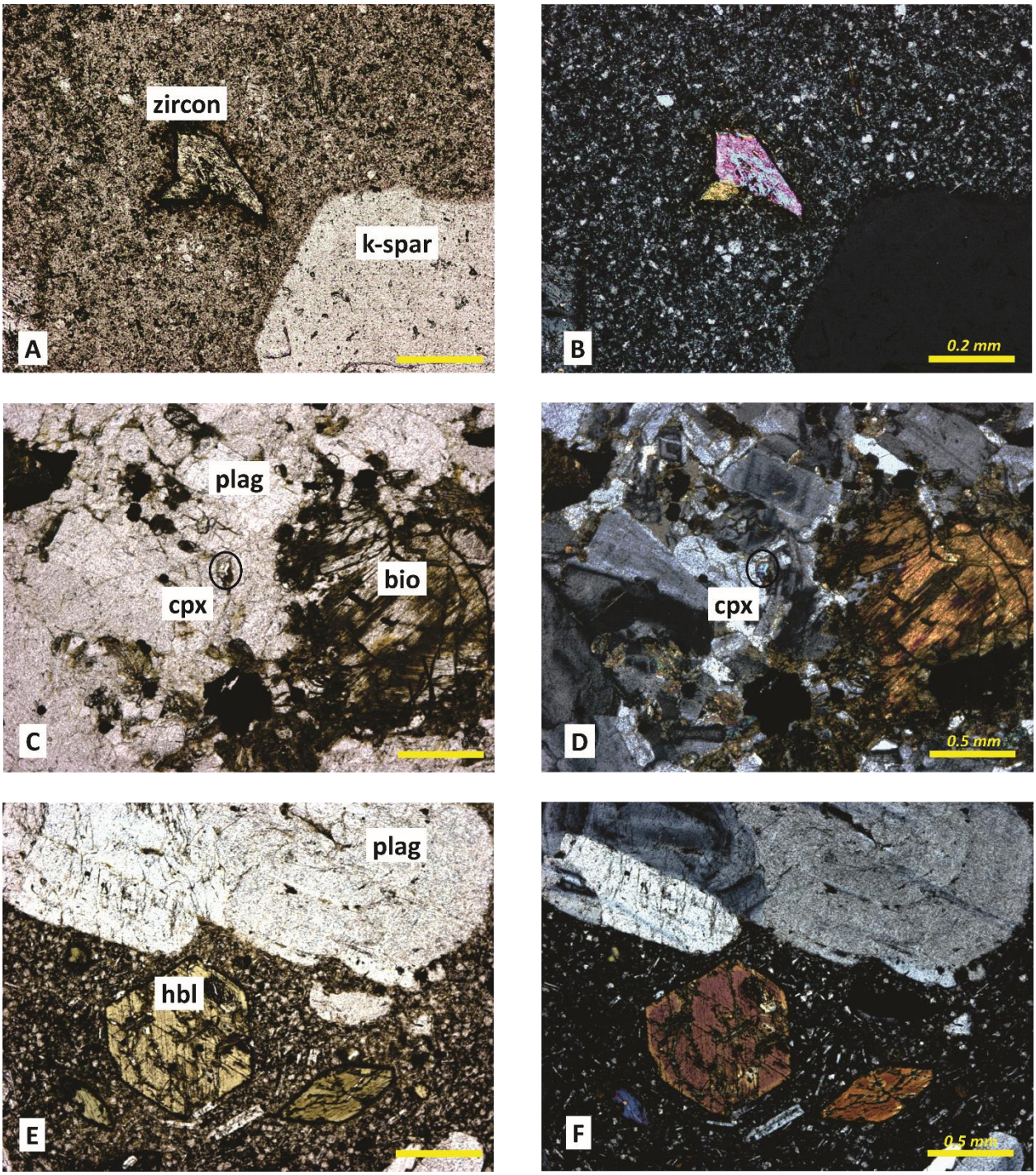

Figure 3.7: Photomicrographs of SCVF thin sections, A) and B) at 10x magnification, all others at 4x. A) PPL and B) XPL images of silicic lava SB15-34, showing zircon fragment and large feldspar phenocryst. C) PPL and D) XPL images of andesite diorite SB15-48 from the intermediate domes, showing intergranular biotite and clinopyroxene and large anhedral cumulate plagioclase crystals. E) PPL and F) XPL images of dacite intermediate dome sample 15JB28LA, showing hornblende and plagioclase phenocrysts.

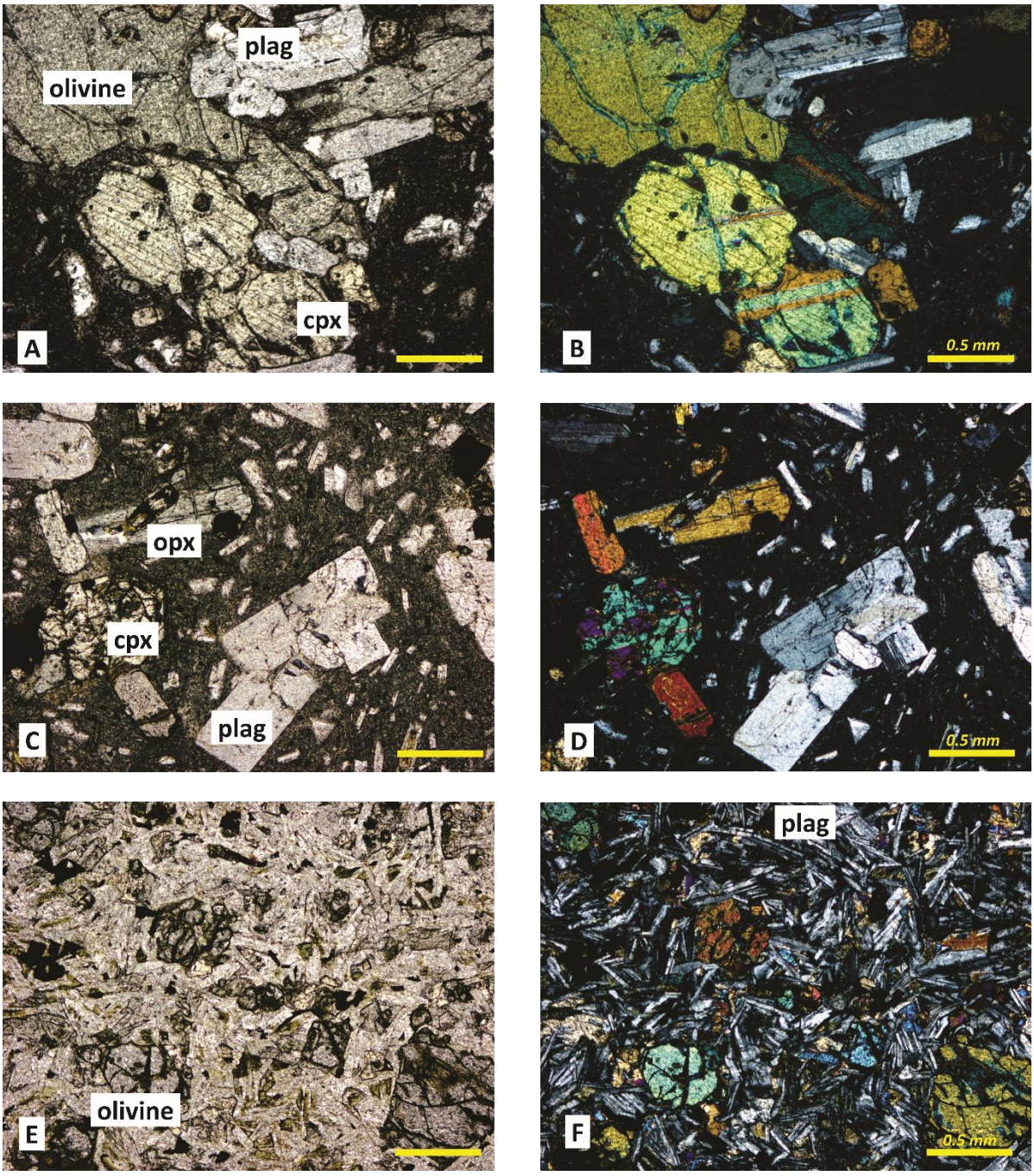

Figure 3.8: Photomicrographs of SCVF thin sections, all at 4x magnification. A) PPL and B) XPL images of Cabin Creek andesite SB15-31, showing large glomerocryst of olivine, orthopyroxene, clinopyroxene, and plagioclase in a glassy groundmass. C) PPL and D) XPL images of Cabin Creek dacite SB15-23, showing porphyritic texture with phenocrysts of plagioclase, orthopyroxene, and clinopyroxene in a glassy groundmass. E) PPL and F) XPL images of Flat Top basalt SB15-39, showing olivine crystals in a coarse-grained groundmass of plagioclase laths, opaque mineras, and clinopyroxene with a sub-ophitic texture.

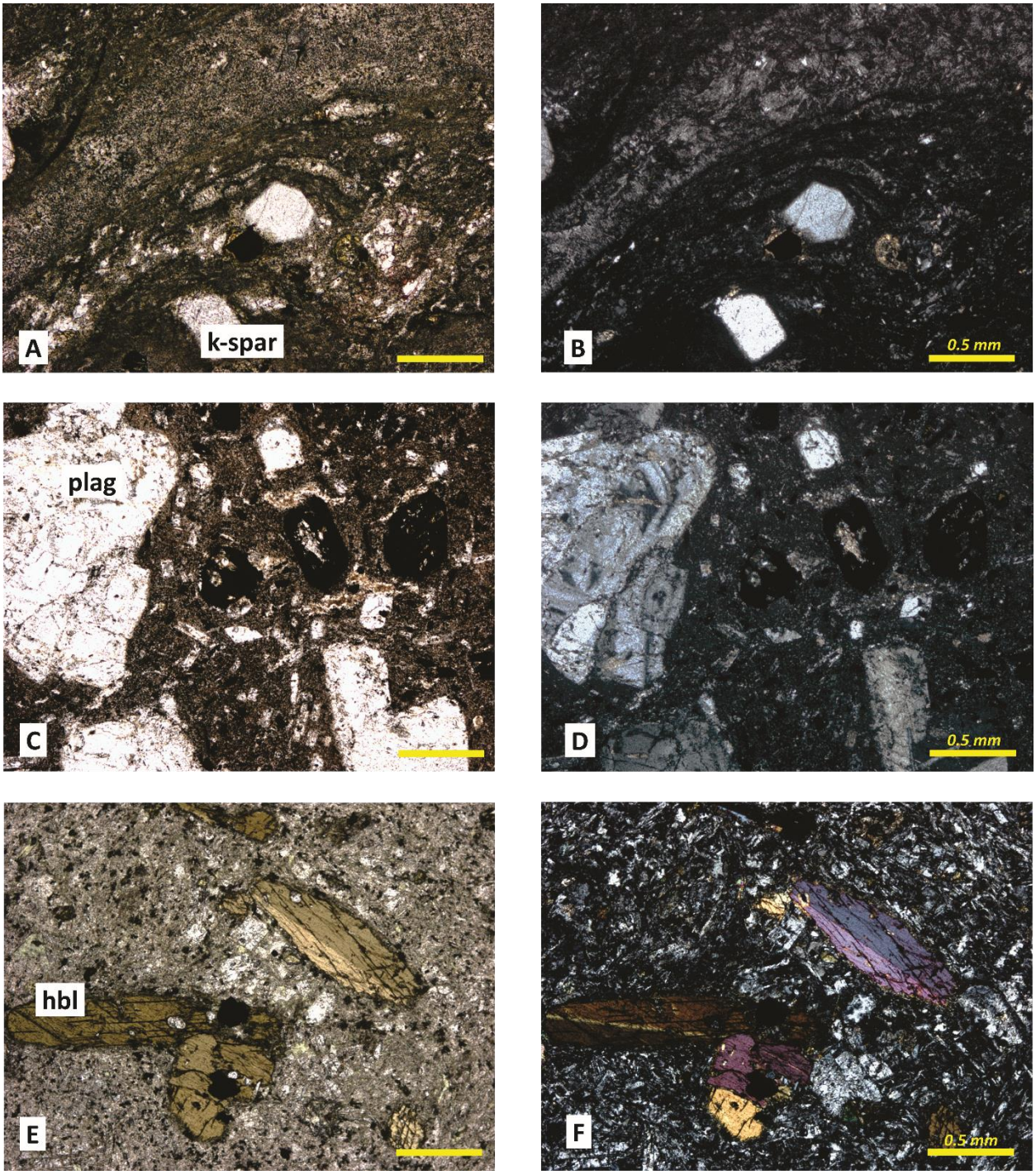

Figure 3.9: Photomicrographs of SCVF rocks, all at 4x magnification. A) PPL and B) XPL images of Flat Top tuff (SB15-40), showing the welded/flow-banded groundmass and phenocrysts of feldspar and clinopyroxene. C) PPL and D) XPL images of dacite Border Lava 15JB46LA, showing large plagioclase phenocryst. E) PPL and F) XPL images of Young Creek andesite lava SB15-52, showing euhedral hornblende phenocrysts.

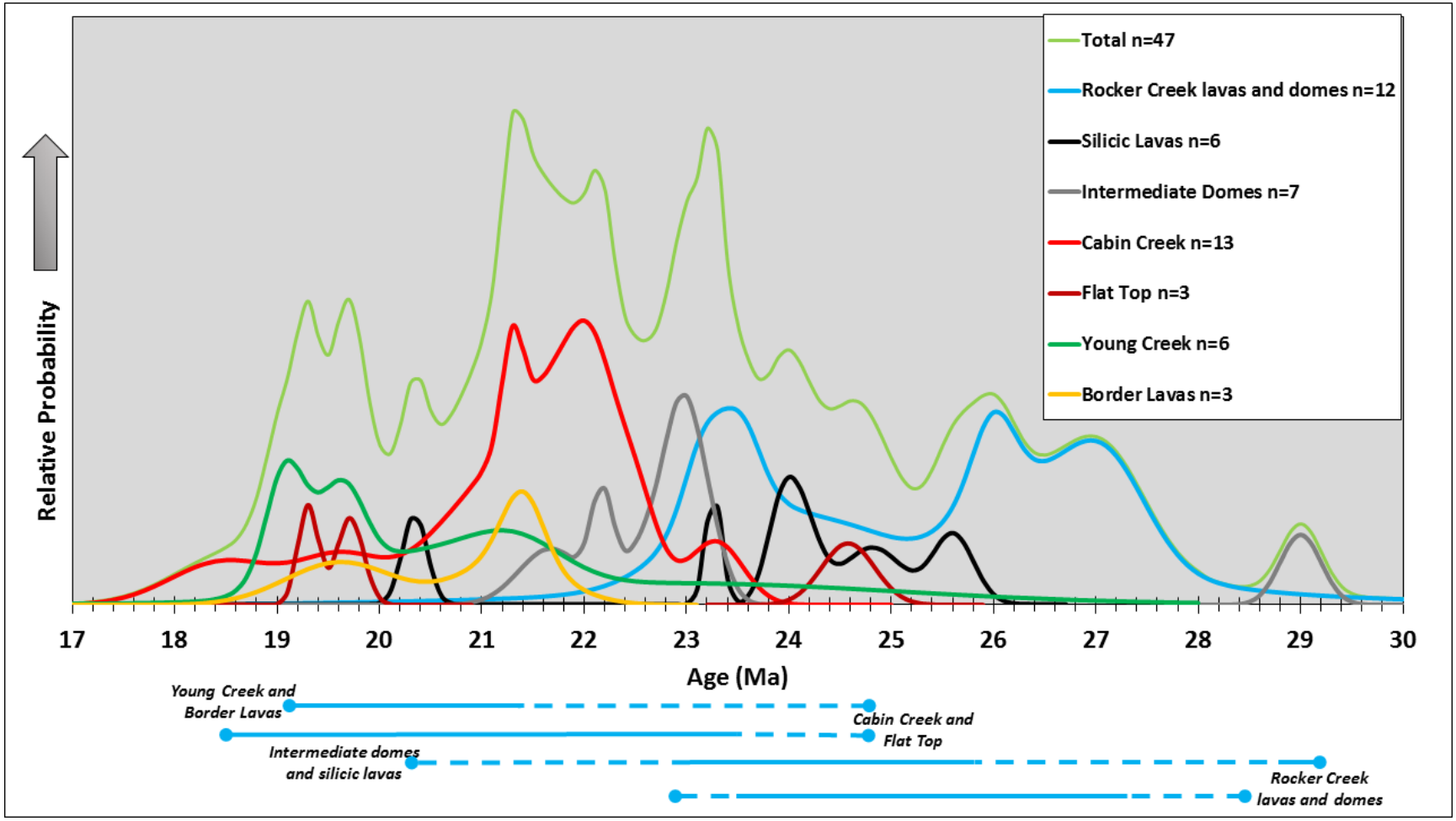

Figure 3.10: Probability distribution diagram (a.k.a. ideogram) for 47 new bedrock 40Ar/39Ar ages, showing the distribution and relative probability of SCVF magmatic activity through time. Blue bars across the bottom show approximate age ranges for each volcanic unit.

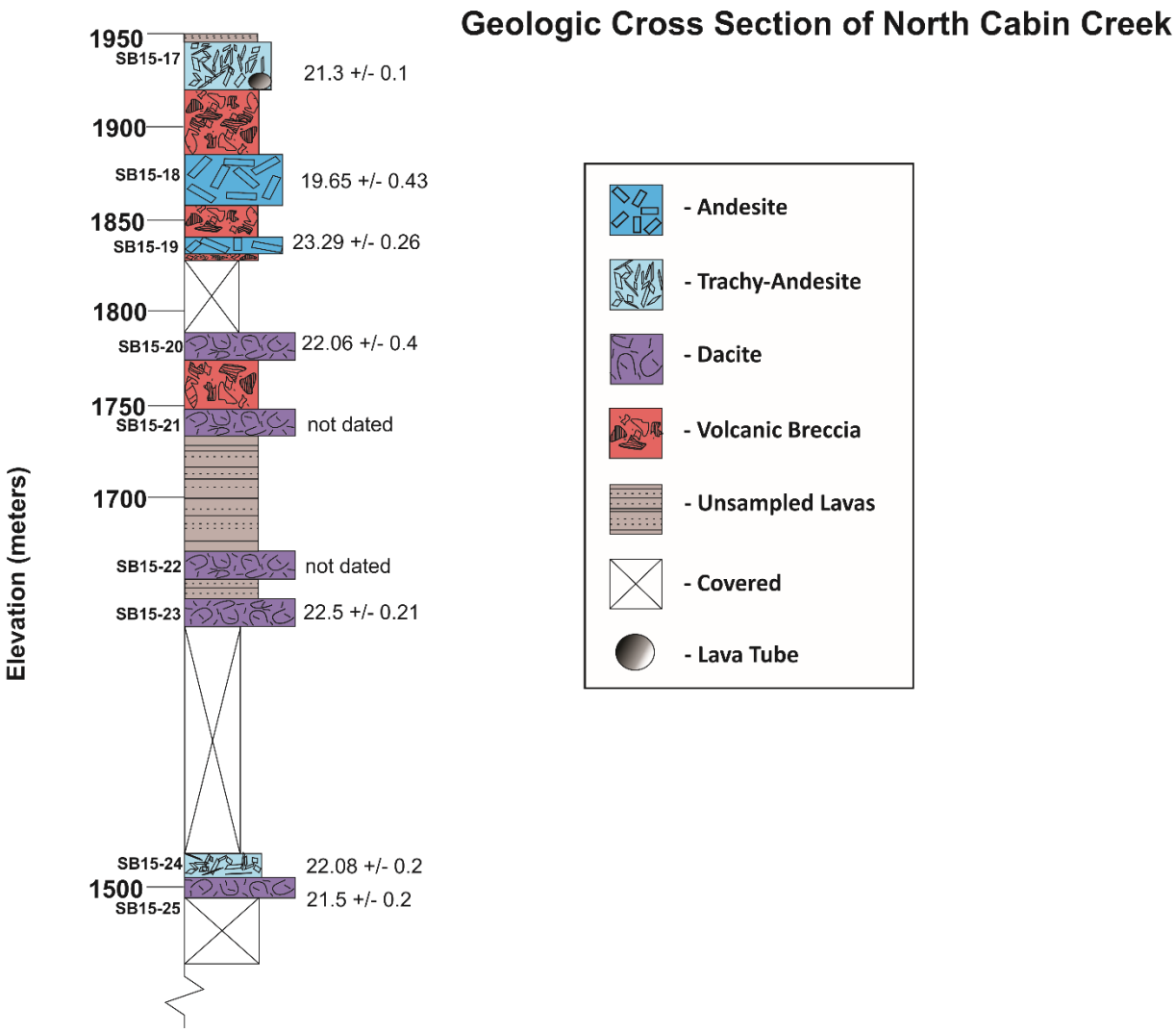

Figure 3.11: Stratigraphic section of North Cabin Creek, showing compositional diversity of lavas, and interbedded volcanic breccias. $^{40}Ar/^{39}Ar$ ages are shown to the right. Compare to the photograph of this section in Figure 3.3A.

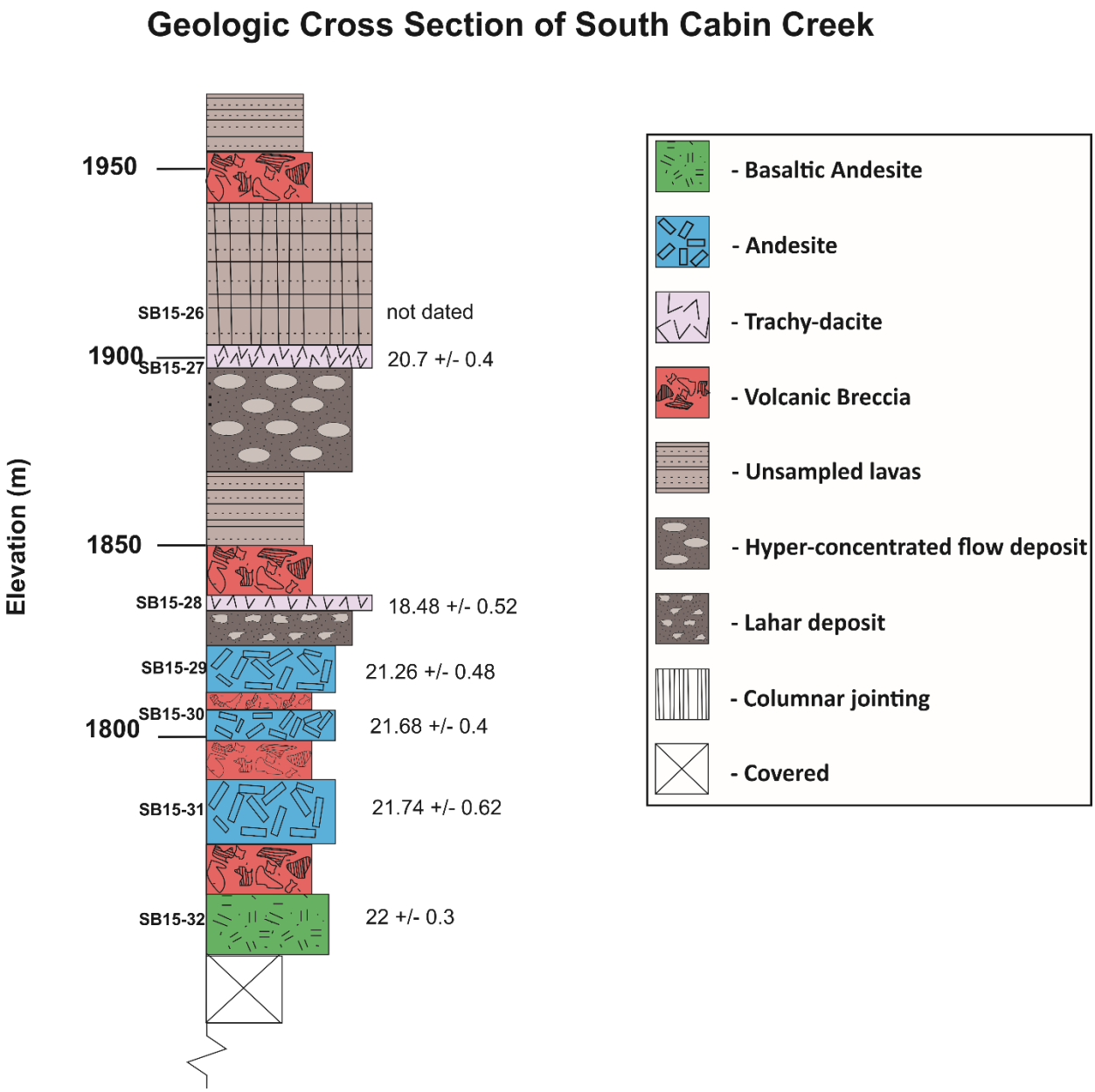

Figure 3.12: Stratigraphic section of South Cabin Creek, showing the lower mafic package with interbedded volcanic breccias, the lahar and debris-flow deposits, and the thick upper trachydacite flow with columnar jointing. $^{40}Ar/^{39}Ar$ ages are shown to the right. Compare to the photograph of this section in Figure 3.3E.

Sample	SB15-27	SB15-31	SB15-39	SB14-40	15JB25LA	15JB47LA	SB15-34	15JB38LA	15JB37LA	SB15-53
Rock Unit	Cabin Creek	Cabin Creek	Flat Top	Flat Top	Rocker Creek	Rocker Creek	Silicic Lavas	Silicic Lavas	Border Lavas	Young Creek
SiO_2	64.26	56.03	48.48	69.69	49.93	59.06	75.33	75.10	67.05	54.65
TiO_2	1.14	1.05	1.37	0.67	1.35	0.77	0.07	0.06	0.77	1.28
Al_2O_3	15.55	16.40	16.65	14.44	16.14	17.17	13.62	14.04	16.30	16.73
Fe_2O_3*	5.47	7.75	10.81	3.15	9.95	6.10	0.81	0.65	3.28	7.96
MnO	0.10	0.12	0.16	0.07	0.15	0.09	0.09	0.05	0.19	0.13
MgO	1.38	5.06	8.39	0.41	7.48	3.31	0.13	0.20	0.35	4.69
CaO	3.37	7.39	9.14	1.42	9.62	6.09	0.74	0.72	3.13	8.35
Na_2O	5.33	4.00	3.34	5.24	3.41	4.33	3.74	3.84	5.00	3.59
K_2O	2.50	1.44	0.60	3.28	0.70	1.31	3.80	3.78	2.72	0.64
P_2O_5	0.36	0.30	0.29	0.10	0.39	0.27	0.07	0.06	0.23	0.37
Total	98.90	98.74	98.14	98.16	98.12	97.88	98.32	98.43	98.66	97.56
LOI	0.60	0.55	1.53	0.71	1.04	1.25	1.53	1.33	1.32	1.92
Rb	50	31	9	67	10	22	102	95	55	7
Sr	397	574	540	189	632	707	116	99	394	617
Y	32	22	23	42	24	17	12	12	23	28
Zr	313	187	108	457	119	152	54	52	209	184
V	84	165	207	28	207	124	7	5	57	163
Ni	4	63	139	4	71	46	3	3	3	60
Cr	0	139	282	2	221	56	3	2	2	96
Nb	14	9	9	15	9	10	17	15	12	9
Ga	19	17	17	18	18	18	16	17	18	18
Cu	8	63	66	5	30	26	4	1	6	47
Zn	75	71	88	56	100	73	37	27	62	82
Ba	609	386	215	834	289	538	835	1286	665	449
U	2.1	1.3	0.4	3.0	0.6	1.1	3.6	3.2	2.7	1.0
Th	5.1	3.2	1.0	7.1	1.5	2.5	4.1	5.1	6.1	2.3
Sc	12	21	31	8	31	13	3	3	9	20
Pb	8	4	2	11	2	4	12	15	8	3
Hf	7.2	4.4	2.6	10.9	2.8	3.6	2.3	2.2	5.3	4.4
Ta	1.0	0.6	0.6	1.1	0.5	0.7	1.9	1.6	0.9	0.6
Cs	0.6	0.5	0.1	0.7	0.2	0.2	2.1	3.1	0.7	0.4
La	26.7	18.4	12.1	33.4	18.5	18.2	6.6	9.3	22.1	17.8
Ce	55.3	38.2	26.9	68.9	39.8	35.9	13.4	18.2	43.2	38.1
Pr	6.9	4.8	3.7	9.1	5.2	4.4	1.6	2.0	5.1	4.9
Nd	27.0	19.3	16.0	35.2	20.2	17.2	6.7	7.1	20.1	20.9
Sm	5.7	4.1	3.8	7.4	4.4	3.5	1.6	1.6	4.4	5.1
Eu	1.7	1.3	1.5	1.7	1.6	1.2	0.2	0.3	1.3	1.6
Gd	6.0	4.3	4.2	7.5	4.8	3.4	1.6	1.6	4.2	5.1
Tb	1.0	0.7	0.7	1.3	0.8	0.5	0.3	0.3	0.7	0.9
Dy	6.1	4.4	4.6	7.9	4.8	3.2	2.0	1.9	4.3	5.4
Ho	1.2	0.9	0.9	1.6	1.0	0.7	0.4	0.4	0.9	1.1
Er	3.4	2.4	2.5	4.5	2.6	1.8	1.1	1.1	2.5	3.0
Tm	0.5	0.3	0.4	0.7	0.4	0.3	0.2	0.2	0.4	0.4
Yb	3.3	2.2	2.2	4.3	2.3	1.7	1.1	1.0	2.4	2.7
Lu	0.5	0.3	0.3	0.6	0.3	0.3	0.2	0.2	0.4	0.4
$^{40}Ar/^{39}Ar$ age (Ma)	20.7±0.4	21.74±0.62	24.58±0.26	19.3±0.1	25.5±2.9	27±0.4	23.92±0.15	23.26±0.08	19.62±0.53	21.31±0.48
$^{87}Sr/^{86}Sr_m$	0.703571	0.703597	0.703734	0.703943	0.704237	0.703789	0.705209	0.70503	*N.D.*	*N.D.*
$^{87}Sr/^{86}Sr_i$	0.703464	0.703549	0.703718	0.703664	0.704221	0.703755	0.704347	0.70411	*N.D.*	*N.D.*
$^{143}Nd/^{143}Nd_m$	0.513014	0.513005	0.512968	0.512988	0.512841	0.512968	0.512988	0.512892	*N.D.*	*N.D.*
$^{143}Nd/^{143}Nd_i$	0.512997	0.512987	0.512945	0.512972	0.512819	0.512929	0.512915	0.512871	*N.D.*	*N.D.*
εNd_i	+7.67	+7.50	+6.76	+7.16	+4.64	+6.76	+7.16	+5.29	*N.D.*	*N.D.*
$^{206}Pb/^{204}Pb$	18.837	18.932	18.814	18.839	18.974	18.966	19.030	18.971	*N.D.*	*N.D.*
$^{207}Pb/^{204}Pb$	15.555	15.563	15.550	15.556	15.571	15.569	15.580	15.578	*N.D.*	*N.D.*
$^{208}Pb/^{204}Pb$	38.288	38.372	38.251	38.290	38.417	38.399	38.456	38.451	*N.D.*	*N.D.*
$^{176}Hf/^{177}Hf_m$	*N.D.*	0.283134	0.283061	0.283147	0.282989	0.283097	*N.D.*	*N.D.*	*N.D.*	*N.D.*
$^{176}Hf/^{177}Hf_i$	*N.D.*	0.283130	0.283053	0.283144	0.282981	0.283092	*N.D.*	*N.D.*	*N.D.*	*N.D.*
εHf_i	*N.D.*	+12.69	+10.02	+13.11	+7.49	+11.45	*N.D.*	*N.D.*	*N.D.*	*N.D.*

Note: All major element data expressed as raw weight % oxides; Fe_2O_3* is total Fe; all other concentrations in ppm. *N.D.* = not determined.

Table 3-1: Representative geochemical analyses of Sonya Creek volcanic field rocks.

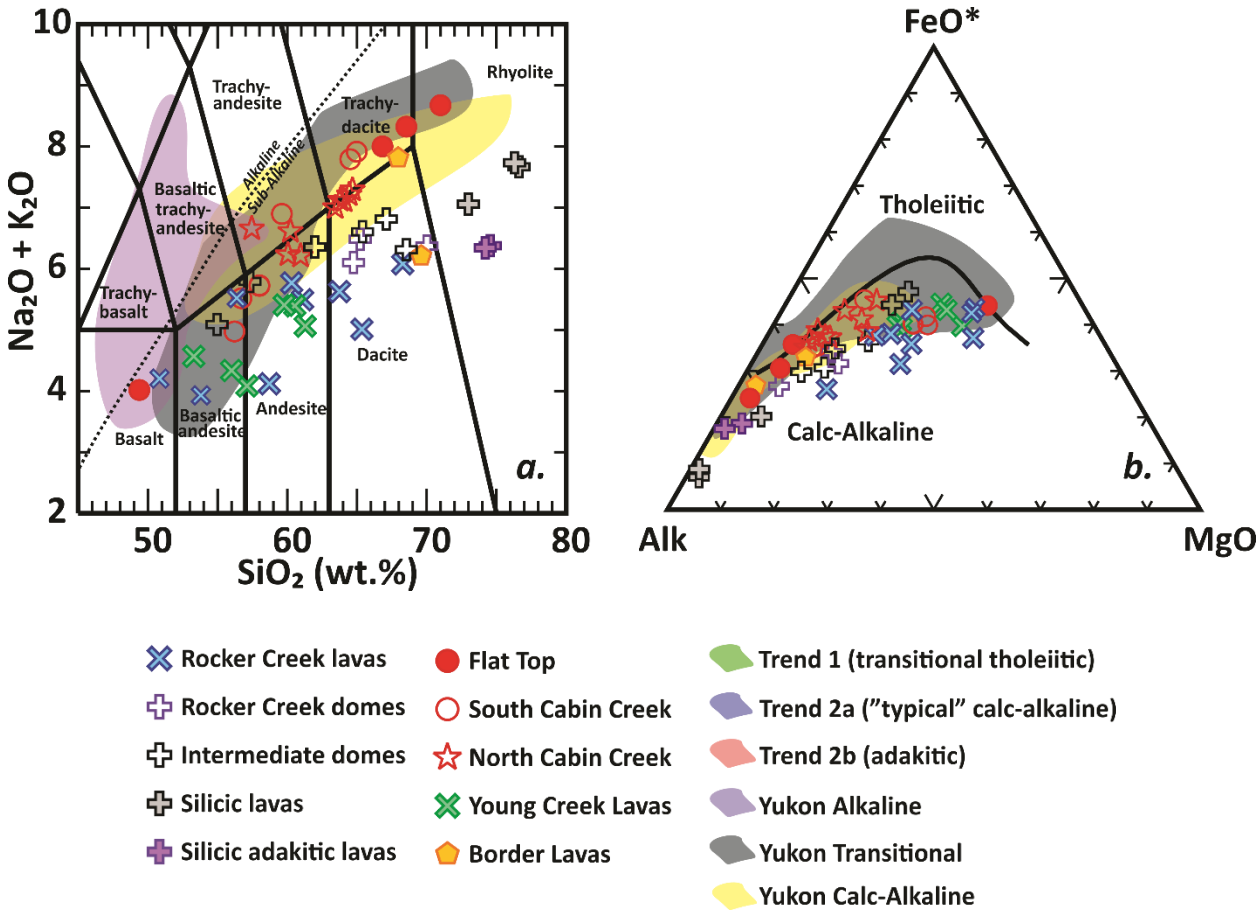

Figure 3.13: (A) Total alkali silica diagram after Le Bas et al. (1986), with the sub-alkaline discrimination line of Irvine and Barager (1971). B) AFM discrimination diagram after Irvine and Barager (1971). Data for Trends 1, 2a, and 2b are from Preece and Hart (2004). Data for Yukon alkaline, transitional, and calc-alkaline fields are from Skulski et al. (1991, 1992).

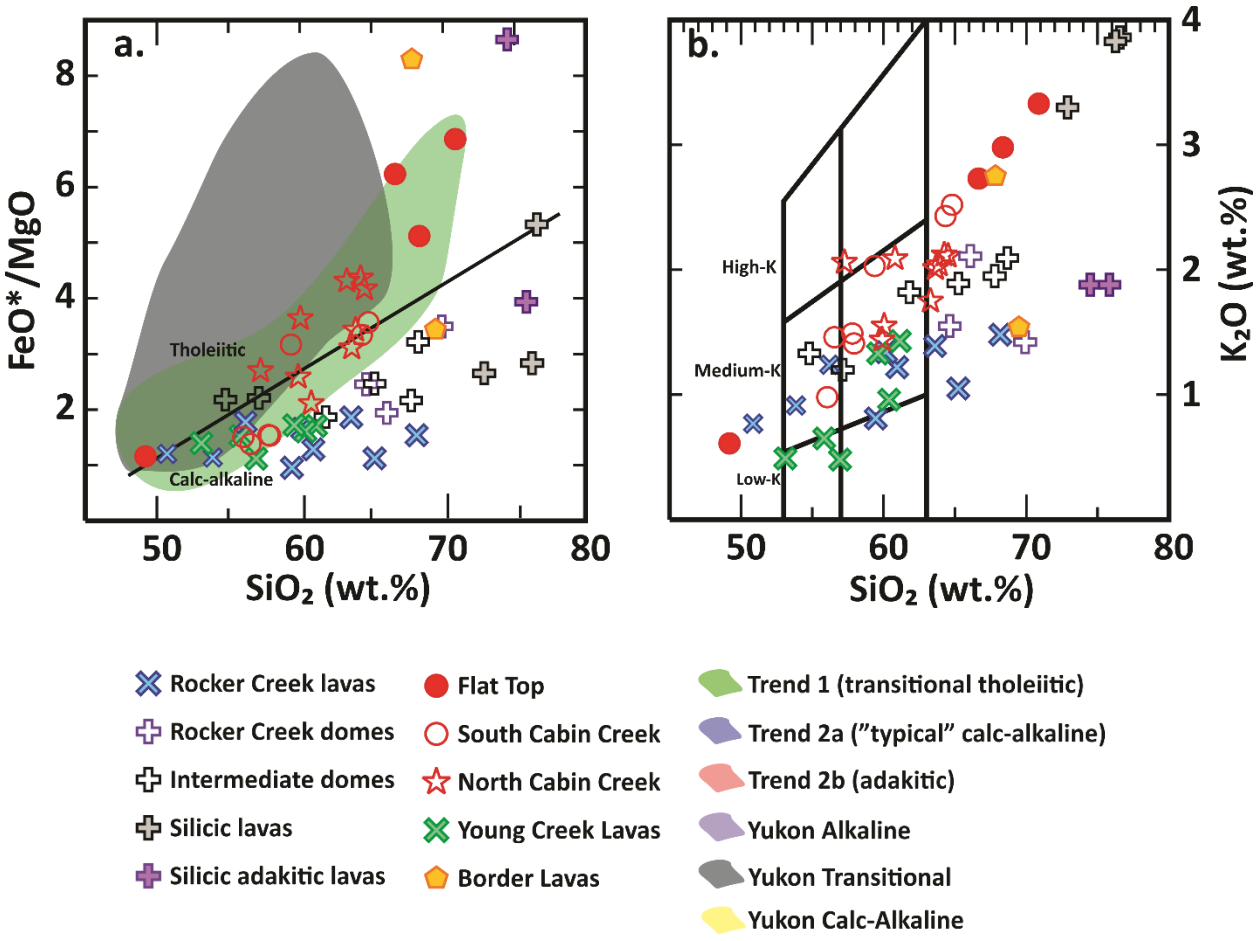

Figure 3.14: A) FeO*/MgO vs. SiO_2 wt. % discrimination diagram after Miyashiro (1974). B) Gill (1981) andesite classification diagram based on K_2O.

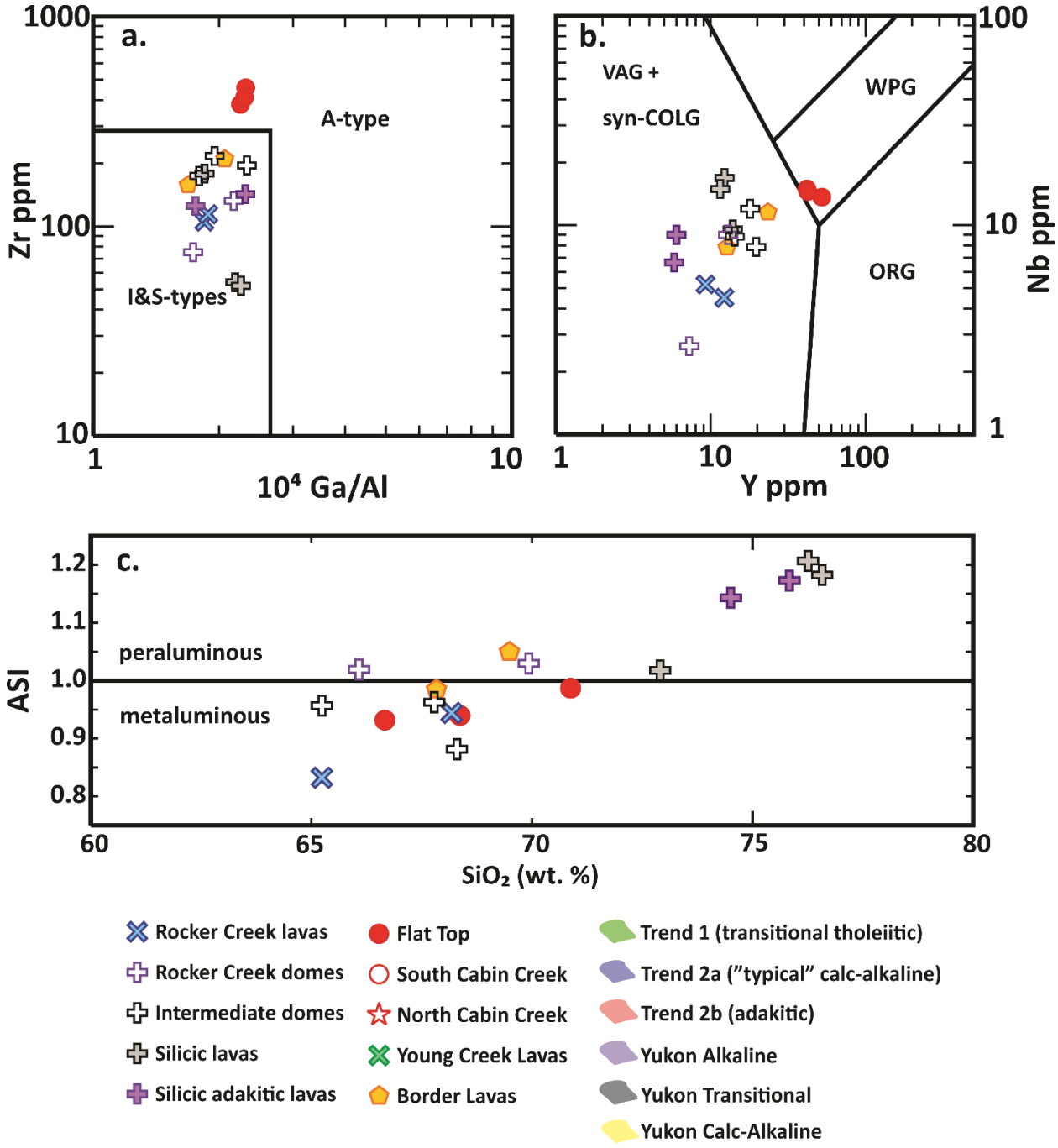

Figure 3.15: Felsic classification diagrams after (A) Whalen et al. (1987), (B) Pearce et al. (1984), and (C) Shand (1943).

Figure 3.16: Harker diagrams illustrating major element variations with wt. % SiO_2. Colored fields are published data plotted for comparison with SCVF data.

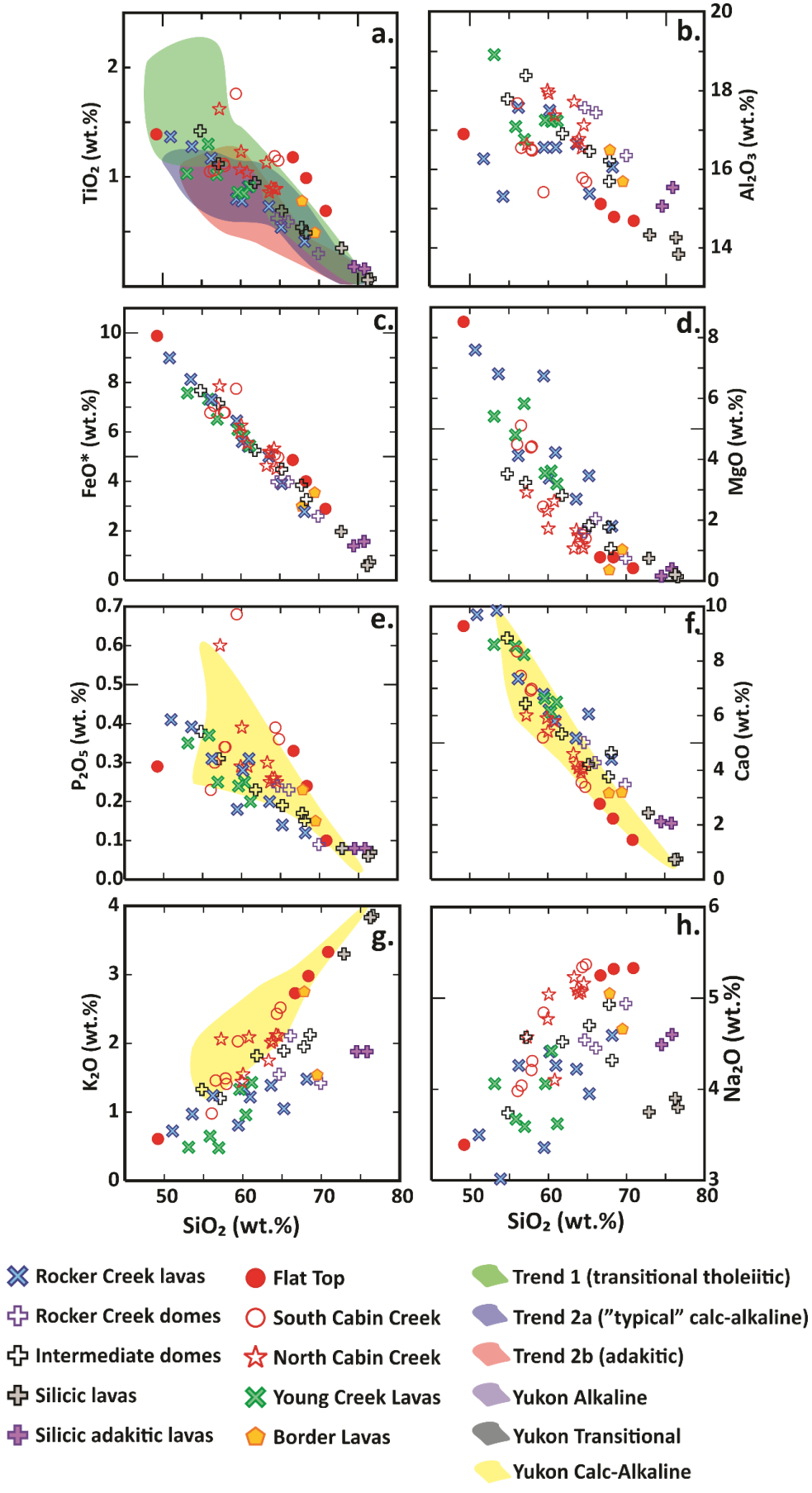
a.
b.
c.
d.
e.
f.
g.
h.
TiO2 (wt.%)
Al2O3 (wt.%)
FeO* (wt.%)
MgO (wt.%)
P2O5 (wt. %)
CaO (wt.%)
K2O (wt.%)
Na2O (wt.%)
SiO2 (wt.%)
SiO2 (wt.%)
Rocker Creek lavas
Rocker Creek domes
Intermediate domes
Silicic lavas
Silicic adakitic lavas
Flat Top
South Cabin Creek
North Cabin Creek
Young Creek Lavas
Border Lavas
Trend 1 (transitional tholeiitic)
Trend 2a ("typical" calc-alkaline)
Trend 2b (adakitic)
Yukon Alkaline
Yukon Transitional
Yukon Calc-Alkaline

Figure 3.17: Harker diagrams illustrating selected trace element variations with wt. % SiO_2. Colored fields are published data plotted for comparison with SCVF data.

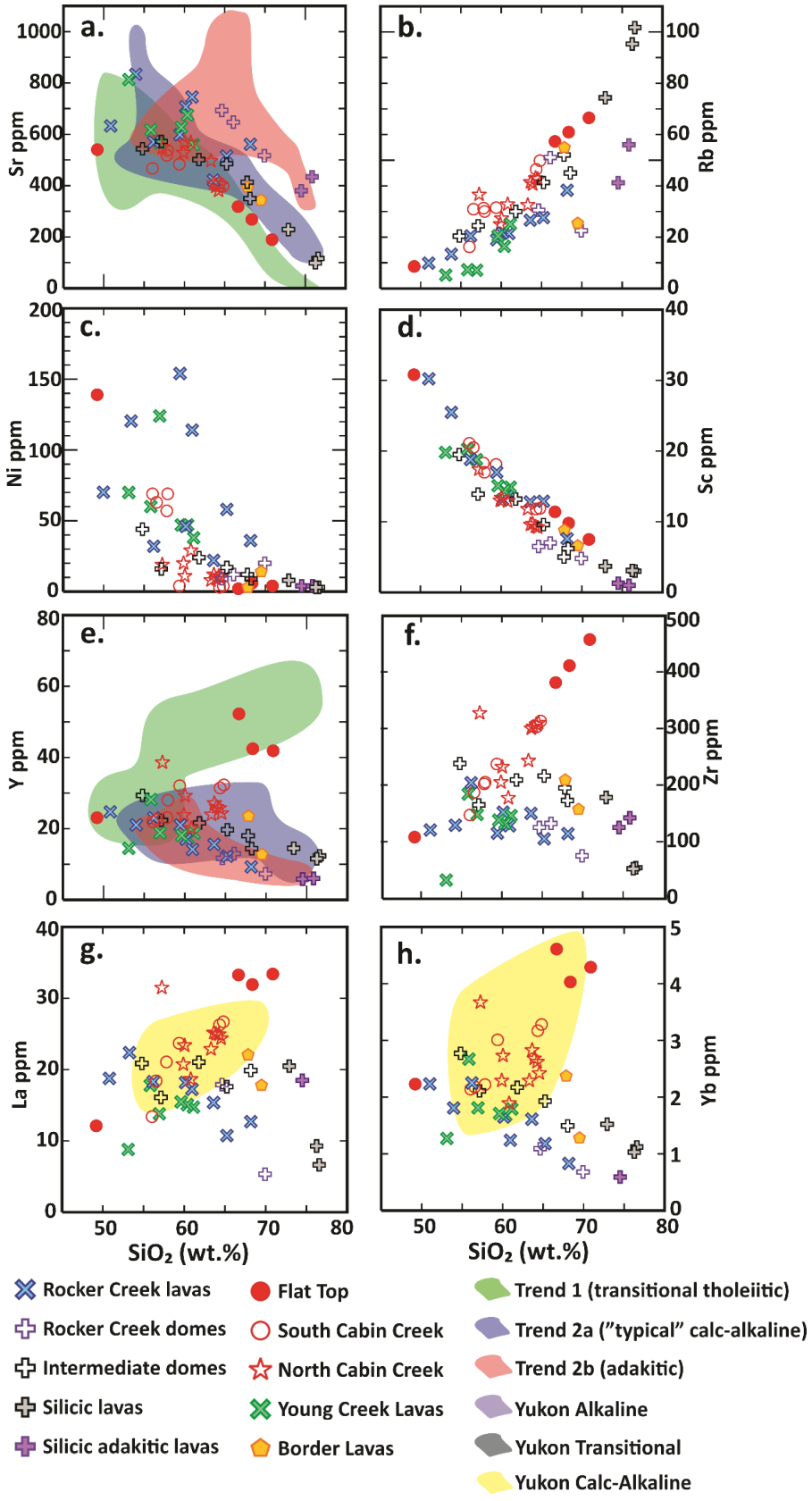
a.
b.
c.
d.
e.
f.
g.
h.
Sr ppm
Rb ppm
Ni ppm
Sc ppm
Y ppm
Zr ppm
La ppm
Yb ppm
SiO2 (wt.%)
SiO2 (wt.%)
Rocker Creek lavas
Rocker Creek domes
Intermediate domes
Silicic lavas
Silicic adakitic lavas
Flat Top
South Cabin Creek
North Cabin Creek
Young Creek Lavas
Border Lavas
Trend 1 (transitional tholeiitic)
Trend 2a ("typical" calc-alkaline)
Trend 2b (adakitic)
Yukon Alkaline
Yukon Transitional
Yukon Calc-Alkaline

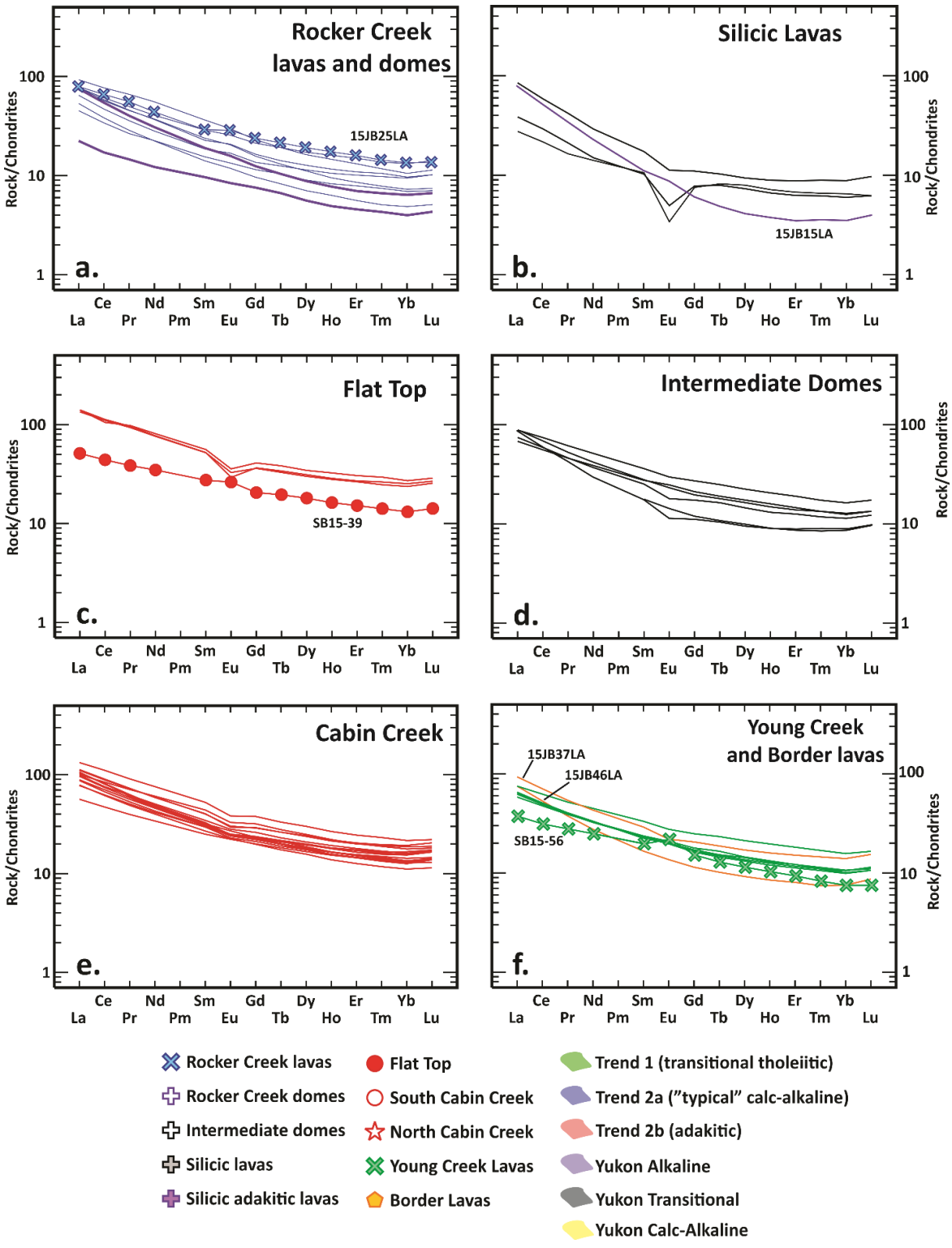

Figure 3.18: Chondrite-normalized rare earth element (REE) data for SCVF rocks samples. Samples with symbols are to highlight differences among the rocks groups that are mentioned in the text. Modified from Sun and McDonough (1989).

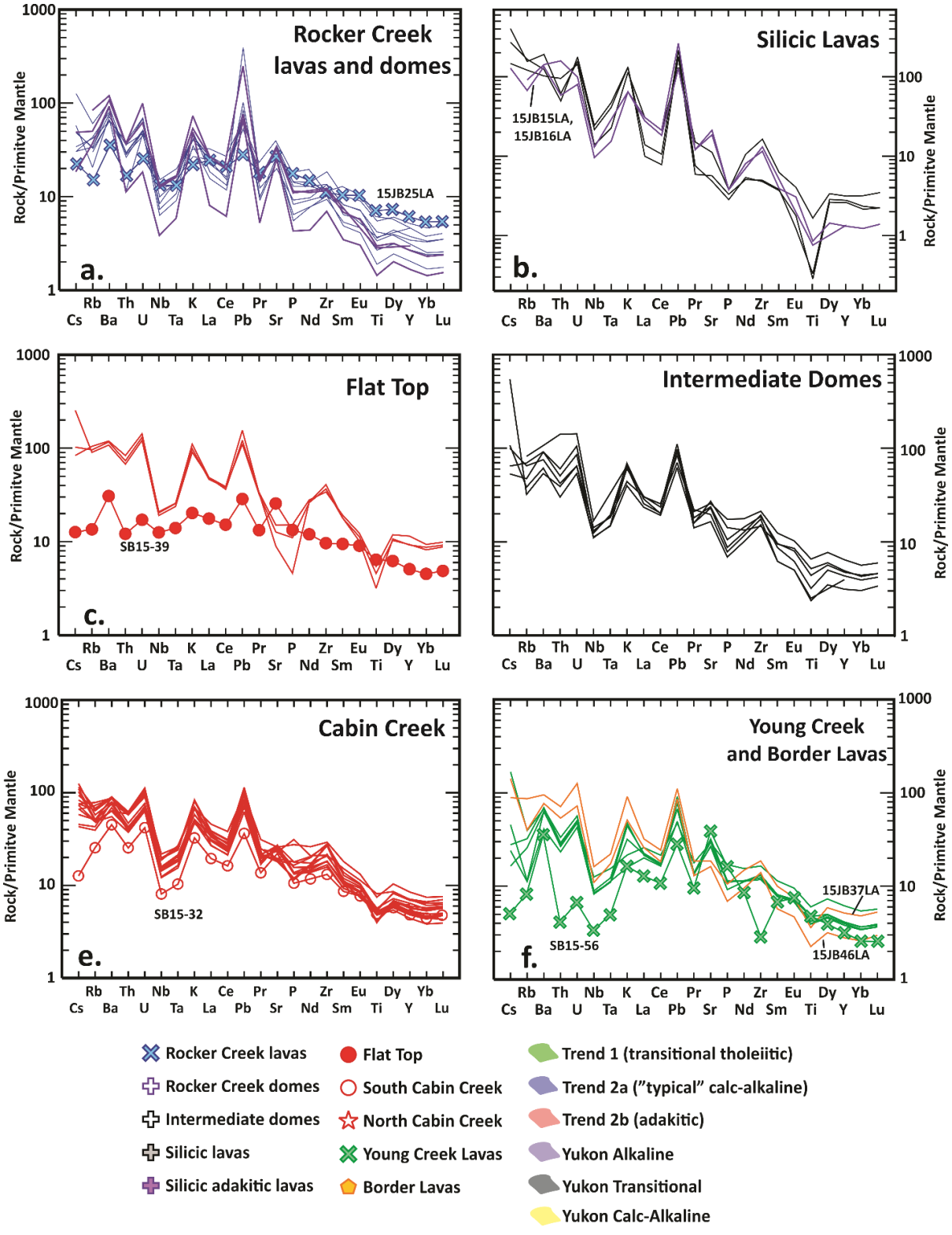

Figure 3.19: Primitive mantle normalized multi-element variation diagrams, of SCVF samples. Note the change in y-axis scale in (B) for the silicic lavas. Modified from Sun and McDonough (1989).

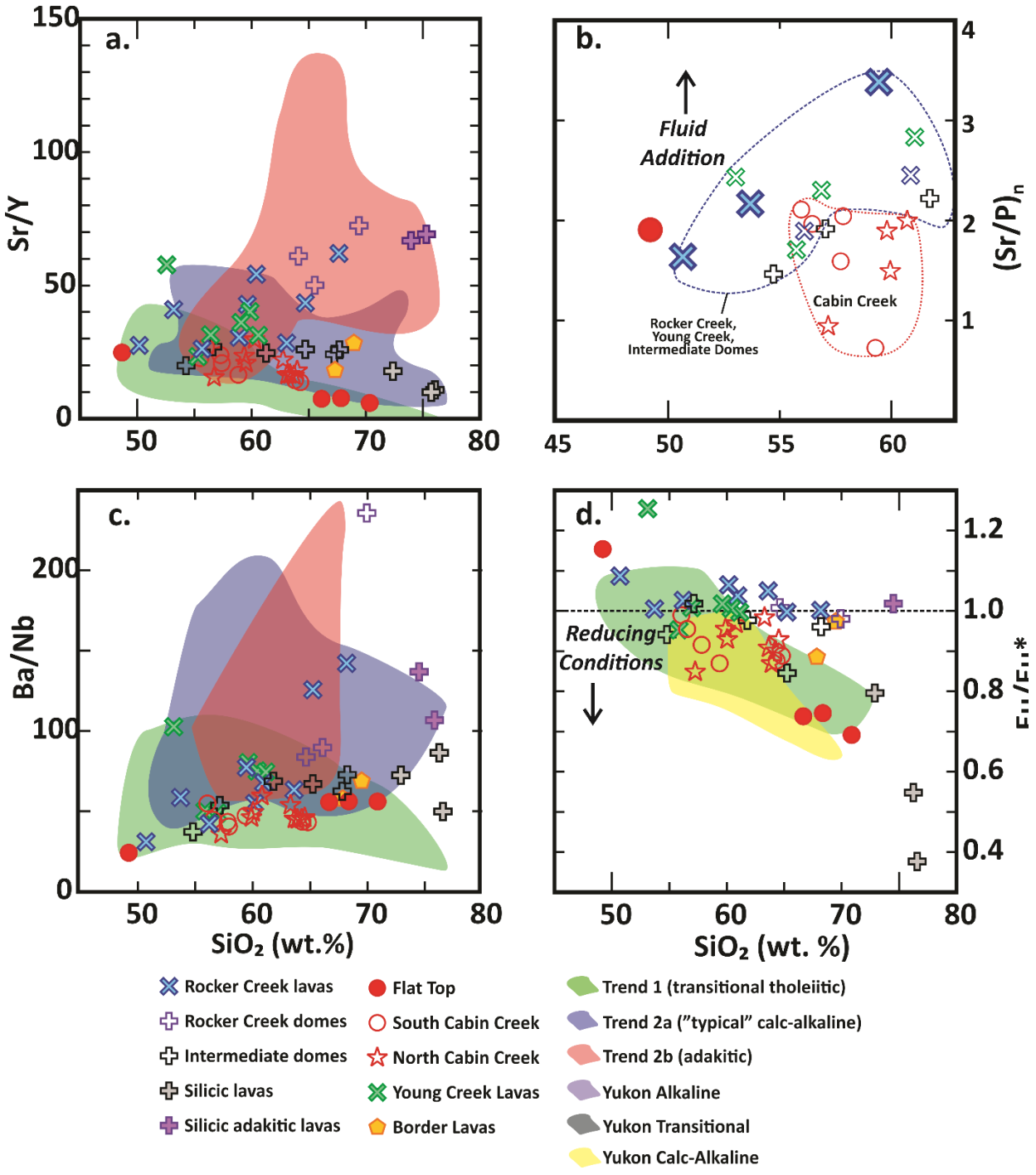

Figure 3.20: Selected trace element ratios plotted against SiO_2. Note the change in x-axis scale in (B), where larger filled symbols have MgO < 6 wt. % per the parameters of Borg et al., (1997). Sr/P is normalized to primitive mantle values of Sun and McDonough (1989).

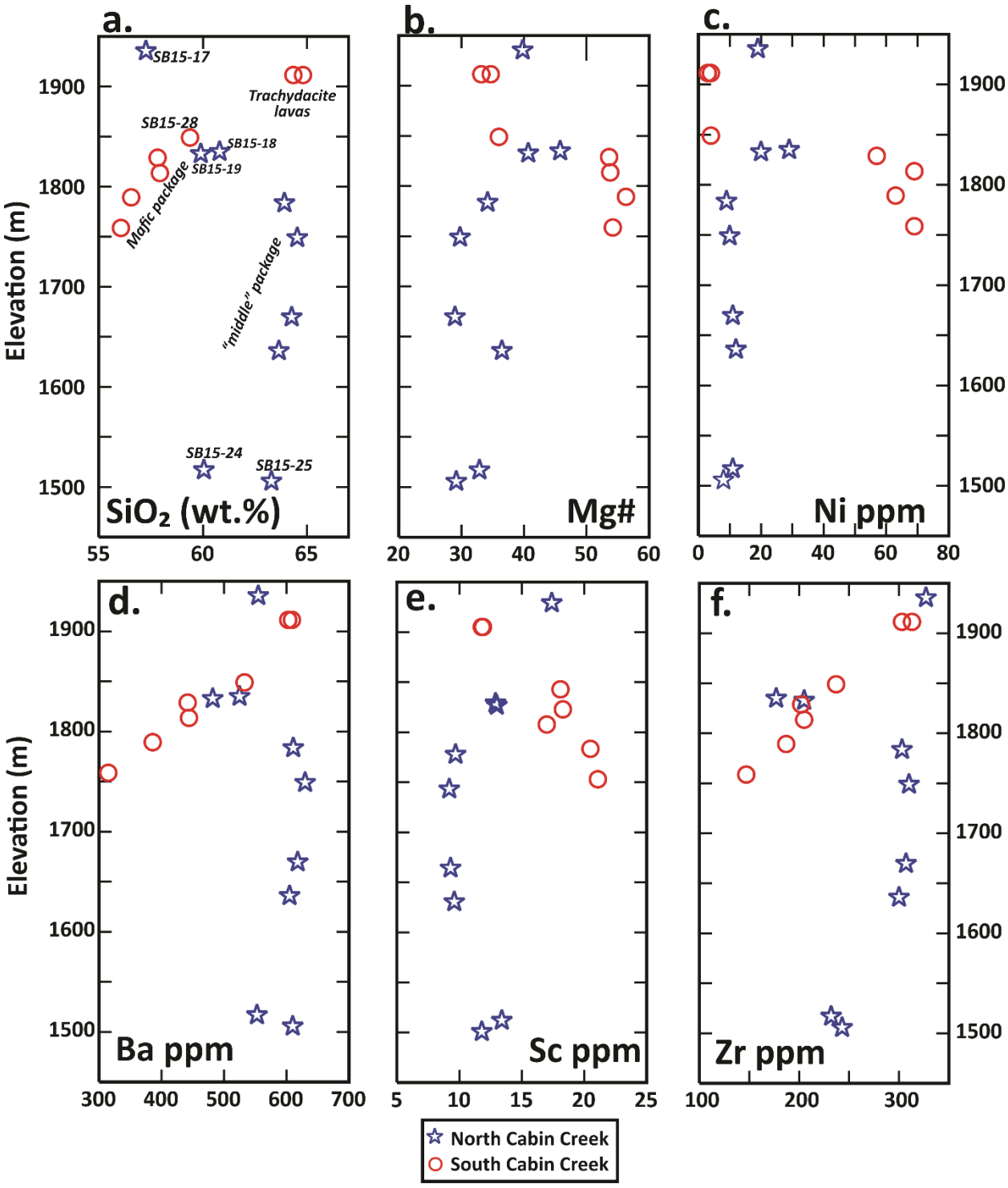

Figure 3.21: Chemo-stratigraphy of the North and South Cabin Creek sections. Names of rock groups used in the text are shown in (A). Compare to the Cabin Creek stratigraphic columns for stratigraphic context (Figs. 3.11 and 3.12).

Figure 3.22: (next page) $^{87}Sr/^{86}Sr$ vs. εNd for eight SCVF samples (sample names in inset). SCVF data are age-corrected to the $^{40}Ar/^{39}Ar$ ages presented in Tables 3-1 and 3-4, and in Appendix B. The fields of reference data are age-corrected to 23 Ma. εNd was calculated using $^{143}Nd/^{144}Nd$=0.512630 and $^{147}Sm/^{144}Nd$=0.1960 for CHUR (Bouvier et al., 2008). Mantle reservoirs are from Stracke (2012). Fields for reference data are from: Aleinikoff et al. (1987; 2000), Chan et al. (2012), Chauvel and Blichert-Toft (2011), Clift et al. (2005), Godfrey (2011), Greene et al. (2008; 2009), Hyeong et al. (2011), Jicha et al. (2004), Lassiter et al. (1995), McLennan et al. (1990), Mezger et al. (2000), Parker et al. (2010), Plank and Langmuir (1998), Preece (1997), Rioux et al. (2007), Samson et al. (1989; 1990; 1991), Snyder and Hart (2007), Vervoort et al. (2005), Von Drach et al. (1986), White et al. (1987), Yogodzinzki et al. (2010; 2015). See Figure 3.23 for a legend. SCVF symbols are the same as in geochemical plots. See Table 3-4 for abbreviations of end-members used in isotope mixing

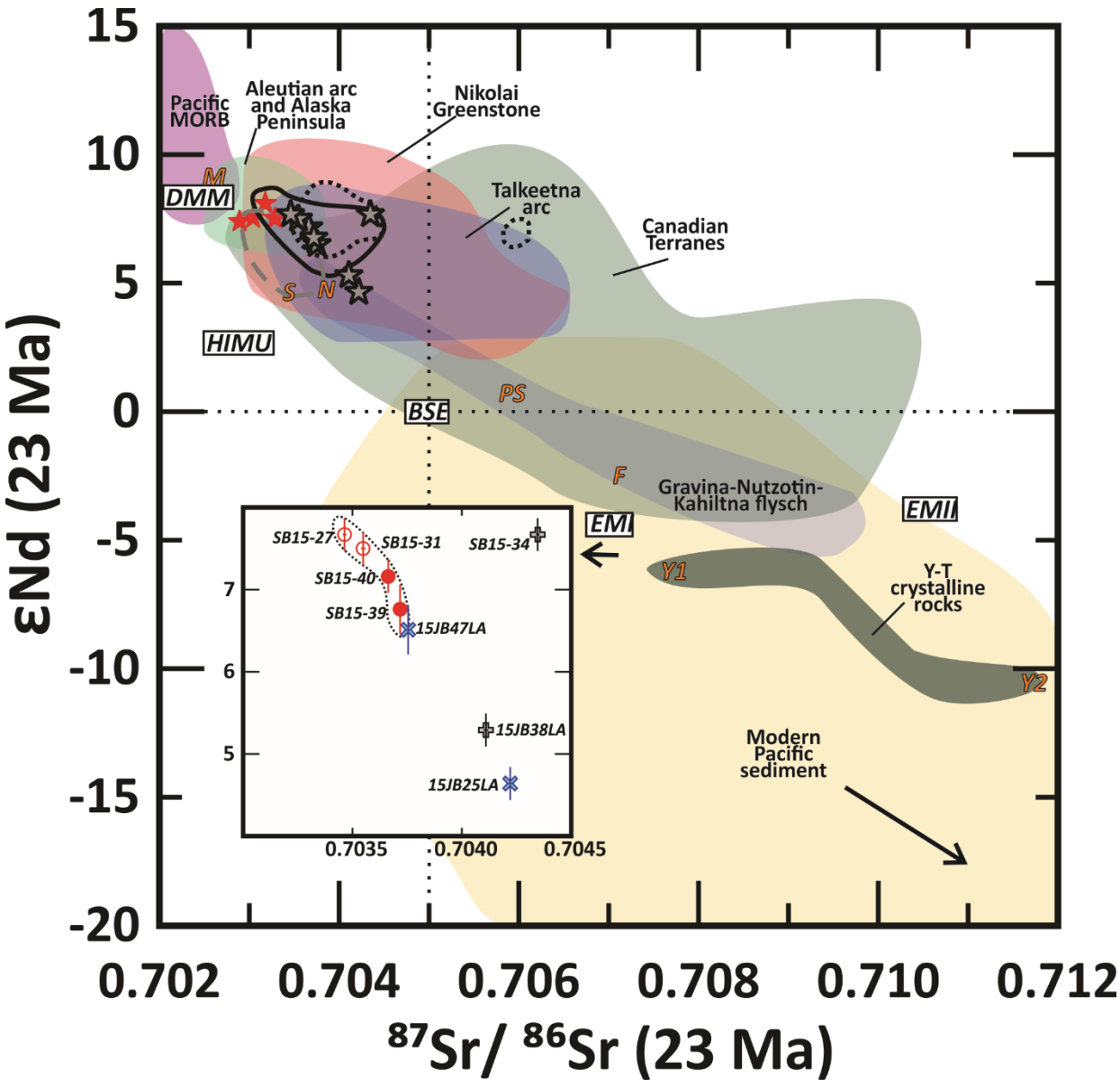

Wrangell Arc and Wrangellia	Offshore	Other Terranes
Sonya Creek Volcanic Field	Siletzia Terrane (Washingon state)	Talkeetna Arc
<5 Ma Wrangell Arc rocks	Pacific MORB	Gravina/Kahiltna flysch
White Mountain Granitoid (Cretaceous)	Modern Pacific Sediment	Yukon-Tanana Terrane crystalline rocks
Chisana lavas (Cretaceous)	Aleutian Arc and Alaska Peninsula	Canadian Terranes
Nikolai Greenstone		Y2 Mixing Model end-member

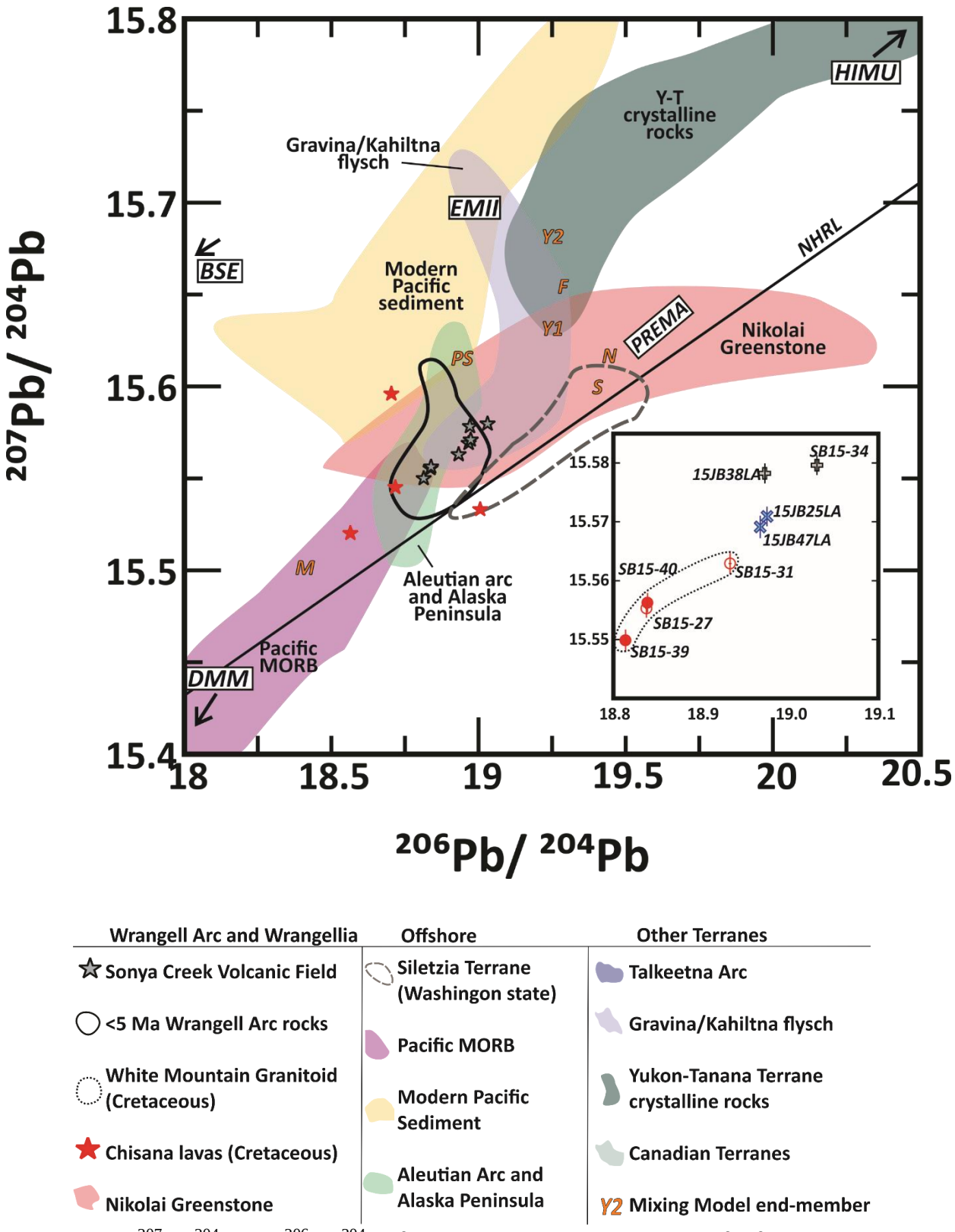

Figure 3.23: $^{207}Pb/^{204}Pb$ vs. $^{206}Pb/^{204}Pb$ for eight SCVF samples. Fields of reference data are from the same citations as in figure 3.22.

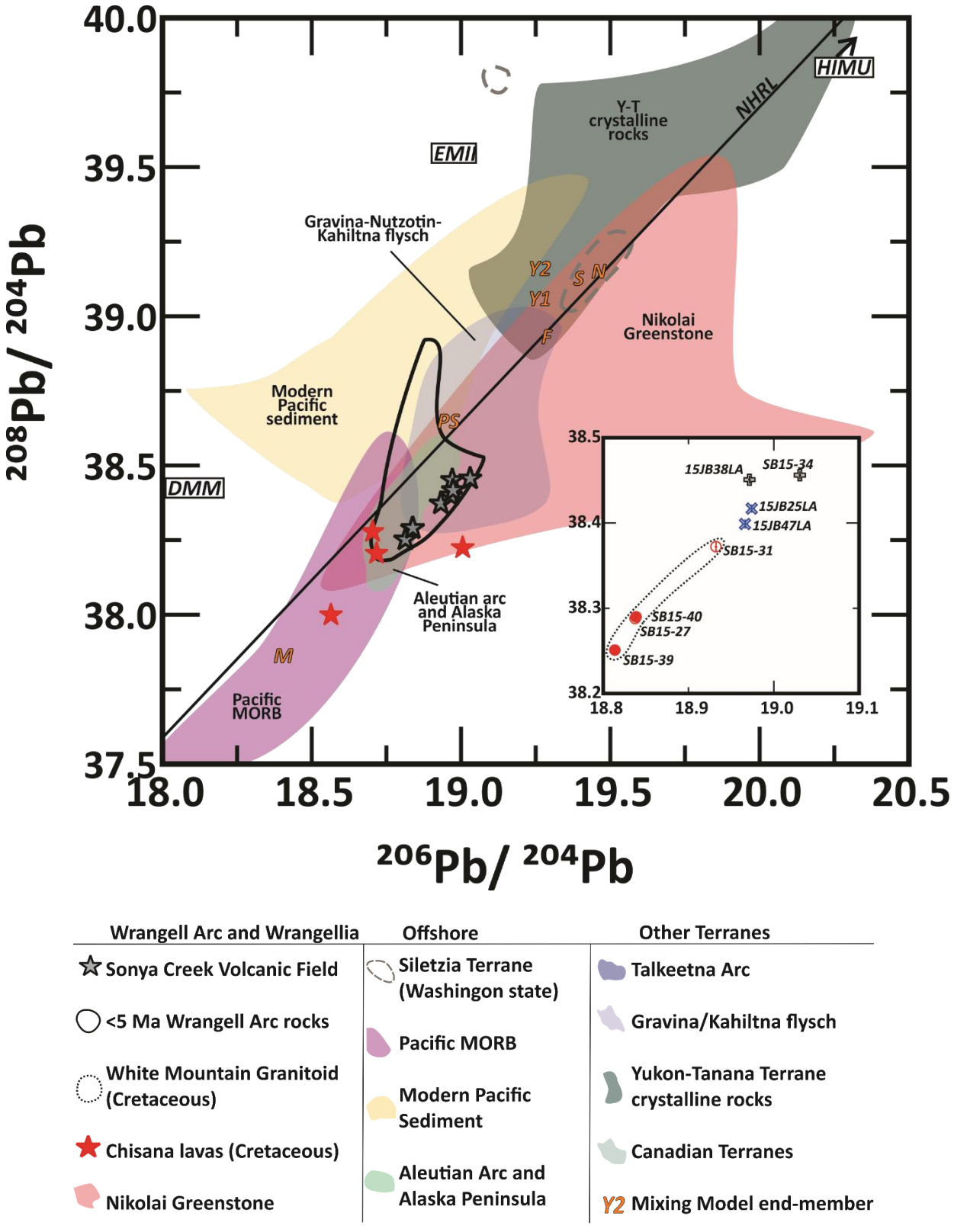

Figure 3.24: $^{208}Pb/^{204}Pb$ vs. $^{206}Pb/^{204}Pb$ for eight SCVF samples. Fields of reference data are from the same citations as in figure 3.22.

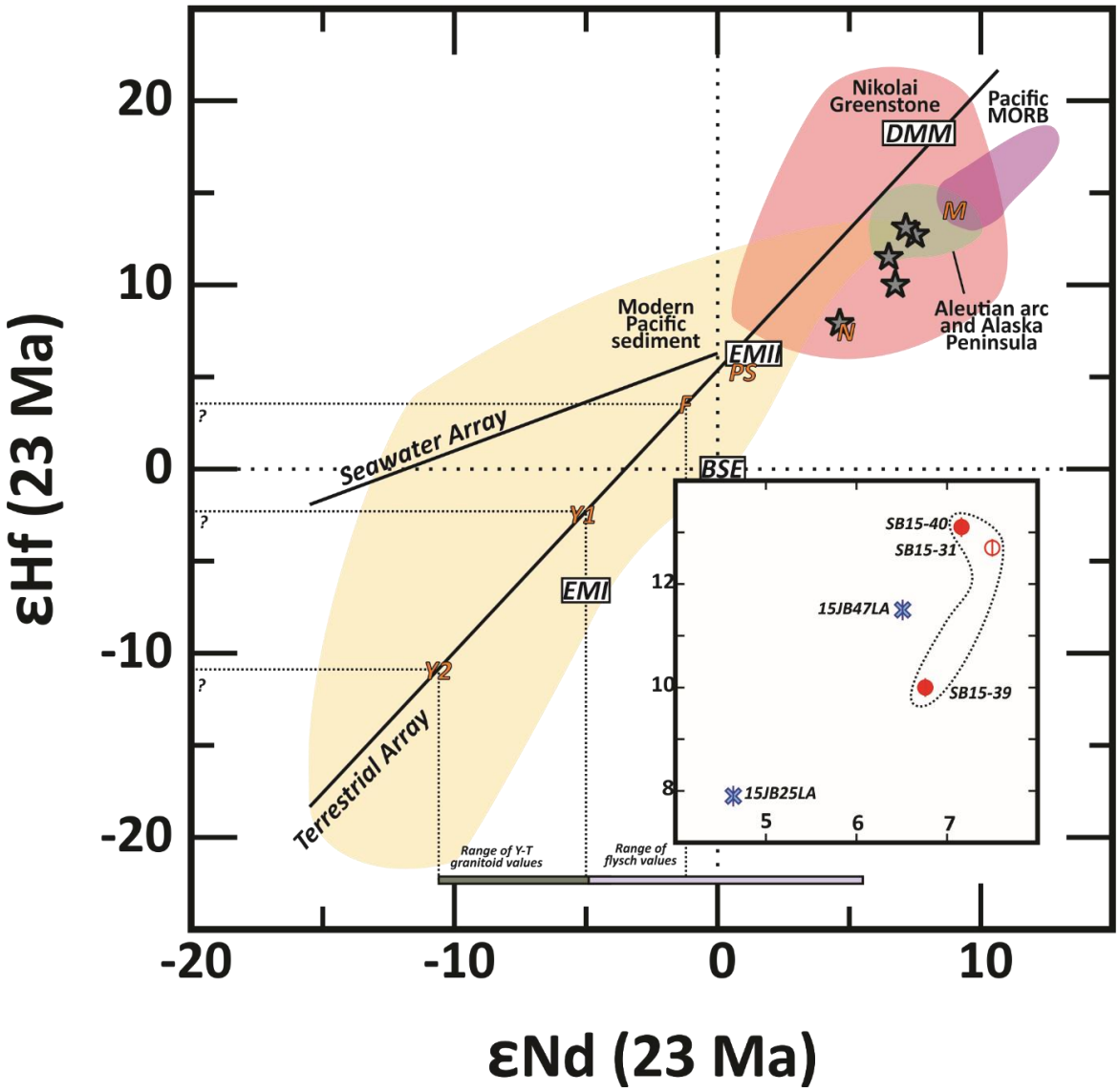

Wrangell Arc and Wrangellia	Offshore	Other Terranes
Sonya Creek Volcanic Field	Siletzia Terrane (Washingon state)	Talkeetna Arc
<5 Ma Wrangell Arc rocks	Pacific MORB	Gravina/Kahiltna flysch
White Mountain Granitoid (Cretaceous)	Modern Pacific Sediment	Yukon-Tanana Terrane crystalline rocks
Chisana lavas (Cretaceous)	Aleutian Arc and Alaska Peninsula	Canadian Terranes
Nikolai Greenstone		Y2 Mixing Model end-member

Figure 3.25: εHf vs. εNd for five SCVF samples. εHf was calculated using $^{176}Hf/^{177}Hf$ = 0.282785 and $^{176}Lu/^{177}Hf$ = 0.0336 for CHUR (Bouvier et al., 2008). Terrestrial array from Vervoort et al. (1999). Seawater array from Albarède et al., 1998). Fields of reference data are from the same citations as in figure 3.22.

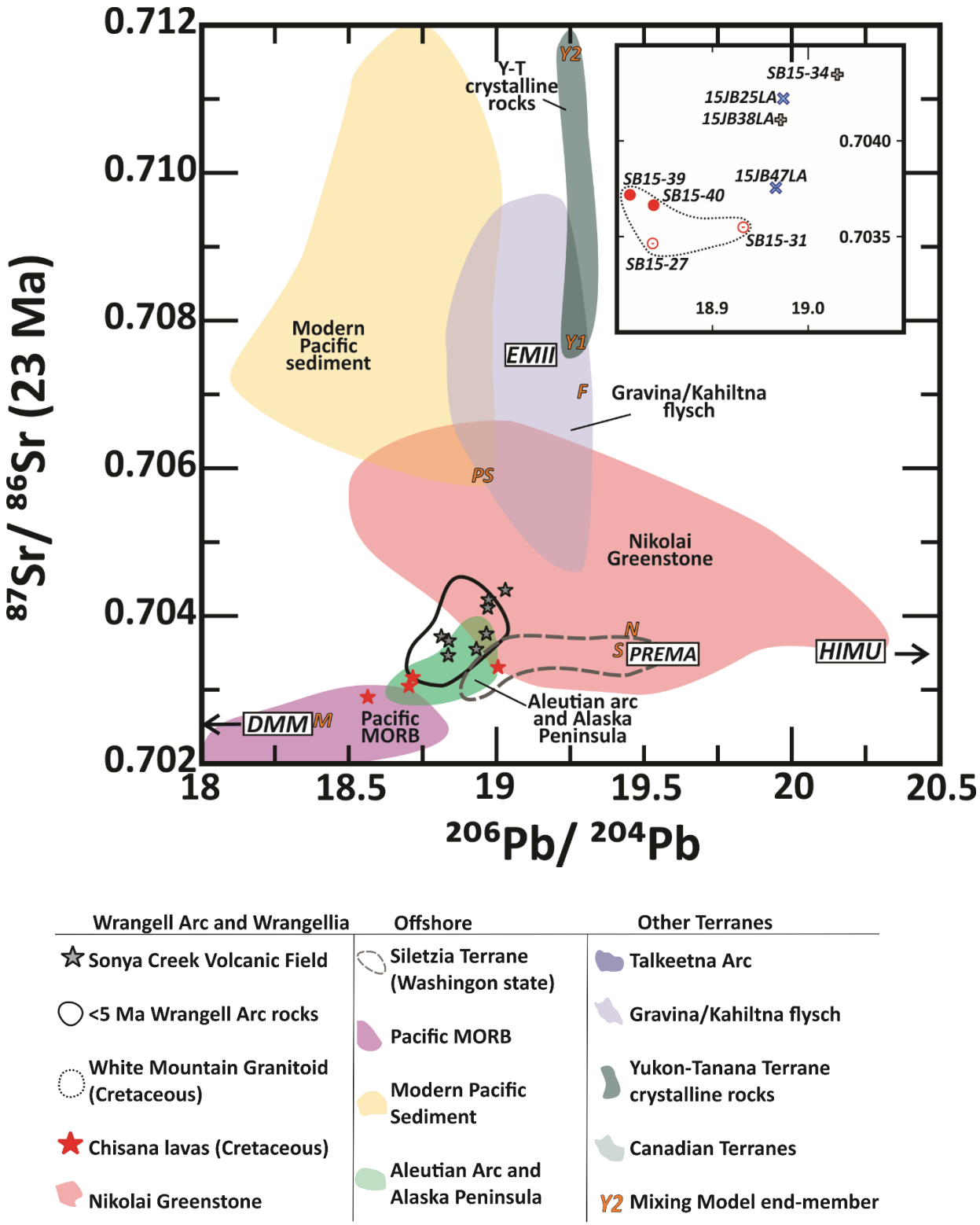

Figure 3.26: $^{87}Sr/^{86}Sr$ vs. $^{206}Pb/^{204}Pb$ for eight SCVF samples. Fields of reference data are from the same citations as in figure 3.22.

	Rocker Creek	Adakitic Domes	Intermediate Domes	Silicic Lavas	Flat Top	Cabin Creek	Young Creek	Border Lavas
Plagioclase	X	X	X	X	X	X	X	X
Clinopyroxene	X	X	X		X	X	X	
Orthopyroxene						X		
Hornblende	X	X	X	X			X	X
Biotite	X		X	X			X	
Olivine	X				X	X	X	
Quartz			X	X				
Zircon				X				
Apatite	X	X	X	X	X	X	X	X

Table 3-2: Phenocryst occurrences among SCVF rock groups. Detailed petrographic descriptions are in Appendix A.

	SB15-27	SB15-31	SB15-34	SB15-39	SB15-40	15JB25LA	15JB38LA	15JB47LA
Location	**Cabin Creek**	**Cabin Creek**	**Silicic Lava**	**Flat Top**	**Flat Top**	**Rocker Creek**	**Silicic Lava**	**Rocker Creek**
Groundmass	90.1%	61.8%	75.6%		91.3%		88.5%	58.8%
Plagioclase	6.3%	23.8%		59%	3.6%	49.7%		27.2%
Clinopyroxene	2%	4.6%		9.2%	1.1%	26.9%		12.1%
Orthopyroxene		4.8%						
Olivine		3.4%		16.8%		11.5%		
Biotite			2.5%				2.5%	
Opaque	1.4%			4%	1.1%	11.9%		1.9%
Sanidine	0.2%		9.3%		1.6%		3.3%	
Anorthoclase					1.2%			
Quartz			12.6%				3.1%	
Vesicles		1.6%					2.6%	
Alteration				11%				
Total points	637	689	690	720	625	782	731	688

Table 3-3: Results from modal point counts of eight SCVF samples that were analyzed for radiogenic isotopes. The two basalts (SB15-39, 15JB25LA) were coarse-grained enough to count minerals in groundmass. Detailed petrographic descriptions are in Appendix A.

Sample	Mineral or Whole rock	Integrated Age (Ma)	Plateau Age (Ma)	Plateau Information	Isochron Age (Ma)	Isochron or other Information
SB15-17	Whole Rock	21.3 ± 0.1	**21.3 ± 0.1**	8 out of 8 fractions 100% ^{39}Ar release MSWD = 1.19	21.3 ± 0.2	8 of 8 fractions $^{40}Ar/^{36}Ar_i$ = 296.2 ± 12.0 MSWD = 1.33
SB15-25	Whole Rock	21.7 ± 0.2	**21.5 ± 0.4**	5 out of 8 fractions 51.6% ^{39}Ar release MSWD = 4.58	N/A	N/A
SB15-27	Whole Rock	21.0 ± 0.2	**20.7 ±0.4***	4 out of 8 fractions 21.2% ^{39}Ar release MSWD = 0.46	N/A	N/A
SB15-32	Whole Rock	20.9 ± 0.3	**22.0 ± 0.3**	7 out of 8 fractions 92.7% ^{39}Ar release MSWD = 0.89	21.7 ± 0.3	7 out of 8 fractions $^{40}Ar/^{36}Ar_i$ = 304.3 ±5.9 MSWD = 0.57
SB15-33	Whole Rock	28.8 ± 0.2	**29.0 ± 0.2**	4 out of 8 fractions 87.2% ^{39}Ar release MSWD = 1.27	N/A	N/A
SB15-40	Whole Rock	19.0 ± 0.1	**19.3 ± 0.2**	7 out of 8 fractions 96.6% ^{39}Ar release MSWD = 2.02	N/A	N/A
SB15-44	Whole Rock	25.2 ± 0.2	**25.6 ± 0.2**	2 out of 8 fractions 75.8% ^{39}Ar release MSWD = 0.01	N/A	N/A
SB15-56	Whole Rock	34.7 ± 1.0	28.7 ± 1.3*	5 out of 8 fractions 75.2% ^{39}Ar release MSWD = 2.09	**22.9 ± 2.2**	5 out of 8 fractions $^{40}Ar/^{36}Ar_i$ = 320.6 ± 10.1 MSWD = 1.11
15JB25LA	Whole Rock	36.1 ± 3.1	**25.5 ±2.9***	2 out of 8 fractions 49.2% ^{39}Ar release MSWD = 1.26	N/A	N/A
15JB26LA	Whole Rock	30.9 ± 0.8	31.4 ± 2.12*	7 out of 8 fractions 95.5% ^{39}Ar release MSWD = 6.25	**26.2 ± 1.2**	7 out of 9 fractions $^{40}Ar/^{36}Ar_i$ = 305.5 ± 2.4 MSWD = 1.34
15JB33LA	Whole Rock	30.5 ±0.5	**26.0 ± 0.2**	4 out of 8 fractions 69.8% ^{39}Ar release MSWD = 1.32	N/A	N/A
15JB42LA	Whole Rock	26.2 ± 0.4	**27.2 ± 0.4**	7 out of 8 fractions 97.2% ^{39}Ar release MSWD = 1.12	27.0 ± 0.4	7 out of 8 fractions $^{40}Ar/^{36}Ar_i$ = 296 ± 3.1 MSWD = 1.29
15JB47LA	Whole Rock	26.5 ± 0.4	**27.0 ± 0.4**	7 out of 8 fractions 95.5% ^{39}Ar release MSWD = 0.57	N/A	N/A
15JB49LA	Whole Rock	20.9 ± 0.1	**21.4 ± 0.2**	3 out of 8 fractions 57.2% ^{39}Ar release MSWD = 1.67	N/A	N/A

Note: Preferred age in bold; *Weighted average presented when all the criteria for a plateau age were not met.

Table 3-4: $^{40}Ar/^{39}Ar$ step-heat data for 14 SCVF rocks. Step-heat spectra are in Appendix C.

Chapter 4 - Discussion

Initiation of Wrangell Arc Magmatism

Published bedrock ages and new $^{40}Ar/^{39}Ar$ bedrock and $^{40}Ar/^{39}Ar$ and U-Pb detrital cobble/sand ages reveal the age range of the entire WA (Trop et a., 2017; Davis et al., 2017). Yukon WA fields were active from 18–10 Ma (Souther and Stanciu, 1975; Dodds and Campbell, 1988; Skulski et al., 1991; 1992), central WA volcanism was active from ~13–5 Ma (Eyles and Eyles, 1989; Trop et al., 2012; B. Morter, pers comm), and western WA volcanism was active from ~5 Ma–11 ka (Richter et al., 1990; Clague, 1995; Preece 1997; Preece and Hart, 2004). New bedrock and detrital geochronology reveal very sparse activity from ~34–29 Ma, followed by continuous magmatism from ~29 Ma to present (Trop et al., 2017; Davis et al., 2017). The SCVF represents the oldest preserved volcanic field of the WA, based on an age range of 28.8–18.5 Ma.

New geochemical, geochronological, and isotopic data provide a new understanding of the complex Sonya Creek volcanic field (SCVF), which was active at the initiation of the Wrangell Arc (WA). The previous age for the initiation of the WA was 26.3 Ma, based on a single K-Ar age from a Rocker Creek lava (Richter et al., 1990; 2000). Our new geochronological data push the oldest *in situ* bedrock age back to at least 28.8 ± 0.22 Ma (dacite dome sample SB15-33, Appendix B). $^{40}Ar/^{39}Ar$ ages of detrital volcanic cobbles collected from the Nabesna and Chisana rivers that drain the north-central portion of the modern WA have been dated to 27.7– 23.9 Ma (± 0.2–0.4), with one age of 34 ± 0.47 Ma (Trop et al., 2017; Davis et al., 2017). Detrital volcanic-lithic sand grains from Rocker Creek have also been dated to 34.4–30.5 Ma (± 0.5–3.15) (Figure 3.10), and U-Pb ages of detrital zircons from the White River have been dated to ~31–32 Ma (± 0.8–1.5) (Trop et al., 2017; Davis et al., 2017).

Volcanic History of the Sonya Creek Volcanic Field (SCVF)

Volcanic Architecture – Geochronology and Field Relations

Locations of eruptive centers are found in Figure 1.2, and schematic cross-sections across the volcanic field are shown in Figure 3.5. Ages presented in this discussion are limited to bedrock $^{40}Ar/^{39}Ar$ ages, both single grain laser-fusion and plateau ages as described in the methods section and presented in Figure 3.10, Table 3-4, and Appendix B. A paleogeographic reconstruction of the SCVF through time is shown in Figure 4.1, and should be referenced in this section.

The earliest phase of volcanism within the SCVF is possibly represented by rocks from the dome field (28.8 ± 0.22 Ma), but low sample numbers with high LOI values limit conclusions that can be made from those rocks. However, the Rocker Creek lavas and domes show an initial pulse of basaltic to dacitic magmatism between 27.2–23.3 and 25.9–23.2 Ma, respectively (Figs. 3.10 and 4.1). The rocks of the dome field overlie the southwest-dipping Rocker Creek lavas, and small faults cut the Rocker Creek package along the margin with the dome field. These simple relative age relationships are supported by new geochronology, which shows that many of the sampled Rocker Creek domes have younger ages than Rocker Creek lavas (Fig. 3.10). The location of the eruptive center(s) for Rocker Creek lavas and domes is uncertain, but geochemistry of these rocks may provide insight and will be discussed below.

Four of the silicic lavas (all rhyolites) erupted from 24.8–23.3 Ma to the north and west of the Rocker Creek lavas domes (the fifth silicic rock (SB15-45) is located to the west of the Rocker Creek lavas and dome rocks, and is younger (20.34 Ma), so it is not likely related to the older silicic lavas). Two silicic lava samples, one from a large rhyolite dome (15JB38LA; Fig. 3.1f) and the faulted rhyolite lava found to the west (SB15-34; Fig. 3.2a), have very similar

mineralogy (Appendix A) and are 0.66 m.y. apart in age (Fig. 3.10). Based on field relations, SB15-34 was assumed to be a part of the marginal-fracture system along the inferred margin of the Sonya Creek shield volcano (Richter et al., 2000), but new age data show this unit to be older than the shield itself (Fig. 3.10). Based on geochemical, geochronological, and petrographic evidence, SB15-34 is more likely to be petrogenetically related to the rhyolite dome that crops out <1 km east of the border in Yukon Territory (15JB38LA), and may represent part of a rhyolite lava that flowed ~8 km from the dome (Figs. 1.2 and 4.1). The two adakitic rhyolite lavas sampled in lower Rocker Creek have nearly identical petrography and are 0.68 m.y. apart in age (Fig. 3.10 and 3.14–3.21). These four silicic dome rocks erupted during the late stages of Rocker Creek eruptive activity, and may be related petrogenetically to Rocker Creek phases.

The intermediate domes are younger than the silicic domes and show a migration of the locus of SCVF volcanism; they erupted from ~21.7–23.2 Ma to the north and west of the Rocker Creek lavas (Fig. 3.10 and 4.1). Among the intermediate dome samples, there is an age migration to the west: two samples collected near Rocker Creek are ~23 Ma, and the samples collected just east of Ptarmigan Lake are ~21.7 – 23 Ma. Petrographic diversity shows that extrusive domes and intrusive sub-volcanic rocks are located closely in space, and new geochronology shows the intrusive rocks are slightly younger. The presence of small tuffaceous and sinter layers suggest small-scale explosive and hydrothermal activity in between eruptions. The intermediate dome rocks erupted during the earliest phases of the Sonya Creek shield volcano to the west (Figs. 3.10 and 4.1).

The Sonya Creek shield volcano formed with the eruption of the Cabin Creek lavas, from 23.3–18.5 Ma. Ten Cabin Creek lava samples fall in the range of 22.5–20.6 Ma, including the "mafic" package and the trachydacite lava from the south side, and the "middle" package from

the north side (Figs. 3.10, 3.11, 3.12). Two samples are younger than 20 Ma (SB15-18; 19.6 Ma, and SB15-28; 18.5 Ma), and one sample is older (SB15-19; 23.2 Ma). The young lavas, which are stratigraphically below older lavas, did not show field evidence of being emplaced as sills, but they were observed in only one location and tracing the lava flows along strike would reveal their emplacement/eruption history. Two samples from the north side (SB15-21 and -22) and one from the south side (SB15-26) were not dated, but stratigraphic and geochemical relationships suggest that they erupted in the range of 22.5–20.6 Ma (Fig. 3.11). Geochemical trends (discussed below) and stratigraphic relationships suggest that the modern Cabin Creek section represents at least two overlapping contemporaneous phases of volcanism.

The south side of Cabin Creek has thick sedimentary interbeds of lahar and debris/hyperconcentrated-flow deposits that record episodes of accumulation of weathered volcanic detritus on the flanks of the volcanic edifice between eruptions (Fig. 3.3e, f; Fig. 3.12). Non-parallel contacts between lava flows suggest complex paleotopography in the middle of the stratigraphic sections. Gravity flows and floods could have entrained the sedimentary packages, possibly during or shortly after eruptions of the volcano. Thin tuffaceous breccias indicate smaller-scale explosive activity. These volcaniclastic sediments likely accumulated on the flanks of the volcano as eruptions from different point sources overlapped with one another. The columnar-jointed trachydacite lava overlies the lahar deposit, which is overlain by lavas until the top of the section (Fig. 3.12). A similar situation is documented by Trop et al. (2012) on a larger scale in the central WA, where sedimentary packages interfinger with lavas lower in the stratigraphy, until volcanoes prograded into sedimentary basins and the depositional environment is then dominated by lavas higher in the stratigraphy.

Age relations and continuation of the geochemical trends of Cabin Creek rocks suggest that rocks from Flat Top represent the younger, outer flanks of the Sonya Creek shield volcano that erupted from ~19.7–19.3 Ma. An exception to this chemo-stratigraphic trend is the Flat Top basalt (SB15-39), which has an age of 24.6 Ma; however, the stratigraphic context of this collected sample is ambiguous (Fig. 3.4a). The original interpretation of the relationship between Cabin Creek and Flat Top units by Richter et al. (2000) was that the Flat Top rocks represented the original shield volcano, and the Cabin Creek rocks were "intra-caldera" lavas that erupted into an inferred 10 by 14 km caldera within the Sonya Creek shield. Sparse structural relations supported this interpretation, and the presence of a dacite "agglutinate" of welded and flattened pumice (Flat Top tuff) was interpreted as evidence for a caldera-collapse eruption.

Given that Cabin Creek rocks are older (23.2–18.5 Ma) than Flat Top rocks (19.7–19.3 Ma), and based on geochemical evidence presented below, we suggest that the Cabin Creek lavas in fact make up the proximal structure of the Sonya Creek volcano and the Flat Top rocks represent the younger, distal flanks of the shield. Additionally, the Flat Top tuff, i.e., the agglutinate of Richter et al. (2000), is most likely not thick enough (25-35 meters thick) to represent an eruption associated with the collapse of a caldera the size of that inferred for the Sonya Creek shield volcano. The inferred caldera from Richter et al. (2000) is approximately 14x10 km in size, and calderas of comparable size in the San Juan volcanic field of southwestern Colorado erupted tuffs that exceed 200 m in proximal thicknesses (Lipman, 2000). The Flat Top tuff is only reported/mapped along the southeast margin of the Sonya Creek shield volcano, and it most likely represents a small-scale collapse of the volcanic margin along faults, related to the later stages of the Cabin Creek lavas. Similar pyroclastic deposits crop out at the <3 Ma Skookum Creek eruptive center and are also not associated with caldera-collapse (Preece, 1997).

Thus, our new data indicate that the Sonya Creek shield volcano is more akin to younger WA shield volcanoes like the Skookum Creek volcanic center and Mt. Wrangell, which also lacked a major caldera-forming eruptive phase.

The Rock Lake diorite (sample SB15-56), collected ~5 km east of the other Young Creek rocks, is 22.9 ± 2.2 Ma and is lumped with the Young Creek rocks in geochemical discussions. Geochemical relationships discussed below indicate that the Rock Lake diorite may represent a sub-volcanic root for the Young Creek and/or Border Lavas. The sample collected is older than any of these extrusive phases, but the large error of ±2.2 Ma, and the complexity of the diorite as evident from field observations suggest the diorite is a complex hypabyssal unit with phases of different ages and lithologies.

The Young Creek lavas erupted from 21.3–19.1 Ma, which overlaps in time with the latest phases of Cabin Creek/Flat Top activity (Figs. 3.10 and 4.1). Young Creek lavas dip to the northwest, and are overlain by flat-lying distal rocks of the Sonya Creek shield volcano which are mapped as the same map units and share structural associations with rocks from Flat Top (Fig. 3.4e; Richter et al., 2000). Despite the sparse geochronological data that shows the Young Creek and Flat Top rocks erupted during the same ~2 m.y. period, the physical field relations show that the Young Creek rocks are older than the overlying Flat Top lavas.

Finally, the two samples that represent the Border Lavas are essentially coeval in age with Young Creek lavas, i.e., 21.3–19.6 Ma. There is very little stratigraphic context for these two samples, other than they were collected from flat-lying lavas in the Rocker Creek area and are geographically close to mapped Border Lavas (shown in Fig. 3.4f; Richter et al., 2000). The thick succession of lava flows (e.g., Fig. 3.4f) from the southeast portion of the map area remain un-sampled.

Geochemical Trends Through Time, and Implications For the Development of the Sonya Creek Volcanic Field

Rocker Creek Lavas and Domes

Rocker Creek lavas and domes show a strong subduction signature (Fig. 3.20a), as well as elevated Sr/Y values (Fig. 3.21). Enrichment in fluid-mobile LILE and depletion in relatively immobile HFSE (relative to primitive mantle) suggests the role of fluids fluxing from the subducting oceanic plate and subsequent melting of mantle wedge peridotite (Stern, 2002). Rocker Creek lavas and domes have elevated $(Sr/P)_n$, and Ba/Nb values (Fig. 3.21b, c), suggesting that they melted under oxidizing conditions in the presence of H_2O and other volatile phases liberated from the subducting slab (Borg et al, 1997). The $(Sr/P)_n$ values for primitive Rocker Creek rocks (1.6–3.4) are similar to the moderately-spiked basalts ($1.3 < (Sr/P)_n < 5.5$) of Borg et al. (1997) which formed via partial melting of a mixed OIB-MORB mantle wedge (i.e., more enriched than a MORB-source mantle wedge alone, not necessarily a true OIB-source mantle) enriched by slab fluids and subducted sediment along the Cascade arc-axis. This is in agreement with the results of the binary isotope mixing models discussed below. The Rocker Creek lavas and domes also contain hydrous phenocrysts (hornblende and biotite) phenocrysts (Fig. 3.6c, d).

Eu/Eu* provides an indication of the oxidation state of a magma, where values less than 1 indicate a reducing environment (i.e., a greater proportion of Eu^{2+} to Eu^{3+}) and a role for plagioclase as a fractionating phase (i.e., distribution coefficient (Kd) for Eu in plagioclase increases as proportion of Eu^{2+} increases; Drake, 1975; Drake and Weill, 1975). Rocker Creek lavas and domes have Eu/Eu* values close to 1 (Fig. 3.21d), suggesting that Eu was dominantly

in the Eu^{3+} valence state, and thus the magma was relatively oxidized. This is in strong agreement with the other trace element data presented above (Fig. 3.21).

Rocker Creek dome rocks are slightly younger and generally more evolved than Rocker Creek lavas (Figs. 3.10 and 3.17), and may represent the late-stage silicic phases of the same vent source that were too viscous to flow as far as the older lavas. Consequently, the eruptive source for Rocker Creek lavas and domes may be buried below the extensive dome field to the west of Rocker Creek (Fig. 1.2, 4.1).

Source of Adakite-like Signature

The term "adakite" was originally introduced by Defant and Drummond (1990) to refer to arc rocks that were inferred to be direct melts of young (≤ 25 Ma) subducted oceanic basalt. Partial-melting of MORB-like oceanic lithosphere metamorphosed to eclogite or garnet amphibolite facies produces adakitic affinities, and are distinguished from normal, mantle wedge-derived arc magmas by high Sr/Y and La/Yb, and low Y and Yb values (Defant and Drummond, 1990). The presence of garnet in the source rock is essential to derive these values, as residual garnet retains Y and Yb (Rapp et al., 1991), meaning that adakites are necessarily derived at pressures where garnet is the stable alumino-silicate phase over plagioclase (10-12 kbar, ~35-45 km depth). It was originally assumed that only young, hot oceanic crust could melt under normal subduction conditions (Peacock et al., 1994; Castillo, 2012), however it has been shown that old oceanic lithosphere can melt under anomalous subduction conditions, such as subduction initiation or termination (Sajona et al., 2003; 1996), highly oblique subduction (Yogodzinski et al., 1995), shallow subduction (Gutscher et al., 2000), melting due to elevated shear stresses (Yogodzinski et al., 1995), and melting of the edge of the slab around a slab-window or slab-tear (Thorkelson and Breitsprecher, 2005; Yogodzinski et al., 2001).

Additionally, continental crust thickened by underplated basalt metamorphosed to eclogite or amphibolite facies can melt and produce adakite-like magmas (Petford and Atherton, 1996; Arculus et al., 1999; Haschke et al., 2002; Karlsi et al., 2011). All the above scenarios are possible causes of SCVF adakite-like magmas, and resolving the nature of magma genesis will have tectonic implications for the initiation of the WA.

Some Rocker Creek lavas and domes have higher Sr/Y values than most other SCVF rocks (Fig. 3.21a and 4.3a, b), which implies a role for garnet or amphibole in the source rock (Defant et al., 1991). Figure 4.2, a plot of Y vs. Rb, shows that the differentiation trend of the Rocker Creek lavas and domes could be controlled by a fractionating and/or residual assemblage of plagioclase ± amphibole ± garnet. However, these rocks do not have the high La/Yb values (>20) that would suggest a strong role for residual garnet, which is inconsistent with the formal usage of the term "adakite" a la Defant and Drummond (1990) (Figs. 4.3b). The Rocker Creek lavas and domes are most chemically similar to the Mt. Drum "transitional" dacites and andesites of the trend 2b suite of Preece and Hart (2004), which have adakite-like Sr, Y, and Sr/Y, but lower La/Yb ratios that adakites *sensu stricto* (Fig. 4.3b). Those rocks plot between the adakite field and the evolved arc-related rocks of trends 1 and 2a, which may represent mixing between an adakite-like melt (slab-melt or mafic lower-crustal melt), and some other primitive magma derived from a subduction-fluxed mantle wedge (Preece and Hart, 2004).

New geochemical and geochronological data for bedrock samples of hypabyssal hornblende dacites, shows that there was adakite-like magmatism from ~29–22 Ma along the northern flank of the WA (data shown in dashed field in Fig. 4.3b, c; ~60-100 km NW of SCVF; Brueseke et al., 2015; Weber et al., 2017). In the SCVF, the two silicic adakite-like lavas (15JB15LA, -16LA; Fig. 4.3b) likely represent the differentiated product of an unseen primitive

adakite (e.g., La/Yb> 20) that seems to be required to generate the adakitic Sr/Y values of the Rocker Creek lavas and domes via mixing.

The two SCVF adakite-like silicic lavas (15JB15LA, -16LA) have high Sr/Y (15JB15LA has high La/Yb), and may represent a differentiated product of an adakite-like magma that formed via melting of a slab-edge or lower crust during subduction initiation (Defant and Drummond, 1990; Sajona et al., 1993; Peacock et al.,1994), and then underwent magma mixing with another primitive mantle-wedge melt to produce the geochemical array of the Rocker Creek lavas and domes. These two adakite-like silicic lavas have Nb and Ta values that are at equal or lower values than the Rocker Creek lavas and domes (Table 3-1). Because Nb and Ta are incompatible in mafic minerals (Gill, 2010), the low values of those elements in the two rhyolites are not likely to result from differentiation of a mafic magma by fractional crystallization. Additionally, the two adakite-like rhyolites have Eu/Eu* values close to one (Fig. 3 21) and low Rb/Sr values (Fig. 4.3), suggesting that plagioclase fractionation was not an important process in magma evolution. Although these two lavas share other major and trace element characteristics with the other silicic lavas (SB15-34 and 15JB38LA, discussed below), they likely belong to some other eruptive system for which crustal melting/assimilation played an important role in magma genesis.

Melting of some mafic lower crustal garnet-bearing rock (i.e., eclogite or garnet-amphibolite) can generate the adakite signature of elevated Sr/Y and La/Yb ratios (Petford and Atherton, 2003; Arculus et al., 1999; Haschke et al., 2002; Karlsi et al., 2011), and characterizing the difference between melting of *in situ* lower crust and melting of lower crust that has delaminated and sunk into the mantle can be accomplished by examining the MgO, Ni, and Cr contents of the resulting magmas (Xu et al., 2002; Wang et al., 2006; Karlsi et al., 2011).

Adakite-like granitoid porphyries from Turkey and the Andes have been demonstrated to form via melting of lower crustal eclogite (Karlsi et al., 2011). This process generates the adakite-like Sr/Y and La/Yb signature, and the lack of interaction with the mantle keeps the wt.% MgO and Mg# of the resulting magma low (Petford and Atherton, 1996; Arculus et al., 1999; Haschke et al., 2002; Karlsi et al., 2011). It has been shown that Sr/Y values of arc magmas can be controlled by crustal thickness, based on the stability of plagioclase and garnet/amphibole at depth and their role in fractionating Sr and Y, respectively (Chiaradia, 2015). Adakites from China are shown to have been derived via melting of underplated basaltic magmas following delamination and sinking into the mantle (Xu et al., 2002; Wang et al., 2006). This allows the melt to equilibrate with mantle peridotite, increasing MgO, Mg#, Ni, and Cr values, and the resulting adakite melt has major and trace element characteristics similar to a direct slab-melt (Peacock et al., 1994), but the isotope ratios of the delaminated crustal-melt retain a continental signature (i.e., higher $^{87}Sr/^{86}Sr$, lower εNd; Xu et al., 2002).

Trace elements for SCVF adakite-like rocks can be used to distinguish between melting of the slab and the lower crust. A plot of Th/U vs. U (Fig. 4.3c) shows that one of the adakite-like silicic lavas (15JB16LA) plots close to the fields for middle continental crust (MCC) and lower continental crust (LCC) derived melts (Rudnick and Gao, 2003; Karlsi et al., 2011), even when the larger error for this XRF data is considered (Fig. 4.3c). However, the other adakite-like silicic lava (15JB15LA) plots close to the field for N-MORB-derived melts, along with the Rocker Creek lavas and domes. This could be evidence that the two adakite-like silicic lavas are not samples from the same lava flow as previously suggested, or secondary alteration by surface processes has changed the values of the fluid-mobile trace elements, U or Th. Regardless, the U and Th element data suggest some amount of lower- to middle-crust involvement in the

generation of at least one of the adakite-like rhyolites. Figure 4.2 shows that the two silicic adakite-like lavas follow the vectors of a fractionating and/or residual assemblage containing amphibole ± garnet, as opposed to the intermediate domes (Pearce and Norry, 1979; and Irving and Frey, 1984). Lower-crustal plutons associated with the Nikolai Greenstone flood basalts metamorphosed to eclogite or amphibolite facies could be such a melt source.

Figure 4.3c shows the Rocker Creek lavas and domes plot near the field for N-MORB-derived melts, so if they were derived from a mafic lower-crustal rock it would have to be more similar to an underplated basalt in composition (more primitive) than global average LCC (Fig. 4.3c; Rudnick and Gao, 2003). The Rocker Creek lavas and domes have Mg#, MgO, Ni, and Cr values (Fig. 3.17 and 3.18, Fig. 4.2b) that suggest interaction with mantle wedge peridotite, and therefore either derivation by melting of delaminated mafic lower crust or melting of subducted oceanic basalt. Cretaceous adakitic andesites and dacites from China have been demonstrated to form via delamination of underplated mafic lower crust that sank into the mantle, equilibrated with mantle peridotite, and partially melted (Xu et al., 2002; Wang et al., 2006). However, Rocker Creek lavas extend to more primitive compositions (six samples with $SiO_2 < 63$ wt.%) and have higher MgO, Cr, and Ni values at a given SiO_2 content than the Chinese adakites (Fig. 4.2b; Xu et al., 2002). Additionally, the Chinese adakites show radiogenic isotope values that overlap with local continental crustal rocks ($^{87}Sr/^{86}Sr$ 0.7045 to 0.707; εNd -18 to +3; Wang et al., 2006), whereas the Rocker Creek lavas and domes have lower $^{87}Sr/^{86}Sr$ and higher εNd (0.70376 to 0.70422; +4.64 to +6.51; Table 3-1) than most local Alaskan basement rocks (Fig. 3.24).

The relatively depleted nature of isotope values (i.e., low $^{87}Sr/^{86}Sr$, high εNd) and MgO, Ni, and Cr values for the SCVF adakite-like rocks strongly suggests that the adakite-like

signature of Rocker Creek lavas and ddomes was not derived via melting of mafic lower crust. A direct melt of the subducted Yakutat slab during subduction initiation is more likely as the source of the adakite-like signature from Rocker Creek and along the northern flank of the WA. However, the SCVF samples overlap with the field for the Nikolai Greenstone in isotope space, and this would be the most feasible crustal source for adakite genesis by melting of lower crust (with or without delamination into the mantle). Isotope data for the two adakite-like silicic lavas (15JB15LA, -16LA) are not available, and REE data are not available for sample 15JB16LA. These data would greatly enhance our ability to discriminate among the many possible origins for the SCVF adakite-like rocks.

Regardless of the exact details pertaining to the origin of the adakite-like signature for the Rocker Creek lavas and domes, and the two adakite-like silicic lavas, the tectonic implications of these data are the following: melting of either the slab-edge itself or some mafic lower crust was triggered by mantle flow around the leading or lateral edge of the slab following the initiation of subduction of the Yakutat oceanic crust. Recent three-dimensional modeling of subduction zones shows that slab-steepening (possibly during subduction initiation) can cause toroidal flow of warm sub-slab mantle around the lateral edge of the slab (Sajona et al., 1993; Jadamec, 2016). This upwelling sub-slab mantle could induce melting of the slab-edge or lower crust, with both melt sources giving rise to adakite-like magmas.

Silicic Lavas

The other silicic lavas (SB15-34, SB15-45, 15JB38LA) are not geographically close to each other, but show generally consistent geochemistry among the three samples. Geochemical characteristics of LILE enrichment and HFSE depletion, and the presence of hydrous phenocryst phases (biotite and/or amphibole), broadly suggests a subduction-related origin (Fig. 3.17, 3.18,

3.6e, f). Sample SB15-45 is ~3 – 4.5 million years younger than the other silicic rocks, so must be considered separately. The remaining two silicic lavas are high-silica rhyolites, and have the highest K_2O contents (>3.8 wt. %) found in the SCVF. Incompatible trace element abundances can give information on the degree of fractionation or crustal contamination. SB15-34 and 15JB38LA have the highest abundances of Nb, Ta, and Rb in the SCVF (Fig. 3.17 and 3.18). These two silicic lavas also have the most negative Eu-anomalies (0.37–0.55, Fig. 3.21d), and Figure 4.2 suggests that they follow the magma evolution path for a fractionating assemblage of plagioclase and amphibole. Figure 4.3d shows these two silicic lavas have the highest Rb/Sr and lowest Zr/Nb values of the entire SCVF array, consistent with fractionation of plagioclase and zircon, respectively. Zircon was observed in sample SB15-34 (Fig. 3.7a, b), so zircon fractionation was likely responsible for the low Zr values.

These trace element data and phenocryst assemblages suggest that these two rhyolite lavas were likely generated by fractional crystallization of some hydrous parental magma, which included plagioclase, amphibole, and zircon fractionation (Drake, 1975; Drake and Weill, 1975). They erupted at 23.2–23.9 Ma, during the latest phases of Rocker Creek eruptive activity (Fig. 3.10), and have similar isotope signatures to the two Rocker Creek samples (15JB25LA, -47LA; insets in Figs. 3.24 to 3.28, Table 3-1), suggesting a potential relationship between the silicic lavas and a magmatic system similar to the Rocker Creek phases. However, the variation trend in Figure 4.2 suggests that the two rhyolites are more closely related to a magmatic system more like the intermediate domes (i.e., hydrous, subduction-related, calc-alkaline magmas without the adakite component). It may well be that these two rhyolites are part of an unseen or unsampled magmatic system, and further field work would be needed to fully describe the petrogenesis of these voluminous rhyolites.

Intermediate Domes

The 20.3–23.2 Ma intermediate dome field lies between the Rocker Creek lavas and domes and Cabin Creek/Flat Top/Young Creek rocks both physically and in geochemical parameters (Figs. 1.2, 3.17), hence the name "intermediate domes." This study presents data from only six samples (11 including the silicic domes) from a dome field that covers approximately 70 km^2 and 600 meters of topographic relief, so any conclusions made should be limited to those rocks sampled, and not the entire dome field. A broad range of geochemical compositions and a variety of petrographic textures (i.e., basaltic-andesite cumulate/intrusive diorites to rhyolitic porphyritic-extrusive lavas and sparse tephras) exist within the restricted area that was sampled. Bulk geochemistry and mineralogy (presence of hydrous phases biotite and amphibole; Fig.3.7c-f) suggest that intermediate dome rocks represent typical hydrous subduction-related processes, but with slightly lower values for slab-fluid signatures than Rocker Creek lavas and domes, i.e., Sr/Y, $(Sr/P)_n$, Ba/Nb; Fig. 3.21. The intermediate dome rocks are chemically similar to trend 2a of Preece and Hart (2004) of the <5 Ma western WA (Fig. 3.18a, e; Fig. 3.21a, c), as well as the central WA Frederika Formation lavas of Trop et al. (2012). Those authors attribute those magma series to melting of the mantle wedge by the addition of fluids from the subducting slab. The presence of hornblende (and biotite) as phenocryst phases agrees with Figure 4.2, which shows the intermediate domes following the vector of a plagioclase ± amphibole fractionating assemblage. The moderate values of trace element ratios (Figure 3.21, Sr/Y, Ba/Nb, $(Sr/P)_n$) that show elevated values of LILE and other fluid-mobile elements over HFSE and other immobile elements, support the interpretation of hydrous melting of mantle wedge as the main control on intermediate dome magma genesis.

Sonya Creek Shield Volcano

The largest volcanic feature of the SCVF is the Sonya Creek shield volcano, which has had much of its edifice removed by erosion and incision by streams (Figs. 3.2f, 3.3). The Sonya Creek shield volcano is composed of >1 k of basaltic to rhyolitic lavas, including an obsidian-bearing unit, termed the Cabin Creek lavas after the valley in which they were sampled (Fig. 1.2). Bulk geochemistry (Fig. 3.14 through 3.22) shows the Cabin Creek lavas (and Flat Top rocks) have elevated levels of HFSE at a given SiO_2 content relative to the rest of the SCVF rocks, and they plot within the fields for trend 1 rocks of Preece and Hart (2004). Those authors interpreted trend 1 rocks as the product of relatively low degree partial melting of subduction-modified MORB-type mantle, but without new input of subduction-related fluids. Cabin Creek/Flat Top rocks are also chemically similar to the "calc-alkaline" data from the Yukon WA volcanic fields (yellow fields in Figs. 3.14–3.21; Skulski et al., 1991; 1992), which are interpreted to represent an input of subduction-related fluids into the transtensional leaky-transform magmatic system active in the Yukon.

These melts would have formed in dry and reducing conditions, which resulted in the lower abundances of LILE and greater abundances of HFSE seen in geochemical trends of Cabin Creek/Flat Top rocks (Figs. 3.17, 3.20, and 3,21). Melting of this kind could be triggered by extensional pressure release (decompression melting) rather than slab fluid causing flux-melting of the mantle wedge (Preece and Hart, 2004). Because these magmas were anhydrous, the crystallization of magnetite was suppressed and Cabin Creek/Flat Top rocks are consequently slightly tholeiitic relative to the other SCVF rocks (Fig. 3.15a). Eu/Eu* values of Cabin Creek/Flat Top rocks (0.69–0.99; excluding the Flat Top basalt, SB15-39) suggest that these magmas formed under relatively reducing conditions, allowing Eu^{2+} to partition into plagioclase as a fractionating phase (Fig. 3.21c; Drake, 1975; Drake and Weill, 1975). The $(Sr/P)_n$ values of

Cabin Creek rocks with SiO_2< 63 wt. % (0.7–2.1; Fig. 3.21b) are similar to the weakly-spiked lavas ($(Sr/P)_n$ < 1.3) of Borg et al. (1997), which formed via melting of mantle wedge following addition of subducted sediment with less slab-derived fluid input than the moderately-spiked lavas. Figure 4.2 shows the Cabin Creek/Flat Top rocks plotting along the vector of a plagioclase ± olivine ± pyroxene (± magnetite) fractionating assemblage, consistent with observed mineralogy.

Cabin Creek Chemostratigraphy

Distinct chemo-stratigraphic trends between the north and south sides of Cabin Creek are evident in Fig. 3.22 and are summarized in the geochemical results section above. The south side basaltic-andesites, andesites, and trachyandesites make up a "mafic package" that is distinctly different in major and trace element compositions than the andesites and dacites from the north side at comparable elevations (Fig. 3.22). This could represent a mafic "pulse" into the Sonya Creek shield volcano magmatic system, as well as be evidence for overlapping volcanic vents. A comparable volcanic system is seen at the 2.25–3.25 Ma Skookum Creek Volcanic Complex, located ~60 km to the northwest of the Sonya Creek shield volcano (Fig. 1.1). The most voluminous volcanic phases there consist of two overlapping shield volcanoes, as well as at least one smaller eruptive center and a late pyroclastic phase (Preece, 1997). Similar to the Sonya Creek shield volcano, the early Skookum Creek volcanic rocks were intruded by later dikes and domes (Preece, 1997; Preece and Hart, 2004).

Flat Top

Flat Top trachydacite lavas and the Flat Top tuff are structurally associated and younger than the bulk of Cabin Creek lavas, and continue the same geochemical trends to high SiO_2 values, suggesting these rocks may be part of the same volcanic system (Fig. 3.10, 3.14 through

3.21). The Flat Top tuff is found only along the southeast margin of the Sonya Creek shield volcano (as mapped by Richter et al., 2000), and the thickness where directly observed in the one location where it was sampled is not as thick as would be expected from a full-scale caldera collapse. We suggest that the Flat Top tuff formed as a result of a small-scale collapse along a marginal fault or fracture of the Sonya Creek shield volcano. This is consistent with the mapping of Richter et al. (2000) showing fracture-associated domes, plugs, dikes, and lava flows along the northeast margin of the SC shield (Fig. 3.4d), but there is no evidence of a large (e.g., Crater Lake-size) caldera.

The basalt sampled from low in the Flat Top stratigraphy (SB15-39) is ~5.3 m.y older than the overlying trachydacites and rhyolite, and is compositionally distinct (Figs. 3.10 and 3.20). The basalt was sampled from an area that is covered in landslide and colluvial deposits, but does not appear to directly underlie the overlying Flat Top rocks (Fig. 3.4a). The age of the Flat Top basalt (24.58 ± 0.26 Ma) falls within the error for the Rocker Creek basalt (15JB25LA; 25.5 ± 2.9 Ma). This relationship likely suggests that the only two basalts sampled from the SCVF represent the same mafic pulse of magmatism into the system. However, radiogenic isotope ratios show that the two basalts are distinct, and likely represent mantle heterogeneity.

Silicic Plug

The silicic dome sample SB15-45 is a calc-alkaline rhyolite with a subduction signature on a spider-diagram (Fig. 3.20b), and has hydrous phenocryst phases (biotite and amphibole, 3.6f), suggesting a subduction-related origin. It is similar in age (20.34 ± 0.12 Ma) to the Flat Top rocks and the youngest Cabin Creek lavas (~20–21 Ma), and was sampled from a small plug with columnar jointing that intruded the intermediate domes to the east of Ptarmigan Lake (Fig. 3.2c). There are four small rhyolitic domes and plugs mapped along the southeastern margin of

the Sonya Creek shield volcano, and SB15-45 may be an unmapped analog to these (Richter et al, 2000). The close spatial and temporal association of the silicic plugs with the Flat Top rocks suggests that the swarm of silicic domes and plugs may represent local crustal melts, silicic differentiation due to filter pressing within the Sonya Creek magma chamber, or resurgent magmatism after the Flat Top tuff eruption, during the late phases of the Sonya Creek shield volcano. The silicic plug (SB15-45) has comparable Rb/Sr, Eu/Eu*, and major element values to the Flat Top trachydacite lavas and the Flat Top tuff, indicting a similar degree of magmatic differentiation between the two rock groups. However, it has hydrous phenocrysts and lacks the elevated values of HFSE and REE seen in the Flat Top rocks (Figs. 3.17, 3.18, 3.20, 3.21). Figure 4.2 shows SB15-45 following the fractionation vector of plagioclase ± amphibole, which is distinctly different from the silicic Flat Top rocks. This discrepancy between the silicic rocks of similar ages suggests a difference in petrogenesis. If this silicic plug is a similar age and geochemically similar to the four plugs that are mapped along the southeast margin of the Sonya Creek shield volcano, they may represent a pulse of calc-alkaline magmatism during the late phases of SCVF activity, and could potentially be related to the Young Creek and/or Border Lava magmatic systems.

Young Creek Rocks

The rocks from Young Creek generally overlap with trend 2a data of Preece and Hart (2004) (Figs. 3.14 through 3.21). Those authors interpret that trend as reflecting “typical” subduction-related geochemical affinities, with enrichments in LILE and depletions in HFSE (Fig. 3.20). The Young Creek lavas erupted during the latest phases of SCVF volcanic activity (19.1– 19.3 Ma) from an unknown source in the extreme southwest of the volcanic field (Figs. 1.2, 3.10, and 4.1). The mafic diorite from Rock Lake (sample SB15-56; 22.9 ± 2.2 Ma) is

included in this group based on chemistry and age data, and may represent a sub-volcanic root of an eruptive source for the Young Creek rocks (Fig. 3.20). Our new geochronological data show that the Young Creek rocks overlap in age with the youngest phases of Cabin Creek/Flat Top magmatism (Fig. 3.10), which contradicts the interpretation of Richter et al. (2000) that Young Creek rocks are at least 23 Ma. However, field relations show flat-lying Flat Top rocks that overlie tilted Young Creek rocks (Fig. 3.4E), indicating that the exact relationship between these geographically close phases is not well understood and may be overlapping in places.

Border Lavas

The two Border Lavas have typical subduction-related chemistry, and are generally similar to Young Creek rocks, but at higher SiO_2 values (Figs. 3.14 through 3.21). Although only two samples were collected for this study, the map of Richter et al. (2000) depicts them as relatively thick and widespread across the southwestern area of the SCVF (Fig. 1.2, 3.4f, 4.1). An eruptive center for the Border Lavas is uncertain, but the mafic intrusive body at Rock Lake (SB15-56), that is a similar age, may be a sub-volcanic root. The Border Lavas overlap in age with the Young Creek rocks (Fig. 3.10), and although they are more silicic than the Young Creek rocks, those two rocks groups show similar spider-diagram profiles (Fig. 3.20). This relationship does not imply that the Border Lavas are petrogenetically related to the Young Creek rocks directly, but the close association in time and space, and their geochemical similarity, could indicate that the two rock groups may have formed from a similar subduction-related magmatic event that erupted via different volcanic systems. Regardless, the Border Lavas and Young Creek rocks represent a shift to calc-alkaline magmatism in a southward direction, away from the Sonya Creek shield volcano. The St. Clare Creek volcanic field in Yukon Territory (~80 km to the southeast) was active immediately following SCVF activity at ~18 Ma, and Young

Creek/Border Lava magmatism may represent the beginning of this southward shift in WA activity.

Discussion of Radiogenic Isotope data

Radiogenic isotope systematics for Sr-Nd-Pb-Hf systems show a limited range of values for the SCVF samples (Figs. 3.24 through 3.28), consistently overlapping with the field for <5 Ma WA magmatism (Preece and Hart, 2004). The small number of samples chosen for isotope analysis limits the conclusions that can be made about the entire SCVF suite, but samples were chosen for a representative set of eruptive packages found within the SCVF (i.e., Rocker Creek, Cabin Creek, Flat Top, silicic lavas), as well as a broad compositional range (i.e., basalt to rhyolite). These rock groups show a clustering that is consistent across all but one isotope system; the two Cabin Creek lavas and two Flat Top rocks have lower $^{87}Sr/^{86}Sr$, $^{206}Pb/^{204}Pb$, $^{207}Pb/^{204}Pb$, and $^{208}Pb/^{204}Pb$ ratios, and higher εNd values, than Rocker Creek lavas and the two silicic lavas (insets in Figs. 3.24 to 3.28). Values of εHf show less of a separation, with the Rocker Creek basaltic-andesite plotting closer to the Flat Top tuff and Cabin Creek basaltic-andesite than the Rocker Creek basalt (inset in 3.27). An additional observation is that the two basalts are not the most isotopically depleted (i.e., closer to DMM/MORB in isotope space) in $^{87}Sr/^{86}Sr$ and εNd systems (SB15-39 and 15JB25LA in Fig. 3.24 inset).

A few conclusions can be made from these simple relationships. The isotopic differences between the two SCVF basalts, which erupted close to each other in time, suggest some degree of mantle wedge heterogeneity. The fact that the two basalts are not the most isotopically depleted argues against significant crustal contamination processes, and suggests more of a mantle-wedge control on magma composition. The clustering of the Cabin Creek/Flat Top samples in more isotopically depleted space than the Rocker Creek/silicic lavas samples agrees

with the conclusions drawn from the bulk geochemistry described above; i.e., Rocker Creek lavas and domes, intermediate domes, and silicic lavas were generated via a greater degree of subduction-fluid contaminating the mantle wedge than were the Cabin Creek/Flat Top rocks, which formed via low-degree partial melting of an already subduction-modified mantle wedge without additional fluid input from the slab. Although this could be a satisfactory explanation of the data, simple binary mixing models were created to better understand the SCVF array in isotope space, in terms of contamination in the mantle wedge, and in the continental crust.

Mixing Models

It has been shown that the isotope ratios of continental arc magmas can be influenced by radiogenic sources from both subducted terrigenous sediment (Borg et al, 1997; Plank and Langmuir, 1998; Jicha et al, 2004) and contamination by continental crust (Hildreth and Moorbath, 1988). In isolation, radiogenic isotope ratios cannot readily distinguish between these two processes. However, the behavior of certain elements can give information on the importance of that crustal contamination in magma generation. K/P ratios are elevated by upper crustal contamination in basalts (Carlson and Hart, 1987), where K/P <3.5 is often considered non-contaminated. The two SCVF basalts have K/P <4, and basaltic-andesites have K/P < 7, and are not the least isotopically depleted among the SCVF array (Inset on Fig. 3.24). Thus, crustal contamination does not likely play a significant role in explaining the isotope systematics of the entire SCVF isotope array, and mantle wedge contamination by subducted terrigenous materials is a more likely explanation for the genesis of mafic and intermediate SCVF magmas. The mantle-contamination mixing curves described below attempt to model such a process. However, the presence of large volumes of evolved lavas (dacites and rhyolites) necessitates the

consideration of crustal contamination, so we will also attempt to model the potential scenario whereby a primitive magma can be contaminated by crustal rocks.

Crustal Contamination of Primitive Magmas

A crustal contamination model simulates the interaction of a primitive mantle-derived magma with upper- or middle-crustal rocks, but no truly primitive composition was found in the SCVF. The two basalts from the SCVF that were sampled are interpreted to be relatively evolved (SiO_2 49.1-50.7 wt. %; MgO 7.6-8.52 wt. %; Mg# 59.8-60.6; Ni 71-139 ppm; Cr 221-282 ppm), and they occupy isotope space within the SCVF data that are not the most isotopically depleted (inset in Fig. 3.22). That is, there are two samples (basaltic-andesite SB15-31 and trachydacite SB15-27) that have lower $^{87}Sr/^{86}Sr$ ratios and higher εNd than the Flat Top basalt (SB15-39). The Rocker Creek basalt (15JB25LA) has the lowest εNd and εHf values, and relatively high Sr and Pb-isotope ratios (Figs. 3.22 to 3.26). This is evidence that crustal contamination did not play a significant role in generating mafic to intermediate magmas found in the SCVF. Thus, a model of crustal contamination of a primitive basalt cannot be created using either of these two SCVF basalts.

Preece (1997) used a high-Ni basalt from a Mt. Tanada cinder cone (0.93 ± 0.27 Ma; SiO_2 50.62 wt. %; Mg# 63.3; Ni 151 ppm; Cr 248 ppm) to model contamination by local basement rocks in the Skookum Creek Volcanic Center, and elemental concentrations from this basalt are used, along with the isotopic ratios from a Pacific MORB sample (Chauvel and Blichert-Toft, 2011). The Hf concentration of the primitive basalt is estimated using the approximate Nd/Hf ratio of SCVF basalts (see Table 4-2).

Isotope ratios and trace element concentrations for end-members used in binary mixing models are shown in Table 4-1. Continental end-members were chosen for a binary mixing

model with the primitive basalt based on location in isotope space to create a realistic mixing curve. These three end-members are Gravina-Nutzotin flysch (F) and the two Yukon-Tanana granitoids (Y1, Y2). One curve with the Nikolai greenstone (N) is plotted on a Pb-Pb plot to show that ~80-90% assimilation of a Nikolai-type rock would be required to generate the SCVF array (Fig. 4.5). These values are thermodynamically unrealistic, given that the Nikolai Greenstone is a flood basalt formation, and such a high degree of assimilation would not generate a rhyolite without large degrees of differentiation subsequent to crustal contamination.

The mixing curve between the primitive basalt and flysch (F) matches the SCVF $^{87}Sr/^{86}Sr$ data over mixing intervals of ~50-80%, and the εNd values over intervals of ~10-50% mixing (Fig. 4.4). εHf values from the mixing curve match the SCVF data over ~10-60% mixing intervals (Fig. 4.6), and ~40-80% mixing is needed to match the Pb-isotope data of the SCVF array (Fig. 4.5). The mixing curve with the Cretaceous Yukon-Tanana granitoid sample Y1 and the primitive basalt replicates the SCVF $^{87}Sr/^{86}Sr$ data over intervals of ~20-70% mixing, the εNd values over intervals of ~5-20% mixing (Fig. 4.4), and the εHf values over mixing intervals of ~2-20% (Fig. 4.6). The Pb-isotope values of SCVF data are matched by the mixing curve with ~4-20% of mixing (Fig. 4.5). The mixing curve between the primitive basalt and the Yukon-Tanana granitoid sample Y2 matches the SCVF $^{87}Sr/^{86}Sr$ values over ~20-50% mixing, the εNd values over intervals of ~10-30% mixing (Fig. 4.4), and the εHf values over intervals of ~2-25% mixing (Fig. 4.6). The Pb-isotopes of the SCVF data are replicated by the Y2 curve over ~3-25% mixing (Fig. 4.5).

Contamination of the primitive basalt with ~20-60% mixing of the flysch end-member can replicate the SCVF data in Sr-Nd-Pb-Hf isotope space (Figs. 4.4 to 4.6). The Y1/Y2 granitoids can replicate the SCVF data over ~2-30% mixing with the primitive basalt (Figs. 4.4

to 4.6), and are more likely to be present in the mid- to lower-crust and have hydrous phases with lower melting temperatures. If the two SCVF rhyolites (SB15-34, 15JB38LA) formed via some component of crustal contamination, this model shows that their isotope ratios could be explained by ~10-25% contamination of a primitive basalt with Pacific MORB-type isotope ratios by a crustal rock with an isotopic composition like a Y1/Y2-type end-member. It should be acknowledged, however, that the model presented above only addresses the isotope systematics of the SCVF and reference data, and is not a full AFC (assimilation and fractional crystallization) model. Nonetheless, the conclusions drawn from the simple isotope mixing curves show that the isotope values of SCVF data could be derived by varying degrees (~2-30%) of contamination of a mantle-derived magma by a crustal rock.

Contamination of the Mantle Wedge by Subducted Sediment

The SCVF magmatic system erupted through the Wrangellia composite terrane, and was proximal (~30-40 km) to the Yukon-Tanana terrane to the north (Fig. 1.1). Basement rocks of these terranes include Paleozoic-Cretaceous marine sedimentary rocks, and intrusive and volcanic rocks from several magmatic arcs (Berg et al., 1972; Plafker and Berg, 1994; Trop et al., 2002: Manuszak et al., 2007; Snyder and Hart, 2007; Greene et al., 2008; 2009). Major rivers delivered eroded sediment from these basement terranes to fore-arc basins and the trench through much of the Oligocene and earlier (Stevenson et al., 1983; Stevenson and Embley, 1987; Plafker et al., 1994; Brennan et al., 2009; Finzel et al., 2011; 2016). Sediment delivered to the trench that wasn't faulted, accreted, or underplated to the continental margin (Christeson et al., 2013) may have been subducted with the Yakutat microplate, and therefore could contribute some isotopic component to SCVF magma generation.

Geologic Evidence for Oligo-Miocene Sediment Delivery to the Trench

To the west of the SCVF, large Miocene fluvial systems delivered sediment from the Yukon-Tanana Terrane (YT) and the Wrangellia Composite Terrane (WCT) towards Cook Inlet (Finzel et al., 2011; 2015; 2016; Bristol et al., 2017; J. Trop, pers. comm). Thick (~6 km) packages of Eocene-Miocene shallow marine sedimentary rocks of the Kulthieth, Poul Creek, Yakataga, and Redwood Formations are exposed where the Yakutat plate is currently subducting below the St. Elias Range, indicating transport of terrigenous sediment to the trench in the ~20 m.y. prior to SCVF activity. The modern position of these sediments due south of the SCVF suggests that equivalent subducted sediments likely

Extensive thermochronologic work done in the St. Elias syntaxis shows that topography of the mountain range developed progressively from mid-Miocene time and more rapidly during Pliocene-Pleistocene time (Enkelmann et al., 2008; Berger et al., 2008a, 2008b; Grabowski et al., 2013; Enkelmann et al., 2010; Falkowski et al., 2014, 2016; Falkwoski and Enkelmann, 2016; Enkelmann et al., 2017). However, thermochronologic data from the Chugach range to the west of the syntaxis shows that the Chugach and Prince William terranes were not being uplifted and exhumed from ~45-35 Ma (Enkelmann et al., 2010; Falkowski et al., 2016). This would feasibly allow a river system to deliver sediment to the trench near the position of the modern Copper River in the ~20-10 m.y. before the onset of SCVF activity. Figure 2 from Eberhart-Phillips et al., (2006) shows that a slab subducting at the current rate of Yakutat convergence of ~46 mm/yr would reach a point below the current position of the SCVF in ~5.5 m.y. This is in good agreement with the time difference between the inferred onset of Yakutat subduction (~35-30 Ma, Finzel et al., 2011) and the initiation of SCVF magmatism at ~29-27 Ma (J. Benowitz, pers

comm; this study), allowing subducted sediment the proper time to contribute to SCVF magma generation.

The Surveyor, Baranof, and Zodiac fans are three large submarine sediment fans found in the modern Alaskan and Aleutian Abyssal Plains. They record voluminous Eocene-modern terrigenous turbidite sedimentation. The upper Eocene-Oligocene Zodiac fan is the oldest of these fans, and received active sedimentation during the time leading up to SCVF magmatism (Stevenson and Embley, 1987). The current position of the Zodiac Fan is >1,000 km to the southwest of the WA (Stenvenson et al., 1983), and the size of the submarine fan and mineralogy implies a drainage area of >500,000 km^2 of a granitic-metamorphic terrane (Stevenson and Embley, 1987). Substantial sediment would have been delivered by major rivers through the Oligocene, and sediments could have conceivably been subducted as the Kula-Pacific plate moved northward through Cenozoic time.

Within the SCVF itself, fluvial conglomerates containing rounded clasts of diverse crystalline rock types are interbedded with sandstones dominated by 71-60 Ma detrital zircon ages (J. Trop, pers comm). This suggests a fluvial system eroding late Cretaceous plutons of the Kluane arc of Plafker et al. (1994) exposed north of the SCVF. Similar sedimentary units from ~30-50 km northwest of SCVF yield pollen, detrital zircon and hornblende ages that constrain deposition to the mid-Cretaceous. These sedimentary units are much older than those found in the Cook Inlet or Zodiac Fan deposits, but they show that for a long time (~30 m.y.) before the onset of SCVF magmatism, crystalline basement rocks of the Yukon-Tanana and Wrangellia Composite terranes were being eroded and transported through the area where the northeastern portion of the WA is located today. It is therefore appropriate to use bedrock samples from these basement terranes to model contamination of the mantle wedge by sediment following

subduction. The Wrangellia and Yukon-Tanana basement rocks (F, Y1, and Y2) occupy isotope space (high Sr and Pb, low Nd and Hf isotope ratios) that is the most likely to produce a mixing curve that passes through the SCVF samples on all plots.

Mixing Models Between Mantle and Subducted Sediment

Figures 4.7 to 4.11 show the results of various mixing models that attempt to explain the petrogenesis of SCVF rocks in terms of variations in isotope systematics. Isotope ratios and elemental concentrations for the endmembers are summarized in Table 4-1. Depleted mantle (M) was chosen to represent the mantle wedge component of all mixing curves. The Nikolai Greenstone (N), Gravina-Nutzotin flysch (F), and Cretaceous granitoids that intrude the Yukon-Tanana Terrane (Y1, Y2) are local crustal rocks that could act as potential terrigenous contaminants. The voluminous accreted Jurassic Talkeetna arc is located ~300-400 km to the west of the SCVF and could represent an important source of crustal material. The Yakutat terrane has been interpreted as a part of the Siletzia terrane that is found in Oregon, Washington, and British Columbia (Chan et al., 2012; Wells et al., 2014). Given a lack of isotope date for the Yakutat microplate itself, a sample from southern Washington is used as an endmember (S) to represent possible Yakutat contribution of SCVF magmatism. Modern Pacific sediment (PS) is the bulk sediment composition from the Gulf of Alaska, and is included as a modern analog as a potential subducted sediment component (Plank and Langmuir, 2008). Binary mixing curves between a depleted mantle end-member and various continentally derived end-members attempt to model the contamination of the mantle wedge following subduction.

Published data for $^{176}Hf/^{177}Hf$ values of mixing end-members F, Y1, and Y2 were not available, but some assumptions can be made based on the similarity of Hf and Nd in igneous systems. Because Hf and Nd are relatively conservative HFS elements (Stern, 2001; Pearce et al.,

1995; 2007), their radiogenic isotope systems behave with a positive correlation. Figure 3.27 shows the range of $^{143}Nd/^{144}Nd$ values for Gravina-Nutzotin flysch and Yukon-Tanana crystalline rocks (Aleinikoff et al., 2000). Using the Terrestrial Array of Vervoort et al. (1999), an approximate $^{176}Hf/^{177}Hf$ value (and therefore εHf) can be inferred from these $^{143}Nd/^{144}Nd$ values (Table 4-2). Hf concentrations of the F, Y1, and Y2 rocks can be approximated by using the average Nd and Hf values of upper continental crust from Rudnick and Gao (2003). Nd/Hf of upper continental crust is 4.48, and adjusting the Hf concentration of F, Y1, and Y2 to maintain this ratio generates Hf concentrations that can be used in mixing calculations (Table 4-2). Similarly, the Hf concentration for the primitive basalt used in the crustal contamination model (described below) was derived by maintaining the approximate Nd/Hf ratio of SCVF basalts (Table 4-2).

The mixing curve M contaminated by Talkeetna arc type material (T) replicates the $^{87}Sr/^{86}Sr$ values for SCVF samples at mixing intervals of ~2-10% and εNd values at intervals of ~5-100% mixing (Fig. 4.7), indicating that this mixing curve does not offer a suitable explanation for the SCVF data.

The Yakutat microplate has been correlated to the Siletzia terrane that underlies much of western Oregon, Washington, and British Columbia (Chan et al., 2012; Wells et al., 2014). Because radiogenic isotope data for the Yakutat microplate itself is unavailable, we use a sample from the Gray's River Volcanics of the Siletzia terrane (S) in southern Washington. In Pb-Pb isotope space (Fig. 4.8), it is clear that the Siletzia (Yakutat) terrane does not represent a suitable end member for the SCVF data arrays. The data extend to high $^{207}Pb/^{204}Pb$ and $^{208}Pb/^{204}Pb$ isotopic values (Figs. 3.23, 3.24, and 3.36), but $^{86}Sr/^{87}Sr$ and εNd values are too similar to the eight SCVF samples to allow for a realistic mixing curve (Figs. 3.22 and 3.26).

The field for Nikolai Greenstone extends to high values of $^{86}Sr/^{87}Sr$, $^{207}Pb/^{204}Pb$, and $^{208}Pb/^{204}Pb$ values (Figs. 3.22 through 3.24). The Nikolai sample used in mixing calculations was chosen to have the lowest possible εNd and εHf values to maximize the mixing curve in Fig. 4.10, as well as the availability of published Pb concentrations. Nonetheless, the resulting mixing curve between the depleted mantle end-member (M) and the Nikolai sample (N) shows that relatively high values of εNd and εHf require a large component of Nikolai contamination to replicate most of the SCVF array, and it doesn't reach the samples with the lowest εNd and εHf values (Figs. 4.7 and 4.10). Despite the good fit of the mix in Pb-isotope space (Figs. 4.8 and 4.9), it cannot explain the SCVF array for the other isotope systems.

Modern Pacific sediment (PS) from the Gulf of Alaska (Plank and Langmuir, 1998) plots in a location in Sr-Nd-Pb-Hf space that could create a viable mixing curve with the depleted mantle end-member (Figs. 3.22 through 3.26). The calculated mix of Pacific sediment with depleted mantle (M) passes through the SCVF array, and ~1-10% mixing is required to generate $^{87}Sr/^{86}Sr$ and εNd values similar to the SCVF data (Fig. 4.7). However, the Pacific sediment end-member does not have a high enough $^{206}Pb/^{204}Pb$ value to match the SCVF data in Pb-Pb isotope space, and therefore cannot explain the SCVF array (Figs. 4.8 and 4.11). Additionally, modern Pacific sediment was not likely to represent a real component that could have contributed to SCVF magma generation at ~17–30 Ma.

The Cretaceous granitoids that intrude the Yukon-Tanana terrane to the north of the SCVF (Y1, Y2), and the Gravina-Nutzotin flysch (F) from the Nutzotin Mountains to the north and east of the SCVF, are located physically close to the modern SCVF, were present as basement rock at the time of SCVF magmatism, and plot in Sr-Nd-Pb-Hf isotope space that could create a realistic mixing curve with depleted mantle (Figs. 3.22 through 3.26). The mixing

curve of flysch with depleted mantle shows that a mix of ~0.5-5% flysch passes through the SCVF array on a plot of $^{86}Sr/^{87}Sr$ vs. εNd (Fig. 4.7), and a mix of ~0.2-1% flysch passes near the SCVF array in Pb-Pb isotope space (Figs. 4.8, 4.9). A mix of ~0.5-10% flysch with depleted mantle passes near the SCVF array on the εHf vs. εNd plot (Fig. 4.10).

Mixing models of Y1 and Y2 with M provide the most feasible models that can be used to explain binary mixing as a model for generation of SCVF isotope systematics. The Y1 mixing curve plots at lower εNd values than the SCVF array, but the Y2 mixing curve passes directly through part of the SCVF array (Fig. 4.7). A mix of ~0.2-3% Y1 or Y2 with depleted mantle can recreate the SCVF data in Sr-Nd isotope space (Fig. 4.7). The εHf vs. εNd plot shows a similar result, with ~0.2-2% mixing of Y1 or Y2 with depleted mantle generating slightly higher εHf values than the SCVF array at a given εNd value (Fig. 4.10). These binary mixing curves are in acceptable agreement with the flysch curve described above, especially for Sr and Nd isotopes. However, the same Y1 and Y2 mixing curves on the $^{207}Pb/^{204}Pb$ vs. $^{206}Pb/^{204}Pb$ and $^{208}Pb/^{204}Pb$ vs. $^{206}Pb/^{204}Pb$ plots (Figs. 4.8, 4.9) show that a much smaller fraction of mixing (<0.2% Y1 or Y2) is required to model the SCVF array.

Problems with the Mixing Model and Adjustment of Pb Concentrations

Plotting the Y2 mixing curve on $^{87}Sr/^{86}Sr$ vs. $^{206}Pb/^{204}Pb$ reveals an inconsistency in the mixing model (Fig. 4.11): ~0.2-1% mixing can explain the $^{87}Sr/^{86}Sr$ values of SCVF data, but <0.2% mixing is required to explain the $^{206}Pb/^{204}Pb$ values. Similarly, the $^{207}Pb/^{204}Pb$ vs. $^{206}Pb/^{204}Pb$ plot shows that <0.2% mixing of Y1 or Y2 could generate the SCVF array, while the N or S mixing curves show that ~1-5% mixing would work (Fig. 4.8). Although the F, Y1, and Y2 mixing curves pass close to the SCVF array, the fraction of mixing required in Pb-isotope

space is so much different from the calculated mixing curves in Sr-Nd-Hf isotope space that the validity of the Pb concentrations of the end-members chosen is called into question.

As described above, it is reasonable to believe that the Yukon-Tanana (YT) Terrane and/or Wrangellia Composite Terrane crystalline basement rocks were eroding and transporting sediment with a crustal isotope signature to the trench, where they were subducted and contributed an isotopic endmember that is necessary to explain the SCVF isotopic array via binary mixing with a mantle wedge endmember. If the YT crystalline basement rocks (metaplutonic and granitoid rocks) and/or the Gravina-Nutzotin flysch were transported by typical fluvial systems before subduction, then concentrations of trace elements should be compared to modern global subducted sediment (GLOSS; Plank and Langmuir, 1998). Because the calculated mixing models tend to agree with each other in Sr-Nd-Hf space (Figs. 3.22, 3.25), the inconsistency lies with the Pb concentrations of the end-members. The high Pb concentrations of the YT granitoids could be diluted by marine phases or other continental sediments upon deposition, and therefore should be lowered in the revised mixing models (Plank and Langmuir, 1998). This can be done by changing the Pb concentration to maintain the Sr/Pb ratio of GLOSS, as described below in Table 4-3. Similarly, the depleted mantle sample chosen to represent the mantle wedge endmember for the mixing calculations is not necessarily an accurate representation of the actual mantle wedge that contributed the bulk of mass of SCVF magmas, and the Pb concentrations should be adjusted to better match the Sr/Pb ratio of a more realistic mantle wedge composition: the primitive mantle (PM) concentrations for Sr and Pb were chosen (Sun and McDonough, 1989).

Table 4-3 shows the original Pb concentrations of F, Y1, and Y2, the original Sr/Pb ratios of 31.8, 1.97 and 4.98, respectively, and the GLOSS Sr/Pb ratio of 16.43 (Plank and Langmuir,

1998). Pb concentrations for F', Y1', and Y2' were then adjusted to maintain the GLOSS Sr/Pb ratio. Table 4-3 also shows the original Pb concentration for M, the original Sr/Pb ratio of 426, and the PM Sr/Pb ratio of 144 (Sun and McDonough, 1989). The Pb concentration for M' was then adjusted to maintain the PM Sr/Pb ratio. The isotope ratios for all end-members were kept constant (Table 4-1).

Figures 4.12 through 4.16 show the mixing curves that result from the adjustments of Pb concentration described above. The plots of $^{207}Pb/^{204}Pb$ and $^{208}Pb/^{204}Pb$ vs. $^{206}Pb/^{204}Pb$ (Figs. 4.12, 4.13) show that the fraction of mixing of F'/Y1'/Y2' with M' required to roughly match the array of SCVF samples is in the range of ~0.2-3% mixing, as opposed to <0.2% mixing for F/Y1/Y2 with M. Plots of $^{87}Sr/^{86}Sr$, εNd, and εHf vs. $^{206}Pb/^{204}Pb$ (Figs. 4.14 to 4.16) show that the Y1'/Y2' curves are less inflected than the original F/Y1/Y2 curves, pass more directly through the SCVF array, and require lower degrees of mixing to match the SCVF data (Figs. 4.14 to 4.16). Some of the SCVF data still lie outside of the two mixing curves, but the mixing curves between M' and F', Y1', or Y2' agree much better with the SCVF data than before the Pb concentrations were altered (i.e., in Figs. 4.8 to 4.11).

By adjusting the Pb concentrations of the depleted mantle (M) end-member and the crustal end-members (F, Y1, and Y2; inferred to have been subducted as sediment) to more closely approximate Sr/Pb ratios of PM and GLOSS, respectively, the modelled mixing curves more closely approximate the SCVF array in Pb-isotope space. This indicates that contamination of a primitive mantle wedge-like material by GLOSS-like sediment derived from crystalline basement rock is a likely mechanism to explain the radiogenic isotope systematics observed in the SCVF.

Comparisons to Other Wrangell Arc Volcanic Centers

The SCVF likely represents the earliest preserved volcanic activity in the WA, and a comparison to other volcanic fields in the younger WA will help place the SCVF into a geologic context with the later history of the WA. The mid-Miocene St. Clare Creek volcanic field and the late-Pliocene Skookum Creek volcanic center are the most similar to the SCVF, in terms of volcanic architecture and showing a geochemical record of tectonic changes, and are discussed here.

The St. Clare Creek volcanic field in Yukon Territory consists of the 18-16 Ma Wolverine and 16-10 Ma Klutlan composite volcanoes ("SC" in Fig. 1.1; Skulski et al, 1991; 1992). These two volcanoes physically overlap one another, and show a limited areal extent with focused distribution along the Duke River fault. Evidence for Oligocene to Miocene motion on the Duke River Fault (Cobbett et al., 2017) supports the idea that transcurrent faulting can focus arc volcanism along faults (Tibaldi et al., 2010). Shifts in lava chemistry from alkaline, to transitional, to calc-alkaline, and back to transitional affinities record the relative importance of the tectonic processes of leaky transform magmatism over a slab-window (alkaline) and subduction (calc-alkaline). The lifespan of the St. Clare Creek volcanic field is comparable to that of the SCVF (~8 m.y.), and the chemistry of eruptive products similarly comprises a record of the tectonics that were active along the southern Alaska-Yukon continental margin. Similarly, the shifts in chemistry also correspond to shifts in eruptive position, as the older Wolverine succession is to the east of the younger Klutlan center (Skulski et al, 1991; 1992). The calc-alkaline series from the St. Clare Creek volcanic rocks is most similar to the Cabin Creek-Flat Top rocks of the SCVF, which corresponds to the trend 1 series of Preece and Hart (2004). This suggests that the subduction-fluid influence the Yukon magmatic system received was minimal,

and is more likely related to the same processes that gave rise to the Yukon transitional magma series and the trend 1 magmas of the <5 Ma WA: relatively low-degree melting of a subduction-modified mantle wedge (Skulski et al., 1991; 1992; Preece and Hart, 2004). The St. Clare Creek volcanic field was active immediately following the cessation of SCVF activity, and other new bedrock and detrital clast geochronologic data suggest that these Yukon volcanic rocks may represent the only WA volcanic activity from ~18–14 Ma (Morter et al., 2016; Trop et al., 2017; Davis et al., 2017).

The Skookum Creek Volcanic Center (3.25–2.25 Ma) is similar to the SCVF in its complex volcanic structure and diversity of styles and compositions of volcanism. Skookum Creek is a complex of overlapping domes, shield and composite volcanoes, and age relations show that the eruptive locus shifted southward and produced at least two overlapping shield volcano-complexes of andesite lavas with feeder dikes in three main eruptive phases. Early-formed bimodal domes and associated lava flows were overridden by the andesitic shield of the Theresa Phase, and followed by late silicic domes that ring the main cones (Preece, 1997). The Pecos Vent is a small sequence of basaltic trachyandesites to trachydacites that partially underlies the Theresa Phase. The Old Faithful Phase is a cone composed of basaltic-andesite to andesites, which was cut by later dacite domes with thick lavas. This migration of volcanism is similar to that seen at the SCVF, but the Skookum Creek Volcanic Center is much shorter lived than the Sonya Creek shield volcano (~1 m.y.). Although the physical structure is similar, the eruptive frequency is not. The Cabin Creek and Flat Top rocks from SCVF are dominantly trend 1, unlike the Theresa and Old Faithful Phases. The main similarities are the overlapping shield-like vent complexes, dominant intermediate lava compositions, and small volumes of pyroclastic material (Preece, 1997).

The <5 Ma WA volcanoes have been well studied (locations in Fig. 1.1; Richter et al., 1990; Richter et al., 1994; Richter et al., 1995a; Richter et al., 1995b; Clague et al., 1995; Preece, 1997). Individual shield volcanoes show physical similarities to the Sonya Creek shield volcano; Tanada Peak is a similar size and is composed of 900 m of andesite lavas and dacite agglutinates; Capital Mountain is smaller and was shorter lived, but is composed of andesite lavas, and minor pyroclastic and lahar deposits; Mt. Wrangell is composed dominantly of lavas. Although the Sonya Creek shield volcano is morphologically similar to the younger WA shield volcanoes, the SCVF as a whole is longer-lived (~10 m.y.), more complex in geochemistry (basalt to rhyolite, and adakite-like to transitional-tholeiitic) and eruptive styles (effusive lavas and domes, minor pyroclastic deposits, and sub-volcanic/hypabyssal rocks).

Comparisons to Global Arc-Transform Settings

The Wrangell Arc is located in a transition zone at the northeastern corner of the Pacific plate, where normal subduction below the Aleutian arc gives way to flat-slab subduction beneath the magmatic gap to the west of the WA, and the slab takes a bend to the east below the WA. This in turn gives way to dextral transform motion within the overriding North American plate (Fig. 1.1). Similar tectonic transition zones exist globally, where both convergent and transform plate boundaries play a role on the position and composition of arc magmatism. Comparisons between global arc-transform settings and the WA can be drawn, and the geographic and temporal position of the SCVF can help us to understand the greater tectonic picture at the initiation of the WA.

Anomalous geochemical signatures are characteristic of arc-transform transition zones, and the presence of adakite-like affinities can have tectonic significance. The presence of SCVF rocks with elevated Sr/Y (20-70), and one sample with elevated La/Yb (~20), suggests the role

of an adakitic component in magma genesis (Fig. 3.21a, b). Adakites can be generated through many different tectonic processes (Castillo, 2012), but the most likely mechanisms in the young (< 5 Ma) WA are the thermal ablation and melting of a slab edge around a tear in the subducting Yakutat slab (Fuis et al., 2008), or because stalled or slowed subduction allows the slab to heat enough to melt (Gutscher et al., 2000; Preece and Hart, 2004). A similar scenario is observed where the Kamchatka arc meets the Aleutian arc at a 90° angle in the northwestern Pacific. Adakitic volcanic rocks there are interpreted to represent the melting of subducted Pacific lithosphere as sub-slab asthenosphere upwells around the edge of a slab window (Yogodzinski et al., 2001; Park et al., 2002).

Adakite-like granitoid porphyries from eastern Anatolia in Turkey are interpreted to have been generated by melting of lower-crustal garnet-bearing amphibolitic rocks, following slab-breakoff and asthenopheric upwelling (Karlsi et al., 2011). This interpretation is based on low Mg# and Sr-Nd isotope data for the granitoids, as well as geologic constraints that rule out slab-melting and lower crustal delamination. At least one of the adakite-like silicic lavas (15JB16LA) may have originated via melting of some mafic lower-crustal rock, but the MgO, Ni, and Cr values of the Rocker Creek lavas and domes suggest that they are more like global subducted oceanic crust-derived adakite rocks, rather than thick mafic lower crust-derived adakitic rocks (Fig. 4.2b). This signature is a temporal record of the initiation of Yakutat subduction at ~30 Ma.

The other significant geochemical aspect of the SCVF (as well as the modern WA) is the presence of transitional-tholeiitic magma series, interpreted here and by other workers to represent melting induced by intra-arc extensional forces (Preece and Hart, 2004: Trop et al., 2012). These rocks have a trace element subduction signature (i.e., LILE enrichment, HFSE

depletion; Fig. 3.19), interpreted to have been inherited from a previously subduction-modified mantle wedge.

Cenozoic collisional volcanism in Eastern Anatolia, Turkey, has similarities to SCVF volcanism (Pearce et al., 1990; Keskin, 2003). Lavas from the Ararat and Kurs volcanoes in the central part of the collision zone are calc-alkaline and have trace element and isotope systematics that indicate a significant inherited subduction signature (Pearce et al., 1990). During continental collision, the subducted portion of the leading oceanic crust steepened and broke off, leading to melting of the asthenospheric mantle (Keskin, 2003; Keskin et al., 2006).

Cenozoic volcanism in Myanmar along the dextral Sangaing transform fault shows chemical similarities to the SCVF specifically and WA in general. Mid-Miocene volcanic rocks are calc-alkaline and inferred to form via typical subduction-fluid related melting of mantle wedge asthenosphere above the subducting Indian oceanic lithosphere (Maury et al., 2005; Lee et al, 2016). Following this was a ~10 m.y. hiatus of volcanism, during which time the Indian subcontinent collided with Asia, causing a change from oblique to dextral convergence and subsequent rollback of the Indian slab. Quaternary small-degree melting of subduction-enriched lithospheric mantle and asthenosphere gave rise to primitive alkaline lavas (Lee et al., 2016).

The Trans-Mexican volcanic belt experienced rollback of the slab over the past 10 m.y. as a result of slowed oceanic plate convergence rate (Ferrari et al., 2001). This allowed deep asthenosphere to flow and introduce heterogeneity into the opening mantle wedge. Additionally, the subduction of the East Pacific Rise spreading ridge leads to adakitic affinities where the edge of the slab is thermally eroded and melted (Luhr, 2000; Ferrari et al., 2001).

A similar magmatic response to plate motion rates is seen in the Northern Cordilleran Volcanic Province (northern British Columbia, central Yukon Territory), which is comprised of

~14 Ma–10 ka bimodal alkaline rocks. Changes in relative plate motions between the Pacific and North American plates ca. 10 Ma allowed asthenosphere to upwell through a slab-window, causing extensional stresses and decompression melting of OIB-like mantle to produce alkaline magmatism (Edwards and Russell, 2000; Thorkelson et al., 2011). Specific volcanic geochemistry depends on the local asthenosphere and lithospheric mantle, but changes in plate motion drove magmatism 100's of km's inboard of the continental margin.

The Medicine Lake shield volcano, located in the southern Cascade arc, is comprised of basaltic to rhyolitic rocks that erupted as lavas, domes, and tuffs over that last ~0.5 Ma (Donnelly-Nolan et al., 2008). This complex volcanic center is located at a confluence of subduction zone volcanism and a major transtensional fault zone, and geochemistry of rocks show dominantly subduction-related affinities, although the extensional environment has strongly affected the eruptive history. This is similar to the Sonya Creek shield volcano, which has the HFSE-depletion subduction signature, but the transitional-tholeiitic affinities suggest dry melting affected by transtensional stresses.

A model similar to the tectonic scenarios presented above can be employed to explain the geochemical changes seen in the SCVF, wherein a change in subduction angle or convergence rate initiated melting of previously modified/enriched mantle. An initial geochemical signature of typical calc-alkaline affinities related to subduction (Rocker Creek lavas and domes, intermediate dome rocks), gave way to transitional-tholeiitic affinities (Cabin Creek/Flat Top), followed by a return to typical calc-alkaline magmatism (Young Creek and Border Lavas).

Tectonic Implications for Wrangell Arc Initiation

These new geochemical, isotopic, and geochronologic data for the Oligo-Miocene Sonya Creek volcanic field place constraints on the tectonic history at the initiation of the Wrangell

Arc. Within the SCVF, initial emplacement of subduction-related calc-alkaline lavas, domes, and sub-volcanic rocks was followed by a geochemical, temporal, and geographic shift to transitional-tholeiitic affinities related to anhydrous melting due to intra-arc extension. An additional pulse of calc-alkaline magmatism marked the end on SCVF activity. The geochemical types found within the SCVF are generally like those found in the central and western WA (~12 Ma-recent), reflecting the dominant roles of subduction and intra-arc extension on magma production. Geochemical exceptions are the presence of adakite-like lavas, which appear to have erupted only at the initiation of the WA (~29–22 Ma) and part of the young WA (<5 Ma) magmatic phase, indicating that some anomalous heating of the subducted slab or lower crust occurred during these times. Additionally, the only alkaline lavas erupted at the St. Clare Creek volcanic field.

Temporal Connections to Regional Research

The geochemical types within the SCVF, and associated tectonic implications, can be correlated to the broader tectonics of the southern Alaskan margin from ~28–17 Ma. Recent thermochronology research in the Chugach-St. Elias Range to the south of the SCVF reveals a record of uplift and exhumation as a result of the progressive subduction, collision, and underthrusting of the Yakutat microplate beneath North America (Berger et al., 2008a, 2008b; McAleer et al., 2009; Enkelmann et al., 2008, 2010; Arkle et al., 2013; Grabowski et al., 2013; Falkowski et al., 2014, 2016; Falkowski and Enkelmann, 2016; Enkelmann et al., 2017; Dunn et al; 2017). After the subduction of a spreading ridge in Eocene time, the eastern Chugach-western St. Elias range experienced relative quiescence until the onset of Yakutat subduction no earlier than 35 Ma (Enkelmann et al., 2010; Falkowski et al., 2014, 2016). Uplift and exhumation of the Chugach-St. Elias range accelerated in mid-Miocene, and the St. Elias syntaxis experienced

rapid exhumation since ~5 Ma (Enkelmann et al., 2010; Grabowski et al., 2013; Falkowski et al., 2016). Modern seismic imaging below south-central Alaska show the presence of thickened (11-22 km thick) oceanic crust as far north as the central Alaska Range (Ferris et al., 2003; Eberhart-Phillips et al., 2006; Gulick et al., 2007; Christeson et al., 2010; Worthington et al., 2012) and the presence of a subducting slab below the modern WA (Eberhart-Phillips et al., 2006; Bauer et al., 2014). These data indicate that subduction of the leading edge of the Yakutat microplate began was active at ~35-30 Ma, subduction of a slab steep enough to cause arc magmatism has been active since ~30 Ma in the WA, and continental collision of the thicker parts of the Yakutat microplate began by ~15-12 Ma, (Christeson et al., 2010; Worthington et al., 2012; Falkowski et al., 2014, 2016).

Our new geochemical and geochronological data indicate that wedge-shaped Yakutat microplate (Cristeson et al., 2010; Worthington et al., 2012) may have transferred some component of strain to the upper plate via the Denali-Totschunda fault system ca. 23–22 Ma, based on the initiation of transitional-tholeiitic Sonya Creek shield volcanism. Immediately following SCVF activity, primitive alkaline lavas erupted ~80 km to the southeast in the Yukon from ~18–16 Ma (Skulski et al., 1991; 1992). These transitional-tholeiitic to alkaline eruptive histories record varying degrees of transtensional melting of mantle wedge, perhaps as subduction slowed and the slab steepened as the thicker portions of the Yakutat microplate began to subduct, from ~23–16 Ma. A steepening slab would induce the suction of mantle into the wedge between the slab and upper plate, and induce melting (Jadamec, 2016), as well as shift the locus of magmatism to the south. Arc-transform transition zones in Turkey, Myanmar, and Mexico show temporal, geochemical, and geographic changes in magmatism as microplate accretion and/or continental collision caused subduction to slow and/or the slab to steepen

(Pearce et al. 1990; Keskin et al., 2003, 2006; Maury et al., 2005; Lee et al., 2016). The timing of this temporal, geochemical, and geographic shift likely indicates inboard effects of thickened Yakutat crust entering the trench, earlier than the thermochronologic cooling signals from further south in the St. Elias syntaxis would indicate (~15-12 Ma, Enkelmann et al., 2010; Falkowski et al., 2014, 2016; Falkowski and Enkelmann et al., 2016; Enkelmann et al., 2017).

Alternatively, extensional stresses across strike-slip faults (i.e., transtension) could initiate pressure release melting of the upper mantle, and changes in degree of partial melting would result in variations in geochemistry (Preece and Hart, 2004). The presence of previously subduction-modified mantle material would impart the trace element subduction signature on transitional to calc-alkaline magmas, similar to what is seen in the "calc-alkaline" rocks from the Yukon WA volcanic fields. The position of arc-volcanism would shift to the south with dextral strike-slip motion along the Totschunda, Denali, and/or Duke River faults, in addition to these faults serving as conduits for magma ascent (Skulski et al., 1991, 1992). In reality, a complex combination of changing subduction angle, rate of convergence, thickness of the subducting plate, and motion along strike-slip faults is likely responsible for the temporal, geochemical, and geographic shifts recorded in by the SCVF and Yukon WA volcanic fields.

Original Position and Subsequent Geographic Migration of the Wrangell Arc

The location of the SCVF, as well as that of geochemically similar hypabyssal rocks from the northern flank of the modern WA that are coeval with SCVF activity (~29–22 Ma), designate the position of the WA at its initiation. If Oligocene to recent dextral motion along the Totschunda fault is approximately restored, the hypabyssal rocks and the SCVF define a <100 km long belt that is offset from the modern axis of the WA to the northeast by ~35–60 km (see Fig. 1.1 for location of hypabyssal rocks and SCVF in relation to modern WA).

The shift of volcanic locus from the SCVF to the Yukon volcanic fields represents a previously undocumented south and eastward shift of magmatism during the early phases of the WA. This is likely due to steepening and/or slowing of the Yakutat slab, or increased dextral motion of the upper plate along the Denali-Duke River-Totschunda fault systems. This was followed by the northwestward migration of WA magmatism that was first documented by Richter et al., (1990) and supported by Preece and Hart (2004) and Trop et al., (2012). Those authors attribute the migration to the progressive northwestward insertion of the northward-tapering Yakutat slab into the continental margin of south-central Alaska. As thicker and more buoyant crust was subducted, the leading edge of the slab continued to move to the northwest. Subduction-related fluids are likely derived from the shallow Yakutat slab, and initiate melting of the mantle wedge below the modern WA. Transitional-tholeiitic eruptive products in the interior of the modern WA suggest an intra-arc extensional regime. Adakite dacite lavas from Mts. Drum and Churchill indicate the melting of the Yakutat slab (Preece and Hart, 2004; Preece et al., 2014).

Final Thought

The temporal, geochemical, and geographic shifts observed in the Sonya Creek volcanic field have implications for continental arc-transform junctions worldwide and throughout earth history. Geochemistry of magmatic products in these transition zones are sensitive to slight shifts in the relative position of the subducting and overriding plates, as well as changes in rate and direction of convergence, angle of subduction, and motion along strike-slip faults. The presence of heterogeneous mantle materials introduces additional complications, as changes in tectonic configuration can cause mantle flow and inheritance of previous geochemical signatures. An along-strike transition to oblique and strike-slip motion is ubiquitous in convergent margins, and

understanding the geochemical signature of magmatic initiation can help to recognize similar situations in the geologic record.

Key Remaining Questions/Future Work

The SCVF presents an intriguing look at the initiation of the WA, but the complex age and structural relations that exist within the volcanic field remain unclear after only one field season. Additional field work with the goal of targeting the volcanic bedrock units that were not sampled or were under-sampled during the 2015 field season would greatly increase the robustness of conclusions made. Some mapped Rocker Creek units were not sampled, including a rhyolite dome and associated pyroclastic rocks. The extensive (intermediate) dome field remains largely un-sampled, and one $^{40}Ar/^{39}Ar$ step-heat plateau age suggests that the earliest bedrock in the SCVF (and thus the WA) may be found there. Additionally, the eruptive source for the adakite-like silicic lavas may be buried somewhere within the dome field. Further measured sections of the Sonya Creek shield volcano would allow for correlation of lava flows, and would likely distinguish eruptive centers and/or overlapping volcanic vents. The obsidian unit was not sampled directly, and a full trace element analysis would assist in the characterization of obsidian archeological artifacts from around Alaska (in progress). The distal Sonya Creek shield volcano rocks (i.e., Flat Top) are voluminous, and measured stratigraphic sections would greatly enhance correlation with the inferred proximal lavas (i.e., Cabin Creek). The Flat Top tuff could be measured along strike, allowing for an estimate of erupted volume. The marginal fracture-associated rocks to the northeast of the Sonya Creek shield volcano show complex field relations, and should be sampled for geochemical and geochronological analysis.

The final stages of SCVF volcanic activity appears to have been complex, with late Cabin Creek lavas, Flat Top lavas and tuff, the Young Creek lavas, and the Border lavas all erupting

within ~4 m.y. of each other (~22-18 Ma), and relatively close together physically. Detailed sampling of these units would allow us to understand the spatial and temporal transition from SCVF activity to St. Clare Creek activity in the Yukon. Lavas from Young Creek dip to the northwest, and a measured section would allow for potential correlation with either the overlying Sonya Creek rocks (Flat Top) or the Border Lavas. The Rock Lake diorite appears complex in photographs, and petrography suggests it is a sub-volcanic intrusion. Detailed sampling would reveal any potential relationship to the various extrusive phases nearby (Flat Top, Young Creek, Border Lavas). The Border Lavas are extensive across the south and east of the map area, and only two collected samples were considered for geochemistry. Stratigraphic sections should be measured, and samples for geochemistry and geochronology should be collected. The SCVF isn't constrained by the rectilinear boundaries of the 1:63.360 scale McCarthy D-1 quadrangle map (Richter et al., 2000), and extends to the south and east into Yukon Territory, and to the West where extensive WA volcanic rocks are mapped on the 1:250,000 scale McCarthy Quadrangle map (MacKevett, 1978). Excursions into this territory would reveal the eruptive extent of the SCVF. A physical connection to the St. Clare Creek volcanic field in the Yukon may exist somewhere along the ~80 km between the two volcanic fields.

The Beaver Creek fault that is mapped to the east in the Yukon appears to cut through the middle of the SCVF. Fieldwork along strike of the fault could constrain timing and nature of fault motion. Evidence for Oligo-Miocene extensional motion along the fault would support a possible hypothesis that this fault was related to intra-arc extension and volcanism at the Sonya Creek shield volcano.

Radiogenic isotope data were obtained for only eight samples from a volcanic field that existed for ~11 m.y. and covers ~600 km^2. Isotope analysis on samples that belong to key rock

groups (i.e., adakite-like silicic lavas, Young Creek lavas, Border lavas, and intermediate domes) would allow for a better interpretation of the existing data. Samples of *in situ* local basement rocks and crystalline clasts from sedimentary units could be collected for isotopic and geochemical analysis and comparison with SCVF igneous units. Put together, a complete AFC (assimilation and fractional crystallization) model could be implemented. The simple binary isotope mixing models presented above suggest interesting conclusions, but detailed petrogenetic modeling would further elucidate the genesis of SCVF volcanic rocks.

Figure 4.1: (Next page). Schematic illustration of the volcanic evolution of the SCVF through time: (A) ~29–25 Ma SCVF activity, (B) ~25–23 Ma SCVF activity, (C) ~23–20 Ma SCVF activity, and (D) ~20–18 Ma SCVF activity. Colors of volcanic units are the same as in Figure 1.2. Outlined fields indicate the volcanic centers active during the time range indicated in that panel, and the transparent colors show older eruptive centers. The black arrows indicate inferred flow directions of volcanic rocks. The dashed line running SW-NE marks the inferred trace of the Beaver Creek fault, and the NW side-down sense of motion is shown. Modern Rock Lake and Ptarmigan Lake are shown for spatial reference.

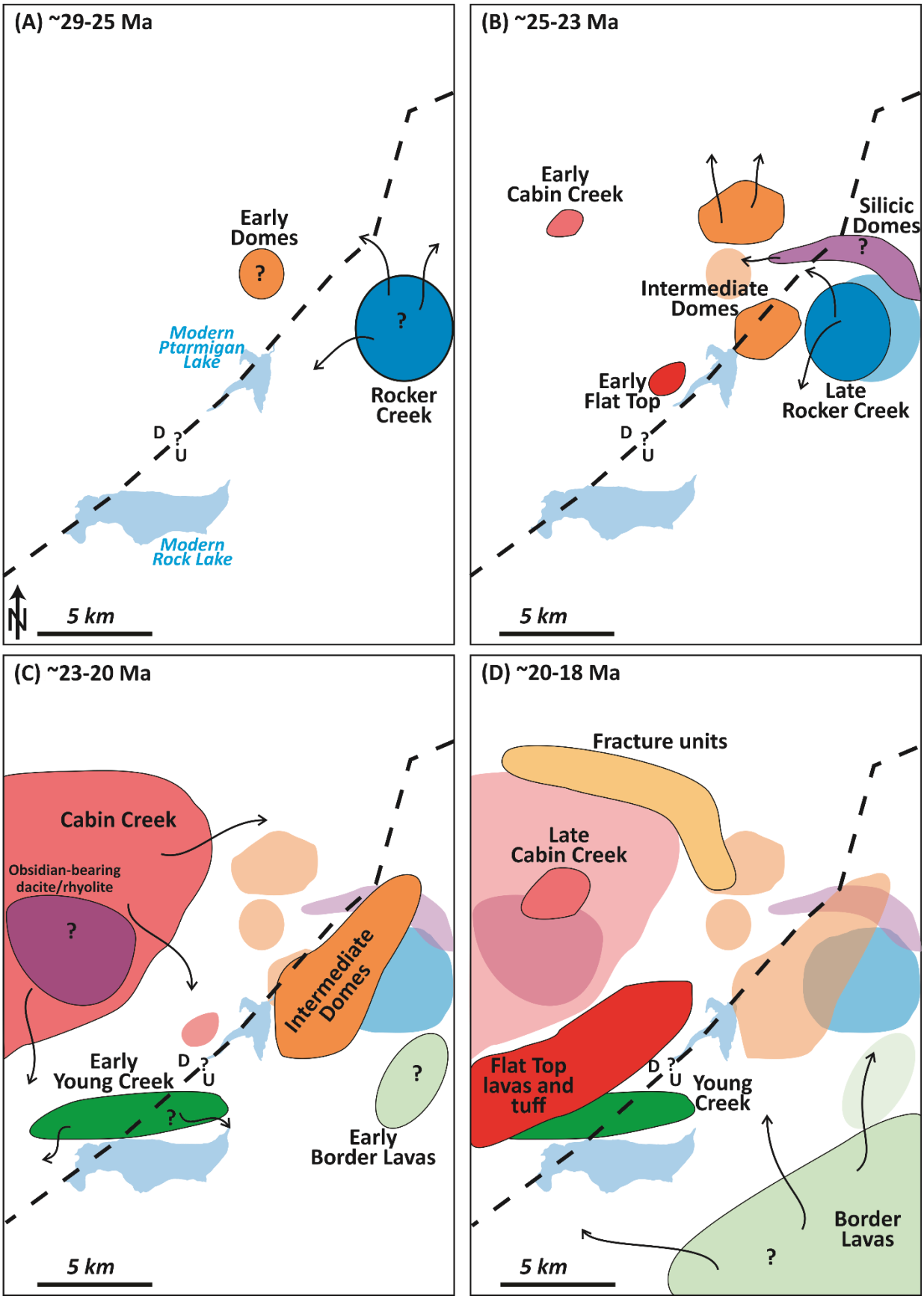
(A) ~29-25 Ma
Early Domes
?
?
Rocker Creek
Modern Ptarmigan Lake
D ? U
Modern Rock Lake
N
5 km
(B) ~25-23 Ma
Early Cabin Creek
Silicic Domes
?
Intermediate Domes
Early Flat Top
Late Rocker Creek
D ? U
5 km
(C) ~23-20 Ma
Cabin Creek
Obsidian-bearing dacite/rhyolite
?
Intermediate Domes
Early Young Creek
D ? U
?
?
Early Border Lavas
5 km
(D) ~20-18 Ma
Fracture units
Late Cabin Creek
Flat Top lavas and tuff
D ? U
Young Creek
Border Lavas
?
5 km

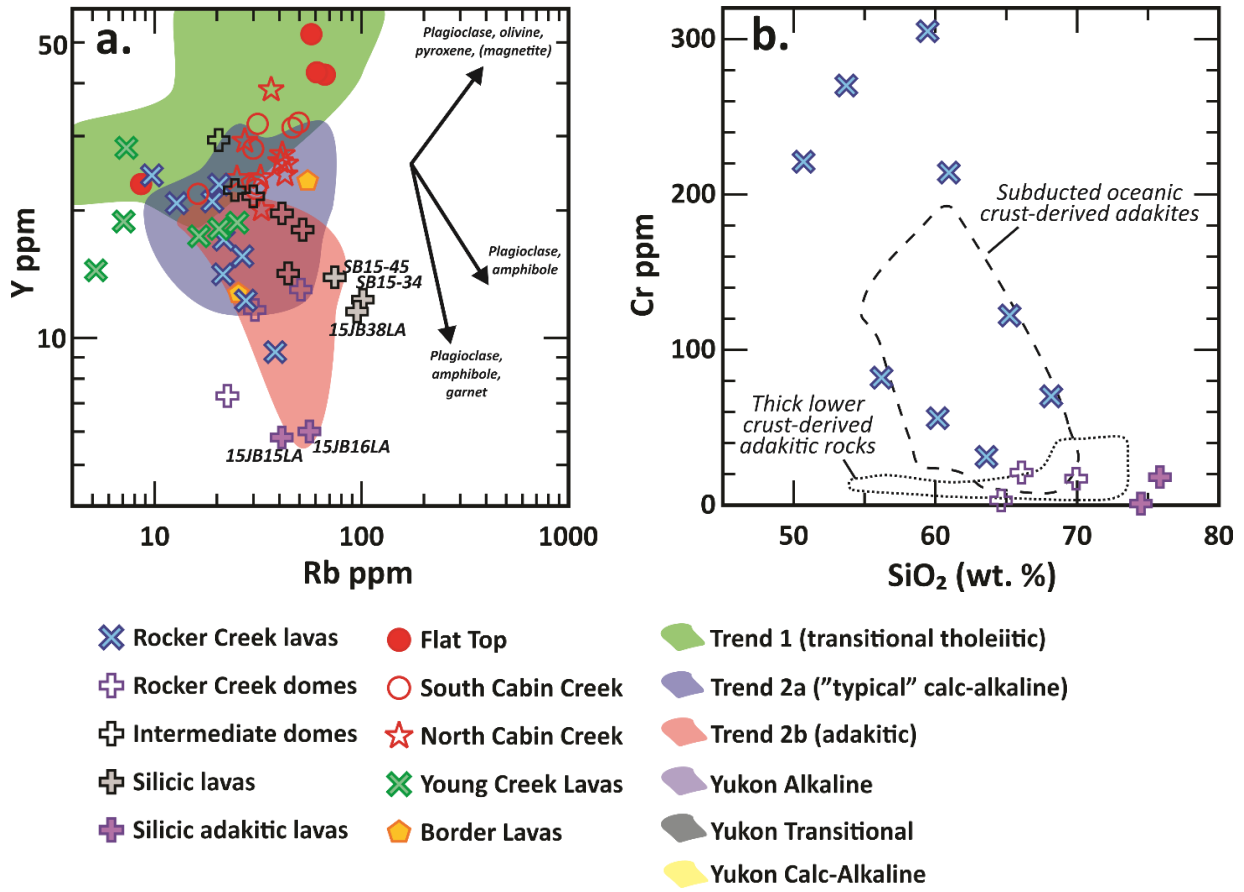

Figure 4.2: (A) Y vs. Rb discrimination diagram, showing the vectors for various fractionating assemblages. The colored fields are for trends 1 (green), 2a (blue), and 2b (red) of <5 Ma WA rocks (Preece and Hart, 2004). Distribution coefficients from Pearce and Norry (1979) and Irving and Frey (1984). (B) Cr vs. SiO_2 variations of Rocker Creek lavas and domes, and adakite-like rhyolites. Fields for subducted oceanic crust-derived adakites and thick lower crust-derived adakitic rocks are taken from Figure 4 of Wang et al. (2006) and references therein.

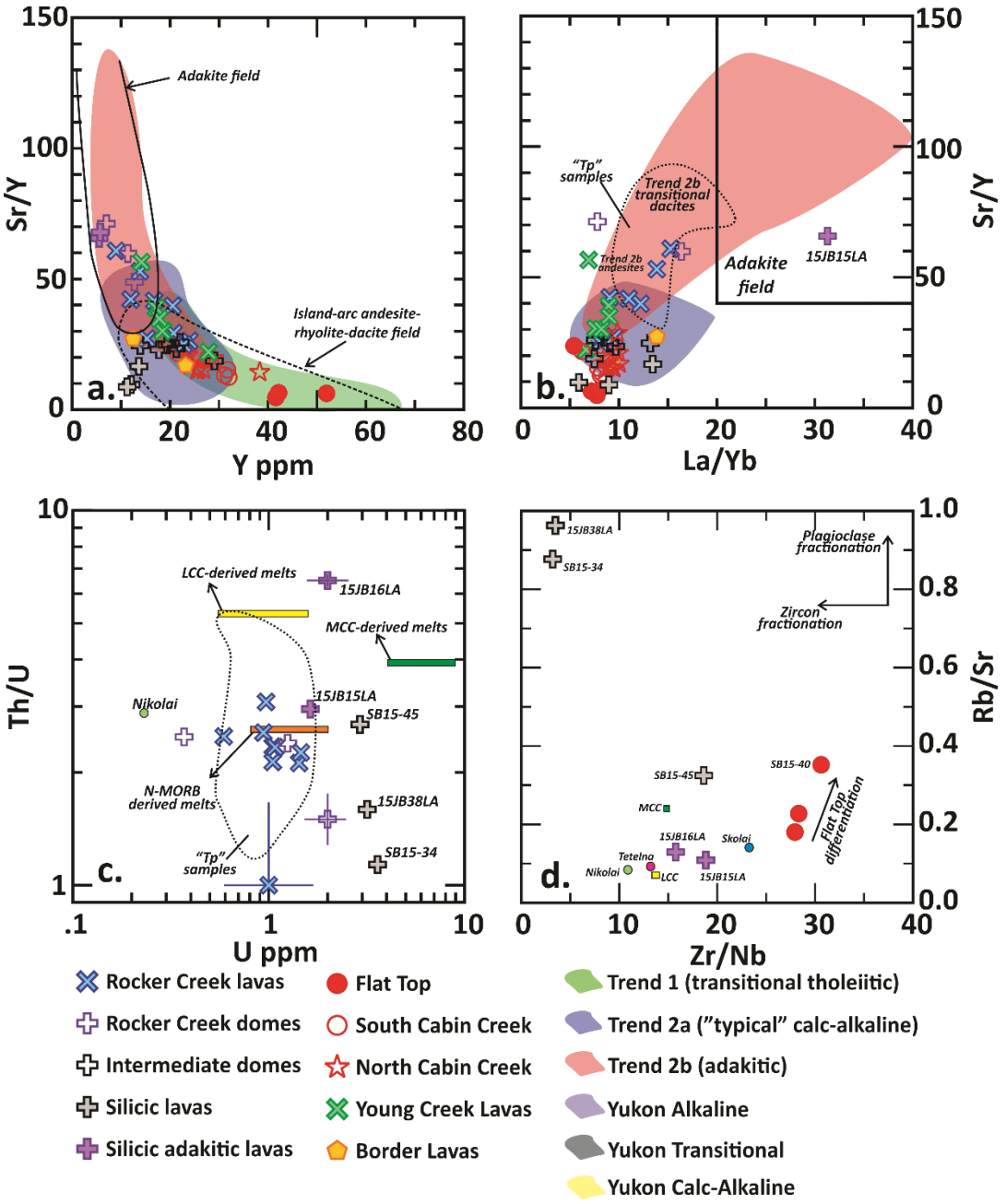

Figure 4.3: A) Sr/Y vs. Y plot after Defant et al. (1991), showing the fields for adakites and island-arc andesite-rhyolite-dacites. Colored fields for <5 Ma WA rock types are the same as in previous diagrams. B) Sr/Y vs. La/Yb plot showing the adakite field. Trend 2b andesites and transitional dacites (Preece and Hart, 2004) have adakitic Sr/Y, Sr, and Y contents, but more moderate REE characteristics. Hypabyssal "Tp" samples from the northern flank of the WA plot within the field marked by the dotted line. C) Th/U vs. U plot after Karlsi et al. (2011), showing fields for N-MORB (Sun et al., 2008), lower and middle continental crust (LCC, MCC; Rudnick and Gao, 2003). Nikolai Greenstone data are from Greene et al. (2008, 2009). Error bars are one standard deviation. D) Rb/Sr vs. Zr/Nb plot after Richter et al. (1994) of silicic SCVF rocks. Nikolai Greenstone and Tetelna volcanics data are from Barker et al. (1990), and Skolai Group data are from Beard and Barker (1989).

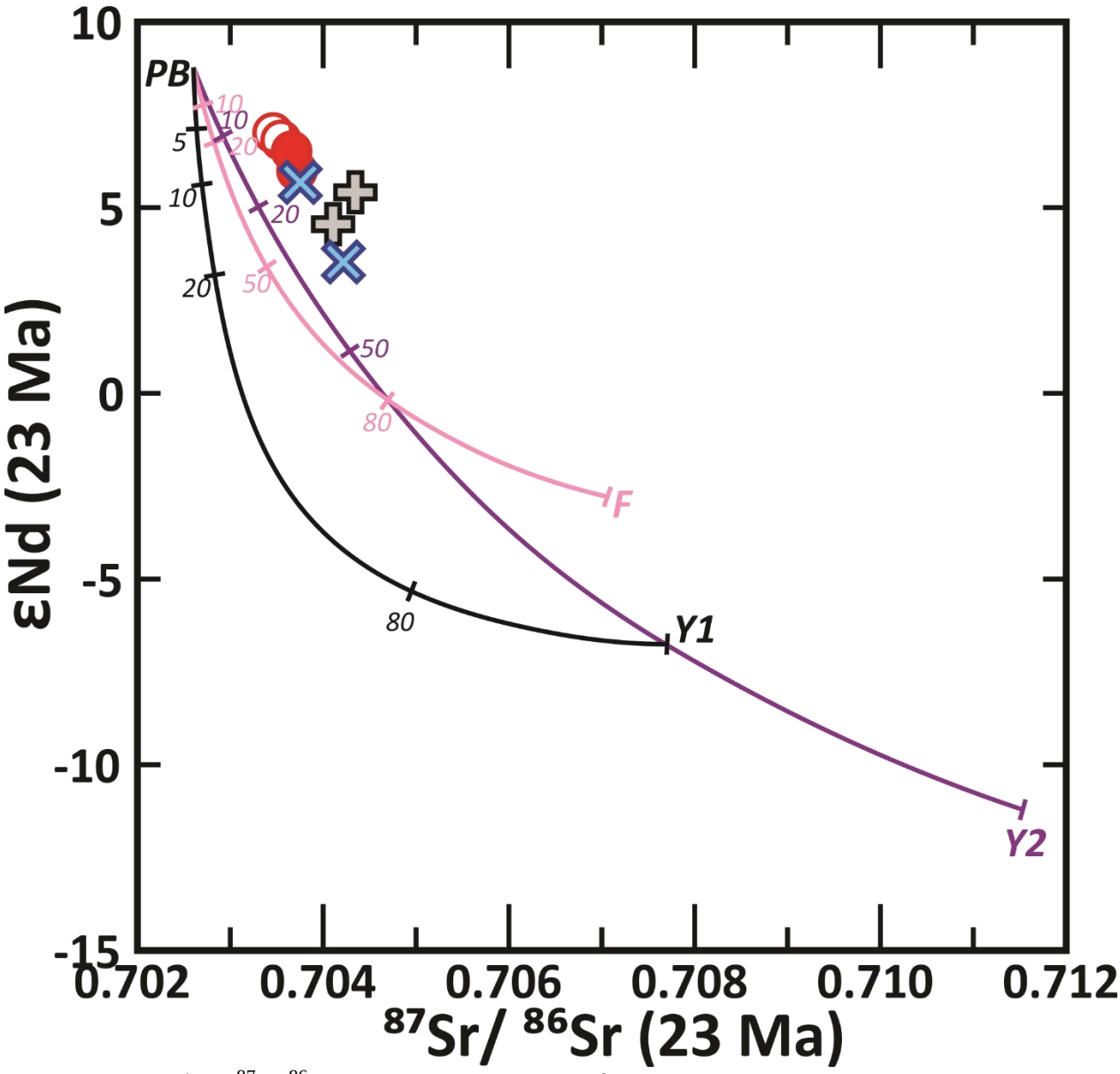

Figure 4.4: εNd vs. $^{87}Sr/^{86}Sr$ plot, showing results of crustal contamination binary mixing calculations, between a primitive basalt (PB) and various end-members, abbreviations for which are shown in Table 4-1.

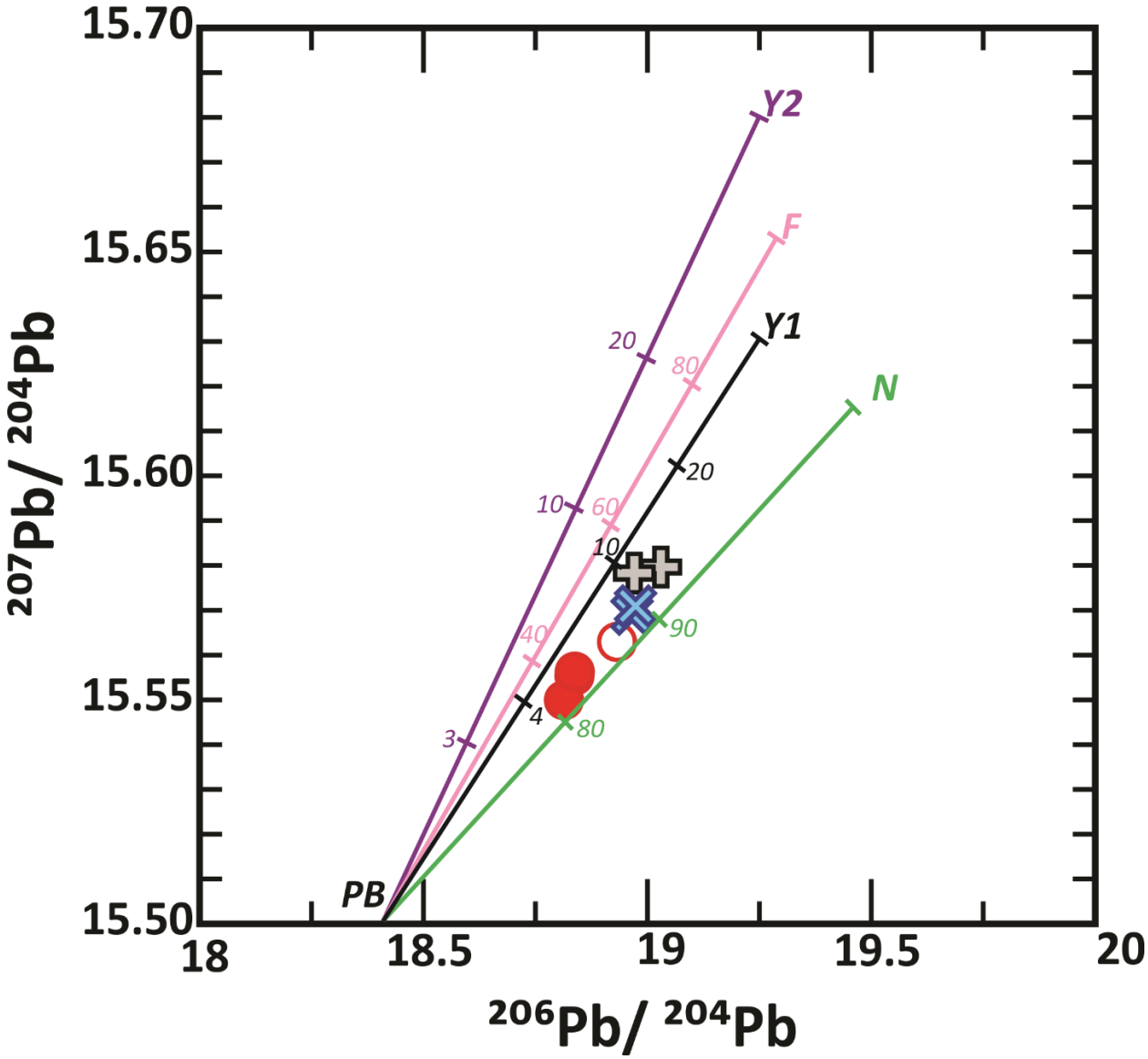

Figure 4.5: $^{207}Pb/^{204}Pb$ vs. $^{206}Pb/^{204}Pb$ plot, showing results of crustal contamination binary mixing calculations, between a primitive basalt (PB) and various end-members, abbreviations for which are shown in Table 4-1.

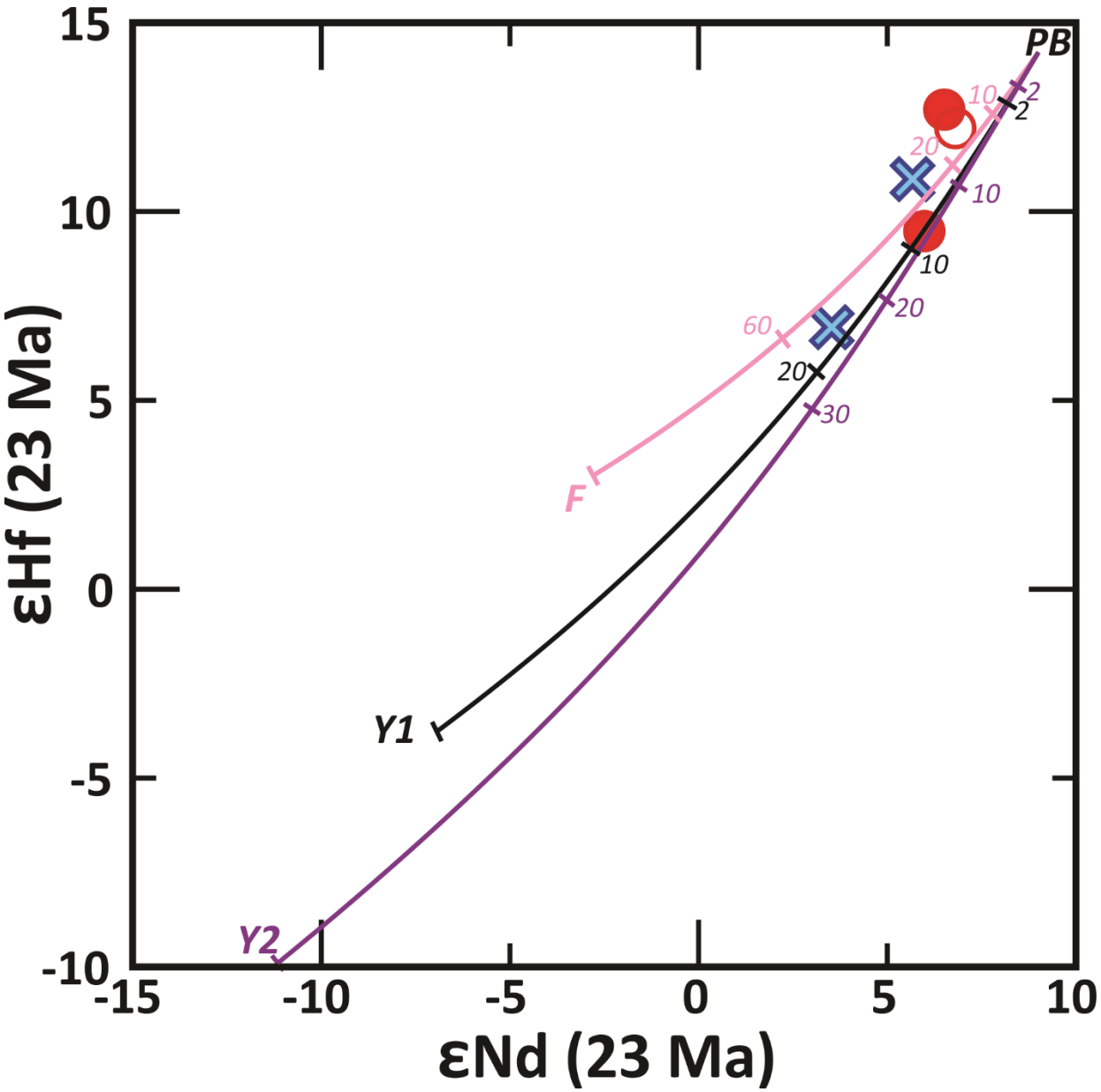

Figure 4.6: εHf vs. εNd plot, showing results of crustal contamination binary mixing calculations, between a primitive basalt (PB) and various end-members, abbreviations for which are shown in Table 4-1.

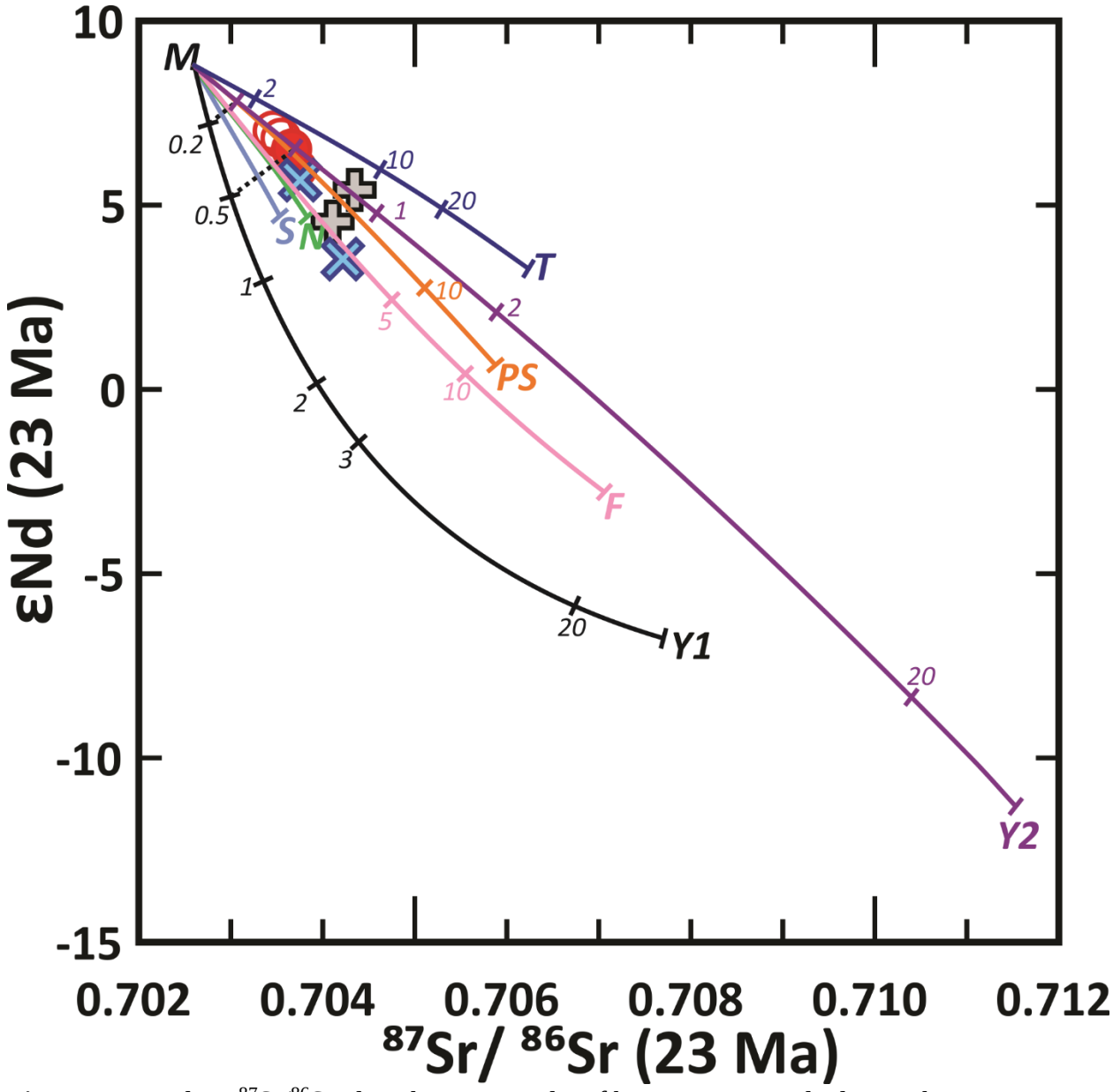

Figure 4.7: εNd vs. $^{87}Sr/^{86}Sr$ plot, showing results of binary mixing calculations between depleted mantle (M) and various end-members, abbreviations for which are shown in Table 4-1.

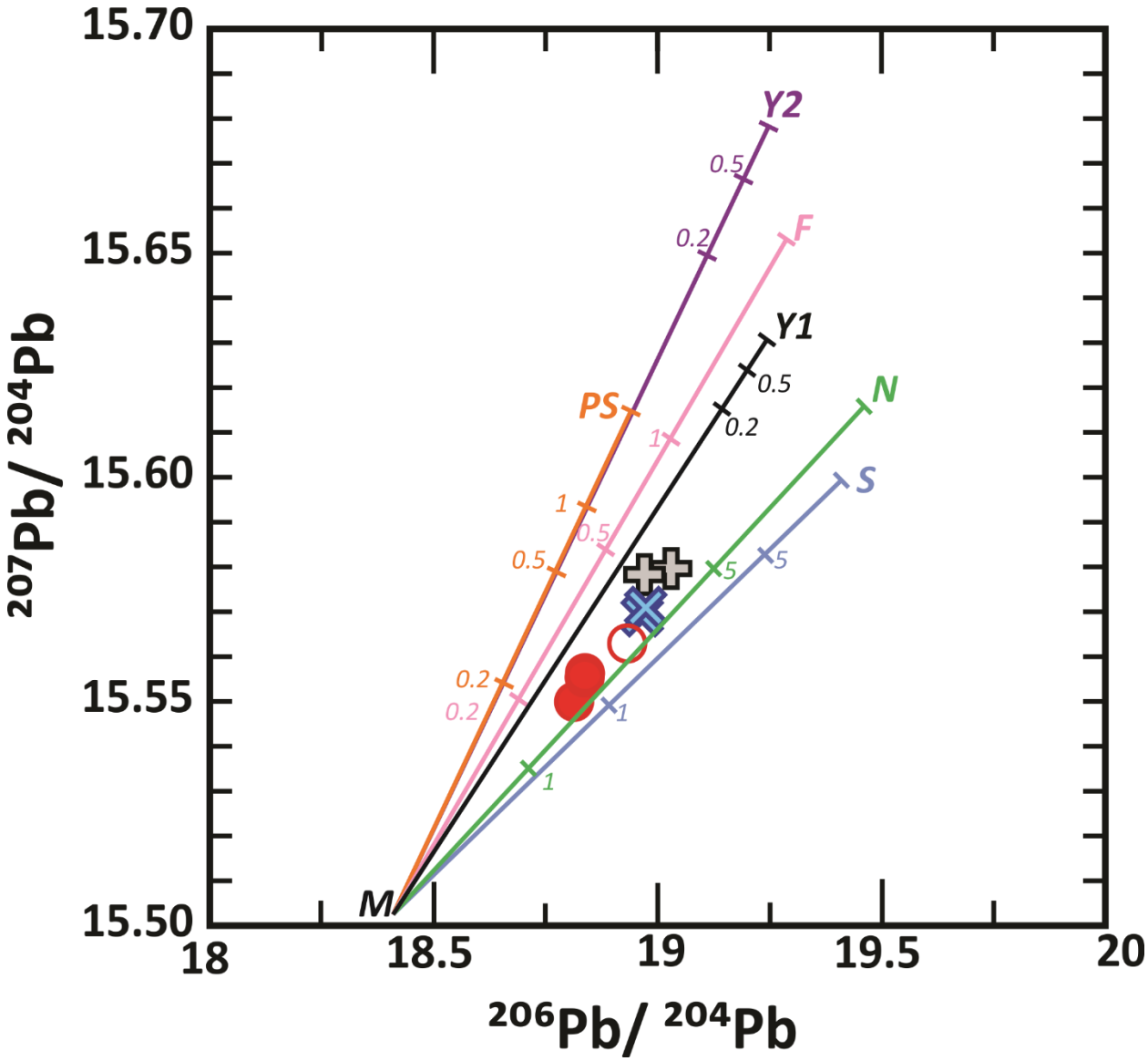

Figure 4.8: $^{207}Pb/^{204}Pb$ vs. $^{206}Pb/^{204}Pb$ plot, showing results of binary mixing calculations between depleted mantle (M) and various end-members, abbreviations for which are shown in Table 4-1.

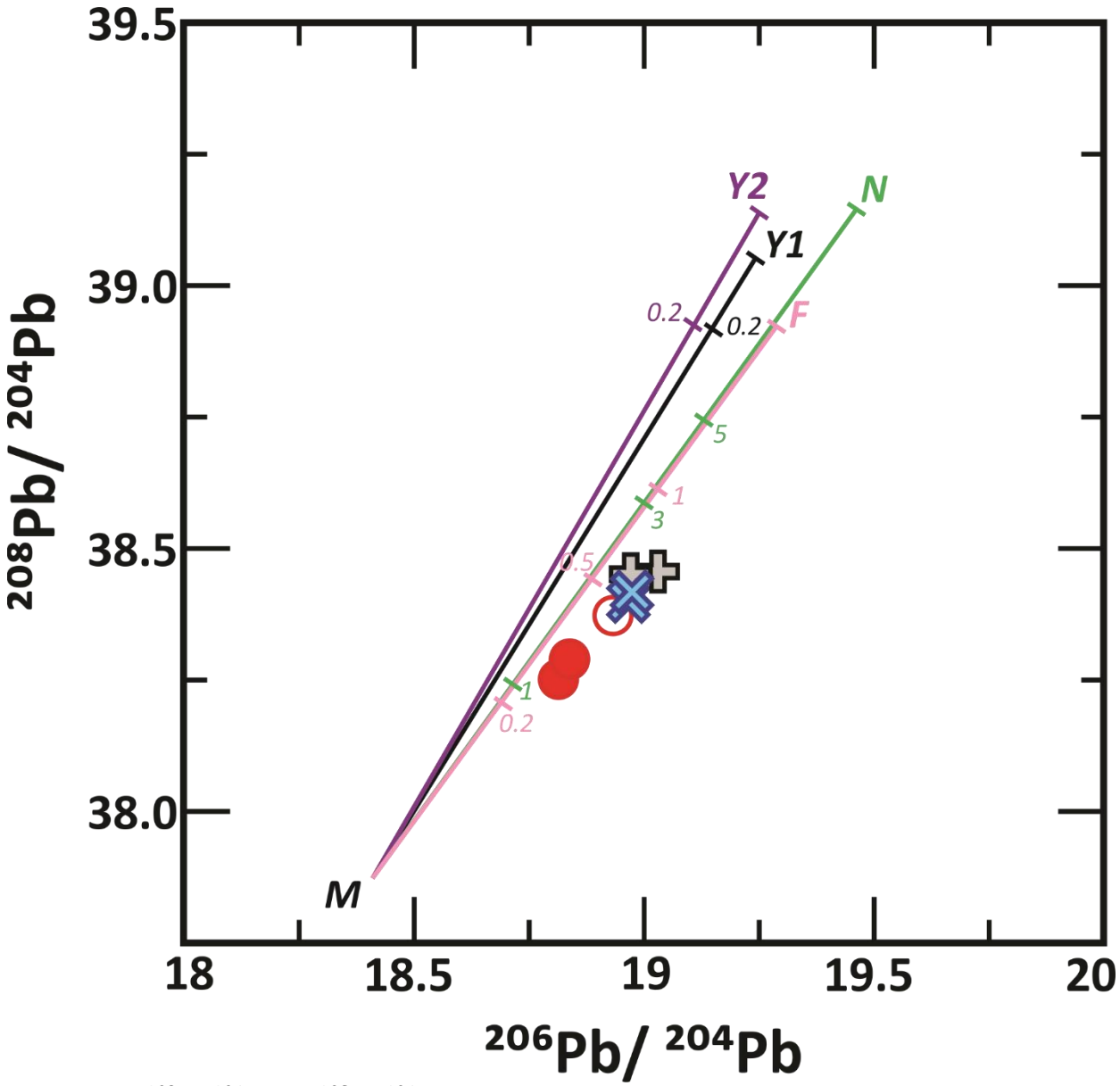

Figure 4.9: $^{208}Pb/^{204}Pb$ vs. $^{206}Pb/^{204}Pb$ plot, showing results of binary mixing calculations between depleted mantle (M) and various end-members, abbreviations for which are shown in Table 4-1.

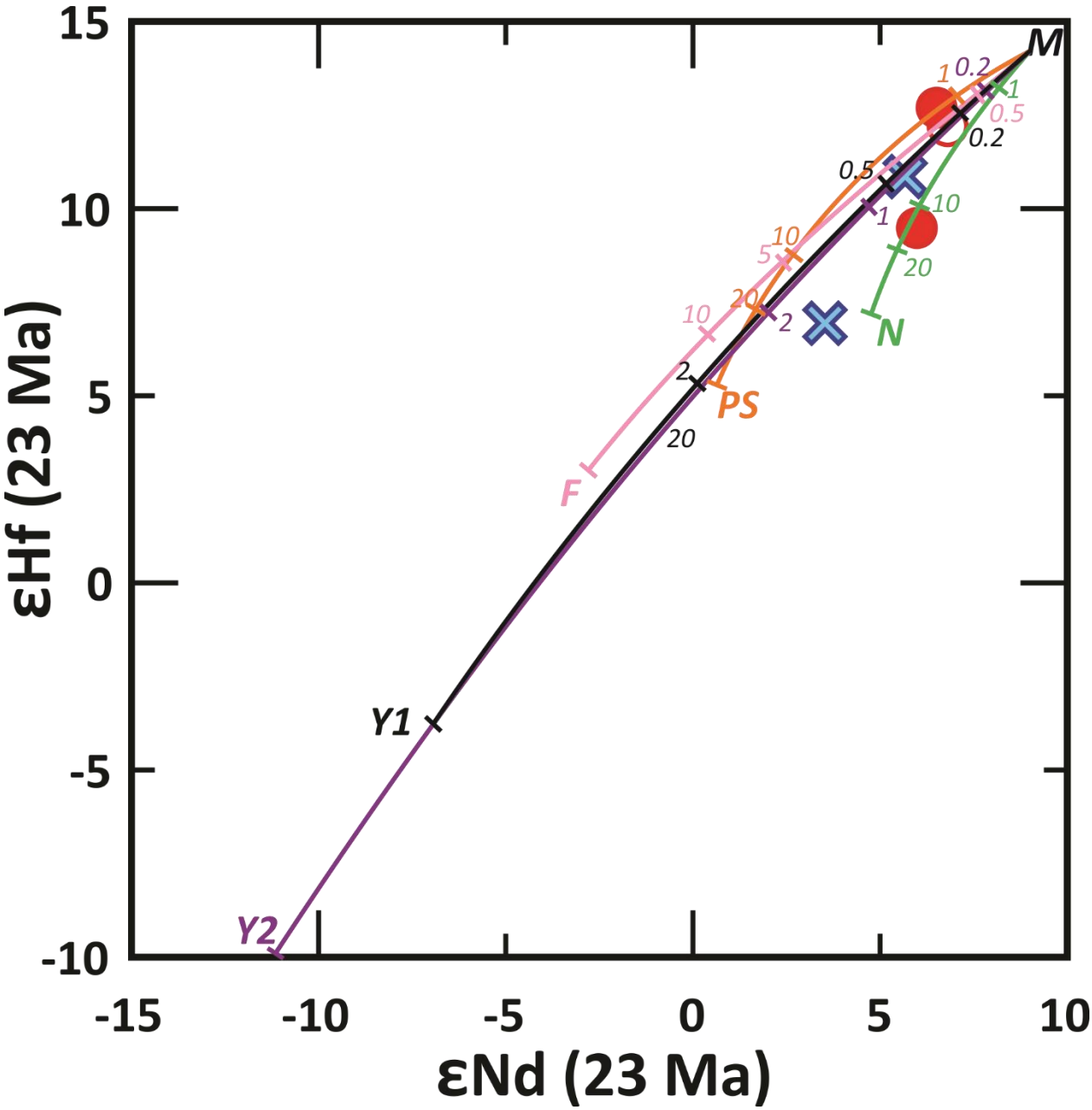

Figure 4.10: εHf vs. εNd plot, showing results of binary mixing calculations between depleted mantle (M) and various end-members, abbreviations for which are shown in Table 4-1.

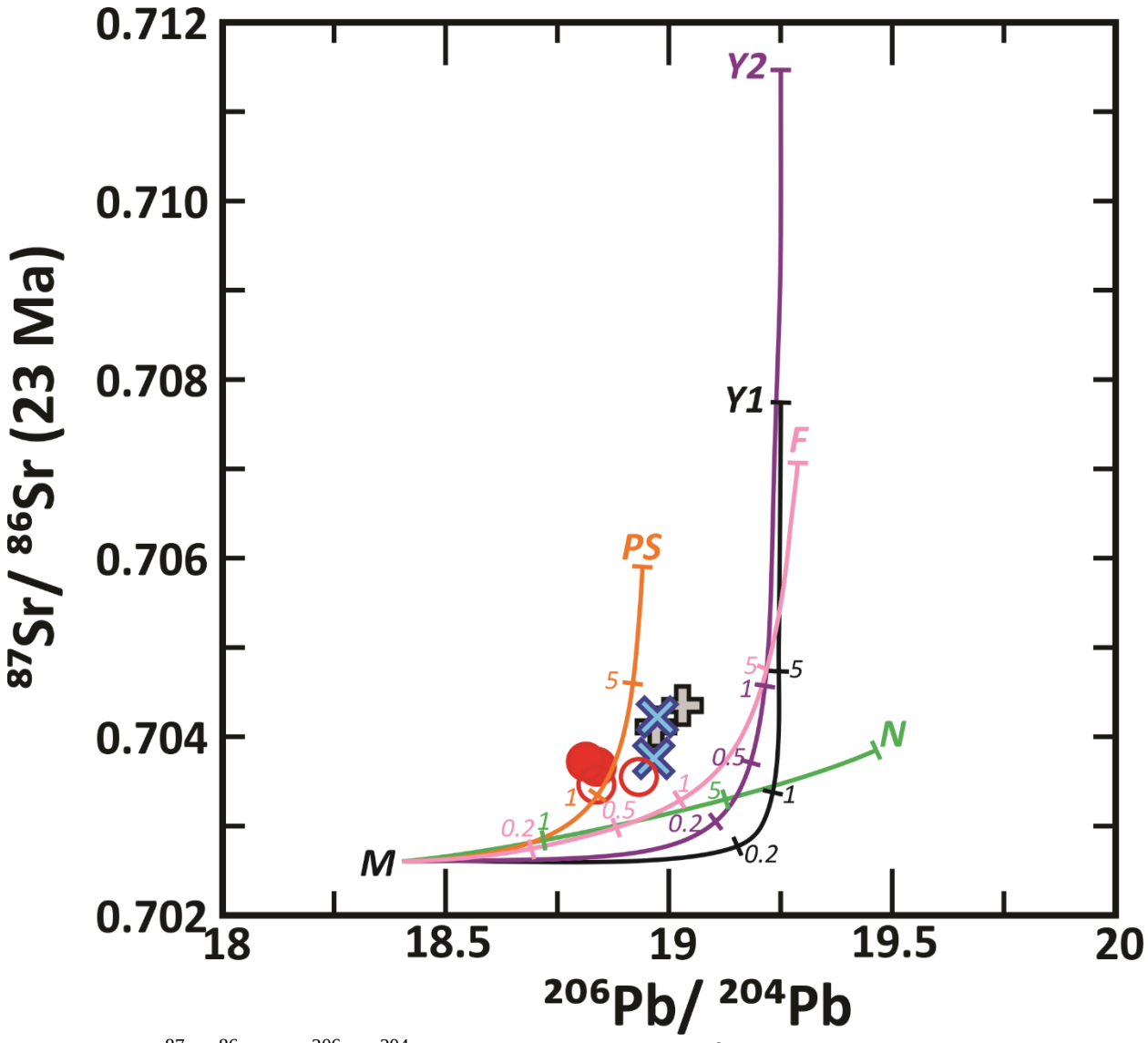

Figure 4.11: $^{87}Sr/^{86}Sr$ vs. $^{206}Pb/^{204}Pb$ plot, showing results of binary mixing calculations between depleted mantle (M) and various end-members, abbreviations for which are shown in Table 4-1.

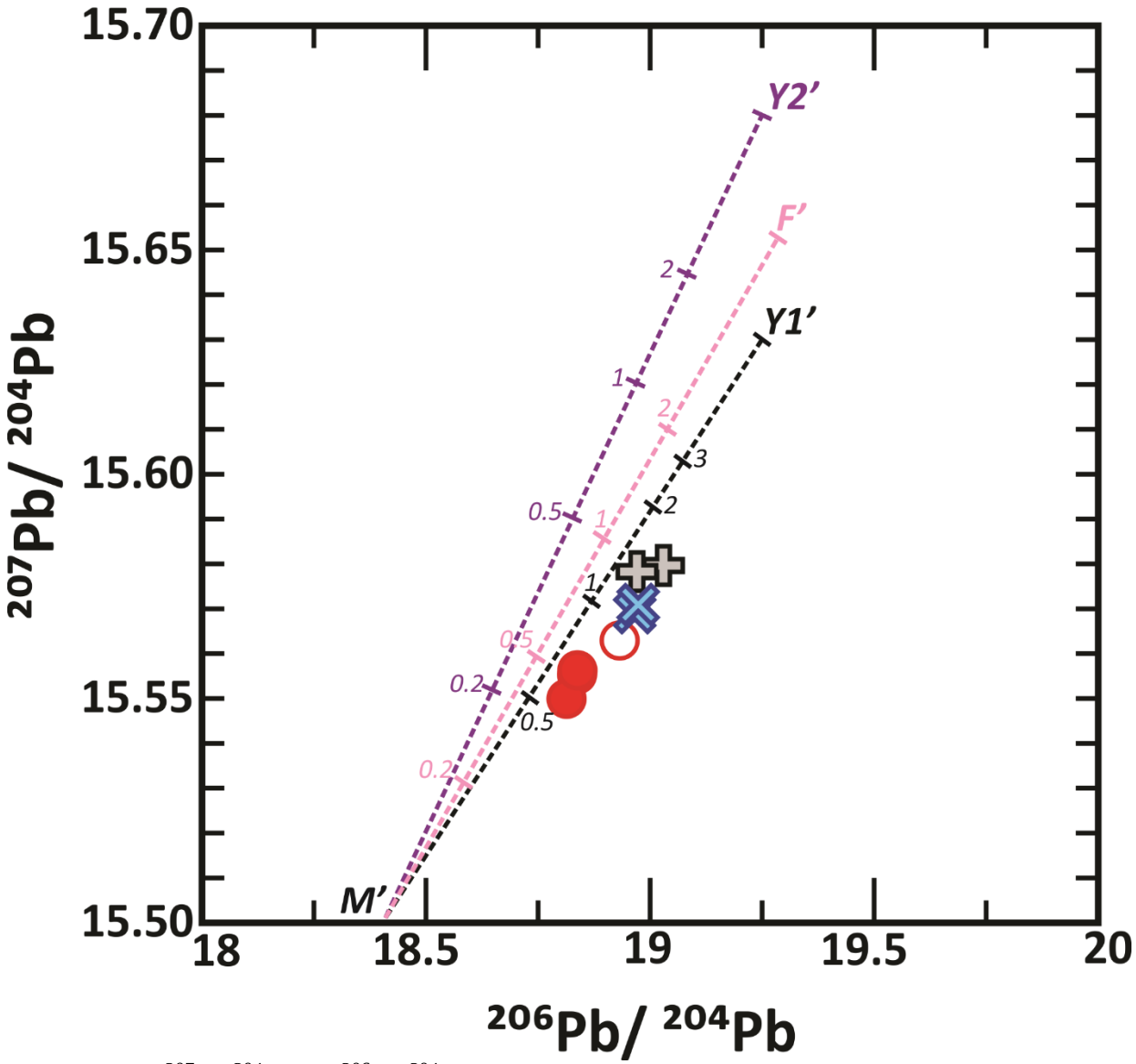

Figure 4.12: $^{207}Pb/^{204}Pb$ vs. $^{206}Pb/^{204}Pb$ showing results of binary mixing model after the adjustment of Pb concentrations in all end-members, as described in the text. Isotope ratios are the same as those shown in Table 4-1 and Figures 4.7 to 4.11, and adjustments to Pb concentrations are shown in Table 4-3.

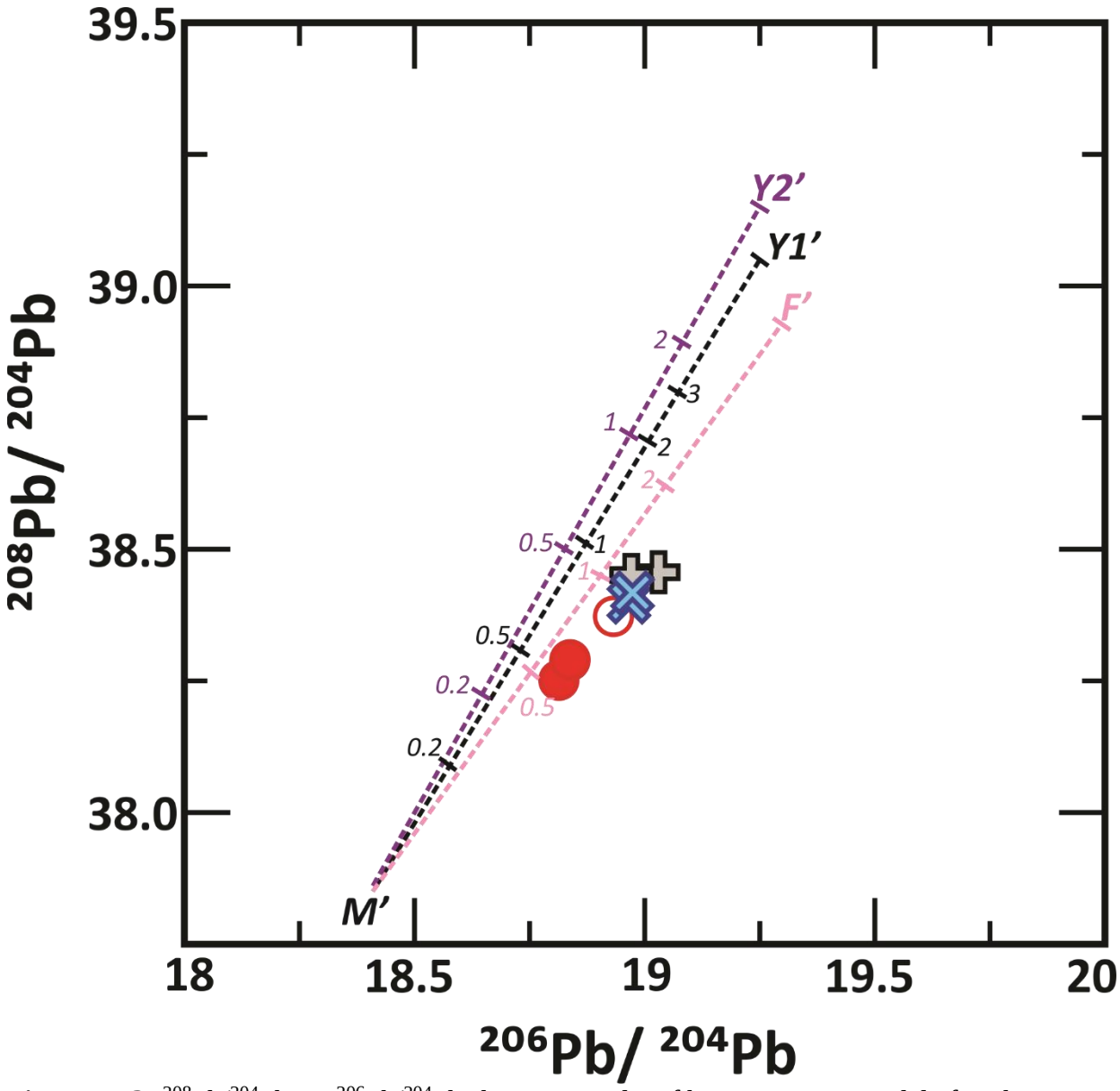

Figure 4.13: $^{208}Pb/^{204}Pb$ vs. $^{206}Pb/^{204}Pb$ showing results of binary mixing model after the adjustment of Pb concentrations in all end-members, as described in the text. Isotope ratios are the same as those shown in Table 4-1 and Figures 4.7 to 4.11, and adjustments to Pb concentrations are shown in Table 4-3.

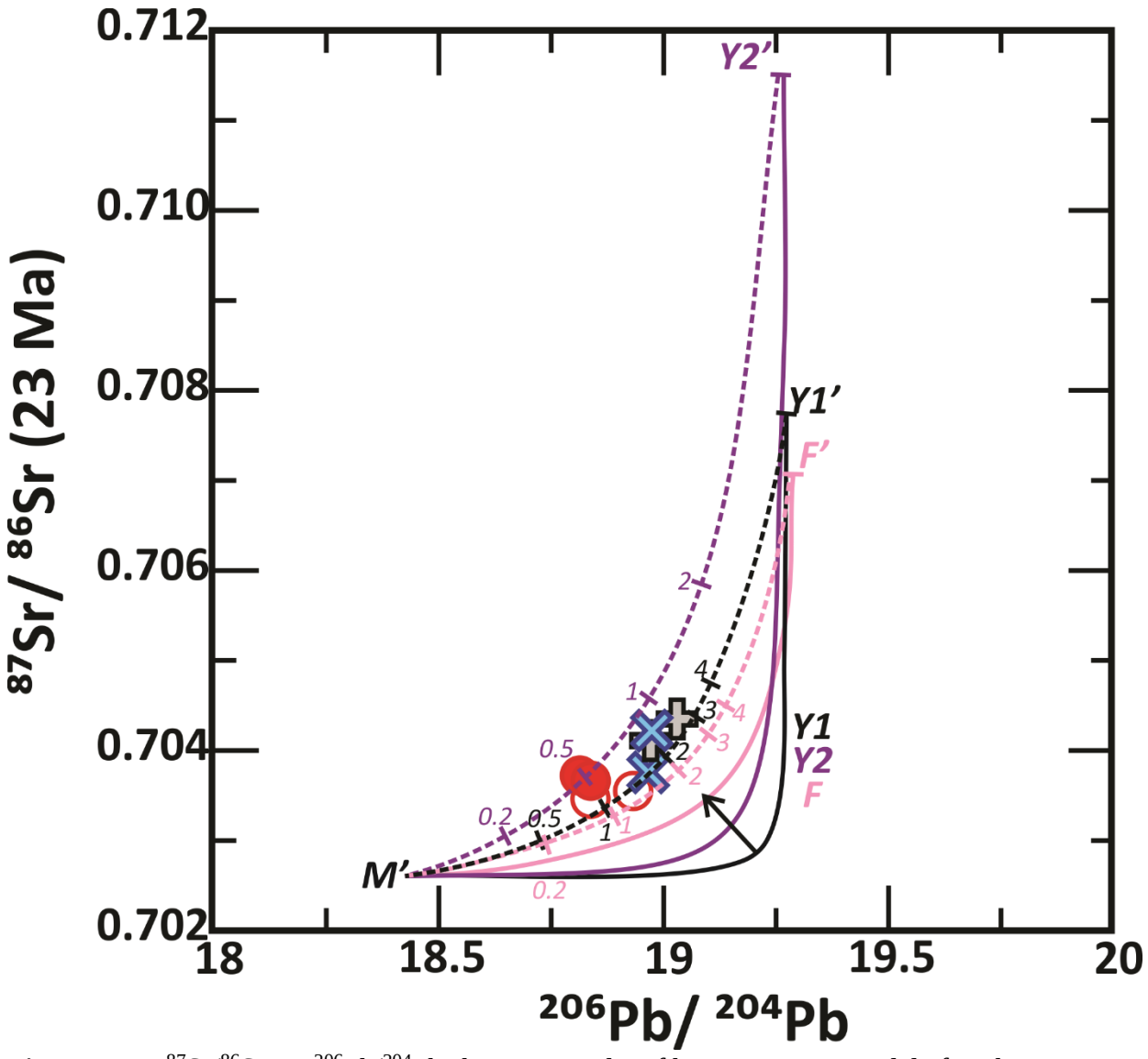

Figure 4.14: $^{87}Sr/^{86}Sr$ vs. $^{206}Pb/^{204}Pb$ showing results of binary mixing model after the adjustment of Pb concentrations in all end-members, as described in the text. The bold lines are before adjustment, and the dashed lines are after adjustment. Isotope ratios are the same as those shown in Table 4-1 and Figures 4.7 to 4.11, and adjustments to Pb concentrations are shown in Table 4-3.

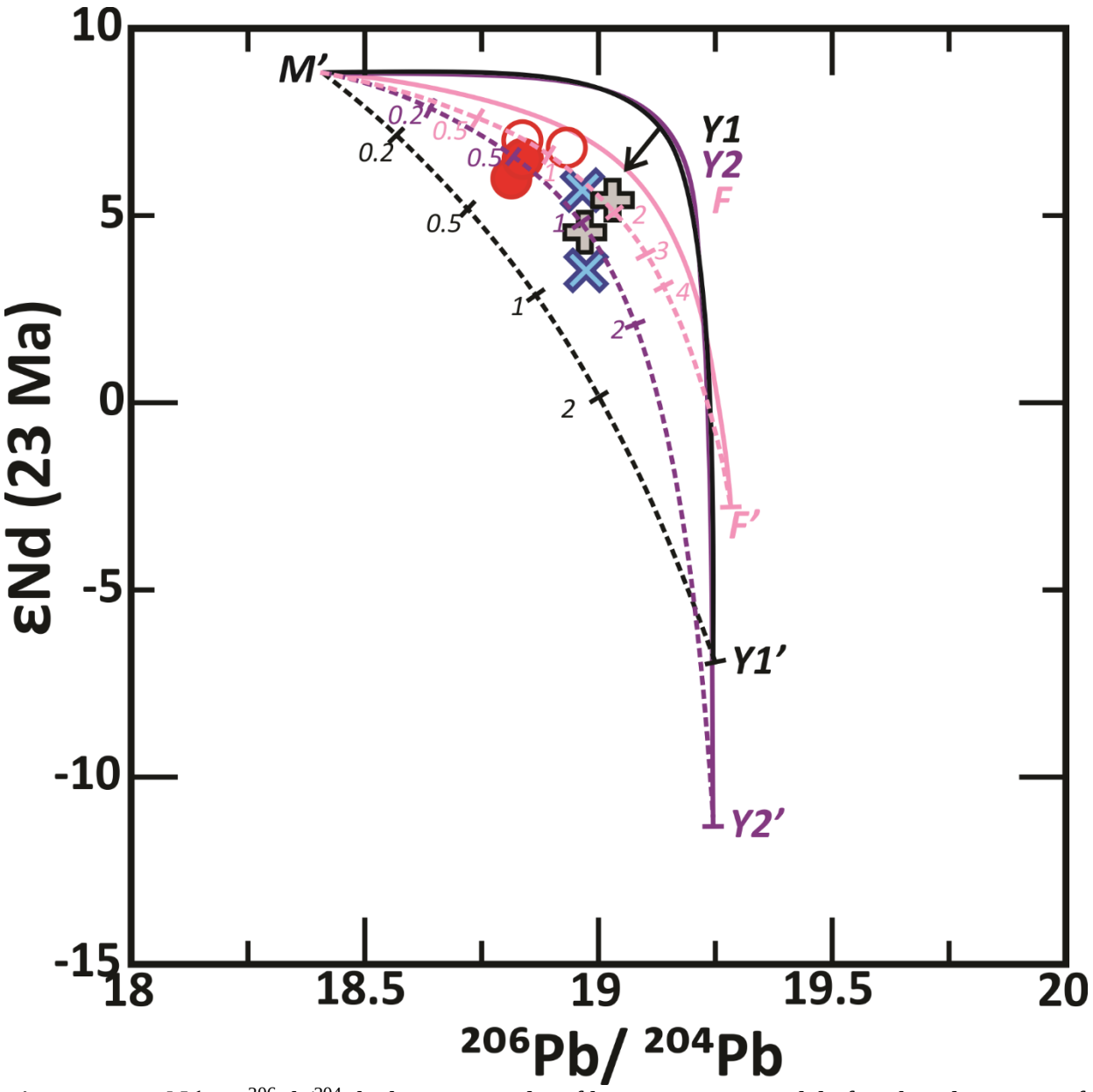

Figure 4.15: εNd vs. $^{206}Pb/^{204}Pb$ showing results of binary mixing model after the adjustment of Pb concentrations in all end-members, as described in the text. The bold lines are before adjustment, and the dashed lines are after adjustment. Isotope ratios are the same as those shown in Table 4-1 and Figures 4.7 to 4.11, and adjustments to Pb concentrations are shown in Table 4-3.

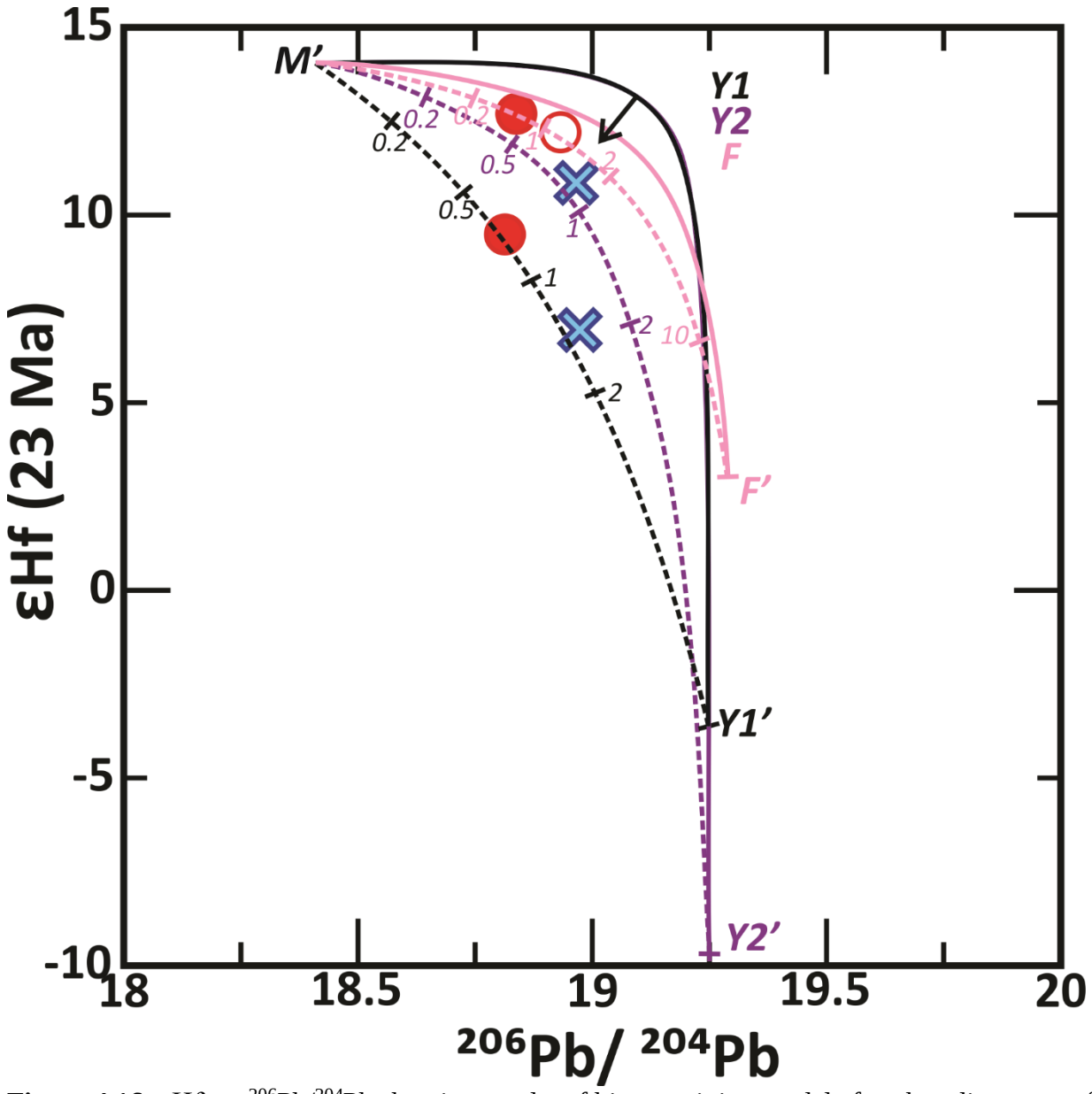

Figure 4.16: εHf vs. $^{206}Pb/^{204}Pb$ showing results of binary mixing model after the adjustment of Pb concentrations in all end-members, as described in the text. The bold lines are before adjustment, and the dashed lines are after adjustment. Isotope ratios are the same as those shown in Table 4-1 and Figures 4.7 to 4.11, and adjustments to Pb concentrations are shown in Table 4-3.

Abbreviation	**M**	**PB**	**Y1**	**Y2**	**F**	**N**	**S**	**PS**	**T**
End-Member	Depleted Mantle[1]	Primitive basalt[2]	Yukon-Tanana granitoid[3]	Yukon-Tanana granitoid[3]	Kahiltna Flysch[3]	Nikolai Greenstone[4]	Siletzia (southern WA)[5]	Modern Pacific Sediment[6]	Talkeetna Arc[7]
$^{87}Sr/^{86}Sr$	0.702583	0.702583	0.70706	0.711535	0.707063	0.703836	0.703535	0.70588	0.706238
Sr (ppm)	9.8	788	169	277	175	239	496	289	112
εNd	8.82	8.82	-6.93	-11.14	-2.79	4.76	4.7	0.62	3.18
Nd (ppm)	0.713	19	43.1	17.9	16.6	14.35	36.94	18.56	6.6
$^{206}Pb/^{204}Pb$	18.41	18.41	19.25	19.25	19.288	19.459	19.41	18.94	
$^{207}Pb/^{204}Pb$	15.501	15.501	15.63	15.68	15.653	15.616	15.599	15.614	
$^{208}Pb/^{204}Pb$	37.86	37.86	39.05	39.15	38.922	39.151	39.125	38.641	
Pb (ppm)	0.023	6	85.7	55.6	5.49	0.95	2.16	10.08	
εHf	14.04	14.04	-3.71	-9.72	3.01	7.36		5.39	
Hf (ppm)	0.199	2.71[8]	9.62[8]	3.97[8]	3.71[8]	2.66		2.84	

[1] Isotope ratios from Chauvel and Blichert-Toft (2011), elemental concentrations Salters and Stracke (2004); [2]Isotope ratios from Chauvel and Blichert-Toft (2011), elemental concentrations from Preece (1997); [3]Aleinikoff et al. (2007); [4]Greene et al. (2008); [5]Chan et al. (2012); [6]Plank and Langmuir (1998) and Vervoort et al. (2005); [7]Rioux et al. (2007); [8]See Table 4-2 for how Hf values were derived.

Table 4-1: Isotope values for endmembers used in binary mixing calculations.

	Avg. UCC[1]	Y1	Y2	F	PB[2]
Nd (ppm)	26	43.1	17.9	16.6	19
Hf (ppm)	5.8	**9.62**	**3.99**	**3.71**	**2.71**
Nd/Hf	*4.48*	*4.48*	*4.48*	*4.48*	*7*[3]

Table 4-2: Calculation of Hf concentrations to maintain relevant Nd/Hf ratios. Numbers in bold are the Hf concentrations that maintain the average upper continental crust (UCC) Nd/Hf ratio. [1]UCC values from Rudnick and Gao (2003). [2]Sample 94SJP120 from Preece (1997). [3]Approximate Nd/Hf ratio of SCVF basalts

	PM[1]	M	M'	GLOSS[2]	F	Y1	Y2	F'	Y1'	Y2'
Sr (ppm)	21.1	9.8	9.8	327	175	169	277	169	169	277
Pb (ppm)	0.185	*0.023*	**0.086**	19.9	*5.49*	*85.7*	*55.6*	**10.65**	**10.28**	**16.85**
Sr/Pb	**114**	*426*	**114**	**16.43**	*31.8*	*1.97*	*4.98*	**16.43**	**16.43**	**16.43**

Table 4-3: Adjustment of Pb concentrations to maintain Sr/Pb ratios of PM and GLOSS. [1] PM values from Sun and McDonough (1989). [2]GLOSS values from Plank and Langmuir (1998). Numbers in bold are to highlight relevant Sr/Pb ratios, and the adjusted Pb concentrations that maintain those ratios.

Chapter 5 - Conclusions

1) New geochronologic bedrock data from the ~29–18 Ma SCVF shows arc magmatism was active at ~29 Ma, which pushes back the age of WA initiation by ~3 m.y. from the ~26 Ma K-Ar age of Richter et al. (1990). These bedrock results agree with new detrital U-Pb zircon and detrital $^{40}Ar/^{39}Ar$ volcanic-lithic ages from modern river sediment (Trop et al., 2017; Davis et al., 2017).
2) Geochemical data for the Rocker Creek lavas and domes document subduction-related calc-alkaline magmatism with an apparent adakite-like component at the initiation of the SCVF. This was followed by the emplacement of the intermediate domes, which show a temporal and spatial transition to continued subduction-related magmatism without the adakite-like component (e.g., mantle wedge melting). Another geochemical and spatial shift is recorded by the eruption of the transitional-tholeiitic lavas of the Sonya Creek shield volcano, which show the influence of local intra-arc extension. An additional pulse of calc-alkaline magmatism, represented by the Young Creek lavas and the Border lavas, marked the end of SCVF activity by ~18 Ma.
3) Magma geochemical types found within the SCVF are similar to those from the <5 Ma WA as defined by Preece and Hart (2004). However, rocks with adakite-like affinities apparently only erupted at the initiation of the WA (~22-29 Ma) and during the young WA (<5 Ma) magmatic phase, reflecting one or more tectonic processes that induced anomalous heating of the Yakutat slab and/or mafic lower crust.
4) SCVF Sr-Nd-Pb-Hf radiogenic isotope data are consistent with melting of a depleted mantle source that was affected by terrigenous sediment input, where the sediment was derived from crystalline basement rocks that crop out in south-central Alaska. Isotope binary mixing

models indicate that ~0.2-2% mixing of Cretaceous granitoid-like sediment match the Cabin Creek/Flat Top isotope ratios, while the Rocker Creek/silicic lavas isotope values are consistent with ~0.5-3% mixing between the same endmembers. A simple test of crustal assimilation (e.g., via binary mixing model) indicates that ~10-25% crustal assimilation of primitive WA basalt by the same Cretaceous granitoid samples can explain the isotope ratios of the two rhyolites (SB15-34, 15JB38LA), although a full AFC model would clarify this.

5) Hypabyssal amphibole dacites (map unit "Tp" of Richter, 1976 and "Th" of MacKevett, 1978) were collected from the northern flank of the WA, where they intrude basement rocks of the Wrangellia Composite terrane, and likely represent sub-volcanic intrusions. Adakite-like affinities and ages that overlap with early SCVF activity (~22–29 Ma) suggest that the SCVF and these hypabyssal units represent the initial position and extent of the WA. The initial axis of the WA was north of its current position, and had a <100 km lateral extent if Oligocene to recent motion along the Totschunda is restored. The eastern WA volcanic fields were active immediately following SCVF activity, representing a previously undocumented southward shift in WA magmatism.
6) Temporal and geochemical shifts within the SCVF are correlated with the tectonic implications from other areas; thermochronological research from the rapidly uplifting and exhuming St. Elias syntaxis to the south, the modern Yakutat flat-slab region to the west, and geophysical studies of the southern Alaskan margin. The Yakutat microplate began to subduct at ~35–30 Ma, and the thicker crust of the wedge-shaped oceanic plateau began to subsequently couple with the upper plate, transferring stress to inboard strike-slip faults and initiating transtensional mantle melting that created the ~23–18 Ma Sonya Creek shield volcano. By ~18 Ma, SCVF activity ceased, and the locus of WA magmatism shifted to the

south and east, where transtension and dextral strike-slip faults served as conduits for "leaky transform" volcanism in the Yukon. From ~12 Ma – Holocene time, WA magmatism migrated generally northwestward from the central WA, and included volcanism at Mounts Blackburn, Sanford, Drum, and Wrangell, which is historically active. Mount Churchill does not fit the pattern of northwestward migration, and adakite-like lavas there suggest modern melting of the Yakutat slab.

7) This study of the long-lived and geochemically diverse Sonya Creek Volcanic Field elucidates the effects of Cenozoic south-central Alaskan tectonics on the initiation of the Wrangell Arc specifically, and more generally demonstrates the sensitivity of arc magmatic geochemistry to tectonic changes in an arc-transform transition zone.

References

Albarède, F., Simonetti, A., Vervoort, J.D., Blichert-Toft, J., and Abouchami, W., 1998, A Hf-Nd isotopic correlation in ferromanganese nodules: Geophysical Research Letters, v. 25, p. 3895-3898.

Aleinikoff, J.N. and Nokleberg, W.J., 1985, Age of Devonian igneous-arc terranes in the northern Mount Hayes quadrangle, eastern Alaska Range: *in* Bartsch-Winkler, S. ed, The United States Geological Survey in Alaska: accomplishments during 1984, United States Geological Survey, Circular 967, p. 44-49.

Aleinikoff, J.N., Dusel-Bacon, C., Foster, H.L., and Nokleberg, W.J., 1987, Lead isotopic fingerprinting of tectonostratigraphic terranes, east-central Alaska: Canadian Journal of Earth Sciences, v. 24, p. 2089-2098.

Aleinikoff, J.N., Farmer, G.L., Rye, R.O., and Nokleberg, W.J., 2000, Isotopic evidence for the sources of Cretaceous and Tertiary granitic rocks, east-central Alaska: inplications for the tectonic evolution of the Yukon-Tanana Terrane: Canadian Journal of Earth Sciences, v. 37, p. 945-956.

Arculus, R.J., Lapierre, H., and Jaillard, E., 1999, Geochemical window into subduction and accretion processes: Raspas metamorphic complex, Ecuador: Geology, v. 27, p. 547-550.

Arkle, J.C., Armstrong, P.A., Haeussler, P.J., Prior, M.G., Hartman, S., Sendziak, K.L., and Brush, J.A., 2013, Focused exhumation in the syntaxis of the western Chugach Mountains and Prince William Sound, Alaska: Geological Society of America Bulletin, v. 125, p. 776-793.

Barker, F., Evans, B.W., Hill, M.D., Irving, A.J., Lull, J.S., Nokleberg, W.J., and Pallister, J.S., 1990, Table of elemental abundances of some accreted rocks of Alaska: United States Geological Survey Open Report 90-291.

Bauer, M.A., Pavlis, G.L., and Landes, M., 2014, Subduction geometry of the Yakutat terrane, southeastern Alaska: Geosphere, v. 10, p. 1161–1176.

Beard, J.S., and Barker, F., 1989, Petrology and tectonic significance of gabbros, tonalites, shoshonites, and anorthosites in a Late Paleozoic arc-root complex in the Wrangellia terrance, southern Alaska: Journal of Geology, v. 97, p. 667-683.

Berg, H.C., Jones, D.L., and Richter, D.H., 1972, The Gravina-Nutzotin Belt-Tectonic significance of an Upper Mesozoic sedimentary and volcanic sequence in southern and southeastern Alaska: U.S. Geological Survey Professional Paper 800–D, p. D1–D24.

Berger, A.L., Spotila, J.A., Chapman, J.B., Pavlis, T.L., Enkelmann, E., Ruppert, N.A., and Buscher, J.T., 2008a, Architecture, kinematics, and exhumation of a convergent orogenic wedge: A thermochronological investigation of tectonic-climatic interactions within the central St. Elias orogen, Alaska: Earth and Planetary Science Letters, v. 270, p. 13-24.

Berger, A. L., Gulick, S.P.S., Spotila, J.A., Upton, P., Jaeger, J.M., Chapman, J.B., Worthington, L.A., Pavlis, T.L., Ridgway, K.D., Willems, B.A., and McAleer, R.J., (2008b), Quaternary tectonic response to intensified glacial erosion in an orogenic wedge: Nature Geoscience, v. 1, p. 793–799.

Benowitz, J.A., Layer, P., Armstrong, P., Perry, S., Haeussler, P., Fitzgerald, P., and VanLaningham, S., 2011, Spatial variations in focused exhumation along a continental-scale strike-slip fault: The Denali fault of the eastern Alaska Range: Geosphere, v. 7, p. 455–467.

Benowitz, J.A., Davis, K.N., Brueseke, M.E., Trop, J.M., and Layer, P., 2014, Investigating the Lost Arc: geological constraints of ~25 million years of magmatism along an arc-transform junction, Wrangell volcanic belt, Alaska: Abstracts with Programs, 2014 Annual Meeting, Geological Society of America.

Benowitz, J. A., Layer, P. W., & Vanlaningham, S., 2014, Persistent long-term (c. 24 Ma) exhumation in the Eastern Alaska Range constrained by stacked thermochronology, *in*, Jourdan, F., Mark, D. F. & Verati, C., eds., Advances in $^{40}Ar/^{39}Ar$ Dating: from Archaeology to Planetary Sciences: Geological Society, London, Special Publications, 385, p. 225-243.

Brennan, P., Ridgway, K.D., Witmer, J., and Valencia, V.A., 2009, Stratigraphy and provenance of the Poul Creek Formation in the Chugach-St. Elias Mountains, southeast Alaska: Insights on Eocene-Miocene sedimentation in the Gulf of Alaska: Geological Society of America Abstracts with Programs, v. 41, p. 306.

Bristol, I.M., Trop, J.M., Benowitz, J.A., and Davis, K.N., 2017, Major Miocene paleodrainage in south-central Alaska: sedimentology, depositional age, and provenance of strata exposed in the southwestern Talkeetna Mountains: Geological Society of America Abstracts with Programs, v. 49.

Brueseke, M. E., Benowitz., J.A., Trop, J.M., Davis, K.D., and Layer, P.W., 2015, New geochemical and age constraints on the initiation of the lost arc, Wrangell Volcanic Belt, Alaska: Abstracts with Programs, 2015 Cordilleran Meeting, Geological Society of America.

Borg, L.E., Clynne, M.A., and Bullen, T.D., 1997, The variable role of slab-derived fluids in the generation of a suite of primitive calc-alkaline lavas from the southernmost cascades, California: The Canadian Mineralogist, v. 35, p. 425-452.

Bouvier, A., Vervoort, J.D., and Patchett, P.J., 2008, The Lu-Hf and Sm-Nd isotopic composition of CHUR: Constraits from unequilibrated chondrites and implications for the bulk composition of terrestrial planets: earth and Planetary Science Letters, v. 273, p. 48-57.

Carlson, R.W. and Hart, W.K., 1987, Crustal genesis on the Oregon Plateau: Journal of Geophysical Research, v., 92, p. 6191-6206.

Castillo, P.R., 2012, Adakite petrogenesis: Lithos, v. 134-135, p. 304-316.

Chan, C.F., Tepper, J.H., and Nelson, B.K., 2012, Petrology of the Grays River volcanics, southwest Washington: Plume-influenced slab window magmatism in the Cascadia forearc: Geological Society of America Bulletin, v. 124, p. 1324-1338.

Chauvel, C., and Blichert-Toft, J., 2001, A hafnium isotope and trace element perspective on melting of the depleted mantle, Earth and Planetary Science Letters, v. 190, p. 137-151.

Chiaradia, M., 2015, Crustal thickness control on Sr/Y signatures of recent arc magmas: An Earth scale perspective: Scientific Reports, v. 5, p. 1-5.

Christeson, G.L., Van Avendonk, H.J.A., Gulick, S.P.S., Reece, R.S., Pavlis, G.L., and Pavlis, T.L., 2010, Moho interface beneath Yakutat terrane, southern Alaska: Journal of Geophysical Research: Solid Earth, v. 118, p. 5084-5097.

Christie-Blick, N., and Biddle, K.T., 1985, Deformation and basin formation along strike-slip faults: *in* Biddle, K.T., and Christie-Blick, N., eds., Strike-slip deformation, Basin formation, and Sedimentation, Society of Economic Paleontologists and Mineralogists Special Publication number 37, p. 1-34.

Clague, J.J., Evans, S.G., Rampton, V.N., and Woodsworth, G.J., 1995, Improved age estimates for the White River and Bridge River tephras, western Canada: Canadian Journal of Earth Sciences, v. 32, p. 1172-1179.

Clift, P.D., Draut, A.E., Kelemen, P.B., Blusztajn, J., and Greene, A., 2005, Stratigraphic and geochemical evolution of an oceanic arc upper crustal section: The Jurassic Talkeetna Volcanic Formation, south-central Alaska: Geological Society of America Bulletin, v. 117, p. 902-925.

Cobbett, R., 2012. Bedrock geology along the Duke River fault near Bullion Creek, Yukon (part of NTS 115G/02): Yukon Geological Survey, Open File 2013-5, scale 1: 10,000.

Cobbett, R., 2013a. Bedrock geology along the Duke River fault near Hoge Creek, Yukon (part of NTS 115G/05): Yukon Geological Survey, Open File 2013-6, scale 1: 10,000.

Cobbett, R., 2013b. Bedrock geology along the Duke River fault near Squaw Creek, Yukon and British Columbia (part of NTS 115A/03 and 114P/14): Yukon Geological Survey, Open File 2013-1, scale 1: 10,000.

Cobbett, R., Israel, S., Mortenson, J., Joyce, N., and Crowley, J., 2017, Structure and kinematic evolution of the Duke River fault, southwestern Yukon: Canadian Journal of Earth Science, v. 54, p. 322-344.

Colpron, M., Israel, S., Murphy, D., Pigage, L., and Moynihan, D., 2016, Yukon bedrock geology map; Yukon Geological Survey, Open File 2016-1, scale 1: 1,000,000, map and legend.

Cook, J. P., 1995, Characterization and Distribution of Obsidian in Alaska: Arctic Anthropology, v.32, p.92-100.

Davis, K.D., Benowitz, J.A., Layer, J.T., and Brueseke, M.E., 2017, Dating the Lost Arc: Constraining the timing of initiation of the Wrangell Arc with a new $^{40}Ar/^{39}Ar$ geochronology approach on modern river detrital lithic grains: Abstracts with Programs, 2017 Cordilleran Meeting, Geological Society of America.

Defant, M.J., and Drummond, M.S., 1990, Derivation of some modern arc magmas by melting of young subducted lithosphere: Nature, v. 347, p. 662-665.

Defant, M.J., Richerson, M., De Boer, J.Z., Stewart, R.H., Maury, R.C., Bellon, H., Drummond, M.S., Feigenson, M.D., and Jackson, T.E., 1991, Dacite genesis via both slab melting and differentiation: petrogenesis of La Yeguada volcanic complex, Panama: Journal of Petrology, v. 32, p. 1101-1142.

Dodds, C.J., and Campbell, R.B., 1988, Potassium-argon ages of mainly intrusive rocks in the St. Elias Mountains, Yukon and British Columbia: Geological Survey of Canada Paper 87-16, 43 p.

Doser, D.I., and Lomas, R., 2000, The transition from strike-slip to oblique subduction in southeastern Alaska from seismological studies: Tectonophysics, v. 316, p. 45–6.

Doser, D.I., 2014, Seismicity of Southwestern Yukon, Canada, and its relation to slip transfer between the Fairweather and Denali fault systems: Tectonophysics, v. 611, p. 121-129.

Drake, M. J., 1975, The oxidation state of europium as an indicator of oxygen fugacity: Geochimica et Cosmochimicha Acta, v. 39, p. 55-64.

Drake, M.J., and Weill, D.F., 1975, Partition of Sr, Ba, Ca, Y, Eu^{2+}, Eu^{3+}, and other REE between plagioclase feldspar and magmatic liquid: an experimental study: Geochimica et Cosmochimicha Acta, v. 39, p. 689-712.

Donnelly-Nolan, J.M., Grove, T.L., Lanphere, M.A., Champion, D.E., and Ramsey, D.W., 2008, Eruptive history and tectonic setting of Medicine Lake Volcano, a large rear-arc volcano in the southern Cascades: Journal of Volcanology and Geothermal Research, v. 177, p. 313-328.

Dunn, C.A., Enkelmann, E., Ridgway, K.D., and Allen, W.K., 2017, Source to sink evaluation of sediment routing in the Gulf of Alaska and Southeast Alaska: A thermochronometric perspective: Journal of Geophysical Research: Earth Surface, v. 122, p. 711-734.

Eberhart-Phillips, D., and 28 others, 2003, The 2002 Denali fault earthquake, Alaska: A large magnitude, slip-partitioned event: Science, v. 300, p. 1113–1118.

Eberhart-Phillips, D., Christensen, D.H., Brocher, T.M., Hansen, R., Ruppert, N.A., Haeussler, P.J., and Abers, G.A., 2006, Imaging the transition from Aleutian subduction to Yakutat

collision in central Alaska with local earthquakes and active source data: Journal of Geophysical Research, v. 111.

Edwards, B.R., and Russell, J.K., 1999, Northern Cordilleran volcanic province: A northern Basin and Range?: Geology, v. 27, p. 243-246.

Edwards, B.R., and Russell, J.K., 2000, Distribution, nature, and origin of Neogene-Quaternary magmatism in the northern Cordilleran volcanic province, Canada: GSA Bulletin, v. 112, p. 1280-1295.

Eiché, G.E., Francis, D.M., and Ludden, J.N., 1987, Primary alkaline magmas associated with the Quaternary Alligator Lake volcanic complex, Yukon Territory, Canada: Contributions to Mineralogy and Petrology, v. 95, p. 191-201.

Elliott, J.L., Larsen, C.F., Freymueller, J.T., Motyka, R.J., 2010, Tectonic block motion and glacial isostatic adjustment in southeast Alaska and adjacent Canada constrained by GPS measurements: Journal of Geophysical Research, v. 115, 21 pages.

Enkelmann, E, Garver, J.I., and Pavlis, T.L., 2008, Rapid exhumation of ice-covered rocks of the Chugach-St. Elias orogen, southeast Alaska: Geology, v. 36, p. 915-918.

Enkelmann, E., Zeitler, P.K., Garver, J.I., Pavlis, T.L., and Hooks, B.P., 2010, The thermochronological record of tectonic and surface process interaction at the Yakutat-North American collision zone in southeast Alaska: American Journal of Science, v. 310, p. 231–260.

Enkelmann, E., Piestrzeniewicz, A., Falkowski, S., Stübner, K., and Ehlers, T.A., 2017, Thermochronology in southeast Alaska and southwest Yukon: Implications for North American Plate response to terrane accretion: Earth and Planetary Science Letters, v. 457, p. 348–358.

Engebretson, D.C., Cox, A., and Gordon, R.G., 1985, Relative motions between oceanic and continental plates in the Pacific basin: Special Paper-Geologic Society of America, v. 206, p. 1-59.

Eyles, C.H., and Eyles, N., 1989, The upper Cenozoic White River “tillites” of southern Alaska: Subaerial slope and fan-delta deposits in a strike-slip setting: Geological Society of America Bulletin, v. 101, p. 1091–1102.

Falkowski, S. and Enkelmann, E., 2016, Upper-crustal cooling of the Wrangellia composite terrane in the northern St. Elias Mountains, western Canada: Lithosphere, v. 8, 0. 359-378.

Falkowski, S., Enkelmann, E., Ehlers, T., 2014, Constraining the area of rapid and deep-seated exhumation at the St. Elias syntaxis, Southeast Alaska, with detrital zircon fission-track analysis: Tectonics, v. 33, p. 597-616.

Falkowski, S., Enkelmann, E., Drost, K., Pfänder, J., Stübner, K., and Ehlers, T.A., 2016, Cooling history of the St. Elias syntaxis, southeast Alaska, revealed by geochronology and thermochronology of cobble-sized glacial detritus: Tectonics, v. 35, p, 447-468.

Ferrari, L., Petrone, C.M., and Francalanci, L., 2001, Generation of oceanic-island basalt-type volcanism in the western Trans-Mexican volcanic belt by slab rollback, asthenosphere infiltration, and variable flux melting: Geology, v. 29, p. 507-510.

Fitch, T.J., 1972, Plate convergence, transcurrent faults, and internal deformation adjacent to southeast Asia and the western Pacific: Journal of Geophysical Research, v. 77, p. 4432-4460.

Finzel, E.S., Trop, J.M., Ridgway, K.D., and Enkelmann, E., 2011, Upper plate proxies for flat-slab subduction processes in southern Alaska: Earth and Planetary Science Letters, v. 303, p. 348–360.

Finzel, E.S., Ridgway, K.D., Trop, J.M., 2015, Provenance signature of changing plate boundary conditions along a convergent margin: Detrital record of spreading-ridge and flat-slab subduction processes, Cenozoic forearc basins, Alaska: Geosphere, v. 11.

Finzel, E.S., Enkelmann, E., Falkowski, S., Hedeen, T., 2016, Long-term fore-arc basin evolution in response to changing subduction styles in southern Alaska: Tectonics, v. 35, p. 1735-1759.

Fletcher, H.J., and Freymueller, J.T., 2003, New constraints on the motion of the Fairweather fault, Alaska, from GPS observations: Geophysical Research Letters, v. 30, p. 1139-1142.

Fuis, G.S., Moore, T.E., Plafker, G., Brocher, T.M., Fisher, M.A., Mooney, W.D., Nokleberg, W.J., Page, R.A., Beaudoin, B.C., Christensen, N.I., Levander, A.R., Lutter, W.J., Saltus, R.W., and Ruppert, N.A., 2008, Trans-Alaska Crustal Transect and continental evolution involving subduction underplating and synchronous foreland thrusting: Geology, v. 36, p. 267–270.

Galer, S.J.G. and Abouchami, W., 1998, Practical application of lead triple spiking for correction of instrumental mass discrimination: Mineralogical Magazine, v. 62A, p. 491-492.

Gill, J.B., 1981, Orogenic andesite and plate tectonics: Springer-Verlag, New York, 390 pp.

Godfrey, L.V., 2002, Temporal changes in the lead isotopic composition of red clays: comparison with ferromanganese crust records: Chemical Geology, v. 185, p. 241-254.

Grabowski, D.M., Enkelmann, E., and Ehlers, T.A., 2013, Spatial extent of rapid denudation in the glaciated St. Elias syntaxis region, SE Alaska: Journal of Geophysical Research: Earth Surface, v. 118, p. 1921-1938.

Greene, A.R., Scoates, J.S., and Weis, D., 2008, Wrangellia flood basalts in Alaska: A record of plume-lithosphere interaction in a Late Triassic accreted oceanic plateau: Geochemistry, Geophysics, Geosystems, v. 9, 34 p.

Greene, A.R., Scoates, J.S., Weis, D., and Israel, S., 2009, Geochemistry of Triassic flood basalts from the Yukon (Canada) segment of the accreted Wrangellia oceanic plateau: Lithos, v. 110, p. 1-19.

Gulick, S.P.S., Reece, R.S., Christeson, G.L., Van Avendonk, H., Worthington, L.L., and Pavlis, T.L., 2013, Seismic images of the transition fault and the unstable Yakutat-Pacific-North American triple junction: Geology, v. 41, p. 571–574, doi: 10.1130/G33900.1.

Gutscher, M-A., Maury, R., Eissen, J-P., and Bourdon, E., 2000, Can slab melting be caused by flat subduction?: Geology, v. 28, p. 535-538.

Haeussler, P.J., 2008, An overview of the neotectonics of interior Alaska: Far-field deformation from the Yakutat microplate collision, *in* Freymueller, J.T., et al., eds., Active tectonics and seismic potential of Alaska: American Geophysical Union Geophysical Monograph 179, p. 269-285.

Haschke, M.R., Scheuber, E., Günther, A., and Reutter, K.J., 2002, Evolutionary cycles during the Andean orogeny: repeated slab breakoff and flat subduction?: Terra Nova, v. 14, p. 49-55.

Hildreth, W. and Moorbath, S., 1988, Crustal contributions to arc magmatism in the Andes of Central Chile: Contributions to Mineralogy and Petrology, v. 98, p. 455-489.

Hyeong, K., Kim, J., Pettke, T., Yoo, C.M., and Hur, S.D., 2011, Lead, Nd, and Sr isotope records of pelagic dust: Source indication versus the effects of dust extraction procedures and authigenic mineral growth: Chemical Geology, v. 286, p. 240-251.

Irvine, T.N., and Baragar, W.R.A., 1971, A guide to the chemical classification of the common volcanic rocks: Canadian Journal of Earth Sciences, v. 8, p. 523-548.

Irving, A.J. and Frey, F.A., 1984, Trace element abundances in megacrysts and their host basaltsL constraints on partition coefficients and megacryst genesis: Geochimica et Cosmochimica Acta, v. 48, p. 1201-1221.

Israel, S., Tizzard, A., and Major, J., 2005, Geological map of the Duke River area (Parts of NTS 115G/2, 3,5,6,7), Yukon: Yukon Geological Survey, Open File 2005-11, scale 1: 50,000.

Israel, S., Cobbett, R., and Fozard, C., 2007a, Bedrock geology of the Miles Ridge area, Yukon (parts of NTS 115F/15, 16 and 115K/1, 2): Yukon Geological Survey, Open File 2007-7, 1: 50,000.

Israel, S., Cobbett, R., and Fozard, C., 2007b Bedrock geology of the Koidern River area, Yukon (parts of NTS 115F/9, 15, 16 and 115G/12): Yukon Geological Survey, Open File 2007-8, scale 1: 50,000.

Israel, S. and Cobbett, R., 2008a, Bedrock geology of the Silver Creek area, Yukon (NTS 115A/3 and parts of 115A/6): Yukon Geological Survey, Open File 2008-21, scale 1: 50,000.

Israel, S. and Cobbett, R., 2008b, Kluane Ranges bedrock geology, White River area (Parts of NTS 115F/9, 15 and 16; 115G/12 and 115K/1, 2), *in* Yukon Exploration and Geology 2007, D.S. Emond, L.R. Blackburn, R.P. Hill and L.H. Weston (eds.), Yukon Geological Survey, p. 153-167.

Israel, S., Colpron, M., Cubley, J., Moynihan, D., Murphy, D.C., and Reif, C., 2014, Preliminary bedrock geology of the Mt. Decoeli area (parts of NTS 115A/12,13 and 115B/9,16): Yukon Geologic Survey, Open File 2014-18, scale 1: 50,000.

Jadamec, M.A., 2016, Insights on slab-driven mantle flow from advances in three-dimensional modeling: Journal of Geodynamics, v. 100, p. 51-70.

Jicha, B.R., Singer, B.S., Brophy, J.G., Fournelle, J.H., Johnson, C.M., Beard, B.L., Lapen, T.J., and Mahlen, N.J., 2004, Variable impact of the subducted slab on Aleutian Island Arc magma sources: evidence from Sr, Nd, Pb, and Hf isotopes and trace element abundances: Journal of Petrology, v. 45, p. 1845-1875.

Johnson, D.M., Hooper, P.R. and Conrey, R.M. 1999, XRF analysis of rocks and minerals for major and trace elements on a single low dilution Li-tetraborate fused bead: Advances in X-ray Analysis, v. 41, p. 843-867.

Kalbas, J.L., Ridgway, K.D., and Gehrels, G.E., 2008, Stratigraphy, depositional systems, and provenance of the Lower Cretaceous Kahiltna assemblage, western Alaska Range: basin development in response to oblique collision, *in* Ridgway, K.D., Trop, J.M., O'Neill, J.M., and Glen, J.M.G., eds., Tectonic growth of a collisional continental margin: crustal evolution of southern Alaska: Geological Society of America Special Paper, p. 307-344.

Karlsi, O., Ketenci, M., Uysal, I., Dokuz, A., Aydin, F., Chen, B., Kandemir, R., and Wijbrans, J., 2011, Adakite-like granitoid porphyries in the Eastern Pontides, NE Turkey: Potential parental melts and geodynamic implications: Lithos, v. 127, p. 354-372.

Knaack, C., Cornelius, S. and Hooper, P.R., 1994, Trace element analysis of rocks and minerals by ICP-MS: Open File Report, Department of Geology. Pullman: Washington State University.

Keskin, M., 2003, Magma generation by slab steepening and breakoff beneath a subduction-accretion complex: An alternative model for collision-related volcanism in Eastern Anatolia, Turkey: Geophysical Research Letters, v. 30.

Keskin, M., Pearce, J.A., Kempton, P.D., Greenwood, P., 2006, Magma-crust interactions and magma plumbing in a postcollisional setting: Geochemical evidence from the Erzurum-Kars volcanic plateau, eastern Turkey. *In*: Y. Dilek and S. Pavlides, *Postcollisional Tectonics and Magmatism in the Mediterranean Region and Asia*, Geological Society of America Special Papers, v. 409, p. 475-505.

Lassiter, J.C., DePaolo, D.J., and Mahoney, J.J., 1995, Geochemistry of the Wrangellia flood basalt province: Implications for the role on continental and oceanic lithosphere in flood basalt genesis: Journal of Petrology, v. 36, p. 983-1009.

Layer, P.W., Hall, C.M. and York, D., 1987, The derivation of $^{40}Ar/^{39}Ar$ age spectra of single grains of hornblende and biotite by laser step heating: Geophysical Research Letters, v. 14, p. 757-760.

Layer, P. W., 1994, $^{40}Ar/^{39}Ar$ dating of Eocene obsidian from the BatzaTena archeological site, west-central Alaska, *in* M.A. Lanphere, G.B. Dalrymple, and B.D. Turin, eds., Abstracts of the Eighth International Conference on Geochronology, Cosmochronology and Isotope Geology: U.S. Geological Survey Circular 1107, p. 187.

Layer, P.W., 1995, Laser $^{40}Ar/^{39}Ar$ dating of obsidian from Alaskan archeological sites as an aid in the determination of artifact sources: Abstracts with Programs, 1995 Cordilleran Meeting, Geological Society of America.

Le Bas, M.J., Le Maitre, R.W., Streckeisen, A., and Zanettin, B.A., 1986, Chemical classification of volcanic rocks based on the total alkali-silica diagram: Journal of Petrology, v. 27, p. 745-750.

Le Maitre, R.W., 1976, Some problems of the projection of chemical data into mineralogical classifications: Contributions to Mineralogy and Petrology, v. 56, no. 2, p. 181-189.

Lee, H.Y., Chung, S.L., and Yang, H.M., 2016, Late Cenozoic volcanism in central Myanmar: Geochemical characteristics and geodynamic significance: Lithos, v. 245, p. 174-190.

Lerbekmo, J.F., and Campbell, F.A., 1969, Distribution, composition, and source of the White River Ash, Yukon Territory: Canadian Journal of Earth Sciences, v. 6, p. 109-116.

Lerbekmo, J.F., 2008, The White River Ash: largest Holocene Plinian tephra: Canadian Journal of Earth Sciences, v. 45, p. 693-700.

Lipman, P. W., 2000, Central San Juan caldera cluster: regional volcanic framework, *in* Bethke, P. M., and Hay, R. L., eds., Ancient Lake Creede: Its volcano-tectonic setting, history of sedimentation, and relation to mineralization in the Creede Mining District: Boulder, Colorado, Geological Society of America Special Paper 346.

Luhr, J., 2000, The geology and petrology of Volcan San Juan Nayarit, Mexico and the compositionally zoned Tepic pumic: Journal of Volcanology and Geothermal Research, v. 95, p. 109-156.

McAleer, R. J., Spotila, J. A., Enkelmann, E., and Berger, A. L., 2009, Exhumation along the Fairweather fault, southeast Alaska, based on low-temperature thermochronometry: Tectonics, v. 28, p. TC1007.

MacKevett, E.M., Jr., 1978, Geologic map of the McCarthy quadrangle, Alaska: U.S. Geological Survey Miscellaneous Investigation Series I-1032, scale 1: 250,000.

Manuszak, J.D., Trop, J.M., Ridgway, K.D., and Gehrels, G.E., 1999, Mesozoic basin development along the outboard and inboard margins of an accreted island arc, southern Alaska: Geological Society of America Abstracts with Programs, v. 31, p. A-296.

Manuszak, J.D. and Ridgway, K.D., 2000, Collisional basin development and deformation along a suture zone, Late Jurassic-early Cretaceous Nutzotin basin, east-central Alaska: Geological Society of America Abstracts with Programs, v. 32, p. A-108.

Manuszak, J.D., Ridgway, K.D., Trop, J.M., and Gehrels, G.E., 2007, Sedimentary record of the tectonic growth of a collisional continental margin: Upper Jurassic–Lower Cretaceous Nutzotin Mountains sequence, eastern Alaska Range, Alaska: *in* Ridgway, K.D., et al., eds., Tectonic growth of a collisional continental margin: Crustal evolution of southern Alaska: Geological Society of America Special Paper 431, p. 345–377

Matmon, A., Schwartz, D.P., Haeussler, P.J., Finkel., R., Kienkaemper, J.J., Stenner, H.D., and Dawson, T.E., 2006, Denali fault slip rates and Holocene-late Pleistocene kinematics of central Alaska: Geology, v. 34, p. 645-644.

Maury, R.C., Pubellier, M., Rangin, C., Wulput, L., Cotton, J., Socquet, A., Bellon, H., Gullaud, J.P., and Htun, H.M., 2004, Quaternary calc-alkaline and alkaline volcanism in a hyper-oblique convergence setting, central Myanmar and western Yunnan: Bulletin de la Société Géologique de France, v. 175, p. 461-472.

McDougall, I. and Harrison, T.M., 1999, Geochronology and Thermochronology by the $^{40}Ar/^{39}Ar$ method-2nd ed, Oxford University Press, New York, 269pp.

McLennan, S.M., Taylor, S.R., McCulloch, M.T., and Maynard, J.B., 1990, Geochemical and Nd-Sr isotopic composition of deep-sea turbidites: Crustal evolution and plate tectonic associations: Geochimica et Cosmochimica Acta, v. 54, p. 2015-2050.

McGimsey, R.G., Richter, D.H., DuBois, G.D., Miller, T.P., 1992, A postulated new source for the White River Ash, Alaska, *in* Bradley, D.C., and Ford, A.B., eds., Geologic studies in Alaska by the U.S. Geological Survey, 1990: U.S. Geological Survey Bulletin 1999, p. 212-218.

Mertzman, S.A., 2000, K-Ar results from the southern Oregon–northern California Cascade Range: Oregon Geology, v. 62, p. 99–122.

Mertzman, S.A., 2015, XRF laboratory: overview and analytical procedures. http://www.fandm.edu/earth-environment/laboratory-facilities/instrument-use-and-instructions (Accessed 4/15/2017).

Mezger, J.E., Creaser, R.A., Erdmer, P., and Johnston, S.T., 2000, A Cretaceous back-arc basin in the Coast Belt of the northern Canadian Cordillera: evidence from geochemical and neodymium isotope characteristics of the Kluane metamorphic assemblage, southwest Yukon: Canadian Journal of Earth Sciences, v. 38, p. 91-103.

Miller, T.P., and Richter, D.H., 1994, Quaternary volcanism in the Alaska Peninsula and Wrangell Mountains, Alaska, *in* Plafker, G., and Berg, H.C., eds., The Geology of Alaska: Boulder, Colorado, Geological Society of America, The Geology of North America, v. G-1, p. 759–779.

Miyashiro, A., 1974, Volcanic rock series in island arcs and active continental margins: American Journal of Science, v. 274, p. 321-355.

Morter, B.K., Brueseke, M.E., Benowitz, J.A., Trop, J.M., Davis, K., and Layer, P.W., 2016, Linking geochemistry of Cenozoic volcanic clasts from the Wrangell Arc, Alaska, to upper plate and subducting slab tectonic processes: Abstracts with Programs, 2016 Annual Meeting, Geological Society of America.

Münker, C., Weyer, S., Scherer, E. and Mezger, K., 2001, Separation of high field strength elements (Nb, Ta, Zr, Hf) and Lu from rock samples for MC-ICPMS measurements: Geochemistry, Geophysics, Geosystems, v. 2.

Nokleberg, W.J. and Aleinikoff, J.N., 1985, Summary of stratigraphy, structure, and metamorphism of Devonian igneous-arc terranes, northeastern Mount Hayes quadrangle, eastern Alaska Range: *in* Bartsch-Winkler, S. ed, The United States Geological Survey in Alaska: accomplishments during 1984, United States Geological Survey, Circular 967, p. 66-71.

Nye, C.J., 1983, Petrology and Geochemistry of Okmok and Wrangell Volcanoes, Alaska: University of California, Santa Cruz, 125 p.

Page, R.A., Biswas, N.N., Lahr, J.C., and Hulpan, H., 1991, Seismicity of continental Alaska, *in* Slemmons, D.B., et al., eds., Neotectonics of North America: Geological Society of America, Decade of North America map volume 1, p. 47–68.

Park, J., Levin, V., Brandon, M., Lees, J., Peyton, V., Gordeev, E., and Ozerov, A., 2002, A dangling slab, amplified arc volcanism, mantle flow and seismic anisotropy in the Kamchatka plate corner, *in*, Plate Boundary Zones, Stein, S., and Freymueller, J.T., eds., American Geophysical Union, Washington D.C., p. 295-324.

Parker, D.F., Hodges, F.N., Perry, A., Mitchener, M.E., Barnes, M.A., and Ren, M., 2010, Geochemistry and petrology of late Eocene Cascade Head and Yachats Basalt and alkali intrusions of the central Oregon Coast Range, U.S.A., Journal of Volcanology and Geothermal Research, v. 198, p. 311-423.

Patterson, J.J., 2008, Late Holocene land use in the Nutzotin Mountains: Lithic scatters, viewsheds, and resource distribution: Arctic Anthropology, v. 45, p. 114-127.

Pavlis, T.L., Enkelmann, E., Gulick, S.P.S., and Pavlis, G.L., 2014, Introduction: Neogene tectonics and climate-tectonic interactions in the southern Alaska orogeny themed issue: Geosphere, v. 10, p. 1-4.

Peacock, S.M., Rushmer, T, Thompson, A.B., 1994, Partial melting of subducting oceanic crust: Earth and Planetary Science Letters, v. 121, p. 227-244.

Pearce, J.A. and Norry, M.J., 1979, Petrogenetic implications of Ti, Zr, Y, and Nb variations in volcanic rocks: Contributions to Mineralogy and Petrology, v.. 69, p. 33-47.

Pearce, J.A., Harris, N.B.W., and Tindle, A.G., 1984, Trace element discrimination diagrams for the tectonic interpretation of granitic rocks: Journal of Petrology, v. 25, p. 956-983.

Pearce, J.A. Bender, J.F., De Long, S.E., Kidd, W.S.F., Low, P.J., Güner, Y., Saroglu, F., Yilmaz, Y., Moorbath, S., and Mitchell, J.G., 1990, Genesis of collision volcanism in Eastern Anatolia, Turkey: Journal of Volcanology and Geothermal Research, v. 44, p. 189-229.

Petford, N., and Atherton, M., 1996, Na-rich partial melts from newly underplated basaltic crust: the Cordillera Blanca batholith, Peru: Journal of Petrology, v. 37, p. 1491-1521.

Plafker, G., and Berg, H.C., 1994, Overview of the geology and tectonic evolution of Alaska, *in* Plafker, G., and Berg, H. C., eds., The Geology of Alaska: Boulder, Colorado, Geological Society of America, The Geology of North America, v. G-1, pp. 989-1021.

Plank, T. and Langmuir, C., 1998, The chemical composition of subducting sediment and its consequences for the crust and mantle: Chemical Geology, v. 145, p. 325-394.

Portnyagin, M., Bindeman, I., Hoernle, K., and Hauff, F., 2013, Geochemistry of Primitive Lavas of the Central Kamchatka Depression: Magma Generation at the Edge of the Pacific Plate: Volcanism and Subduction: The Kamchatka Region, p. 199–239.

Preece, S.J., 1997, Geochemical variation in the <5 Ma Wrangell Volcanic Field, Alaska with an emphasis on the Skookum Creek Volcanic Complex, PhD thesis, Miami University, Oxford, Ohio.

Preece, S.J., and Hart, W.K., 2004, Geochemical variations in the <5 Ma Wrangell Volcanic Field, Alaska: Implications for the magmatic and tectonic development of a complex continental arc system: Tectonophysics, v. 392, p. 165–191.

Preece, S.J., McGimsey, R.G., Westgate, J.A., Pearce, N.J.G., Hart, W.K., and Perkins, W.T., 2014, Chemical complexity and source of the White River Ash, Alaska and Yukon: Geosphere, v. 10, p. 1020-1042.

Qi, C., Zhao, D.P., and Chen, Y., 2007, Search for deep slab segments under Alaska: Physics of the Earth and Planetary Interiors, v. 165, p. 68–82.

Rapp, R.P., Watson, E.B., and Miller, C.F., 1991, Partial melting of amphibolite/eclogite and the origin of Archean trondhjemites and tonalites: Precambrian Research, v. 51, p.1-25.

Rasic, J.T., Houlette, C., Slobodina, N., Reuther, J., Florey, V., and Speakman, R.J., 2009, A twelve-thousand-year history of obsidian prospecting in eastern Beringia: Geological Society of America Abstracts with Programs, v. 41, p. 679.

Renne, P. R., Mundil, R., Balco, G., Min, K., and Ludwig, K. R., 2010, Joint determination of ^{40}K decay constants and $^{40}Ar*/^{40}K$ for the Fish Canyon sanidine standard, and improved accuracy for $^{40}Ar/^{39}Ar$ geochronology: Geochimica et Cosmochimica Acta, v. 74, p. 5349.

Richter, D.H., and Matson, J.A., 1971, Quaternary faulting in the eastern Alaska Range: Bulletin of the Geological Society of America, v. 82, p. 1529–1540.

Richter, D.H., 1976, Geologic map of the Nabesna quadrangle, Alaska: U.S. Geological Survey Miscellaneous Geological Investigations Series Map I-932, scale 1: 250,000.

Richter, D.H., Smith, J.G., Lanphere, M.A., Dalrymple, G.B., Reed, B.L., and Shew, N., 1990, Age and progression of volcanism, Wrangell volcanic field, Alaska: Bulletin of Volcanology, v. 53, p. 29-44

Richter, D.H., Moll-Stalcup, E.J., Miller, T.P., Lanphere, M.A., Dalrymple, G.B., and Smith, R.L., 1994, Eruptive history and petrology of Mount Drum volcano, Wrangell Mountains, Alaska: Bulletin of Volcanology, v. 56, p. 29–46.

Richter, D.H., Preece, S.J., McGimsey, R.G., and Westgate, J.A., 1995, Mount Churchill, Alaska: source of the late Holocene White River Ash: Canadian Journal of Earth Sciences, v. 32, p. 741–748.

Richter, D.H., Ratté, J.C., Leeman, W.P., and Menzies, M., 2000, Geologic map of the McCarthy D-1 quadrangle, Alaska: U.S. Geological Survey Geologic Investigations Series I-2695, scale 1: 63,360.

Richter, D.H., Preller, C.C., Labay, K.A., and Shew, N.B., 2006, Geologic map of the Wrangell–Saint Elias Park and Preserve, Alaska: U.S. Geological Survey Scientific Investigations Map 2877, scale 1: 350,000.

Ridgway, K.D., Trop, J.M., Nokleberg, W.J., Davidson, C.M., and Eastham, K.R., 2002, Mesozoic and Cenozoic tectonics of the eastern and central Alaska Range: Progressive basin development and deformation in a suture zone: Geological Society of America Bulletin, v. 114, p. 1480-1504.

Rioux, M., Hacker, B., Mattinson, J., Kelemen, P., Blusztajn, J., and Gehrels, G., 2007, Magmatic development of an intra-oceanic arc: High-precision U-Pb zircon and whole-rock isotopic analyses from the accreted Talkeetna arc, south-central Alaska: Geologic Society of America Bulletin, v. 119, p. 1168-1184.

Roddick, J.C., 1978, The application of isochron diagrams in $^{40}Ar/^{39}Ar$ dating: A discussion: Earth and Planetary Science Letters, v. 41, p. 233-244.

Roddick, J.C., Cliff, R.A., and Rex, D.C., 1980, The evolution of excess argon in alpine biotites – a $^{40}Ar/^{39}Ar$ analysis: Earth and Planetary Science Letters, v. 48, p. 185-208.

Rudnick, R.L. and Gao, S., 2003, Composition of the Continental Crust, *in*: Holland, H.D., Turekian, K.K., eds., Treatise on Geochemistry, v. 3, p. 1-64.

Sajona, F.G., Maury, R.C., Bellond, H., Cotten, J., Defant, M.J., and Pubellier, M., 1993, Initiation of subduction and the generation of slab melts in western and eastern Mindanao, Philippines: Geology, v. 21, p. 1007-1010.

Salters, V.J.M., and Stracke, A., 2004, Composition of the depleted mantle: Geochemistry, Geophysics, Geosystems, v. 5, 27 pp.

Sample, J.C., and Karig, D.E., 1982, A volcanic production rate for the Mariana Island arc: Journal of Volcanology and Geothermal Research, v. 13, p. 73-82.

Samson, S.D., McClelland, W.C., Patchett, P.J., Gehrels, G.E., and Anderson, R.G., 1989, Evidence from neodymium isotopes for mantle contributions to Phanerozoic crustal genesis in the Canadian Cordillera: Nature, v. 337, p. 705-709.

Samson, S.D., Patchett, P.J., Gehrels, G.E., and Anderson, R.G., 1990, Nd and Sr isotopic characterization of the Wrangellia Terrane and implications for crustal growth of the Canadian Cordillera: The Journal of Geology, v. 98, p. 749-762.

Samson, S.D., Patchett, P.J., McClelland, W.C., and Gehrels, G.E., 1991, Nd isotopic characterization of metamorphic rocks in the Coast Mountains, Alaskan and Canadian Cordillera: Ancient crust bounded by juvenile terranes: Tectonics, v. 10, p. 770-780.

Shand, S.J., 1943, Eruptive rocks, their genesis, composition, classification, and their relation to ore deposits, with a chapter on meteorites (revised second edition), Thomas Murby & Co.: London, United Kingdom.

Skulski, T., Francis, D., and Ludden, J., 1992, Volcanism in an arc-transform transition zone: the stratigraphy of the St. Clare Creek volcanic field, Wrangell volcanic belt, Yukon, Canada: Canadian Journal of Earth Sciences, v. 29, p. 446–461.

Skulski, T., Francis, D., and Ludden, J., 1991, Arc-transform magmatism in the Wrangell volcanic belt: Geology, v. 19, p. 11–14.

Śliwiński, M., Bąbel, M., Nejbert, K., Olszeska-Nejbert, D., Gąsiewicz, A., Schreiber, B.C., Benowitz, J.A., and Layer, P.W., 2012, Badenian-Sarmatian chronostratigraphy in the Polish Carpathian Foredeep: Paleogeography, Paleoclimatology, Paleoecology, p. 326-328, 12-29.

Snyder, D.C., and Hart, W.K., 2007, The White Mountain Granitoid suite: Isotopic constraints on source reservoirs for Cretaceous magmatism within the Wrangellia Terrane, *in:* Ridgway, K.D., Trop, J.M., O'Neill, J.M., and Glen, J.M.G., eds., Tectonic growth of a collisional continental margin: crustal evolution of southern Alaska: Geological Society of America Special Paper 431, p. 379-399.

Souther, J.G., and Stanciu, C., 1975, Operation Saint Elias, Yukon Territory: Tertiary volcanic rocks, in Report of activities, part A: Geological Society of Canada Paper 74–1A, p. 39–41.

Stern, R.J., 2002, Subduction Zones, Reviews of Geophysics, v. 40, p. 1012

Stevenson, A.J., Scholl, D.W., and Vallier, T.L., 1983, Tectonic and geologic implications of the Zodiac fan, Aleutian Abyssal Plain, northeast Pacific: Geological Society of America Bulletin, v. 94, p. 259-273.

Stevenson, A.J. and Embley, R., 1987, Deep-sea fan bodies, terrigenous turbidite sedimentation, and petroleum geology, Gulf of Alaska: Earth Science Series, v. 6, p. 503-522.

Stolber, R.E., and Carr, M.J., 1974, Quaternary volcanic and tectonic segmentation of Central America: Bulletin of Volcanology, v. 37, p. 304-325.

Stracke, A., 2012, Earth's heterogeneous mantle: A product of convection-driven interaction between crust and mantle: Chemical Geology, v. 330-331, p 274-299.

Sun, S.S., and McDonough, W.F., 1989, Chemical and isotopic systematics of oceanic basalts; implications for mantle composition and processes: Special Publication - Geological Society of London, v. 42, p. 313-345.

Sun, W.D., Hu, Y.H., Kamenetsky, V.S., Eggins, S.M., Chen, M., and Arculus, R.J., 2008, Constancy of Nb/U in the mantle revisited: Geochimica et Cosmochimica Acta, v. 72, p. 3542-3549.

Thorkelson, D.J. and Taylor, R.P., 1989, Cordilleran slab windows: Geology, v. 17, p. 833–836.

Thorkelson, D.J., Madsen, J.K., and Slugget, C.L., 2011, Mantle flow through the Northern Cordilleran slab window revealed by volcanic geochemistry: Geology, v. 39, p. 267-270.

Thorkelson, D.J. and Breitsprecher, K., 2005, Partial melting of slab window margins: genesis of adakitic and non-adakitic magmas: Lithos, v. 79, p. 25-41.

Tibaldi, A., Pasquarè, F., and Tormey, D., 2010, Volcanism in reverse and strike-slip fault settings, in: New Frontiers in Integrated Solid Earth Sciences, p. 315–348, Springer-Verlag, Dordrecht, The Netherlands.

Trop, J.M., Ridgway, K.D., Manuszak, J.D., and Layer, P.W., 2002, Sedimentary basin development on the allocthonous Wrangllia composite terrane, Mesozoic Wrangell Mountains basin, Alaska: A long-term record of terrane migration and arc construction: Geological Society of America Bulletin, v. 114, p. 693-717.

Trop, J.M., Hart, W.K., Snyder, D.C., and Idleman, B., 2012, Miocene basin development and volcanism along a strike-slip to flat-slab subduction transition: Stratigraphy, geochemistry, and geochronology of the central Wrangell volcanic belt, Yakutat – North America collision zone: Geosphere, v. 8, p. 805–834.

Trop, J.M., Benowitz, J.A., Brueseke, M.E., Davis, K.N., Berkelhammer, S.E., Morter, B.K., Layer, P.W., and Weber, M.A., 2017, Investigating the lost arc: Geologic constraints on ~29 million years of continuous magmatism along an arc-transform junction, Wrangell Arc, Alaska: Abstracts with Programs, 2017 Cordilleran Meeting, Geological Society of America.

Vervoort, J.D. and Blichert-Toft, J., 1999, Evolution of the depleted mantle: Hf isotope evidence from juvenile rocks through time: Geochimica et Cosmochimica Acta, v. 63, p. 533-556.

Vervoort, J.D., Patchett, P.J., Soderlund, U., and Baker, M., 2004, Isotopic composition of Yb and the determination of Lu concentrations and Lu/Hf ratios by isotope dilution using MC-ICPMS: Geochemistry, Geophysics, Geosystems, v. 5, Q11002.

Vervoort, J.D., Plank, T., and Prytulak, J., 2005, The Hf-Nd isotopic composition of marine sediments: Geochimica et Cosmochimica Acta, v. 75, p. 5903-5926.

Von Drach, V., Marsh, B.D., and Wasserburg, G.J., 1986, Nd and Srr isotopes in the Aleutians: multicomponent parenthood of island-arc magmas: Contributions to Mineralogy and Petrology, v. 92, p. 13-34.

Wang, Q., Xu, J.F., Jian, P., Bao, Z.W., Zhao, Z.H., Li, C.F., Xiong, X.L., and Ma, J.L., 2006, Petrogenesis of adakitic porphyries in an extensional tectonic setting, Dexing, South China: Implications for the genesis of porphyry copper mineralization: Journal of Petrology, v. 47, p. 119-144.

Weber, M.A., Brueseke, M.E., Benowitz, J.A., Trop, J.M., Berkelhammer, S.E., Davis, K.N., Layer, P.W., Morter, B.K., and Mertzman, S.A., 2017, Geological and geochemical constraints on Oligo-Miocene hypabyssal intrusive bodies from the Wrangell Arc, Alaska: Abstracts with Programs, 2017 Cordilleran Meeting, Geological Society of America.

Wells, R., Bukry, D., Friedman, R., Pyle, D., Duncan, R., Haeussler, P., and Wooden, J., 2014, Geologic history of Siletzia, a large igneous province in the Oregon and Washington Coast Range: Correlation to the geomagnetic polarity time scale and implications for a long-lived Yellowstone hotspot: Geosphere, v. 10, p. 692-719.

Whalen, J.B., Currie, K.L., and Chappell, B.W., 1987, A-type granites; geochemical characteristics, discrimination and petrogenesis: Contributions to Mineralogy and Petrology, v. 95, p. 407-419.

White, W.M., Hofmann, A.W., and Puchelt, H., 1987, Isotope geochemistry of Pacific mid-ocean ridge basalt: Journal of geophysical research, v. 92,p.4881-4893.

White, W.M., Albarède, F. & Télouk, P., 2000, High-precision analysis of Pb isotope ratios by multi-collector ICP-MS: Chemical Geology, v. 167, p.257-270.

Worthington, L.L., Van Avendonk, H.J.A., Gulick, S.P.S., Christeson, G.L., and Pavlis, T.L., 2012, Crustal structure of the Yakutat terrane and the evolution of subduction and collision in southern Alaska: Journal of Geophysical Research, v. 117.

Xu, J. F., Shinjio, R., Defant, M. J., Wang, Q. and Rapp, R. P., 2002, Origin of Mesozoic adakitic intrusive rocks in the Ningzhen area of east China: partial melting of delaminated lower continental crust?: Geology, v. 12, p. 1111–1114.

Yogodzinski, G.M., Kay, R.W., Volynets, O.N., Koloskov, A.V., and Kay, S.M., 1995, Magnesian andesite in the western Aleutian Komandorsky region: Implications for slab melting and processes in the mantle wedge: GSA Bulletin, v. 107, p. 505-519.

Yogodzinski, G.M., Lees, J.M., Churikova, T.G., Dorendorf, F., Wöerner, G., and Volynets, O.N., 2001, Geochemical evidence for the melting of subducting oceanic lithosphere at plate edges: Nature, v. 409, p. 500-504.

Yogodzinski, G.M., Vervoort, J.D., Brown, S.T., and Gerseny, M., 2010, Subduction controls of Hf and Nd isotopes in lavas of the Aleutian island arc: Earth and Planetary Letters, v. 300, p. 226-238.

Yogodzinski, G.M., Brown, S.T., Kelemen, P.B., Vervoort, J.D., Portnyagin, M., Sims, K.W.W., Hoernle, K., Jicha, B.R., and Werner, R., 2015, The role of subducted basalt in the source of island arc magmas: Evidence from seafloor lavas in the Western Aleutians: Journal of Petrology, v. 56, p. 441-492.

York, D., Hall, C.M., Yanase, Y., Hanes, J.A. & Kenyon, W.J., 1981, $^{40}Ar/^{39}Ar$ dating of terrestrial minerals with a continuous laser: Geophysical Research Letters, v. 8., p. 1136-1138.

Appendix A - Sample Locations and Petrographic Descriptions

All locations are presented in UTM coordinates based off the NAD27 CONUS datum with all samples plotting in UTM Zone 7. Rock type classifications are based on total alkali vs. silica classification from LeBas et. al. 1986. Samples that received isotope analysis were point counted, and the resulting modes are beneath each thin section description with the heading "Mode." Hand sample descriptions are taken from field notes.

Sample ID: SB15-17 **Easting:** 486570
Rock Type: Trachyandesite **Northing:** 6864269

Hand Sample: Vesicular, porphyritic basaltic-andesite. Fresh plagioclase with slight alignment, fine grained groundmass. Some secondary vesicle fill. Unit has lava tubes. Highest sample in North Cabin Creek section

Thin Section: Phaneritic, hypocrystalline, vesicular, porphyritic rock. Plagioclase phenocrysts are subhedral, tabular to equant in shape, display polysynthetic twinning, and range in size from 0.5-3 mm. Few plagioclase crystals show moderate sieve texture and minor sericite alteration. Clinopyroxene phenocrysts are anhedral and tabular in shape, show simple twinning, and range in size from 0.5-3.5 mm. Orthopyroxene phenocrysts are subhedral and are less than 0.6 mm in size. Olivine phenocrysts are anhedral, form small glomerocrysts with clinopyroxene and plagioclase, and range in size from 0.125–0.8 mm. Rare apatite needles <1.75 mm are found in phenocrysts. Vesicles are oval-shaped and range in size from 0.5-3.25 mm. Groundmass is hypocrystalline with a pilotaxitic texture, and consists of roughly 40% glass, and 60% plagioclase laths, opaque minerals, and rare clinopyroxene.

Sample ID: SB15-18 **Easting:** 486666
Rock Type: Andesite **Northing:** 6864143

Hand Sample: Porphyritic basal vitrophyre. Pyroxene crystal are < 3 mm, plagioclase crystals are < 1 mm. Groundmass is glassy and dark gray to black. Platy (jointed) flow interior is above, and grades down into oxidized basal breccia.

Thin Section: Phaneritic, hypocrystalline, vitrophyric rock. Plagioclase phenocrysts are euhedral, tabular to equant in shape, show polysynthetic twinning and undulatory extinction, and range in size from 0.125-7 mm. Clinopyroxene phenocrysts are subhedral to anhedral and equant in shape, show simple twinning, and range in size from 0.05-1.75 mm. Orthopyroxene phenocrysts are similar in size to clinopyroxene, and show similar low degrees of alteration opaque minerals and chlorite. Groundmass is hypocrystalline with a vitrophyric texture, consisting of roughly 50% glass, 20% plagioclase laths, and 30% opaque minerals.

Sample ID: SB15-19 **Easting:** 486637
Rock Type: Andesite **Northing:** 6864171

Hand Sample: Platy dacite outcrop, possibly and effect of ramping. Altered plagioclase crystals are < 4 mm, with a dark gray groundmass.

Thin Section: Phaneritic, hypocrystalline, porphyritic rock. Plagioclase phenocrysts are subhedral, tabular to equant in shape, show polysythentic twinning and concentric zoning, and range in size from 0.1-2.5 mm. Few plagioclase crystals show minor alteration to sericite along fractures. Clinopyroxene and orthopyroxene phenocrysts are anhedral crystals, equant in shape, form few glomerocrysts with anhedral plagioclase fragments, and range in size from 0.2-1 mm. Groundmass is hypocrystalline with a trachytic texture, consisting of roughly 25% glass, 25% opaque minerals, and 50% plagioclase laths.

Sample ID: SB15-20 **Easting:** 486709
Rock Type: Dacite **Northing:** 6864000

Hand Sample: Pink dacite rock. Quartz crystals are < 5 mm, sanidine crystals are < 3mm, and a dark mafic mineralis visible. Rounded weathering, and may be a thick unit.

Thin Section: Phaneritic, hypocrystalline, glomeroporphyritic rock. Plagioclase phenocrysts are euhedral, tabular to equant in shape, show polysynthetic twinning and undulatory extinction, and range in size from 0.1-2 mm. Some plagioclase crystals show extensive sieve texture and are euhedral. Clinopyroxene phenocrysts are euhedral and form glomerocrysts with plagioclase, and range in size from 0.1-0.5 mm. Clinopyroxene crystals are pink in plane-polarized light, and may be titanaugite. Rare orthopyroxene crystals are smaller than clinopyroxene, and show similar degree of alteration to chlorite and opaque minerals. Groundmass is red in color, displays a hyalopilitic texture (plagioclase laths aligned in a glassy matrix), and consists of roughly 40% glass, 30% plagioclase laths, 20% clinopyroxene, and 10% opaque minerals.

Sample ID: SB15-21 **Easting:** 486724
Rock Type: Trachydacite **Northing:** 6863891

Hand Sample: Porphyritic andesite or dacite. Plagioclase crystals are < 4 mm, sanidine crystals are < 4 mm, with trace quartz. Weathering similar to SB15-20, but not as felsic. Basal part of SB15-20, or another unit.

Thin Section: Phaneritic, hypocrystalline, glomeroporphyritic rock. Plagioclase phenocrysts are subhedral to anhedral, tabular to equant in shape, show polysynthetic and simple twinning, undulatory extinction, and range in size from 0.1-2.5 mm. Clinopyroxene phenocrysts are subhedral and tabular in shape, and form glomerocrysts with plagioclase and opaque minerals. Most clinopyroxene crystals show moderate to extreme alteration to chlorite. Groundmass is hypocrystalline with a felty texture, and consists of roughly 70% glass, 20% plagioclase, and 10% opaque minerals.

Sample ID: SB15-22 **Easting:** 486702
Rock Type: Dacite **Northing:** 6863746

Hand Sample: Tall, jagged outcrop. Plagioclase crystals are < 3 mm, dark mafic crystals are < 1 mm, with a light gray groundmass.

Thin Section: Phaneritic, hypocrystalline, glomeroporphyritic rock. Plagioclase phenocrysts are subhedral to anhedral, tabular to equant in shape, show polysynthetic and simple twinning, undulatory extinction, and range in size from 0.1-2.5 mm. Few plagioclase crystals show moderate alteration to sericite. Clinopyroxene phenocrysts form glomerocrysts with plagioclase and opaque minerals, and range from 0.1-1 mm. Most clinopyroxenes show alteration to chlorite, and few show alteration of crystal rims to opaque minerals. Groundmass is hypocrystalline with a pilotaxitic texture, and consists of roughly 50% glass, 20% plagioclase laths, and 30% opaque minerals.

Sample ID: SB15-23 **Easting:** 486592
Rock Type: Dacite **Northing:** 6863706

Hand Sample: Big blocky outcrop of dacite lava, although not a fresh sample. Plagioclase crystals are not fresh, maybe a dark gray mafic mineral.

Thin Section: Phaneritic, hypocrystalline, glomeroporphyritic rock. Plagioclase phenocrysts are euhedral to anhedral, tabular in shape, show polysynthetic and simple twinning, undulatory extinction, and range in size from 0.5-2.5 mm. Clinopyroxene phenocrysts are euhedral and equant in shape, show simple twinning, and form glomerocrysts with plagioclase and opaque minerals. Clinopyroxene crystals are pink in plane-polarized light, and may be titanaugite. Most clinopyroxene crystals show some degree of alteration to chlorite. Orthopyroxene phenocrysts are less abundant than clinopyroxene, but show similar habit and degrees of alteration, and are mainly found in glomerocrysts with clinopyroxene, plagioclase, and opaque minerals. Apatite needles occur in plagioclase phenocrysts and are no longer than 0.35 mm. Groundmass is aphanitic and hypocrystalline with a felty texture, and consists of roughly 65% glass, 20% plagioclase laths, and 15% opaque minerals.

Sample ID: SB15-24 **Easting:** 486494
Rock Type: Trachyandesite **Northing:** 6863542

Hand Sample: Light gray aphanitic flow, with platy jointing that may be due to ramping. Rare plagioclase phenocrysts are < 2 mm.

Thin Section: Phaneritic, hypocrystalline, porphyritic rock. Plagioclase phenocrysts are subhedral to anhedral and tabular in shape, show polysynthetic twinning and undulatory extinction, and range in size from 0.5-2 mm. Few plagioclase crystals show sieve texture and have very anhedral shapes. Clinopyroxene phenocrysts are euhedral and equant in shape, show simple twinning, and are less than 0.75 mm in size. Clinopyroxene crystals are pink in plane-polarized light, and may be titanaugite. Orthopyroxene phenocrysts are euhedral to subhedral, show simple twinning, and are <0.5 mm in size. Clinopyroxene, orthopyroxene, plagioclase, and opaque minerals form small glomerocrysts. Groundmass is aphanitic and hypocrystalline with a pilotaxitic texture, and consists of roughly 40% glass, 30% plagioclase laths, and 30% opaque minerals.

Sample ID: SB15-25 **Easting:** 486464
Rock Type: Dacite **Northing:** 6863514

Hand Sample: Light gray aphanitic flow, with a dark mafic mineral < 2 mm. Bottom of North Cabin Creek section.

Thin Section: Phaneritic, hypocrystalline, porphyritic rock. Plagioclase phenocrysts are subhedral to anhedral, elongate to equant in shape, show polysynthetic twinning and undulatory extinction, and range in size from 0.25-3 mm. Plagioclase phenocrysts have sieve texture, and few are altered to sericite. Clinopyroxene phenocrysts are euhedral and equant in shape, show simple twinning, and are <1 mm in size. Some clinopyroxene crystals occur as small glomerocrysts with plagioclase and opaque minerals, and may be xenocrysts. Orthopyroxene phenocrysts <1 mm are sudbhedral and equant. Rare apatite needles less than 0.07 mm occur in plagioclase crystals. Groundmass is aphanitic and hypocrystalline with a pilotaxitic texture, and consists of roughly 20% glass, 60% plagioclase laths, and 20% opaque minerals.

Sample ID: SB15-26 **Easting:** 485795
Rock Type: Trachydacite **Northing:** 6862121

Hand Sample: ~30-m-thick rhyolite flow, with large columnar jointing. Aphanitic and medium gray. Top of South Cabin Creek section.

Thin Section: Aphanitic, hypocrystalline, porphyritic rock. Plagioclase phenocrysts are subhedral to euhedral, tabular to equant in shape, display polysynthetic and simple twinning and undulatory extinction, and range in size from 0.3-1.5 mm. Sieve texture is uncommon on plagioclase, but many crystals are fractured and embayed. Clinopyroxene phenocrysts are subhedral and elongate to tabular in shape, show simple twinning, and range in size from 0.125-1 mm. Clinopyroxene crystals have reacted crystal rims, and their pink color in plane-polarized light suggest that they are titanaugite. Opaque phenocrysts <0.25 mm are equant in shape. Rare apatite needles <0.25 mm are found in plagioclase and clinopyroxene crystals. Groundmass is aphanitic and hypocrystalline with a pilotaxitic texture, and consists of roughly 5% clinopyroxene, 30% opaque minerals, 50% plagioclase laths, and 15% glass.

Sample ID: SB15-27 **Easting:** 485795
Rock Type: Trachydacite **Northing:** 6862121

Hand Sample: Porphyritic basal vitrophyre of SB15-26. Quartz(?) crystals are < 3 mm, and sanidine crystals are < 5 mm. Phenocrysts show slight alignment. Medium gray groundmass.

Thin Section: Aphanitic, hypocrystalline, porphyritic rock. Plagioclase and sanidine phenocrysts are euhedral to anhedral, and elongate, tabular, and equant. The most anhedral crystals show extensive sieve texture and embayments, as well as undulatory extinction. The most euhedral crystals are fresh and show well-developed polysynthetic twinning. Plagioclase and sanidine phenocrysts range in size from 0.05-1 mm. Clinopyroxene phenocrysts are subhedral and equant in shape, show simple twinning, and range in size from 0.1-0.75 mm. Clinopyroxene crystal rims are altered, and in some cases the entire crystal has been replaced by an opaque mineral. Opaque phenocrysts are equant in shape and range in size from 0.05-0.25 mm. Groundmass is aphanitic and hypocrystalline with a pilotaxitic texture, and consists of roughly 30% glass, 40% plagioclase

laths, and 30% opaque minerals. Macroscopic flow-banding is evident even in thin section, from discrete zones showing a slightly greater glass component.

Mode: 90.1% groundmass; 6.3% plagioclase; 2% clinopyroxene; 1.4% opaque minerals; 0.2% sanidine. 637 total points

Sample ID: SB15-28 **Easting:** 485852
Rock Type: Trachyandesite **Northing:** 6862172

Hand Sample: Basal vitrophyre of dacite flow. Aphanitic, glassy, and slightly vesicular. Vesicles are < 1 cm long and aligned. Rare phenocrysts are < 3 mm.

Thin Section: Hypocrystalline, aphanitic, vesicular rock. Very few plagioclase phenocrysts are euhedral and elongate, show polysynthetic and simple twinning and undulatory extinction, and are <0.75 mm in size. Most plagioclase crystals have sieve texture and form glomerocrysts with clinopyroxene. Clinopyroxene phenocrysts are subhedral and show simple twinning, and are <1.5 mm in size. Clinopyroxene may be titanaugite. Few opaque phenocrysts are equant in shape and are <0.5 mm in size. Vesicles are well-formed and range in size from 0.075-2.5 mm. Rare apatite needles are found in plagioclase crystals and are <0.1 mm in length. Groundmass is aphanitic and hypocrystalline with a hyalopilitic texture, and consists of roughly 60% glass, 20% plagioclase laths, 15% opaque minerals, and 5% clinopyroxene.

Sample ID: SB15-29 **Easting:** 485847
Rock Type: Andesite **Northing:** 6862295

Hand Sample: Porphyritic andesite. Fresh plagioclase crystals are < 4 mm, pyroxene crystals are < 5 mm. Really nice sample. Highest of four benches on ridge below thick rhyolite flow.

Thin Section: Phaneritic, hypocrystalline, seriate porphyritic rock. Rare euhedral plagioclase phenocrysts are elongate to tabular, relatively unaltered, and show polysynthetic twinning. Anhedral plagioclase fragments are more abundant, show polysynthetic twinning and undulatory extinction, and sieve textures in crystal cores and rims. Plagioclase ranges in size from 0.25-5 mm, and alteration to sericite is uncommon. Large euhedral clinopyroxene phenocrysts are <1.5 mm, show simple twinning and concentric zoning, and have altered crystal rims. Subhedral to anhedral clinopyroxene phenocrysts are <1.5 mm, and have altered crystal rims. Clinopyroxene may be titanaugite. Orthopyroxene phenocrysts are subhedral and in less abundance than clinopyroxene, and are <1.25 mm in size. Olivine <0.2 mm in size is found in the groundmass, and is altered to iddingsite. Rare apatite needles are found in plagioclase crystals and are <0.3 mm in length. Vesicles <1 mm in size are irregularly shaped. Some plagioclase and pyroxene crystals project into vesicles, giving this rock a diktytaxitic texture. Groundmass is aphanitic and hypocrystalline with a felty texture, and consists of roughly 35% opaque minerals, 25% plagioclase laths, 30% glass, and 10% clinopyroxene. There is a continuous range in grain size from the groundmass to phenocrysts, making this rock seriate porphyritic.

Sample ID: SB15-30 **Easting:** 485859

Rock Type: Andesite **Northing:** 6862309

Hand Sample: Porphyritic andesite. Plagioclase crystals are < 8 mm, pyroxene crystals are < 3 mm, with a light gray groundmass. Slope-forming breccia between this sample and SB15-29.

Thin Section: Phaneritic, hypocrystalline, seriate porphyritic rock. Plagioclase phenocrysts are subhedral to anhedral, and elongate to tabular in shape. Plagioclase displays polysynthetic and simple twinning, undulatory extinction, and sieve texture of crystal rims and interiors. Plagioclase is <3 mm in size, and ranges continuously in size to a cryptocrystalline part of the groundmass. Orthopyroxene phenocrysts are subhedral and elongate to equant in shape, show simple twinning and reaction rims, and are <2.75 mm in size. Euhedral clinopyroxene phenocrysts show simple twinning and fresh crystal edges, whereas subhedral to anhedral clinopyroxene phenocrysts show sieve texture and reaction rims. Clinopyroxene crystals are <2 mm in size, and may be titanaugite. Anhedral olivine <0.5 mm is found in the groundmass and is altered to iddingsite. Groundmass is aphanitic and hypocrystalline with a hyalopilitic texture, and consists of roughly 45% opaque minerals, 20% plagioclase laths, 20% clinopyroxene, and 15% glass. There is a continuous range in grain size from the groundmass to phenocrysts, making this rock seriate porphyritic.

Sample ID: SB15-31 **Easting:** 485891
Rock Type: Basaltic-Andesite **Northing:** 6862349

Hand Sample: Porphyritic (phaneritic) andesite. Plagioclase crystals are < 6 mm, pyroxene crystals are < 2 mm, with a gray groundmass.

Thin Section: Phaneritic, hypocrystalline, seriate porphyritic rock. Subhedral plagioclase phenocrysts are elongate to tabular in shape, display polysynthetic twinning, and are relatively fresh crystals. Fewer anhedral plagioclase phenocrysts show undulatory extinction and sieve texture, with clinopyroxene inclusions. All plagioclase crystals are <4.5 mm in size. Clinopyroxene phenocrysts are euhedral to subhedral, equant in shape with simple twinning, <1.75 mm in size, and may be titanaugite. Orthopyroxene phenocrysts are subhedral to anhedral, show reaction rims, and are <1.5 mm in size. Plagioclase, clinopyroxene, and orthopyroxene form clots <1.25 mm. Olivine phenocrysts are subhedral crystal fragments, show iddingsite alteration and reaction rims, and are <1 mm in size. Plagioclase, pyroxene, and olivine crystals grade in size to be a cryptocrystalline part of the groundmass. Rare apatite needles <0.125 mm are found in plagioclase crystals. Groundmass is aphanitic and hypocrystalline with a felty texture, and consists of roughly 40% glass, 30% plagioclase laths, 20% opaque minerals, and 10% clinopyroxene.

Mode: 61.8% groundmass; 23.8% plagioclase; 4.8% orthopyroxene; 4.6% clinopyroxene; 3.4% olivine; 1.6% vesicles; 689 total points

Sample ID: SB15-32 **Easting:** 485940
Rock Type: Basaltic-Andesite **Northing:** 6862401

Hand Sample: Aphanitic basalt or basaltic-andesite with a thick weathering rind. Few plagioclase crystals are evident, with a dark gray groundmass. Lowest sample in South Cabin Creek section.

Thin Section: Phaneritic, holocrystalline, seriate porphyritic rock. Plagioclase phenocrysts <2.5mm are subhedral to anhedral, equant to tabular in shape, and show polysynthetic twinning. The most anhedral plagioclase crystals show extensive sieve texture with clinopyroxene inclusions, and have sericite alteration. Clinopyroxene phenocrysts <1 mm are anhedral, show simple twinning, have reaction rims, and form glomerocrysts with plagioclase. Orthopyroxene phenocrysts have been entirely replaced by serpentine, except one euhedral crystal 3.25 mm large that has an intact core. Groundmass is aphanitic and holocrystalline with a felty texture, and consists of roughly 50% plagioclase laths, 30% clinopyroxene, 10% opaque minerals, and 10% olivine.

Sample ID: SB15-33 **Easting:** 0492264
Rock Type: Dacite **Northing:** 6862027

Hand Sample: Crystalline equigranular sample of “Tdh" unit. Plagioclase crystals are < 6 mm, and hornblende crystals are < 7 mm, with coarse groundmass.

Thin Section: Aphanitic, hypocrystalline, porphyritic rock. Intense alteration of both phenocrysts and groundmass makes mineral identification difficult. Feldspars are completely altered to sericite, and a mafic mineral, either clinopyroxene or hornblende, is altered to chlorite and opaque minerals.

Sample ID: SB15-34 **Easting:** 0492784
Rock Type: Rhyolite **Northing:** 6862815

Hand Sample: Sample of "Tr" unit. Rhyolite flow with quartz crystals < 4 mm, sanidine crystals < 4 mm, and hornblende < 3 mm. Groundmass is light gray and chalky, most likely recrystallized. Vertical contact with "TKs" sedimentary unit.

Thin Section: Phaneritic, holocrystalline, porphyritic rock. Quartz phenocrysts are anhedral and embayed, show undulatory extinction, and range in size from 0.1-2 mm. Sanidine phenocrysts <2 mm in size are euhedral to subhedral, equant to tabular in shape, and show simple twinning and undulatory extinction. Sieve texture and calcite alteration is extensive on most sanidine crystals. Subhedral and elongate biotite pseudomorphs are extensively altered to opaque and translucent iron oxy-hydroxides and birefringent calcite. Rare apatite needles <0.2 mm are found in quartz and sanidine crystals. Very few zircon crystal fragments showing alteration haloes are present in the groundmass, one being 1.5 mm in size. Groundmass is aphanitic and microcrystalline with a felty texture, and consists of roughly equal proportions of quartz and feldspar crystals, with trace biotite psuedomorphs and apatite.

Mode: 75.6% groundmass; 12.6% quartz; 9.3% sanidine; 2.5% biotite pseudomorphs; 690 total points

Sample ID: SB15-36 **Easting:** 0492812
Rock Type: Basaltic-Andesite **Northing:** 6862546

Hand Sample: Sample of "Ti" dike unit that cuts "TKs" sedimentary unit. Fresh sample.

Thin Section: Phaneritic, hypocrystalline, seriate glomeroporphyritic rock. Plagioclase phenocrysts are subhedral, elongate to tabular, show polysynthetic twinning, and range in size from microcrystalline to 3 mm. Plagioclase crystals show extensive resorption and sieve texture, with alteration to sericite and calcite. Clinopyroxene phenocrysts are euhedral to subhedral and equant in shape, show simple twinning, and range in size from 0.1-2.5 mm. Clinopyroxene phenocrysts form glomerocrysts, and most clinopyroxene crystals have been replaced by extensive chlorite and calcite alteration. Groundmass is hypocrystalline with a felty groundmass, and consists of roughly 40% plagioclase laths, 20% opaque minerals, 20% chlorite; and 20% glass.

Sample ID: SB15-37 **Easting:** 0492834
Rock Type: Basaltic-Andesite **Northing:** 6862336

Hand Sample: "Tsp" basaltic plug that intrudes "TKs" unit.

Thin Section: Phaneritic, hypocrystalline, porphyritic rock. Rare plagioclase psuedomorphs are anhedral, range in size from 02.-2.5 mm, and are almost entirely replace by sericite alteration. Phenocrysts make up roughly 5% of the rock. Groundmass is hypocrystalline with a pilotaxitic to trachytic texture, and consists of roughly 10% opaque minerals, 30% glass, 30% chlorite, and 30% plagioclase laths. Very altered rock.

Sample ID: SB15-38 **Easting:** 0492754
Rock Type: Basaltic-Andesite **Northing:** 6862281

Hand Sample: "Tsb" unit.

Thin Section: Phaneritic, hypocrystalline, porphyritic rock. Plagioclase psuedomorphs are completely replaced by sericite and calcite alteration, are subhedral, and range in size from 0.1-1.5 mm. Phenocrysts make up roughly 1% of the rock. Groundmass makes up the majority of the rock, is microcrystalline and hypocrystalline, with a trachytic texture, and consists of roughly 30% opaque minerals, 20% glass, 20% chlorite; 30% plagioclase laths. Very weathered rock.

Sample ID: SB15-39 **Easting:** 0489056
Rock Type: Basalt **Northing:** 6858382

Hand Sample: Platy outcrop of aphanitic, equigranular basaltic andesite. Very minor chlorite alteration.

Thin Section: Phaneritic, holocrystalline, seriate porphyritic rock. Crystals range in size from 0.05 mm in the groundmass to 1.5 mm phenocrysts. Clinopyroxene phenocrysts are subhedral, show simple twinning, and varying degrees of alteration to chlorite and serpentine. Olivine phenocrysts are euhedral to subhedral, and show moderate iddingsite alteration. Groundmass consists of

euhedral plagioclase laths and clinopyroxene showing an ophitic to sub-ophitic texture, intergranular olivine and opaque minerals, and areas of chlorite and serpentine alteration on clinopyroxene. Some olivine crystals show poikilitic texture with plagioclase laths in the groundmass. Relatively fresh rock.

Mode: 59% plagioclase; 16.8% olivine; 9.2% clinopyroxene; 4% opaque minerals; 11% chlorite/serpentine alteration. 720 total points

Sample ID: SB15-40 **Easting:** 0487798
Rock Type: Rhyolite **Northing:** 6857840

Hand Sample: Proximal welded tuff, ~30-m-thick. Fresh quartz and sanidine crystals, with altered mafic crystals in matrix. Welded and elongate lithic fragments, and pumice blocks falling out of outrop.

Thin Section: Phaneritic, hypocrystalline, porphyritic rock. Plagioclase, anorthoclase, and sanidine phenocrysts are present as subhedral crystals to anhedral crystal fragments. Plagioclase phenocrysts show polysynthetic twinning, concentric zoning, and undulatory extinction. Anorthoclase phenocrysts show polysynthetic and pericline twinning, concentric zoning, and undulatory extinction. Sanidine shows simple twinning and undulatory extinction. All feldspar phenocrysts range in size from 0.1-2.5 mm. Most feldspar crystals are fresh, with few showing alteration to sericite and calcite. Clinopyroxene phenocrysts are rare, but euhedral to subhedral crystals show simple twinning, reaction rims, and range in size from 0.1-1.25 mm. Clinopyroxene crystals show varying degrees of replacement by chlorite and opaque minerals, and clinopyroxene forms rare glomerocrysts with feldspar, opaque minerals, and one biotite crystal. Opaque minerals less than 0.2 mm in size are also found. Apatite needles less than 0.1 mm long are found on feldspars. Groundmass is cryptocrystalline with a vitrophyric to eutaxitic texture, with elongate zones consisting of a microcrystalline quartz polymorph, which is likely tridymite or cristobalite. Groundmass consists of roughly 80% glass, 15% quartz polymorphs, and 5% feldspar. Rare vesicles are less than 1 mm in size.

Mode: 91.3% groundmass (60.4% fine-grained, 30.9% coarse-grained); 3.6% plagioclase; 1.6% sanidine; 1.2% anorthoclase; 1.1% clinopyroxene; 1.1% opaque minerals; 625 total points

Sample ID: SB15-41 **Easting:** 0487836
Rock Type: Trachydacite **Northing:** 6857984

Hand Sample: Upper vesicular zone of dacite flow. Fresh, aligned plagioclase crystals are < 8 mm, sanidine crystals are < 4 mm, with an aphanitic medium gray groundmass. Elongate, aligned vesicles are < 1 cm long.

Thin Section: Phaneritic, hypocrystalline, vesicular porphyritic rock. Rare plagioclase phenocrysts are subhedral to anhedral, tabular to equant in shape, show polysynthetic and simple twinning, undulatory extinction, and range in size from 0.2-2 mm. Some plagioclase crystals show sieve texture. Rare clinopyroxene phenocrysts are anhedral, show simple twinning, reaction rims, and are less than 0.25 mm in size. Opaque minerals <1.25 mm in size, and apatite needles <0.15

mm are found. One glomerocryst <0.75 mm in size contains plagioclase, clinopyroxene, and opaque minerals. Abundant elongate vesicles range in size from 0.25-1.25 mm, and show concentric zones of alteration that extend outward from the vesicle, probably the alteration of glass . Groundmass is aphanitic and hypocrystalline with a trachytic texture, and consists of roughly 40% glass, 40% plagioclase laths, and 20% opaque minerals.

Sample ID: SB15-42 **Easting:** 0487926
Rock Type: Trachydacite **Northing:** 6858099

Hand Sample: Sample from the interior of a dacite flow. Plagioclase crystals are < 7 mm, and are aligned along flow banding. Groundmass is crystalline and medium gray.

Thin Section: Phaneritic, holocrystalline, sparsely porphyritic rock. Phenocrysts make up approximately 5% of the rock. Plagioclase phenocrysts are subhedral to anhedral, equant to tabular in shape, show polysynthetic twins, concentric zoning, and undulatory extinction. Plagioclase phenocrysts range in size from 0.25-2.25 mm, and very few crystals show alteration to sericite. Clinopyroxene and orthopyroxene phenocrysts are euhedral to subhedral, equant to tabular in shape, show simple twinning, and range in size from 0.25-1 mm. Both clinopyroxene and orthopyroxene crystals have reaction rims and opaque overgrowths. Clinopyroxene and orthopyroxene form rare glomerocrysts with plagioclase and opaque minerals. Microcrystalline and equigranular groundmass with a felty texture makes up the majority of this rock. Groundmass consists of roughly 60% plagioclase laths, 20% opaque minerals, and 20% pyroxene, with zones showing alteration to chlorite and opaque minerals after pyroxene. Overall a very fresh rock.

Sample ID: SB15-43 **Easting:** 0492721
Rock Type: Andesite **Northing:** 6858777

Hand Sample: Rhyo-dacite with fresh plagioclase crystals < 6 mm, sanidine crystals < 4 mm, and a dark mafic mineral < 4 mm. Light gray, crystalline, equigranular groundmass. White "sinter" above outcrop may represent a paleo-hot springs.

Thin Section: Phaneritic, holocrystalline, seriate porphyritic rock. Plagioclase phenocrysts are subhedral to anhedral, show polysynthetic twinning, concentric zoning, and undulatory extinction, and range in size from a microcrystalline part of the groundmass to 4 mm. Plagioclase crystals show sieve texture and other resorption features, and show varying degrees of sericite alteration, with some plagioclase crystals completely replace by sericite. Groundmass has undergone extensive alteration, with chlorite, epidote, serpentine, and sericite in abundance throughout. Plagioclase is replaced by sericite, chlorite, and epidote. Original clinopyroxene crystals are not seen, and have likely been replaced by serpentine, chlorite, and epidote. Opaque minerals are found through the rock, closely associated with serpentine, chlorite, and epidote alteration.

Sample ID: SB15-44 **Easting:** 0492721
Rock Type: Tuff **Northing:** 6858762

Hand Sample: Fine-grained, chalky white rock with faint laminations visible.

Thin Section: Aphanitic, hypocrystalline, pyroclastic rock. Anhedral orthoclase crystal fragments are embayed and fractured, and are 0.05-0.6 mm in size. Plagioclase psuedomorphs are the same size, and have been entirely replaced by sericite. Groundmass is cryptocrystalline and consists of roughly 60% glass and 40% crystals.

Sample ID: SB15-45 **Easting:** 0492754
Rock Type: Rhyolite **Northing:** 6858664

Hand Sample: Rhyolite/rhyo-dacite plug, with ~10 cm wide "columns." Hornblende crystals are < 6 mm, plagioclase crystals are < 6 mm, and quartz crystals are < 4mm. Light gray, equigranular, crystalline groundmass.

Thin Section: Phaneritic, hypocrystalline, porphyritic rock. Hornblende phenocrysts are euhedral to subhedral, equant to elongate in shape, and range in size from 0.1-1.25 mm. Few hornblende crystals are fractured and show alteration to chlorite, and one large hornblende phenocryst is very altered and may be a xenocryst. Biotite phenocrysts are more abundant than hornblende, form anhedral crystals, and ranges in size from 0.05 -1.25 mm. Biotite shows varying degrees of alteration to chlorite, opaque minerals, and an iron oxy-hydroxide mineral. Plagioclase phenocrysts are euhedral to subhedral, show polysynthetic twinning, concentric zoning, and undulatory extinction. Plagioclase crystals are fractured and show little sericite alteration. Apatite needles <0.15 mm are found in plagioclase and biotite crystals, and rare zircons <0.05 mm are found in the groundmass. Many plagioclase crystals show alteration to some zeolite phase, especially along crystal fractures and edges. Groundmass is microcrystalline with a felty texture, and consists of roughly 70% glass, 20% plagioclase laths, and 10% combined biotite and opaque minerals.

Sample ID: SB15-46 **Easting:** 0493185
Rock Type: Basaltic-Andesite **Northing:** 6858351

Hand Sample: Porphyritic andesite, found as float from uphill. Plagioclase crystals are < 5 mm.

Thin Section: Phaneritic, hypocrystalline, seriate porphyritic rock. Plagioclase phenocrysts are euhedral to subhedral, tabular to equant in shape, show polysynthetic and pericline twinning, undulatory zoning, and range in size from 0.125-6.75 mm. Sieve texture is seen on the largest plagioclase crystals, as well as alteration to sericite and calcite along fractures. Clinopyroxene phenocrysts have been almost entirely replaced by serpentine, chlorite and opaque minerals. Some of these pseudomorphs may have originally been olivine. Groundmass is aphanitic and hypocrystalline with a felty texture, and consists of roughly 45% plagioclase laths, 20% opaque minerals with equant and acicular habits, 25% glass and chlorite alteration, and 10% olivine and pyroxene.

Sample ID: SB15-47 **Easting:** 0493642

Rock Type: Dacite **Northing:** 6859355

Hand Sample: Diorite sample with visible quartz, hornblende, and/or biotite crystals. Rock is equigranular and light gray. Platy outcrop.

Thin Section: Phaneritic, equigranular diorite rock. Anhedral plagioclase crystals are <2.5 mm and show polysynthetic, pericline, and simple twinning, undulatory extinction, and sieve texture and embayments of crystal edges. Alteration to sericite is seen in sieved plagioclase crystals, and calcite is present in fractures. Interstitial quartz, is found between larger plagioclase crystals as anhedral, irregular masses, and show few signs of alteration. Biotite is interstitial and <1.75 mm in size. Biotite shows alteration to chlorite, epidote, opaque minerals, and in some cases biotite is entirely replaced by these phases. Rare interstitial amphibole is altered to chlorite and opaque minerals. Apatite needles <0.1 mm are found in plagioclase crystals.

Sample ID: SB15-48 **Easting:** 0493183
Rock Type: Andesite **Northing:** 6859903

Hand Sample: Equigranular aphanitic andesite from a blocky outcrop.

Thin Section: Phaneritic, equigranular, diorite rock. Plagioclase crystals are anhedral and intergrown, with a few large tabular crystals as large as 3.75 mm in size. Plagioclase displays pericline and polysynthetic twinning, concentric zoning in places, and undulatory extinction. Plagioclase shows calcite alteration along crystal fractures. Biotite <2.5 mm in size is interstitial to plagioclase crystals and shows alteration to chlorite, epidote, and opaque minerals. Clinopyroxene <1.8 mm in size is interstitial to plagioclase, and shows alteration to chlorite, opaque minerals, and possibly serpentine. Rare pyroxene inclusions in plagioclase are <0.5 mm in size. Apatite needles <0.5 mm are found in plagioclase crystals.

Sample ID: SB15-50 **Easting:** 0482769
Rock Type: Andesite **Northing:** 6852721

Hand Sample: Sample from a dike cutting "Tol" unit. Plagioclase crystals are < 5 mm, in a blue-gray groundmass with epidote alteration. Dike strikes north-south.

Thin Section: Phaneritic, porphyritic, hypocrystalline rock. Plagioclase phenocrysts are euhedral to subhedral, elongate to tabular, and are less than 4 mm in size. Plagioclase crystals are extensively altered to sericite and epidote. Clinopyroxene phenocrysts are euhedral and less than 1.5 mm in size. Rare olivine crystals are subhedral and less than 0.6 mm in size. Groundmass is cryptocrystalline and glassy. The rock is extensively altered, with veins containing chlorite, epidote, and a quartz polymorph that may be tridymite or cristobalite.

Sample ID: SB15-51 **Easting:** 0482778
Rock Type: Basaltic-Andesite **Northing:** 6852738

Hand Sample: Medium gray aphanitic lava flow from massive unit. Very fine-grained and equigranular, with few visible plagioclase phenocrysts.

Thin Section: Phaneritic, porphyritic, hypocrystalline rock. Plagioclase phenocrysts are subhedral to anhedral, elongate to tabular and shape, show polysynthetic twinning, and are less than 1 mm in size. Plagioclase crystals show sieve texture and alteration to sericite and epidote. Clinopyroxene phenocrysts are euhedral to subhedral, show simple twinning, occur as small glomerocrysts, and are less than 2.25 mm in size. Clinopyroxene crystals show varying degrees of alteration to chlorite, with some whole crystals replaced by chlorite. Rare olivine crystals are euhedral to subhedral and relatively fresh. Groundmass is microcrystalline and hypocrystalline with a pilotaxitic texture, and consists of roughly 60% glass, 20% plagioclase laths, and 20% opaque minerals.

Sample ID: SB15-52 **Easting:** 0482784
Rock Type: Andesite **Northing:** 6852788

Hand Sample: Phaneritic lava flow with hornblende crystals < 1 cm, plagioclase crystals < 4 mm, in a light green-gray groundmass.

Thin Section: Phaneritic, hypocrystalline, porphyritic rock. Hornblende phenocrysts are subhedral to anhedral, elongate to equant in shape, show characteristic pleochroism, and are altered to chlorite and opaque minerals. Hornblende crystals are less than 2 mm in size, and some are embayed. Plagioclase phenocrysts are subhedral to anhedral, tabular to equant, show simple twinning, and show heavy sieve texture and alteration to sericite and epidote. Rare clinopyroxene phenocrysts are heavily altered to chlorite. Groundmass is microcrystalline and hypocrystalline with a felty texture, and consists of roughly 70% plagioclase laths, 20% glass, and 10% opaque minerals.

Sample ID: SB15-53 **Easting:** 0482784
Rock Type: Basaltic-Andesite **Northing:** 6852788

Hand Sample: Plagioclase-rich andesite found as float. Plagioclase crystals are < 5 mm, and hornblende crystals are < 3 mm.

Thin Section: Phaneritic, porphyritic, hypocrystalline rock. Plagioclase phenocrysts are euhedral to subhedral, elongate to tabular in shape, and range in size from a microcrystalline part of the groundmass to 5.3 mm. Plagioclase crystals show sieve texture and alteration to sericite, epidote, and calcite along fractures. Clinopyroxene phenocrysts are euhedral to subhedral, and some are heavily altered to chlorite and opaque minerals. Rare fresh clinopyroxene crystals show reaction rims. Groundmass is microcrystalline and hypocrystalline with a felty texture, and consists of roughly 30% plagioclase laths, 20% glass, 20% opaque minerals, 10% olivine, 10% pyroxene, and 10% chlorite alteration.

Sample ID: SB15-54 **Easting:** 0486364
Rock Type: Andesite **Northing:** 6852946

Hand Sample: Sample found as float, with plagioclase crystals < 7 mm, green groundmass, and quartz amygdules.

Thin Section: Phaneritic, porphyritic, hypocrystalline rock. Plagioclase phenocrysts are subhedral, tabular to equant in shape, show sieve texture, and range in size from a microcrystalline part of the groundmass to 3.5 mm. Plagioclase crystals show sieve texture with clinopyroxene inclusions, and alteration to sericite and epidote. Clinopyroxene phenocrysts are subhedral to anhedral, show simple twinning, and range in size from a microcrystalline part of the groundmass to 1.5 mm. Clinopyroxene crystals show varying degrees of alteration, from relatively fresh crystals with reaction rims to some crystals entirely replaced by chlorite and opaque minerals. Amygdules of quartz polymorphs (tridymite or cristobalite) and chlorite are less than 2.5 mm in size, and may be related to veins filled with chlorite, epidote, a quartz polymorph mineral, and a zeolite mineral. Groundmass is microcrystalline and hypocrystalline with a felty texture, and consists of roughly 40% chlorite alteration, 30% plagioclase laths, 20% glass, 5% epidote, and 5% opaque minerals.

Sample ID: SB15-55 **Easting:** 0488026
Rock Type: Andesite **Northing:** 6852764

Hand Sample: Equigranular, medium grained diorite, with plagioclase crystals < 5 mm.

Thin Section: Phaneritic, hypocrystalline, seriate glomeroporphyritic rock. Plagioclase phenocrysts range in size from 4.25 mm to a microcrystalline part of the groundmass. Plagioclase crystals range from euhedral and tabular with polysynthetic and concentric twinning, to anhedral and fractured with undulatory extinction and sericite alteration. Large plagioclase crystals have inclusions of pyroxene. Clinopyroxene phenocrysts are euhedral to subhedral, show simple twinning, and range in size from 0.25-3.5 mm. Clinopyroxene crystals show varying degrees of alteration to chlorite, with many clinopyroxene crystals completely replaced by chlorite. Rare olivine crystals are subhedral and are found in glomerocrysts with clinopyroxene and plagioclase. Groundmass is microcrystalline with a felty texture, and consists of roughly 60% plagioclase laths, 20% opaque minerals 10% pyroxene, and 10% glass.

Sample ID: SB15-56 **Easting:** 0488026
Rock Type: Basaltic-Andesite **Northing:** 6852764

Hand Sample: Fine-grained diorite, medium gray and equigranular. Plagioclase crystals and dark mafic mineral are visible. Fresh sample.

Thin Section: Phaneritic, equigranular, holocrystalline, intrusive rock. Subhedral to anhedral, elongate to tabular plagioclase crystals make up approximately 60% of the rock, the largest crystal being ~3.75 mm long. Plagioclase shows polysynthetic and pericline twinning, contains inclusions of clinopyroxene, and shows rare alteration to sericite. Anhedral clinopyroxene crystals are intergranular to plagioclase, and they show a sub-ophitic texture in places where clinopyroxene is as large as 1.5 mm. Clinopyroxene is replaced by chlorite and opaque minerals. Intergranular biotite pseudomorphs are altered to chlorite and possibly a clay mineral. Apatite needles are found in plagioclase crystals and are less than 0.2 mm long.

Sample ID: 15JB15LA
Rock Type: Rhyolite
Easting: 499075
Northing: 6862322

Hand Sample: Light gray porphyritic rock, with altered feldspar phenocrysts no larger than 1 mm and fresh aphanitic groundmass.

Thin Section: Aphanitic, holocrystalline, porphyritic rock. Groundmass makes up approximately 90% of the rock. Groundmass is microcrystalline with a pilotaxitic texture showing moderate alignment of plagioclase laths, and consists of roughly 80% feldspar crystals, 10% opaque minerals, and 10% translucent oxy-hydroxide minerals. Calcite alteration may also be present in the groundmass. Rare phenocrysts are likely pseudomorphs after sanidine. Relatively fresh rock. This sample may be the same as 15JB16LA.

Sample ID: 15JB16LA
Rock Type: Rhyolite
Easting: 498896
Northing: 6862528

Hand Sample: Light gray porphyritic rock, with rare altered phenocrysts no larger than 1 mm and fresh aphanitic groundmass.

Thin Section: Aphanitic, holocrystalline, sparsely porphyritic rock. Groundmass makes up approximately 95% of the rock. Groundmass is microcrystalline with a pilotaxitic texture, and consists of roughly 70% feldspar crystals, 20% opaque minerals, and 10% translucent oxy-hydroxide minerals. Calcite alteration is seen on larger crystals within the groundmass. Rare phenocrysts are likely pseudomorphs after sanidine. This sample may be the same as 15JB15LA.

Sample ID: 15JB17LA
Rock Type: Andesite
Easting: 498770
Northing: 6862679

Hand Sample: Dark gray aphanitic rock with visible small (<0.5 mm) black phenocrysts.

Thin Section: Phaneritic, hypocrystalline, porphyritic rock. Few plagioclase phenocrysts are fresh and show original twinning, while most are altered to sericite and minor calcite. Pseudomorphs of amphibole are altered to chlorite and opaque minerals. Groundmass is microcrystalline with a felty texture, and consists of roughly 50% plagioclase laths, 10% opaque minerals, and 40% chlorite alteration.

Sample ID: 15JB19LA
Rock Type: Tuff
Easting: 497347
Northing: 6863995

Hand Sample: Light gray to white aphanitic rock with no visible phenocrysts.

Thin Section: Equigranular, aphanitic, hypocrystalline rock. Consists entirely of microcrystalline groundmass with a felty texture. Feldspar, glass, opaque minerals make up approximately equal parts the rock, with minor calcite alteration.

Sample ID: 15JB20LA **Easting:** 497347
Rock Type: Basaltic-Andesite **Northing:** 6863995

Hand Sample: Dark gray equigranular phaneritic rock with elongate plagioclase crystals that are less than 2 mm long and fresh. Weathering rind is medium brown and no more than 3 mm thick.

Thin Section: Phaneritic, hypocrystalline, seriate porphyritic rock. Plagioclase phenocrysts are subhedral to anhedral, elongate to tabular, show polysynthetic and simple twinning, and undulatory extinction. Anhedral plagioclase crystals have embayments and show sieve texture. All plagioclase crystals range in size from a microcrystalline part of the groundmass to 2.5 mm. Pseudomorphs after clinopyroxene are altered to chlorite and possibly serpentine. Groundmass is microcrystalline with a felty texture, and consists of roughly 30% opaque minerals, 40% plagioclase laths, 20% chlorite alteration, and 10% glass.

Sample ID: 15JB21LA **Easting:** 497447
Rock Type: Basalt **Northing:** 68640005

Hand Sample: Chalky white rock with <1mm long elongate hornblende phenocrysts.

Thin Section: Equigranular, aphanitic, hypocrystalline rock. Groundmass makes up >95% of the rock, and consists of cryptocrystalline feldspar and glass in approximately equal abundance. Rare elongate pseudomorphs after amphibole are <1.5 mm.

Sample ID: 15JB25LA **Easting:** 499932
Rock Type: Basalt **Northing:** 6860643

Hand Sample: Dark gray aphanitic rock with no visible phenocrysts. Weathered surfaces and joints are medium brown, but rock is otherwise fresh.

Thin Section: Aphanitic, holocrystalline, seriate porphyritic rock. Olivine phenocrysts are subhedral to anhedral, equant in shape, and range in size from a microcrystalline part of the groundmass to 1.75 mm. Olivine crystals are fractured and show alteration to iddingsite and opaque minerals, and possibly serpentine. The largest olivine phenocrysts only show secondary alteration along fractures, but smaller phenocrysts are almost entirely replaced by secondary phases. Olivine crystals in the groundmass are largely unaltered. Few glomerocrysts of olivine and opaque minerals are found. Rare clinopyroxene crystals are anhedral and elongate, and are <0.5 mm in size. Groundmass is microcrystalline with a pilotaxitic texture, and consists of roughly 45 plagioclase laths, 10% opaque minerals, 30% pyroxene, and 15% alteration products after olivine (iddingsite or serpentine). Plagioclase in the groundmass is very fresh and shows no sign of alteration.

Mode: 49.7% plagioclase; 26.9% clinopyroxene; 11.9% opaque minerals; 11.5% olivine; 782 points total.

Sample ID: 15JB26LA **Easting:** 499842
Rock Type: Basaltic-Andesite **Northing:** 6860694

Hand Sample: Dark gray aphanitic rock with no visible phenocrysts, with medium brown weathering and other secondary alteration in joints/cracks.

Thin Section: Phaneritic, hypocrystalline, seriate porphyritic rock. Plagioclase phenocrysts are anhedral, fractured, and embayed. Polysynthetic twinning on plagioclase crystals is fresh, and some show undulatory extinction. Plagioclase crystals range in size from a microcrystalline part of the groundmass to 1.25 mm. Pseudomorphs after clinopyroxene or olivine are entirely replaced to chlorite and calcite, but retain original crystal shapes. Groundmass is hypocrystalline and microcrystalline with a pilotaxitic to trachyitic texture, and consists of roughly 30% plagioclase laths, 30% glass, 10% opaque minerals, and 30% chlorite alteration after pyroxene. A thin vein (0.1 mm wide) of chlorite, calcite, and an oxy-hydroxide mineral cuts the rock. Broad areas of a silica polymorph mineral (tridymite or cristobalite) are seen in the groundmass as well. Not a fresh rock.

Sample ID: 15JB27LA
Rock Type: Dacite
Easting: 499032
Northing: 6859885

Hand Sample: Porphyritic rock with tabular plagioclase phenocrysts (< 2 mm) and a medium gray groundmass showing pervasive alteration. Few xenoliths are present as well.

Thin Section: Phaneritic, hypocrystalline, porphyritic rock. Plagioclase phenocrysts are anhedral, equant to tabular, show polysynthetic twinning and undulatory zoning, and range in size from 0.1-3 mm. Most plagioclase crystals are fractured, show sieve texture, and have alteration to sericite and calcite on crystal rims and along fractures. Pseudomorphs after hornblende are anhedral, equant to elongate in shape, and range in size from 0.05-1.5 mm. Hornblende crystals are almost entirely replaced by chlorite, opaque minerals, calcite, and an oxy-hydroxide mineral, with only the largest crystals showing an unaltered crystal core. Groundmass is microcrystalline with a felty texture, and consists of roughly equal parts glass and plagioclase crystals, with minor opaque minerals.

Sample ID: 15JB28LA
Rock Type: Dacite
Easting: 498638
Northing: 6859936

Hand Sample: Light brown/tan porphyritic rock, with phenocrysts of equant plagioclase no more than 3 mm large and elongate hornblende no more than 1 mm long.

Thin Section: Phaneritic, hypocrystalline, porphyritic rock. Plagioclase phenocrysts are anhedral, equant to tabular in shape, show polysynthetic and pericline twinning, and range in size from 0.3-4.55 mm. Some plagioclase crystals are embayed and show sieve texture and undulatory extinction, as well as minor alteration to sericite. Hornblende phenocrysts are euhedral to subhedral, elongate to equant, and range in size from 0.1-2 mm. Hornblende crystals are altered to chlorite and opaque minerals on crystal rims and along fractures. Rare apatite needles <0.1 mm are found in plagioclase crystals. Groundmass is microcrystalline and hypocrystalline with a felty texture, and consists of roughly 65% plagioclase laths, 15% glass, 15% chlorite, and 5% opaque minerals.

Sample ID: 15JB30LA
Rock Type: Dacite
Easting: 498459
Northing: 6860065

Hand Sample: Dark gray phaneritic rock with no visible phenocrysts. Crystal faces of what may be plagioclase are visible. Dark green alteration is visible along fracture surfaces.

Thin Section: Phaneritic, hypocrystalline, vitrophyric rock. Clinopyroxene phenocrysts are subhedral to anhedral, and most are entirely altered to chlorite and serpentine. Few fresh clinopyroxene crystals are euhedral. Clinopyroxene crystal sizes range from a microcrystalline part of the groundmass to 2.5 mm. Plagioclase phenocrysts are subhedral to anhedral and elongate in shape, show polysynthetic twinning and undulatory extinction. Plagioclase crystals are altered to sericite and calcite along fractures. Plagioclase crystals are less than 1.5 mm in size. Apatite needles < 0.05 mm long are found in plagioclase crystals. Groundmass is almost entirely composed of glass and is completely altered in places.

Sample ID: 15JB31LA
Rock Type: Andesite
Easting: 498385
Northing: 6860256

Hand Sample: Dark gray phaneritic rock with few plagioclase phenocrysts (< 3 mm) visible among an altered groundmass.

Thin Section: Phaneritic, hypocrystalline, porphyritic rock. Clinopyroxene phenocrysts are subhedral and elongate in shape, show simple twinning, and range in size from 0.1-2.25 mm. Clinopyroxene crystals are altered to chlorite, serpentine, and opaque minerals, especially on crystal rims and along fractures. Plagioclase phenocrysts are subhedral and elongate in shape, show simple and polysynthetic twinning and undulatory extinction, and range in size from a microcrystalline part of the groundmass to 2.5 mm. Plagioclase crystals are altered to sericite. Plagioclase and clinopyroxene are found as glomerocrysts. Groundmass is microcrystalline and is comprised of roughly 80% glass and 20% plagioclase crystals. Portions of the groundmass are composed entirely of glass.

Sample ID: 15JB32LA
Rock Type: Dacite?
Easting: 498328
Northing: 6860873

Hand Sample: Gray phaneritic rock with visible plagioclase crystals <1.5 mm and hornblende crystals <0.5 mm in an aphanitic groundmass. Small sample with a weathering rind.

Thin Section: Phaneritic, holocrystalline, porphyritic rock. Hornblende phenocrysts are euhedral to subhedral, range in size from 0.1- 1.5 mm. Some hornblende crystals are very fresh with only altered rims, but most are almost completely altered to chlorite, serpentine, and opaque minerals. Biotite crystals are anhedral and are altered to chlorite and opaque minerals along crystal rims. Plagioclase phenocrysts are euhedral to subhedral, show polysynthetic and pericline twinning and concentric zoning. Plagioclase crystals range in size from a microcrystalline part of the groundmass to 3.25 mm. Groundmass is microcrystalline and consists of roughly 80% plagioclase crystals, 10% opaque minerals, and 10% chlorite alteration.

Sample ID: 15JB33LA
Rock Type: Andesite
Easting: 498649
Northing: 6861256

Hand Sample: Medium gray phaneritic rock with no phenocrysts visible. Weathered surfaces are brown and red and extend along fractures.

Thin Section: Phaneritic, holocrystalline, seriate porphyritic rock. Plagioclase phenocrysts are subhedral to anhedral, show polysynthetic and simple twinning, undulatory extinction, and range in size from a microcrystalline part of the groundmass to 1.5 mm. Plagioclase crystals show moderate sieve texture. Clinopyroxene phenocrysts are subhedral, show simple twinning, and range in size from a microcrystalline part of the groundmass to 1.5 mm. Clinopyroxene crystals are altered to chlorite, serpentine, and opaque minerals along crystal rims and fractures. Plagioclase and clinopyroxene are found as glomerocrysts. Groundmass is holocrystalline and consists of roughly 60% plagioclase crystals, 20% opaque minerals, and 20% clinopyroxene.

Sample ID: 15JB34LA
Rock Type: Dacite
Easting: 498843
Northing: 6861610

Hand Sample: Medium gray phaneritic rock with < 3 mm tabular and elongate plagioclase phenocrysts visible. Groundmass appears fresh, with minimal alteration.

Thin Section: Phaneritic, hypocrystalline, vitrophyric rock. Plagioclase phenocrysts are anhedral to subhedral, elongate to tabular, show resorption textures, and range in size from 0.05-3 mm. Large plagioclase crystals have concentric zoning, and pericline and simple twinning. Clinopyroxene phenocrysts are subhedral and tabular, range in size from 0.1-1 mm, and are altered to chlorite and serpentine on crystal fractures. Clinopyroxene and plagioclase are found together in glomerocrysts. Groundmass is holohyaline.

Sample ID: 15JB37LA
Rock Type: Dacite
Easting: 500358
Northing: 6860832

Hand Sample: Brown-gray porphyritic rock, with a moderately altered and very aphanitic groundmass and visible quartz and plagioclase phenocrysts. Rare vesicles are angular and stretched.

Thin Section: Phaneritic, hypocrystalline, porphyritic rock. Plagioclase phenocrysts are subhedral to anhedral, show polysynthetic and pericline twinning, concentric zoning, and intense sieve and resorption textures. Plagioclase crystals range in size from 0.1-2 mm and are altered to sericite and calcite along crystal fractures. Rare pseudomorphs after clinopyroxene are composed of chlorite and an oxy-hydroxide mineral, with reaction rims of opaque minerals. Groundmass is microcrystalline and hypocrystalline with a pilotaxitic texture, and consists of roughly 40% plagioclase, 50% glass, and 10% opaque minerals.

Sample ID: 15JB38LA
Rock Type: Rhyolite
Easting: 500652
Northing: 6860990

Hand Sample: Yellow-brown porphyritic rock, with quartz and feldspar phenocrysts visible in a moderately altered groundmass. Heavily weathered along fractures.

Thin Section: Phaneritic, holocrystalline, porphyritic rock. Quartz phenocrysts are anhedral, some with a round shape and some with embayments, and most have patchy zoning and undulatory extinction. Quartz ranges in size from 0.1-1.5 mm. Sanidine phenocrysts are euhedral to subhedral, equant to tabular in shape, show polysynthetic and simple twinning and undulatory extinction, and range in size form 0.1-2.25 mm. Few sanidine phenocrysts have biotite inclusions, and sanidine overall shows few signs of alteration. Biotite phenocrysts range in shape and habit from euhedral sheets, to anhedral crystal fragments, and range in size from 0.1-1.5 mm. Most biotite crystals are relatively fresh, but a few phenocrysts have been partially to completely replaced by an oxy-hydroxide mineral. Rare vesicles are angular in shape and range in size from 0.1-1.75 mm. Groundmass is holocrystalline and microcrystalline, and consists of roughly 10% biotite, 45% sanidine, and 45% quartz. Patches of the groundmass contain an mostly isotropic brown alteration product.

Mode: 88.5% groundmass (2.3% altered); 3.1% quartz; 3.3% sanidine; 2.5% biotite (1.1% altered); 2.6% vesicles. 731 points total.

Sample ID: 15JB39LA
Rock Type: Dacite
Easting: 498259
Northing: 6859902

Hand Sample: Medium gray porphyritic rock, with visible quartz phenocrysts and aligned hornblende phenocrysts in a fresh groundmass.

Thin Section: Phaneritic, holocrystalline, seriate porphyritic rock. Plagioclase crystals range in size from a microcrystalline part of the groundmass to 1.25 mm. Plagioclase crystals are euhedral to subhedral and elongate in shape, and show simple and pericline twinning and undulatory extinction. Pseudomorphs after hornblende have been altered to opaque minerals and chlorite, the largest of which is 2.5 mm long. Groundmass is holocrystalline with a pilotaxitic to trachytic texture, and consists of approximately 20% opaque minerals and 80% plagioclase laths.

Sample ID: 15JB40LA
Rock Type: Dacite
Easting: 498017
Northing: 6860250

Hand Sample: Dark gray porphyritic rock, with rare hornblende phenocrysts in a fresh groundmass.

Thin Section: Phaneritic, hypocrystalline, porphyritic rock. Hornblende phenocrysts are euhedral to subhedral and elongate and tabular in shape, and are less than 0.8 mm in size. Rare hornblende crystals are altered to chlorite and opaque minerals along crystal edges and interiors. Plagioclase phenocrysts are euhedral to subhedral crystal fragments, show polysynthetic and pericline twinning, concentric zoning, undulatory extinction, and range in size from 0.1-2 mm. Plagioclase crystals show extensive sieve texture in crystal cores, and are altered to sericite and calcite along fractures. Groundmass is microcrystalline with a trachytic texture showing a strong alignment of

plagioclase laths and hornblende crystals, and consists of roughly 50% plagioclase laths, 25% glass, 20% opaque minerals, and 5% hornblende.

Sample ID: 15JB41LA **Easting:** 497423
Rock Type: Dacite **Northing:** 6860685

Hand Sample: Light gray vesicular porphyritic rock, with hornblende phenocrysts up to 7 mm long, altered feldspar phenocrysts, and elongate vesicles up to 2 cm long. Vesicles are partially filled with secondary alteration.

Thin Section: Phaneritic, hypocrystalline, porphyritic rock. Hornblende phenocrysts are subhedral and elongate in shape, and range in size from 0.05-2 mm long. Hornblende crystals are altered to chlorite and opaque minerals (and possibly serpentine) on crystal rims and along fractures. Plagioclase phenocrysts are subhedral and tabular in shape, and show extensive alteration to sericite. The rare fresh plagioclase crystals show moderate sieve texture, and plagioclase ranges in size from 0.1-2.5 mm. Elongate vesicles are abundant and range in size from 0.15-2 mm. Vesicles are filled with secondary oxide and oxy-hydroxide minerals, as well as chlorite, calcite, and possibly a quartz polymorph (tridymite or cristobalite). Groundmass is microcrystalline with a felty texture, and consists of roughly 50% plagioclase, 30% opaque minerals, and 20% glass.

Sample ID: 15JB42LA **Easting:** 497423
Rock Type: Basaltic-Andesite **Northing:** 6860685

Hand Sample: Dark gray aphanitic rock, with pervasive dark red weathering/alteration.

Thin Section: Phaneritic, hypocrystalline, seriate porphyritic rock. Plagioclase phenocrysts are euhedral to subhedral and elongate to tabular in shape, show polysynthetic and pericline twinning, concentric zoning and undulatory extinction, and range in size from a microcrystalline part of the groundmass to 4.75 mm. Most of the large plagioclase crystals have sieved cores and show alteration to sericite. Few plagioclase crystals have pyroxene inclusions. Clinopyroxene phenocrysts are subhedral to anhedral, show simple twinning, and range in size from a microcrystalline part of the groundmass to 1.5 mm. Clinopyroxene crystals show varying degrees of alteration to chlorite, serpentine, and opaque minerals, with most being completely replaced. Opaque minerals are equant in shape and are no larger than 0.1 mm. Apatite needles <0.1 mm are found in plagioclase crystals. Rare glomerocrysts of plagioclase, clinopyroxene, and opaque minerals are <1.5 mm in size. Groundmass has a pilotaxitic texture and consists of roughly 50% plagioclase, 20% opaque minerals, 20% glass, and 10% clinopyroxene.

Sample ID: 15JB43LA **Easting:** 496861
Rock Type: Lava **Northing:** 6860891

Hand Sample: Grey-green rock, with plagioclase phenocrysts visible. Very altered hand sample.

Thin Section: Phaneritic, porphyritic rock. Plagioclase phenocrysts are euhedral and tabular in shape, show characteristic twinning and zoning, and are <3 mm in size. Pervasive serpentine or epidote alteration is found as a replacement of a mafic phase. Very altered rock.

Sample ID: 15JB44LA **Easting:** 498249
Rock Type: Dacite **Northing:** 6861624

Hand Sample: Light gray aphanitic rock, with no visible phenocrysts. Rust colored alteration in fractures.

Thin Section: Phaneritic, hypocrystalline, porphyritic rock. Sample consists almost entirely of plagioclase, as phenocrysts and in the groundmass. Plagioclase phenocrysts are subhedral, show pericline and polysynthetic twinning, and are no larger than 2 mm in size. Pseudomorphs after a mafic mineral have been replaced entirely to calcite and opaque minerals. Groundmass shows a pilotaxitic texture, and consists of roughly 85% plagioclase, 10% glass, and 5% opaque minerals.

Sample ID: 15JB45LA **Easting:** 496074
Rock Type: Dacite **Northing:** 6857982

Hand Sample: Gray/green porphyritic rock, with visible plagioclase phenocrysts no larger than 2 mm in a relatively fresh groundmass.

Thin Section: Phaneritic, hypocrystalline, seriate porphyritic rock. Plagioclase phenocrysts are subhedral to anhedral, show characteristic zoning and twinning, and some are resorbed on crystal edges. Plagioclase crystals are altered to sericite and in crystal cores, and range in size from a microcrystalline part of the groundmass to 3 mm. Clinopyroxene phenocrysts are subhedral and tabular in shape, and altered to serpentine and calcite to varying degrees. Rare hornblende crystals are euhedral and <0.75 mm in size, and show reaction rims of opaque minerals. Groundmass is microcrystalline with a felty texture, and consists of roughly 40% plagioclase, 20% opaque minerals, 20% glass, and 20% serpentine alteration.

Sample ID: 15JB46LA **Easting:** 496074
Rock Type: Dacite **Northing:** 6858230

Hand Sample: Purple/gray porphyritic rock, with < 3 mm tabular plagioclase crystals in an aphanitic groundmass that shows chlorite alteration.

Thin Section: Phaneritic, hypocrystalline, seriate porphyritic rock. Hornblende pseudomorphs <1 mm have been entirely replaced by opaque minerals and calcite, but make up approximately 20% of the rock. Plagioclase phenocrysts are subhedral to anhedral, show polysynthetic and pericline twinning, concentric zoning, undulatory extinction, and range in size from a microcrystalline part of the groundmass to 2 mm. Apatite needles <0.1 mm are found in plagioclase crystals. Groundmass is microcrystalline with a felty texture, and consists of roughly 40% plagioclase, 40% glass, and 20% opaque minerals.

Sample ID: 15JB47LA **Easting:** 496706
Rock Type: Andesite **Northing:** 6858539

Hand Sample: Black phaneritic rock, with no visible phenocrysts. Other than a thin weathering rind, a fresh rock.

Thin Section: Phaneritic, holocrystalline, seriate porphyritic rock. Clinopyroxene phenocrysts are euhedral to subhedral, show simple twinning and undulatory extinction, and range in size from 0.05-2.25 mm. Most large clinopyroxene crystals are fresh, but most small clinopyroxene crystals (and much of the groundmass) are altered to chlorite and opaque minerals on crystal rims and along fractures. Plagioclase phenocrysts are euhedral crystals to anhedral crystal fragments, and show characteristic polysynthetic and pericline twinning, concentric zoning, and undulatory extinction. Large plagioclase crystals show sieved interiors and moderate sericite alteration along crystal fractures. Plagioclase crystals range in size from a microcrystalline part of the groundmass to 2.5 mm. Glomerocrysts as large as 2.5 mm are comprised of plagioclase, clinopyroxene, and opaque minerals. Groundmass is microcrystalline with a felty texture, and consists of roughly 70% plagioclase, 15% opaque minerals, and 15% clinopyroxene.

Mode: 58.8% groundmass; 27.2% plagioclase; 12.1% clinopyroxene; 1.9% opaque minerals; 688 points total.

Sample ID: 15JB49LA
Rock Type: Trachyandesite
Easting: 499080
Northing: 6862200

Hand Sample: Light gray aphanitic rock, with no visible phenocrysts.

Thin Section: Phaneritic, hypocrystalline, porphyritic rock. Plagioclase phenocrysts are subhedral to anhedral, show extensive sieve texture and resorption textures, and are <1.5 mm in size. Other phenocryst phases, as well as rare vesicles, appear to have been completely replaced by calcite. Groundmass is microcrystalline with a felty texture, and consists of roughly 50% glass, 30% plagioclase laths, 10% opaque minerals, and 10% calcite alteration.

Appendix B - Geochemical and Geochronologic Data

Major and trace elements analyzed at Franklin and Marshall College were by XRF. Major and trace elements analyzed at Washington State University were by XRF, and REE and other select trace elements were by ICP-MS. All major element data is expressed as raw wt %, Fe_2O_3* is total Fe, and all other concentrations are in ppm. A "--" symbol shows an element not determined for that sample. Font of the data (italics, bold, or normal) denotes the method of analysis used for that element for that particular sample, and correspond to the three columns showing precision (one standard deviation) at the end of the Appendix; italicized and left-indented font is ICP-MS data from WSU, normal and right-indented font is XRF data from WSU, and bold and right-indented font is XRF data from Franklin and Marshall College. $^{40}Ar/^{39}Ar$ data with analytical uncertainty for each sample from UAF is in the bottom two rows. Samples that were excluded from geochemical consideration are noted by an asterisk after the sample number.

Sample ID	SB15-17	SB15-18	SB15-19	SB15-20	SB15-21	SB15-22	SB15-23	SB15-24	SB15-25
Rock Unit/Location	Cabin Creek	Cabin Creek	Cabin Creek	Cabin Creek	Cabin Creek	Cabin Creek	Cabin Creek	Cabin Creek	Cabin Creek
SiO_2	56.49	59.91	59.23	63.24	63.96	63.55	63.28	59.19	62.59
TiO_2	1.60	1.02	1.06	0.89	0.88	0.88	0.85	1.22	1.12
Al_2O_3	16.41	17.11	17.82	16.59	16.97	16.36	16.59	17.67	17.53
Fe_2O_3*	8.60	6.05	6.54	5.66	4.96	5.86	5.73	6.85	5.08
MnO	0.13	0.09	0.09	0.07	0.06	0.08	0.10	0.11	0.05
MgO	2.87	2.58	2.27	1.49	1.07	1.21	1.66	1.70	1.06
CaO	5.93	5.72	5.85	4.04	4.03	3.91	4.22	5.34	4.55
Na_2O	4.51	4.04	4.72	5.00	5.11	5.01	5.06	4.97	5.17
K_2O	2.03	2.05	1.43	2.02	2.09	2.10	1.99	1.53	1.74
P_2O_5	0.59	0.29	0.28	0.26	0.25	0.26	0.25	0.39	0.30
Total	98.29	98.26	98.61	98.68	98.88	98.61	99.15	98.26	98.65
LOI	1.26	0.96	1.14	0.97	1.10	1.02	0.47	1.05	0.87
Rb	*36.6*	*32.8*	*25.0*	*40.6*	*42.7*	*43.0*	*41.4*	*27.3*	*32.5*
Sr	*547*	*568*	*528*	*396*	*404*	*380*	*408*	*568*	*496*
Y	*38.58*	*20.09*	*23.80*	*26.10*	*24.29*	*25.77*	*27.13*	*29.18*	*23.93*
Zr	*327*	*177*	*205*	*303*	*310*	*307*	*300*	*232*	*243*
V	160	125	137	75	90	84	72	126	114
Ni	19	29	20	9	10	11	12	11	8
Cr	17	27	12	6	5	5	4	1	3
Nb	*15.55*	*8.83*	*10.47*	*13.65*	*13.74*	*13.71*	*13.40*	*11.24*	*11.35*
Ga	20	18	18	18	19	19	17	19	19
Cu	60	34	55	25	25	16	20	31	18
Zn	101	73	75	61	74	58	67	82	81
Co	--	--	--	--	--	--	--	--	--
Ba	*555*	*525*	*482*	*611*	*630*	*618*	*605*	*553*	*610*
La	32	18	21	28	24	24	23	21	24
Ce	67	35	41	48	48	48	50	49	44
U	*1.90*	*1.43*	*1.39*	*2.22*	*2.36*	*2.22*	*2.20*	*1.47*	*1.61*
Th	*4.91*	*3.36*	*3.32*	*5.15*	*5.29*	*5.21*	*5.07*	*3.63*	*3.98*
Sc	*17.4*	*12.9*	*13.0*	*9.7*	*9.2*	*9.3*	*9.6*	*13.4*	*11.8*
Pb	*6.85*	*6.06*	*5.13*	*7.33*	*7.18*	*7.29*	*6.68*	*7.38*	*5.61*
Hf	*7.64*	*4.28*	*4.72*	*6.74*	*6.93*	*6.88*	*6.70*	*5.34*	*5.48*
Ta	*1.06*	*0.67*	*0.76*	*1.09*	*1.09*	*1.09*	*1.06*	*0.83*	*0.87*
Cs	*0.99*	*0.87*	*0.34*	*0.66*	*0.74*	*0.91*	*0.60*	*0.36*	*0.46*
La	*31.48*	*18.65*	*20.72*	*24.98*	*24.36*	*24.93*	*25.17*	*23.40*	*22.86*
Ce	*67.77*	*37.72*	*41.16*	*49.59*	*50.21*	*50.03*	*49.20*	*46.41*	*45.42*
Pr	*8.63*	*4.65*	*5.05*	*5.98*	*5.75*	*5.97*	*5.92*	*5.88*	*5.57*
Nd	*35.37*	*18.67*	*20.04*	*22.91*	*22.12*	*22.86*	*22.71*	*23.64*	*21.81*
Sm	*8.04*	*4.12*	*4.52*	*5.01*	*4.78*	*4.93*	*4.82*	*5.28*	*4.87*
Eu	*2.22*	*1.31*	*1.43*	*1.42*	*1.45*	*1.44*	*1.45*	*1.63*	*1.57*
Gd	*7.77*	*4.07*	*4.56*	*4.87*	*4.66*	*4.73*	*4.86*	*5.36*	*4.79*
Tb	*1.24*	*0.65*	*0.75*	*0.79*	*0.75*	*0.78*	*0.81*	*0.86*	*0.79*
Dy	*7.64*	*3.99*	*4.63*	*4.94*	*4.52*	*4.98*	*5.06*	*5.31*	*4.74*
Ho	*1.51*	*0.78*	*0.93*	*1.02*	*0.93*	*1.01*	*1.03*	*1.09*	*0.94*
Er	*4.06*	*2.09*	*2.51*	*2.83*	*2.57*	*2.72*	*2.87*	*2.97*	*2.54*
Tm	*0.59*	*0.30*	*0.36*	*0.41*	*0.38*	*0.40*	*0.42*	*0.43*	*0.37*
Yb	*3.67*	*1.89*	*2.29*	*2.68*	*2.42*	*2.62*	*2.83*	*2.73*	*2.29*
Lu	*0.56*	*0.29*	*0.36*	*0.42*	*0.37*	*0.42*	*0.44*	*0.43*	*0.35*
Age	21.3	19.65	23.29	22.06	--	--	22.5	22.08	21.5
error	0.1	0.43	0.26	0.4	--	--	0.21	0.2	0.2

Sample ID	SB15-26	SB15-27	SB15-28	SB15-29	SB15-30	SB15-31	SB15-32	SB15-33*	SB15-34
Rock Unit/Location	Cabin Creek	Cabin Creek	Cabin Creek	Cabin Creek	Cabin Creek	Cabin Creek	Cabin Creek	Dome Field	Silicic Lava
SiO_2	63.86	64.26	59.09	57.11	**57.48**	56.03	55.01	63.07	75.33
TiO_2	1.18	1.14	1.75	1.11	**1.09**	1.05	1.03	0.36	0.07
Al_2O_3	15.66	15.55	15.35	16.31	**16.35**	16.40	17.34	15.43	13.62
Fe_2O_3*	5.60	5.47	8.55	7.43	**7.47**	7.75	7.37	3.24	0.81
MnO	0.11	0.10	0.12	0.11	**0.12**	0.12	0.14	0.06	0.09
MgO	1.51	1.38	2.43	4.34	**4.39**	5.06	4.41	1.74	0.13
CaO	3.52	3.37	5.18	6.83	**6.93**	7.39	8.19	4.43	0.74
Na_2O	5.30	5.33	4.81	4.16	**4.28**	4.00	3.91	4.17	3.74
K_2O	2.41	2.50	2.02	1.48	**1.40**	1.44	0.96	1.39	3.80
P_2O_5	0.39	0.36	0.68	0.33	**0.34**	0.30	0.22	0.12	0.07
Total	98.96	98.90	99.12	98.46	**99.85**	98.74	97.83	93.68	98.32
LOI	0.65	0.60	0.52	0.69	**0.63**	0.55	1.22	6.12	1.53
Rb	*46.4*	*49.8*	*31.5*	*31.3*	**30**	*30.9*	*16.2*	*30.3*	*101.7*
Sr	*410*	*397*	*483*	*518*	**538**	*574*	*467*	*485*	*116*
Y	*31.41*	*32.26*	*32.03*	*23.07*	**28**	*22.48*	*21.89*	*7.87*	*12.30*
Zr	*303*	*313*	*237*	*202*	**205**	*187*	*147*	*93*	*54*
V	88	84	187	153	**161**	165	163	62	7
Ni	3	4	4	57	**69**	63	69	39	3
Cr	0	0	0	100	**119**	139	77	62	3
Nb	*13.91*	*14.13*	*11.32*	*10.21*	**11**	*8.66*	*5.76*	*4.92*	*16.79*
Ga	19	19	19	18	**20**	17	17	15	16
Cu	8	8	30	57	**80**	63	76	25	4
Zn	75	75	92	77	**81**	71	67	45	37
Co	--	--	--	--	**25**	--	--	--	--
Ba	*603*	*609*	*533*	*442*	**444**	*386*	*315*	*587*	*835*
La	25	26	22	23	**21**	20	13	10	3
Ce	51	50	51	42	**39**	37	30	18	9
U	*2.08*	*2.11*	*1.38*	*1.50*	**2**	*1.33*	*0.88*	*1.08*	*3.59*
Th	*4.96*	*5.12*	*3.23*	*3.47*	**5**	*3.18*	*2.16*	*2.66*	*4.07*
Sc	*11.8*	*11.9*	*18.1*	*18.3*	**17**	*20.5*	*21.1*	*8.0*	*3.0*
Pb	*7.13*	*8.07*	*5.90*	*5.06*	**<1**	*4.43*	*2.58*	*5.61*	*12.18*
Hf	*7.13*	*7.19*	*5.60*	*4.75*	--	*4.44*	*3.51*	*2.45*	*2.28*
Ta	*0.98*	*1.00*	*0.78*	*0.74*	--	*0.63*	*0.42*	*0.41*	*1.86*
Cs	*0.52*	*0.60*	*0.81*	*0.58*	--	*0.53*	*0.10*	*0.61*	*2.08*
La	*26.27*	*26.69*	*23.69*	*21.06*	--	*18.42*	*13.39*	*12.09*	*6.64*
Ce	*54.25*	*55.29*	*51.57*	*43.13*	--	*38.24*	*28.87*	*21.53*	*13.43*
Pr	*6.88*	*6.91*	*6.73*	*5.36*	--	*4.81*	*3.77*	*2.45*	*1.58*
Nd	*27.71*	*27.46*	*28.29*	*21.40*	--	*19.35*	*15.91*	*9.15*	*5.48*
Sm	*6.13*	*6.16*	*6.73*	*4.65*	--	*4.52*	*3.83*	*1.83*	*1.46*
Eu	*1.75*	*1.71*	*1.91*	*1.39*	--	*1.33*	*1.29*	*0.63*	*0.20*
Gd	*5.94*	*5.99*	*6.55*	*4.53*	--	*4.34*	*4.11*	*1.68*	*1.57*
Tb	*0.98*	*0.98*	*1.04*	*0.74*	--	*0.71*	*0.68*	*0.25*	*0.31*
Dy	*6.04*	*6.13*	*6.32*	*4.45*	--	*4.41*	*4.24*	*1.48*	*2.04*
Ho	*1.21*	*1.24*	*1.25*	*0.89*	--	*0.89*	*0.87*	*0.30*	*0.41*
Er	*3.31*	*3.38*	*3.33*	*2.42*	--	*2.39*	*2.39*	*0.77*	*1.13*
Tm	*0.49*	*0.50*	*0.48*	*0.35*	--	*0.34*	*0.34*	*0.11*	*0.17*
Yb	*3.17*	*3.28*	*3.01*	*2.22*	--	*2.18*	*2.14*	*0.72*	*1.12*
Lu	*0.48*	*0.52*	*0.46*	*0.35*	--	*0.33*	*0.35*	*0.11*	*0.16*
Age	--	20.7	18.48	21.26	21.68	21.74	22	28.8	23.92
error	--	0.4	0.52	0.48	0.4	0.62	0.3	0.2	0.15

Sample ID	SB15-36*	SB15-37*	SB15-38*	SB15-39	SB15-40	SB15-41	SB15-42	SB15-43	SB15-45
Rock Unit/Location	Dome Field	Dome Field	Dome Field	Flat Top	Flat Top	Flat Top	Flat Top	Intermediate Domes	Silicic Lava
SiO_2	53.91	52.70	56.20	48.48	69.69	65.96	67.68	59.94	69.65
TiO_2	1.14	0.89	0.93	1.37	0.67	1.17	0.98	0.92	0.33
Al_2O_3	16.71	18.71	18.94	16.65	14.44	14.95	14.64	16.40	13.69
Fe_2O_3*	7.42	7.44	5.49	10.81	3.15	5.34	4.40	5.65	2.09
MnO	0.12	0.11	0.07	0.16	0.07	0.06	0.06	0.12	0.04
MgO	4.33	2.61	1.50	8.39	0.41	0.77	0.77	2.73	0.70
CaO	7.94	7.69	5.68	9.14	1.42	2.74	2.21	5.17	2.33
Na_2O	3.43	4.00	4.77	3.34	5.24	5.19	5.27	4.39	3.58
K_2O	0.70	0.42	1.45	0.60	3.28	2.70	2.95	1.76	3.15
P_2O_5	0.28	0.42	0.42	0.29	0.10	0.32	0.24	0.23	0.07
Total	95.22	94.22	94.89	98.14	98.16	98.66	98.76	96.73	95.43
LOI	4.72	5.18	4.62	1.53	0.71	1.38	0.98	2.95	3.44
Rb	*11.0*	*9.3*	*24.6*	*8.6*	*66.5*	*57.3*	*60.9*	*30.0*	*74.3*
Sr	*552*	*935*	*854*	*540*	*189*	*318*	*268*	*501*	*229*
Y	*27.23*	*20.41*	*20.55*	*23.08*	*41.88*	*52.24*	*42.44*	*21.59*	*13.90*
Zr	*235*	*188*	*179*	*108*	*457*	*381*	*411*	*209*	*178*
V	166	120	127	207	28	53	38	112	27
Ni	46	3	4	139	4	2	6	24	8
Cr	71	0	0	282	2	0	0	30	5
Nb	*9.75*	*10.42*	*10.23*	*8.94*	*14.90*	*13.61*	*14.48*	*9.32*	*9.55*
Ga	18	20	19	17	18	18	18	18	14
Cu	50	13	18	66	5	3	2	26	11
Zn	70	92	93	88	56	84	69	73	34
Co	--	--	--	--	--	--	--	--	--
Ba	*759*	*384*	*371*	*215*	*834*	*756*	*813*	*639*	*691*
La	20	20	20	8	32	35	31	19	21
Ce	39	43	45	26	61	61	70	41	34
U	*1.61*	*0.85*	*0.85*	*0.36*	*3.00*	*2.55*	*2.75*	*1.80*	*2.92*
Th	*3.82*	*2.39*	*2.32*	*1.03*	*7.08*	*5.73*	*6.24*	*4.31*	*7.83*
Sc	*19.5*	*10.2*	*11.2*	*30.8*	*7.5*	*11.4*	*9.8*	*13.2*	*3.7*
Pb	*5.62*	*4.16*	*3.76*	*2.03*	*11.04*	*8.59*	*7.84*	*7.88*	*9.02*
Hf	*5.37*	*4.20*	*4.11*	*2.66*	*10.96*	*9.22*	*9.97*	*4.92*	*4.72*
Ta	*0.71*	*0.66*	*0.65*	*0.57*	*1.05*	*0.97*	*1.04*	*0.76*	*0.89*
Cs	*0.36*	*1.20*	*1.35*	*0.10*	*0.66*	*2.01*	*0.81*	*0.42*	*1.12*
La	*19.66*	*22.35*	*21.24*	*12.11*	*33.39*	*33.27*	*31.92*	*21.04*	*20.48*
Ce	*41.05*	*45.71*	*44.01*	*26.92*	*68.93*	*64.48*	*67.56*	*41.89*	*36.48*
Pr	*5.13*	*5.62*	*5.57*	*3.66*	*9.12*	*9.29*	*8.87*	*4.99*	*4.04*
Nd	*20.83*	*23.02*	*22.61*	*16.23*	*35.94*	*37.82*	*35.52*	*19.48*	*13.81*
Sm	*4.81*	*4.72*	*4.69*	*4.20*	*7.98*	*8.56*	*7.94*	*4.26*	*2.68*
Eu	*1.40*	*1.60*	*1.63*	*1.52*	*1.70*	*2.07*	*1.90*	*1.34*	*0.66*
Gd	*4.94*	*4.22*	*4.29*	*4.22*	*7.50*	*8.42*	*7.42*	*4.02*	*2.29*
Tb	*0.84*	*0.67*	*0.67*	*0.73*	*1.27*	*1.43*	*1.23*	*0.67*	*0.39*
Dy	*5.22*	*3.91*	*3.96*	*4.58*	*7.90*	*8.74*	*7.61*	*4.16*	*2.41*
Ho	*1.06*	*0.80*	*0.82*	*0.92*	*1.62*	*1.84*	*1.58*	*0.84*	*0.51*
Er	*2.87*	*2.15*	*2.16*	*2.51*	*4.46*	*5.04*	*4.37*	*2.29*	*1.47*
Tm	*0.41*	*0.32*	*0.31*	*0.36*	*0.67*	*0.75*	*0.63*	*0.34*	*0.23*
Yb	*2.67*	*1.99*	*2.01*	*2.23*	*4.29*	*4.61*	*4.03*	*2.17*	*1.52*
Lu	*0.41*	*0.32*	*0.33*	*0.36*	*0.68*	*0.73*	*0.65*	*0.34*	*0.25*
Age	23.67	28.03	--	24.58	19.3	19.71	--	22.95	20.34
error	0.64	3.09	--	0.26	0.1	0.13	--	0.16	0.12

Sample ID	SB15-46	SB15-47	SB15-48	SB15-50*	SB15-51	SB15-52	SB15-53	SB15-54	SB15-55
Rock Unit/Location	Intermediate Domes	Intermediate Domes	Intermediate Domes	Young Creek	Young Creek	Young Creek	Young Creek	Young Creek	Young Creek
SiO_2	52.93	64.66	56.18	58.04	55.52	59.10	54.65	58.46	58.73
TiO_2	1.37	0.68	1.10	1.02	0.99	0.88	1.28	0.82	0.85
Al_2O_3	17.18	16.31	18.08	13.79	16.34	16.65	16.73	16.67	17.00
Fe_2O_3*	8.22	4.94	7.81	7.36	7.05	5.84	7.96	6.25	6.66
MnO	0.18	0.08	0.12	0.10	0.11	0.09	0.13	0.11	0.10
MgO	3.40	1.81	3.19	5.31	5.68	3.09	4.69	3.49	3.49
CaO	8.54	4.17	6.34	6.93	8.02	6.28	8.35	5.93	6.54
Na_2O	3.62	4.66	4.49	2.79	3.50	3.50	3.59	4.28	4.00
K_2O	1.29	1.87	1.18	0.30	0.47	1.39	0.64	0.93	1.31
P_2O_5	0.37	0.19	0.30	0.17	0.25	0.20	0.37	0.24	0.23
Total	96.25	98.87	97.99	95.07	97.20	96.42	97.56	96.55	98.24
LOI	3.11	0.73	1.85	4.30	2.35	2.89	1.92	2.31	1.31
Rb	*20.4*	*41.3*	*24.4*	*6.0*	*7.1*	*25.1*	*7.3*	*16.4*	*20.5*
Sr	*543*	*485*	*572*	*426*	*566*	*560*	*617*	*675*	*627*
Y	*29.34*	*19.68*	*22.33*	*18.31*	*18.83*	*18.72*	*28.13*	*17.38*	*18.10*
Zr	*238*	*216*	*165*	*115*	*148*	*146*	*184*	*132*	*138*
V	173	96	153	136	155	120	163	132	135
Ni	44	17	16	94	124	38	60	47	47
Cr	39	15	8	160	183	48	96	34	32
Nb	*10.15*	*7.89*	*8.02*	*4.16*	*5.88*	*6.34*	*8.95*	*5.86*	*6.06*
Ga	19	17	18	15	17	17	18	18	16
Cu	54	39	33	37	54	39	47	42	29
Zn	84	60	81	64	70	76	82	73	69
Co	--	--	--	--	--	--	--	--	--
Ba	*376*	*528*	*429*	*218*	*287*	*471*	*449*	*439*	*486*
La	23	18	18	7	11	16	17	14	15
Ce	43	32	33	20	27	27	41	29	28
U	*1.36*	*1.36*	*1.13*	*0.41*	*0.90*	*1.19*	*1.00*	*1.05*	*1.06*
Th	*3.32*	*3.59*	*2.56*	*1.04*	*1.98*	*2.83*	*2.26*	*2.38*	*2.48*
Sc	*19.5*	*9.6*	*13.9*	*20.1*	*18.8*	*14.9*	*20.3*	*14.4*	*15.1*
Pb	*4.99*	*6.55*	*4.41*	*2.89*	*3.52*	*6.45*	*3.37*	*5.58*	*4.79*
Hf	*5.45*	*5.33*	*3.90*	*2.78*	*3.50*	*3.55*	*4.39*	*3.26*	*3.42*
Ta	*0.74*	*0.61*	*0.60*	*0.30*	*0.46*	*0.50*	*0.63*	*0.45*	*0.45*
Cs	*4.33*	*0.79*	*0.85*	*3.00*	*0.19*	*1.33*	*0.36*	*0.13*	*0.22*
La	*20.85*	*17.59*	*16.10*	*9.09*	*13.80*	*14.73*	*17.78*	*15.08*	*15.46*
Ce	*45.26*	*36.00*	*34.13*	*20.42*	*29.09*	*30.01*	*38.12*	*30.38*	*31.10*
Pr	*5.81*	*4.38*	*4.36*	*2.80*	*3.70*	*3.73*	*4.92*	*3.76*	*3.84*
Nd	*23.91*	*17.22*	*18.06*	*12.31*	*15.31*	*15.10*	*20.92*	*15.27*	*15.54*
Sm	*5.51*	*3.85*	*4.20*	*3.10*	*3.61*	*3.53*	*5.07*	*3.50*	*3.42*
Eu	*1.72*	*1.04*	*1.43*	*1.13*	*1.21*	*1.16*	*1.60*	*1.14*	*1.15*
Gd	*5.57*	*3.56*	*4.33*	*3.39*	*3.67*	*3.52*	*5.11*	*3.34*	*3.43*
Tb	*0.93*	*0.61*	*0.71*	*0.57*	*0.62*	*0.57*	*0.87*	*0.54*	*0.56*
Dy	*5.68*	*3.68*	*4.41*	*3.54*	*3.68*	*3.63*	*5.38*	*3.35*	*3.46*
Ho	*1.16*	*0.74*	*0.90*	*0.71*	*0.75*	*0.73*	*1.11*	*0.68*	*0.71*
Er	*3.14*	*2.08*	*2.41*	*1.95*	*2.01*	*2.02*	*3.01*	*1.86*	*1.93*
Tm	*0.44*	*0.30*	*0.34*	*0.28*	*0.29*	*0.28*	*0.43*	*0.27*	*0.28*
Yb	*2.77*	*1.93*	*2.11*	*1.72*	*1.81*	*1.79*	*2.67*	*1.68*	*1.71*
Lu	*0.44*	*0.31*	*0.34*	*0.27*	*0.28*	*0.29*	*0.42*	*0.27*	*0.27*
Age	22.64	22.17	21.67	--	20.23	19.67	21.31	19.22	19.07
error	0.24	0.11	0.31	--	0.7	0.2	0.48	0.3	0.17

Sample ID	SB15-56	15JB15LA	15JB16LA	15JB17LA*	15JB20LA*	15JB25LA	15JB26LA	15JB27LA	15JB28LA
Rock Unit/Location	Young Creek	Silicic Lava	Silicic Lava	Rocker Creek	Rocker Creek	Rocker Creek	Rocker Creek	Rocker Creek	Rocker Creek
SiO_2	51.87	72.85	**73.94**	59.46	52.12	49.93	51.88	65.59	**67.00**
TiO_2	1.01	0.18	**0.16**	0.60	1.11	1.35	1.25	0.49	**0.53**
Al_2O_3	18.48	14.73	**15.15**	15.89	16.87	16.14	14.83	15.09	**16.03**
Fe_2O_3*	8.21	1.50	**1.70**	4.72	7.53	9.95	8.68	3.44	**4.21**
MnO	0.13	0.06	**0.06**	0.08	0.12	0.15	0.13	0.08	**0.08**
MgO	5.29	0.16	**0.39**	4.18	3.26	7.48	6.62	0.94	**1.75**
CaO	8.40	2.07	**2.01**	5.68	8.12	9.62	9.56	4.42	**3.72**
Na_2O	3.97	4.39	**4.48**	4.23	4.01	3.41	2.90	4.12	**4.87**
K_2O	0.48	1.84	**1.83**	1.19	0.79	0.70	0.92	2.00	**1.93**
P_2O_5	0.34	0.08	**0.08**	0.17	0.33	0.39	0.38	0.15	**0.17**
Total	97.33	97.70	**99.80**	95.72	93.50	98.12	96.26	95.98	**100.29**
LOI	1.58	1.76	**2.31**	3.94	5.84	1.04	3.03	3.51	**1.45**
Rb	*5.2*	*41.2*	**56**	*21.9*	*7.5*	*9.7*	*12.8*	*44.2*	**52**
Sr	*813*	*380*	**434**	*663*	*940*	*632*	*823*	*347*	**413**
Y	*14.43*	*5.81*	**6**	*10.37*	*20.20*	*24.20*	*20.80*	*14.20*	**18**
Zr	*32*	*125*	**142**	*97*	*152*	*119*	*124*	*171*	**195**
V	197	9	**12**	104	157	207	208	53	**60**
Ni	70	4	**4**	86	27	71	121	9	**12**
Cr	58	1	**18**	122	40	221	270	8	**29**
Nb	*2.41*	*6.63*	**9**	*5.64*	*8.62*	*9.36*	*8.49*	*8.85*	**12**
Ga	20	14	**19**	16	19	18	17	15	**20**
Cu	27	1	**5**	36	49	30	65	10	**23**
Zn	77	73	**46**	53	84	100	95	50	**56**
Co	--	--	**<1**	--	--	--	--	--	**7**
Ba	*247*	*906*	**960**	*595*	*346*	*289*	*496*	*642*	**747**
La	9	19	**29**	13	17	16	24	18	**25**
Ce	17	25	**38**	25	40	37	48	35	**41**
U	*0.14*	*1.63*	**2**	*0.98*	*1.06*	*0.59*	*0.97*	*2.22*	**3**
Th	*0.35*	*4.81*	**13**	*2.28*	*2.45*	*1.47*	*2.99*	*5.12*	**12**
Sc	*19.8*	*1.3*	**1**	*13.0*	*17.7*	*30.6*	*25.4*	*6.0*	**5**
Pb	*1.99*	*8.75*	**18**	*4.99*	*3.73*	*2.23*	*4.37*	*6.89*	**6**
Hf	*0.87*	*3.25*	--	*2.47*	*3.63*	*2.90*	*3.29*	*4.08*	--
Ta	*0.20*	*0.61*	--	*0.41*	*0.59*	*0.53*	*0.54*	*0.79*	--
Cs	*0.04*	*0.98*	--	*0.61*	*0.06*	*0.19*	*0.45*	*0.51*	--
La	*8.80*	*18.48*	--	*13.25*	*17.22*	*18.50*	*22.03*	*19.71*	--
Ce	*18.97*	*31.39*	--	*25.50*	*35.77*	*39.79*	*47.19*	*35.62*	--
Pr	*2.63*	*3.23*	--	*3.08*	*4.49*	*5.23*	*6.28*	*3.90*	--
Nd	*11.54*	*10.60*	--	*11.98*	*18.28*	*21.82*	*25.93*	*13.67*	--
Sm	*3.00*	*1.68*	--	*2.64*	*4.13*	*5.14*	*5.57*	*2.75*	--
Eu	*1.26*	*0.50*	--	*0.86*	*1.35*	*1.64*	*1.73*	*0.84*	--
Gd	*3.10*	*1.23*	--	*2.29*	*3.95*	*4.83*	*4.74*	*2.49*	--
Tb	*0.48*	*0.18*	--	*0.35*	*0.65*	*0.79*	*0.72*	*0.41*	--
Dy	*2.89*	*1.03*	--	*2.04*	*3.95*	*4.80*	*4.15*	*2.56*	--
Ho	*0.58*	*0.21*	--	*0.40*	*0.78*	*0.97*	*0.83*	*0.52*	--
Er	*1.54*	*0.57*	--	*1.07*	*2.10*	*2.60*	*2.18*	*1.45*	--
Tm	*0.21*	*0.09*	--	*0.15*	*0.31*	*0.36*	*0.30*	*0.22*	--
Yb	*1.27*	*0.59*	--	*0.93*	*1.93*	*2.25*	*1.80*	*1.49*	--
Lu	*0.19*	*0.10*	--	*0.14*	*0.31*	*0.34*	*0.29*	*0.25*	--
Age	22.9	24.13	24.81	--	--	25.5	26.2	22.94	23.18
error	2.2	0.17	0.3	--	--	2.9	1.2	0.19	0.18

Sample ID	15JB30LA	15JB31LA	15JB33LA	15JB34LA	15JB37LA	15JB38LA	15JB39LA	15JB40LA	15JB41LA
Rock Unit/Location	Rocker Creek	Rocker Creek	Rocker Creek	Rocker Creek	Border Lava	Silicic Lava	Rocker Creek	Rocker Creek	Rocker Creek
SiO_2	63.29	**58.40**	59.27	66.54	67.05	75.10	68.76	62.99	**64.75**
TiO_2	0.56	**0.79**	0.89	0.40	0.77	0.06	0.30	0.60	**0.58**
Al_2O_3	14.92	**16.27**	16.11	15.67	16.30	14.04	16.08	17.12	**17.09**
Fe_2O_3*	4.20	**7.02**	5.85	3.00	3.28	0.65	2.83	4.30	**4.33**
MnO	0.07	**0.13**	0.09	0.05	0.19	0.05	0.03	0.04	**0.07**
MgO	3.35	**6.62**	4.11	1.76	0.35	0.20	0.73	1.58	**2.01**
CaO	5.88	**6.66**	5.64	4.30	3.13	0.72	3.42	4.89	**4.19**
Na_2O	3.83	**3.30**	4.14	4.48	5.00	3.84	4.86	4.42	**4.36**
K_2O	1.02	**0.80**	1.19	1.44	2.72	3.78	1.40	1.51	**2.07**
P_2O_5	0.13	**0.18**	0.31	0.12	0.23	0.06	0.09	0.24	**0.23**
Total	96.82	**100.17**	97.00	97.45	98.66	98.43	98.20	97.24	**99.68**
LOI	2.49	**1.93**	2.40	1.92	1.32	1.33	1.62	1.92	**1.70**
Rb	*27.6*	**19**	*21.4*	*38.3*	*54.9*	*95.3*	*22.5*	*30.5*	**51**
Sr	*515*	**598**	*745*	*561*	*394*	*99*	*517*	*693*	**647**
Y	*12.24*	**21**	*14.12*	*9.25*	*23.46*	*11.53*	*7.28*	*11.63*	**13**
Zr	*105*	**115**	*128*	*114*	*209*	*52*	*75*	*125*	**132**
V	94	**136**	115	61	57	5	34	79	**85**
Ni	58	**154**	114	36	3	3	20	9	**12**
Cr	122	**305**	214	70	2	2	17	3	**21**
Nb	*4.50*	**6**	9.31	5.21	11.53	14.90	2.64	8.58	**9**
Ga	15	**19**	17	16	18	17	15	17	**20**
Cu	26	**48**	29	21	6	1	12	30	**36**
Zn	53	**65**	62	48	62	27	40	57	**59**
Co	--	**29**	--	--	--	--	--	--	**8**
Ba	*565*	**463**	*630*	*740*	*665*	*1286*	*622*	*718*	**806**
La	9	**17**	18	11	20	10	8	15	**20**
Ce	19	**27**	35	22	42	19	10	35	**39**
U	*1.05*	**<0.5**	*0.94*	*1.43*	*2.65*	*3.18*	*0.37*	*1.25*	**2**
Th	*2.24*	**1**	*2.40*	*3.03*	*6.05*	*5.06*	*0.92*	*2.99*	**3**
Sc	*12.9*	**17**	*13.8*	*7.6*	*8.8*	*3.1*	*4.8*	*6.5*	**7**
Pb	*6.02*	**28**	*4.66*	*7.26*	*7.86*	*14.78*	*4.61*	*5.14*	**17**
Hf	*2.69*	--	*3.11*	*2.88*	*5.31*	*2.21*	*2.20*	*3.04*	--
Ta	*0.37*	--	*0.65*	*0.44*	*0.90*	*1.62*	*0.23*	*0.63*	--
Cs	*0.24*	--	*0.38*	*1.00*	*0.70*	*3.08*	*0.14*	*0.37*	--
La	*10.73*	--	*17.23*	*12.70*	*22.07*	*9.28*	*5.32*	*17.88*	--
Ce	*20.88*	--	*34.90*	*23.47*	*43.17*	*18.19*	*10.52*	*33.40*	--
Pr	*2.53*	--	*4.32*	*2.73*	*5.14*	*2.03*	*1.39*	*3.83*	--
Nd	*10.54*	--	*17.43*	*10.47*	*20.08*	*6.90*	*5.72*	*14.43*	--
Sm	*2.37*	--	*3.65*	*2.16*	*4.44*	*1.68*	*1.48*	*2.91*	--
Eu	*0.78*	--	*1.19*	*0.69*	*1.27*	*0.29*	*0.49*	*0.92*	--
Gd	*2.37*	--	*3.24*	*1.99*	*4.22*	*1.62*	*1.56*	*2.57*	--
Tb	*0.39*	--	*0.49*	*0.31*	*0.70*	*0.30*	*0.25*	*0.39*	--
Dy	*2.30*	--	*2.84*	*1.80*	*4.33*	*1.88*	*1.43*	*2.25*	--
Ho	*0.47*	--	*0.54*	*0.36*	*0.90*	*0.38*	*0.28*	*0.44*	--
Er	*1.31*	--	*1.42*	*0.93*	*2.50*	*1.05*	*0.76*	*1.16*	--
Tm	*0.19*	--	*0.20*	*0.13*	*0.37*	*0.16*	*0.11*	*0.17*	--
Yb	*1.18*	--	*1.24*	*0.83*	*2.37*	*1.03*	*0.68*	*1.09*	--
Lu	*0.18*	--	*0.19*	*0.13*	*0.39*	*0.16*	*0.11*	*0.17*	--
Age	24.49	23.4	26	26.58	19.62	23.26	23.17	25.96	23.53
error	0.57	0.49	0.2	0.49	0.53	0.08	0.19	0.38	0.19

Sample ID	15JB42LA	15JB44LA	15JB45LA	15JB46LA	15JB47LA	15JB49LA*	WSU XRF	*WSU ICP-MS*	F&M XRF
Rock Unit/Location	**Rocker Creek**	**Rocker Creek**	**Rocker Creek**	**Border Lava**	**Rocker Creek**	**Rocker Creek**			
SiO_2	55.27	67.27	61.28	66.79	59.06	57.14	0.035		**0.0487**
TiO_2	1.15	0.27	0.70	0.47	0.77	0.68	0.0065		**0.0049**
Al_2O_3	17.29	15.76	16.05	15.08	17.17	13.87	0.02		**0.0179**
Fe_2O_3*	7.97	2.64	5.35	3.78	6.10	4.72	0.01		**0.0128**
MnO	0.15	0.02	0.09	0.04	0.09	0.09	0.001		**0.0004**
MgO	4.05	0.99	2.59	0.99	3.31	2.27	0.055		**0.0071**
CaO	7.23	3.68	4.99	3.06	6.09	6.76	0.015		**0.009**
Na_2O	4.19	4.82	4.07	4.48	4.33	4.33	0.035		**0.0042**
K_2O	1.22	0.97	1.34	1.48	1.31	2.16	0.005		**0.0014**
P_2O_5	0.31	0.09	0.20	0.14	0.27	0.21	0.0015		**0.0009**
Total	98.02	96.25	96.11	95.95	97.88	91.76			
LOI	1.62	2.80	3.19	3.39	1.25	7.48			
Rb	*20.5*	*23.4*	*26.6*	*25.4*	*21.6*	*44.0*		*0.28*	**0.46**
Sr	*570*	*503*	*421*	*343*	*707*	*962*		*2.72*	**3.69**
Y	*23.02*	*6.27*	*15.57*	*12.73*	*17.05*	*21.56*		*0.23*	**0.29**
Zr	*204*	*82*	*150*	*157*	*152*	*179*		*0.77*	**1.94**
V	140	51	117	48	124	63	6.0		**2.28**
Ni	32	47	22	14	46	4	0.5		**0.70**
Cr	82	84	31	15	56	0	1.0		**9.60**
Nb	*10.67*	*2.45*	*7.09*	*7.83*	*9.82*	*9.66*		*0.05*	**0.42**
Ga	19	16	17	14	18	15	1.0		**0.13**
Cu	30	20	30	10	26	4	1.5		**3.49**
Zn	79	36	66	46	73	71	2.0		**0.50**
Co	--	--	--	--	--	--			**1.11**
Ba	*449*	*466*	*448*	*538*	*538*	*571*		*2.82*	**7.21**
La	18	4	12	20	18	19	7.5		**1.25**
Ce	35	9	30	30	35	36	9.0		**0.87**
U	*1.05*	*0.54*	*1.46*	*1.52*	*1.08*	*2.02*		*0.01*	**0.48**
Th	*2.46*	*1.17*	*3.30*	*4.56*	*2.52*	*4.92*		*0.03*	**0.47**
Sc	*18.8*	*6.1*	*12.8*	*6.6*	*13.1*	*8.4*		*0.42*	**0.64**
Pb	*4.35*	*4.15*	*5.30*	*6.10*	*3.73*	*6.99*		*0.17*	**0.40**
Hf	*4.43*	*2.32*	*3.56*	*3.78*	*3.60*	*4.41*		*0.03*	
Ta	*0.80*	*0.21*	*0.59*	*0.71*	*0.69*	*0.74*		*0.01*	
Cs	*0.38*	*0.19*	*0.27*	*1.12*	*0.24*	*0.44*		*0.01*	
La	*18.31*	*5.71*	*15.36*	*17.79*	*18.18*	*18.59*		*0.10*	
Ce	*37.41*	*10.99*	*28.77*	*32.52*	*35.86*	*36.66*		*0.23*	
Pr	*4.73*	*1.36*	*3.41*	*3.57*	*4.36*	*4.41*		*0.03*	
Nd	*19.02*	*5.49*	*13.17*	*12.87*	*17.38*	*16.94*		*0.15*	
Sm	*4.42*	*1.39*	*2.84*	*2.54*	*3.62*	*3.74*		*0.06*	
Eu	*1.49*	*0.45*	*0.98*	*0.79*	*1.21*	*1.08*		*0.02*	
Gd	*4.37*	*1.33*	*2.81*	*2.35*	*3.39*	*3.66*		*0.05*	
Tb	*0.72*	*0.20*	*0.47*	*0.38*	*0.53*	*0.61*		*0.01*	
Dy	*4.39*	*1.22*	*2.91*	*2.34*	*3.24*	*3.83*		*0.06*	
Ho	*0.91*	*0.24*	*0.60*	*0.48*	*0.66*	*0.81*		*0.01*	
Er	*2.49*	*0.66*	*1.68*	*1.33*	*1.81*	*2.25*		*0.04*	
Tm	*0.35*	*0.09*	*0.25*	*0.19*	*0.27*	*0.34*		*0.01*	
Yb	*2.25*	*0.58*	*1.61*	*1.28*	*1.65*	*2.16*		*0.03*	
Lu	*0.36*	*0.09*	*0.26*	*0.22*	*0.26*	*0.35*		*0.01*	
Age	27.2	117.07	23.43	21.27	27	21.4			
error	0.4	3.13	0.67	0.48	0.4	0.2			

Appendix C - $^{40}Ar/^{39}Ar$ Step-Heat Spectra

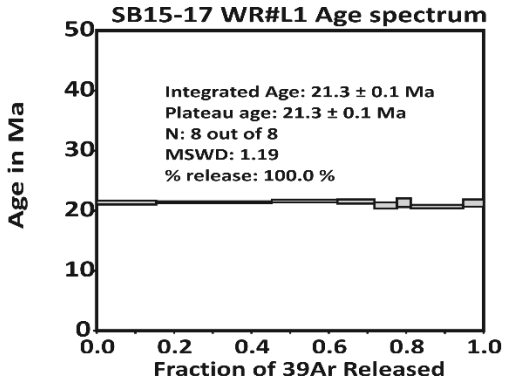

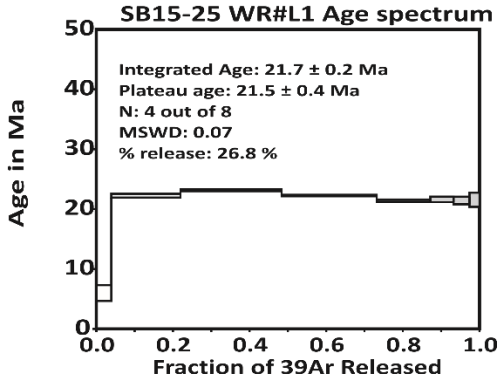

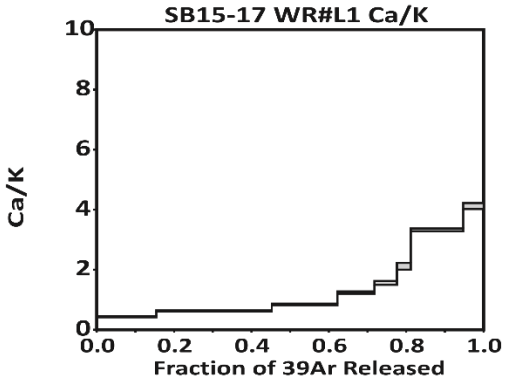

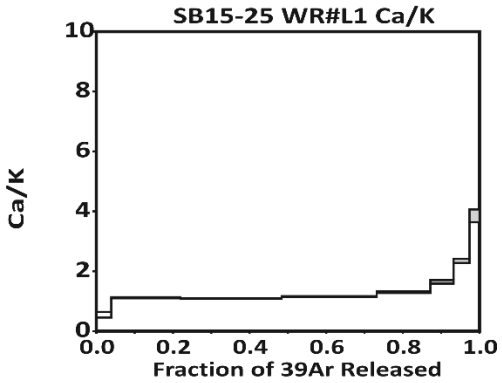

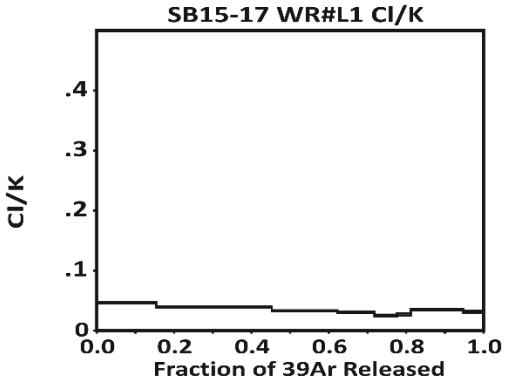

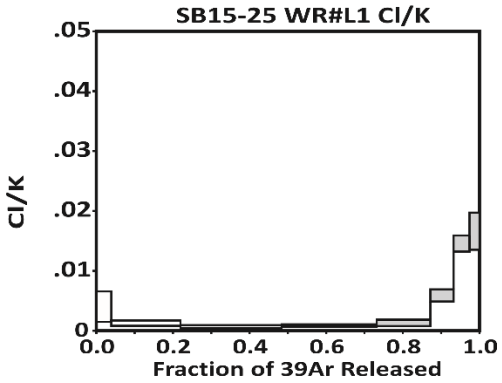

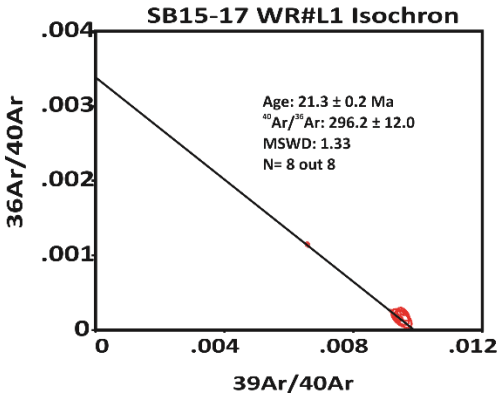

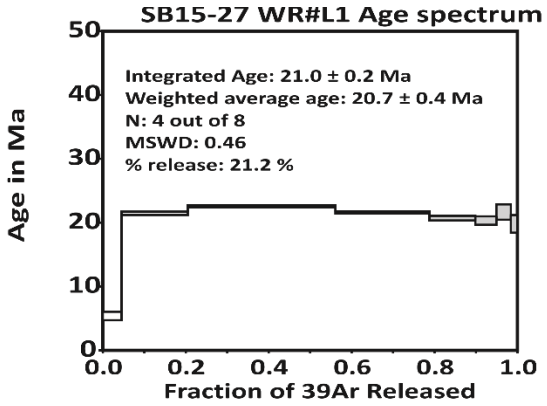
SB15-27 WR#L1 Age spectrum
Integrated Age: 21.0 ± 0.2 Ma
Weighted average age: 20.7 ± 0.4 Ma
N: 4 out of 8
MSWD: 0.46
% release: 21.2 %
Age in Ma
Fraction of 39Ar Released

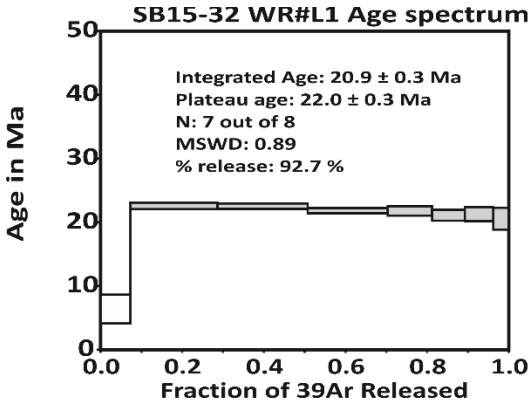
SB15-32 WR#L1 Age spectrum
Integrated Age: 20.9 ± 0.3 Ma
Plateau age: 22.0 ± 0.3 Ma
N: 7 out of 8
MSWD: 0.89
% release: 92.7 %
Age in Ma
Fraction of 39Ar Released

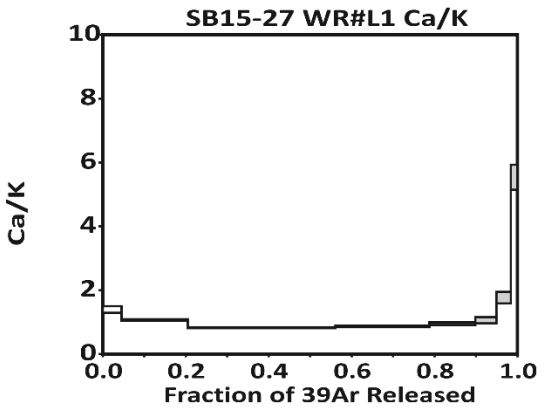
SB15-27 WR#L1 Ca/K
Ca/K
Fraction of 39Ar Released

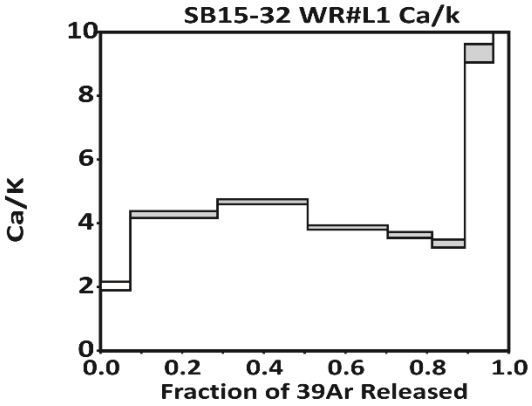
SB15-32 WR#L1 Ca/k
Ca/K
Fraction of 39Ar Released

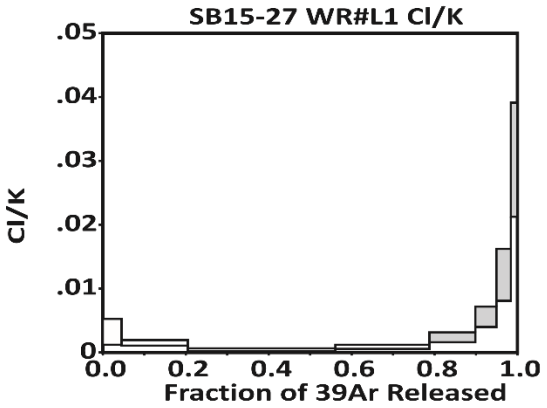
SB15-27 WR#L1 Cl/K
Cl/K
Fraction of 39Ar Released

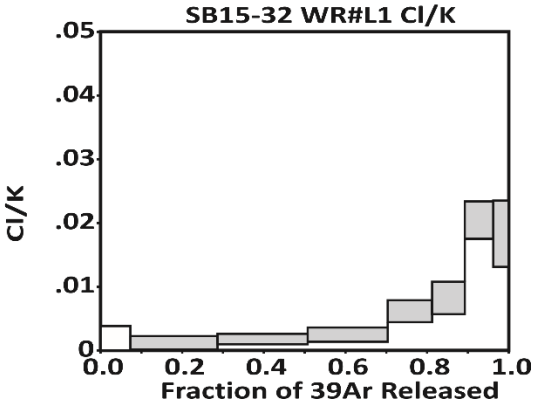
SB15-32 WR#L1 Cl/K
Cl/K
Fraction of 39Ar Released

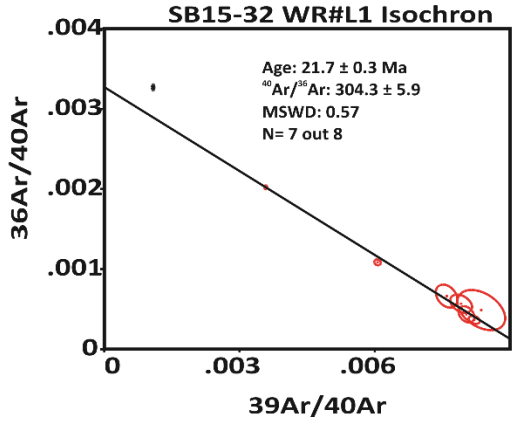
SB15-32 WR#L1 Isochron
Age: 21.7 ± 0.3 Ma
40Ar/36Ar: 304.3 ± 5.9
MSWD: 0.57
N= 7 out 8
36Ar/40Ar
39Ar/40Ar

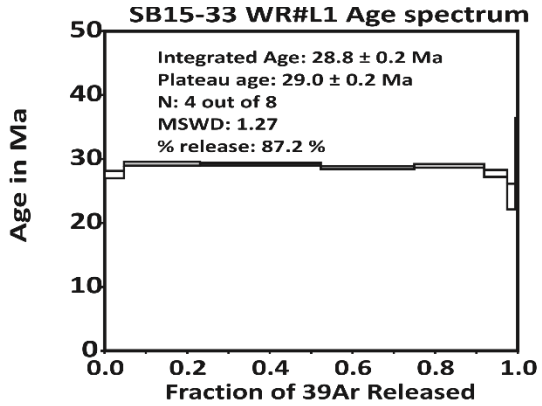
SB15-33 WR#L1 Age spectrum
Integrated Age: 28.8 ± 0.2 Ma
Plateau age: 29.0 ± 0.2 Ma
N: 4 out of 8
MSWD: 1.27
% release: 87.2 %
Age in Ma
Fraction of 39Ar Released

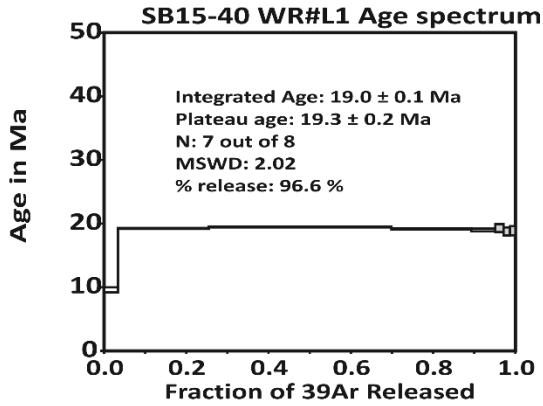
SB15-40 WR#L1 Age spectrum
Integrated Age: 19.0 ± 0.1 Ma
Plateau age: 19.3 ± 0.2 Ma
N: 7 out of 8
MSWD: 2.02
% release: 96.6 %
Age in Ma
Fraction of 39Ar Released

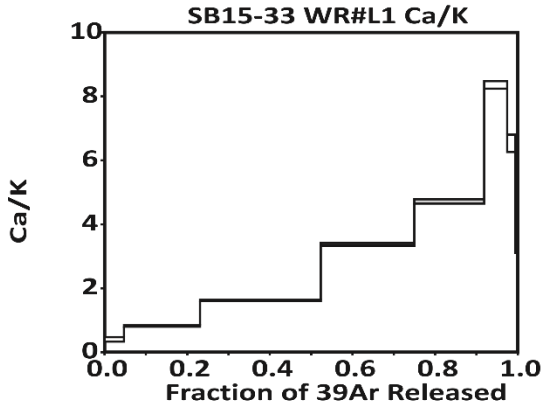
SB15-33 WR#L1 Ca/K
Ca/K
Fraction of 39Ar Released

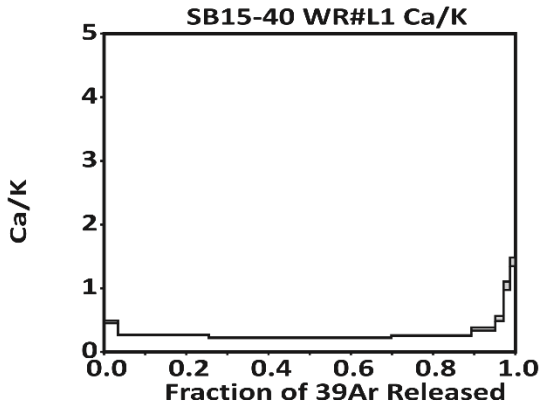
SB15-40 WR#L1 Ca/K
Ca/K
Fraction of 39Ar Released

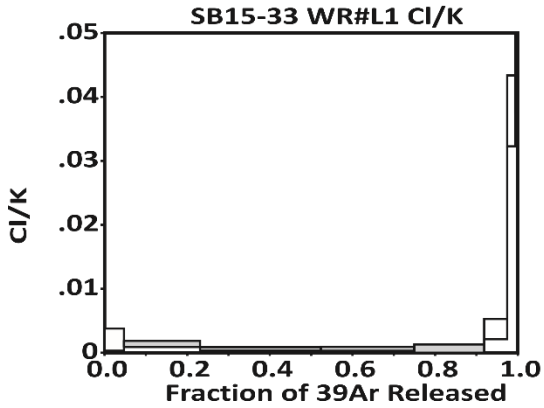
SB15-33 WR#L1 Cl/K
Cl/K
Fraction of 39Ar Released

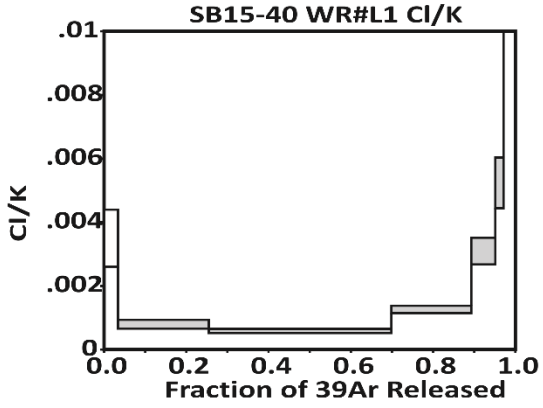
SB15-40 WR#L1 Cl/K
Cl/K
Fraction of 39Ar Released

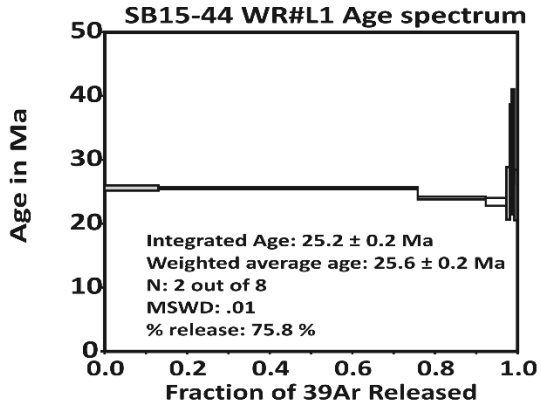
SB15-44 WR#L1 Age spectrum
Age in Ma
Integrated Age: 25.2 ± 0.2 Ma
Weighted average age: 25.6 ± 0.2 Ma
N: 2 out of 8
MSWD: .01
% release: 75.8 %
Fraction of 39Ar Released

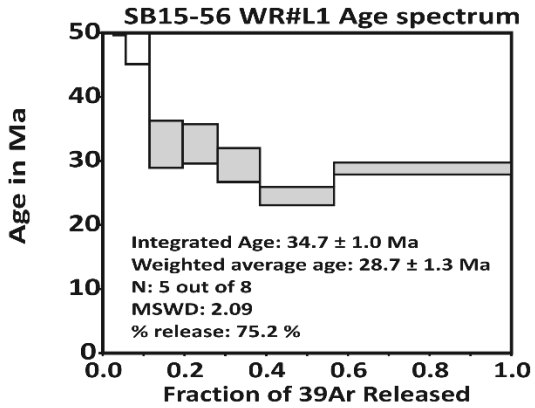
SB15-56 WR#L1 Age spectrum
Age in Ma
Integrated Age: 34.7 ± 1.0 Ma
Weighted average age: 28.7 ± 1.3 Ma
N: 5 out of 8
MSWD: 2.09
% release: 75.2 %
Fraction of 39Ar Released

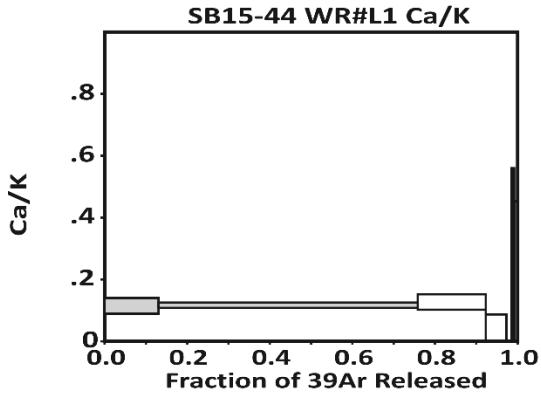
SB15-44 WR#L1 Ca/K
Ca/K
Fraction of 39Ar Released

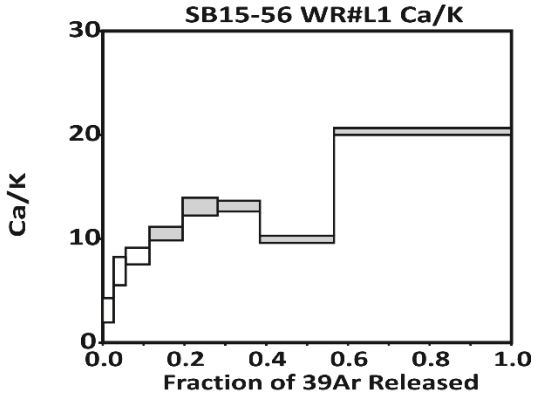
SB15-56 WR#L1 Ca/K
Ca/K
Fraction of 39Ar Released

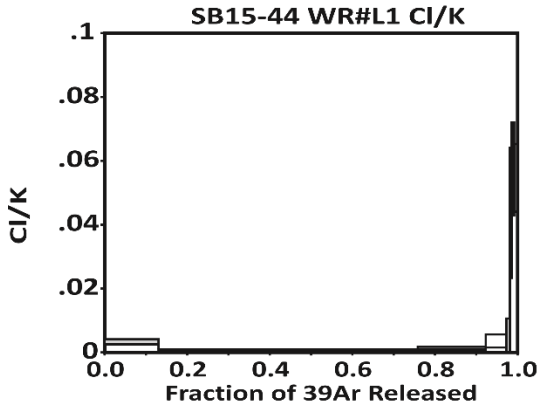
SB15-44 WR#L1 Cl/K
Cl/K
Fraction of 39Ar Released

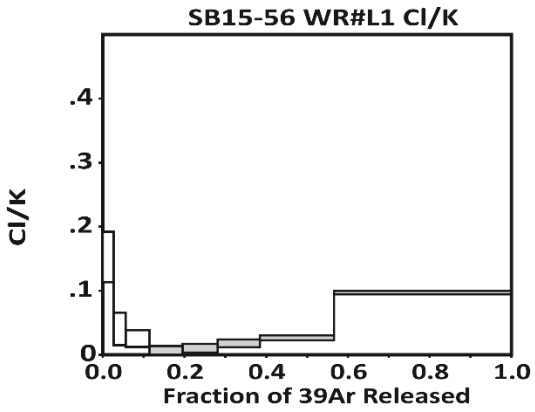
SB15-56 WR#L1 Cl/K
Cl/K
Fraction of 39Ar Released

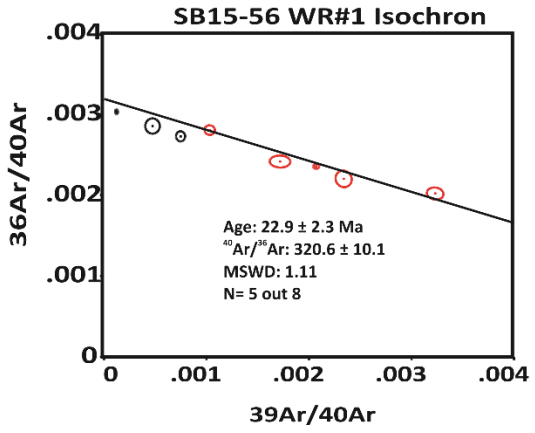
SB15-56 WR#1 Isochron
36Ar/40Ar
Age: 22.9 ± 2.3 Ma
40Ar/36Ar: 320.6 ± 10.1
MSWD: 1.11
N= 5 out 8
39Ar/40Ar

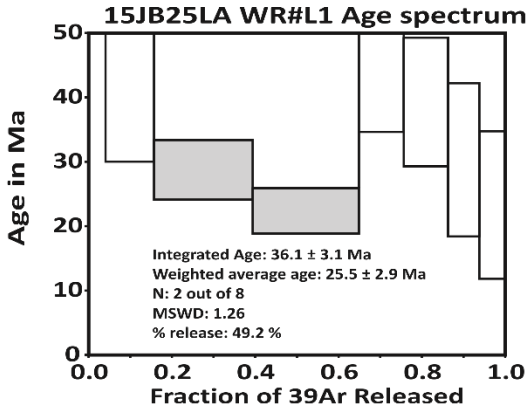
15JB25LA WR#L1 Age spectrum
Age in Ma
Integrated Age: 36.1 ± 3.1 Ma
Weighted average age: 25.5 ± 2.9 Ma
N: 2 out of 8
MSWD: 1.26
% release: 49.2 %
Fraction of 39Ar Released

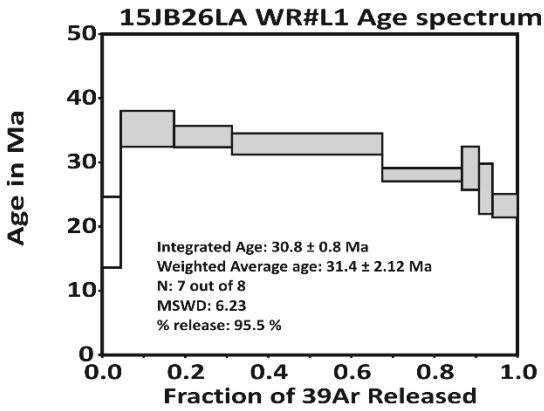
15JB26LA WR#L1 Age spectrum
Age in Ma
Integrated Age: 30.8 ± 0.8 Ma
Weighted Average age: 31.4 ± 2.12 Ma
N: 7 out of 8
MSWD: 6.23
% release: 95.5 %
Fraction of 39Ar Released

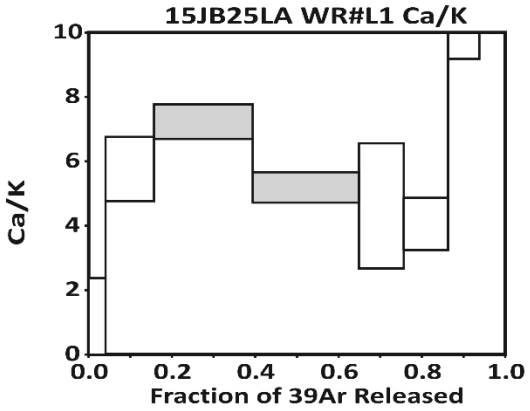
15JB25LA WR#L1 Ca/K
Ca/K
Fraction of 39Ar Released

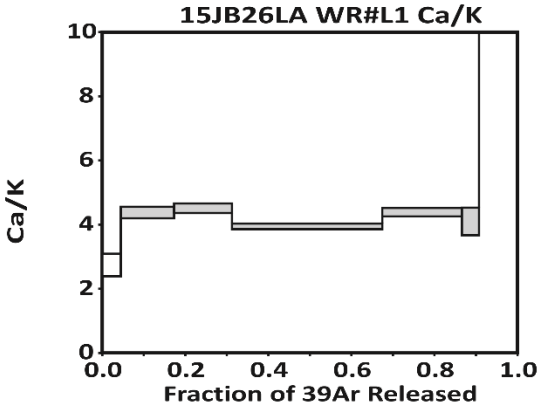
15JB26LA WR#L1 Ca/K
Ca/K
Fraction of 39Ar Released

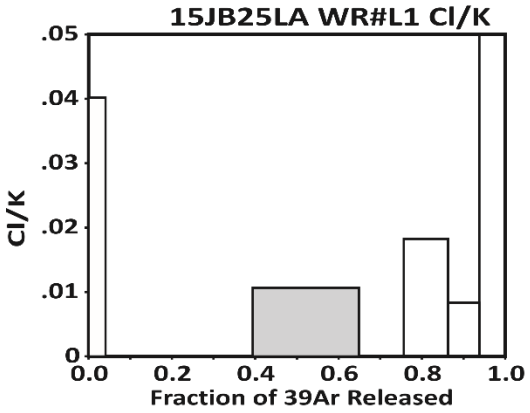
15JB25LA WR#L1 Cl/K
Cl/K
Fraction of 39Ar Released

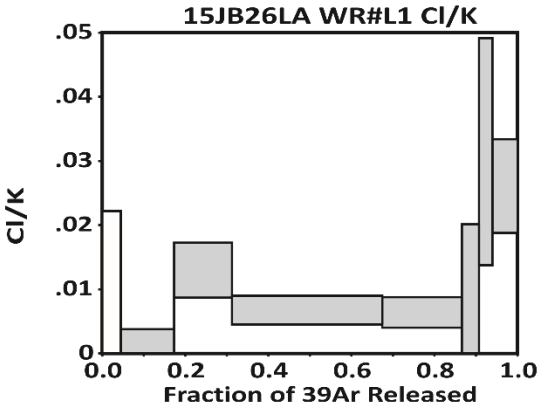
15JB26LA WR#L1 Cl/K
Cl/K
Fraction of 39Ar Released

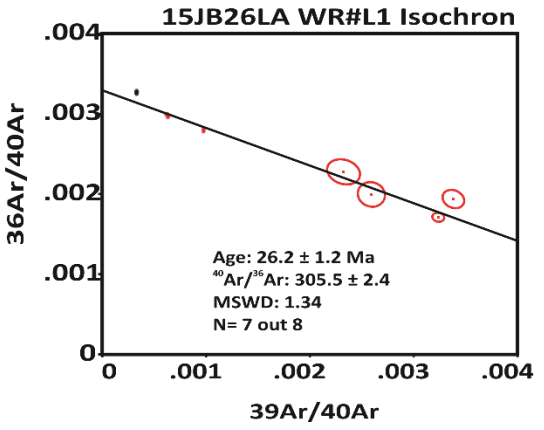
15JB26LA WR#L1 Isochron
36Ar/40Ar
Age: 26.2 ± 1.2 Ma
40Ar/36Ar: 305.5 ± 2.4
MSWD: 1.34
N= 7 out 8
39Ar/40Ar

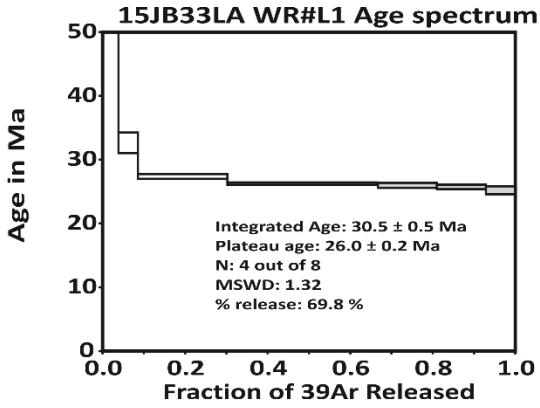
15JB33LA WR#L1 Age spectrum
Age in Ma
Integrated Age: 30.5 ± 0.5 Ma
Plateau age: 26.0 ± 0.2 Ma
N: 4 out of 8
MSWD: 1.32
% release: 69.8 %
Fraction of 39Ar Released

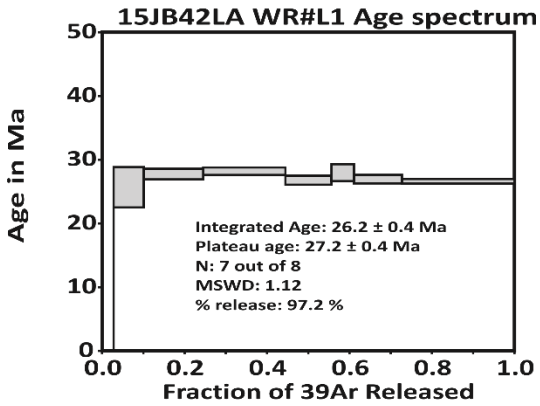
15JB42LA WR#L1 Age spectrum
Age in Ma
Integrated Age: 26.2 ± 0.4 Ma
Plateau age: 27.2 ± 0.4 Ma
N: 7 out of 8
MSWD: 1.12
% release: 97.2 %
Fraction of 39Ar Released

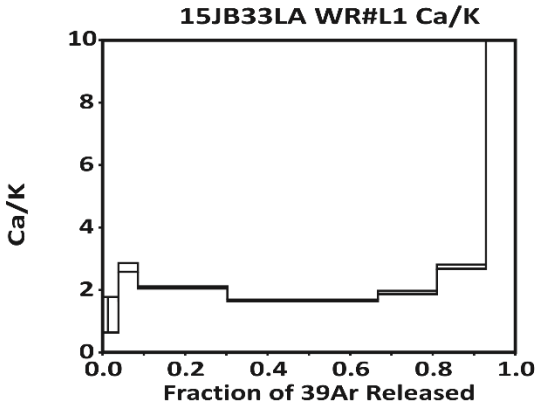
15JB33LA WR#L1 Ca/K
Ca/K
Fraction of 39Ar Released

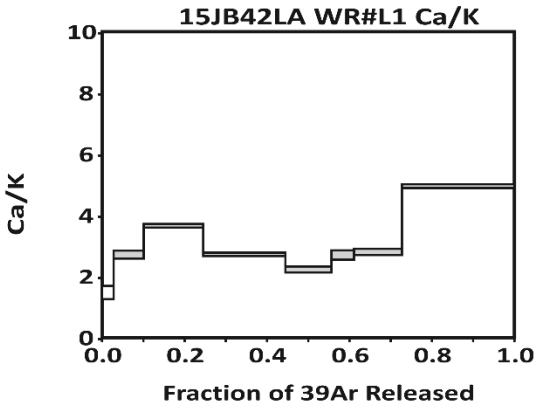
15JB42LA WR#L1 Ca/K
Ca/K
Fraction of 39Ar Released

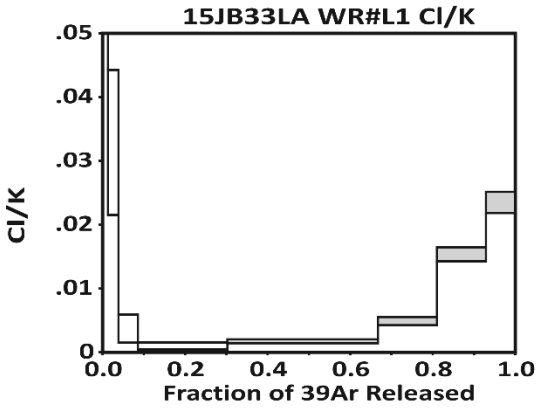
15JB33LA WR#L1 Cl/K
Cl/K
Fraction of 39Ar Released

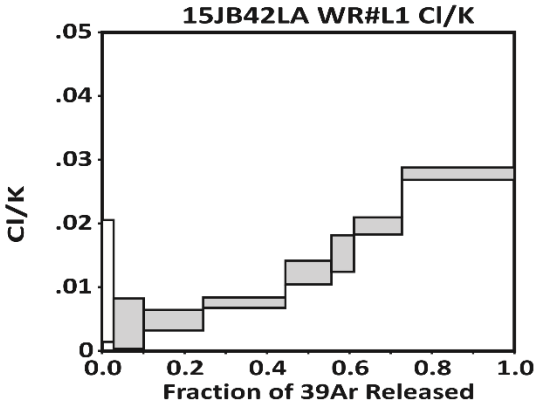
15JB42LA WR#L1 Cl/K
Cl/K
Fraction of 39Ar Released

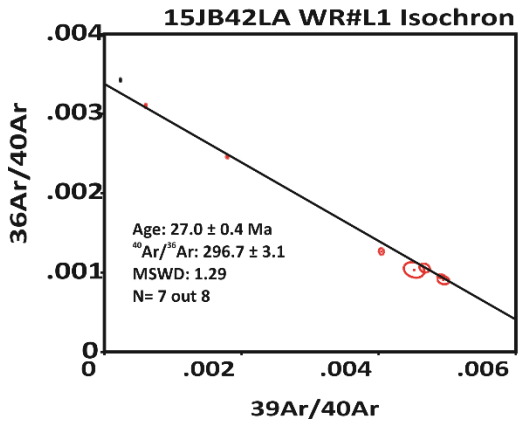
15JB42LA WR#L1 Isochron
36Ar/40Ar
Age: 27.0 ± 0.4 Ma
40Ar/36Ar: 296.7 ± 3.1
MSWD: 1.29
N= 7 out 8
39Ar/40Ar

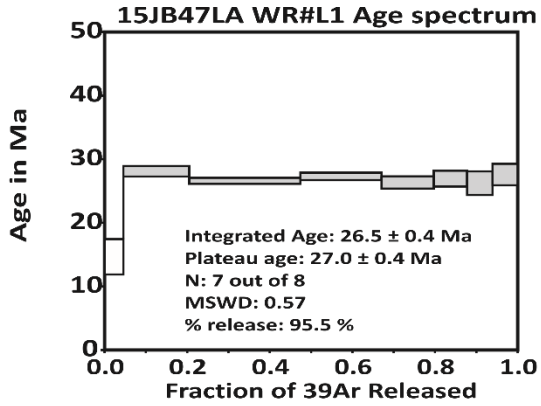
15JB47LA WR#L1 Age spectrum
Age in Ma
Integrated Age: 26.5 ± 0.4 Ma
Plateau age: 27.0 ± 0.4 Ma
N: 7 out of 8
MSWD: 0.57
% release: 95.5 %
Fraction of 39Ar Released

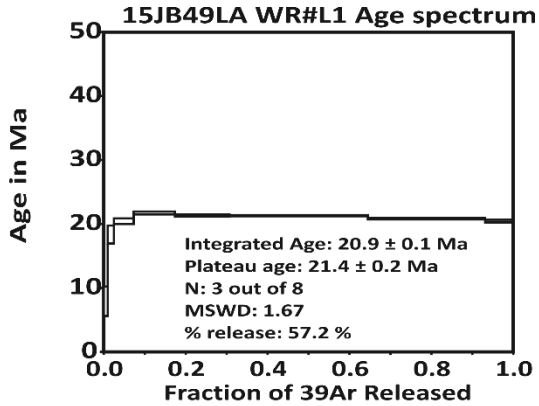
15JB49LA WR#L1 Age spectrum
Age in Ma
Integrated Age: 20.9 ± 0.1 Ma
Plateau age: 21.4 ± 0.2 Ma
N: 3 out of 8
MSWD: 1.67
% release: 57.2 %
Fraction of 39Ar Released

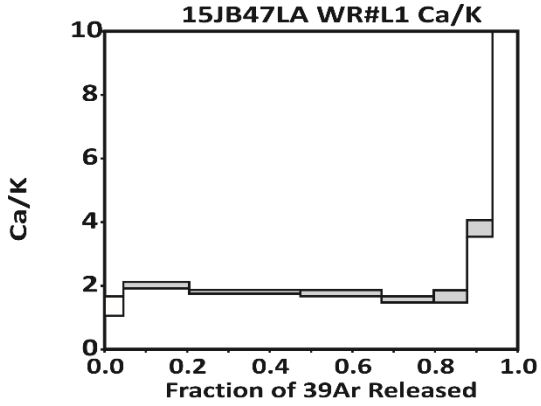
15JB47LA WR#L1 Ca/K
Ca/K
Fraction of 39Ar Released

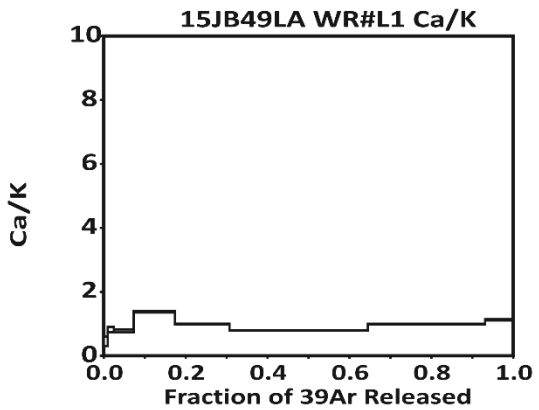
15JB49LA WR#L1 Ca/K
Ca/K
Fraction of 39Ar Released

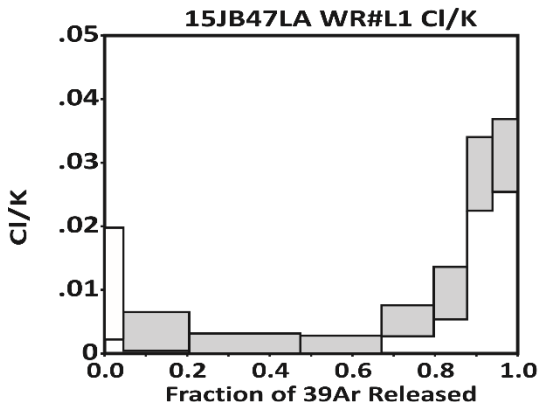
15JB47LA WR#L1 Cl/K
Cl/K
Fraction of 39Ar Released

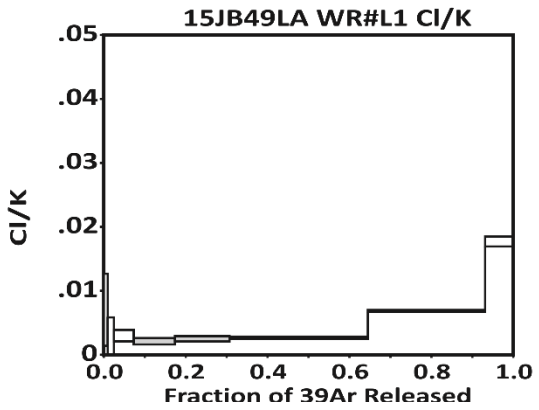
15JB49LA WR#L1 Cl/K
Cl/K
Fraction of 39Ar Released